About AECL

Atomic Energy of Canada Limited (AECL) is Canada's premiere nuclear science and technology laboratory. For over 60 years, AECL has been a world leader in developing peaceful and innovative applications of nuclear technology through its expertise in physics, metallurgy, chemistry, biology and engineering.

Today, AECL continues its commitment to ensure that Canadians and the world receive energy, health, environmental and economic benefits from nuclear science and technology with confidence that nuclear safety and security are assured.

COVER PHOTO
Secondary electron image of the fracture face of irradiated inconel. This photo is courtesy of the Reactor Chemistry and Corrosion Branch, Atomic Energy of Canada Limited (2013).

INVITED ARTICLES

FULL ARTICLES

TECHNICAL NOTES

ERRATUM

For nickel-containing alloys irradiated in thermalized neutron fluxes, the formation and reaction of ^{59}Ni with thermal neutrons can lead to time-varying changes in displacement damage rate, expressed as displacements per atom per second (dpa.s^{-1}), gas formation and nuclear heating. Ni-rich alloys are used in PWR and BWR reactors as spacers within fuel assemblies but also as tensioning springs for these same assemblies. Flux thimbles have also been made from Ni-rich alloys in the past but are gradually being replaced by thimbles made from other alloys containing substantially less Ni. In a CANDU® reactor, Ni-alloys are used as tensioning springs, fuel channel spacers (in the form of garter springs) and as cable sheathing and core wires in flux-detector assemblies. Prediction of the irradiation processes that affect the functionality of these CANDU internals, such as irradiation embrittlement and irradiation creep, especially under conditions of extended operation, necessitates a consideration of the effect of the transmutation of Ni.

Over the past 10 years, there has been a considerable increase in the understanding of the effects of irradiation on the properties of components made from Ni-rich alloys. The nuclear processes and the effects of irradiation damage on the performance of components made from these alloys will be described.

The Effect of Irradiation on Ni-containing Components in CANDU® Reactor Cores: A Review

M.Griffiths[*]
*Atomic Energy of Canada Limited, Chalk River Laboratories, Chalk River, Ontario, Canada K0J 1J0

*Corresponding author: (613) 584-3311, griffithsm@aecl.ca

1. Introduction

Nickel forms the basis of a large class of materials called super-alloys that have good mechanical strength and good creep properties at high temperatures. Ni-alloys are therefore widely used in turbine engines and, because they also have good corrosion properties, they are used in a wide variety of industrial applications. Ni-alloys are mainly used in the cores of nuclear reactors as fasteners (bolts), spacers, and springs. They are not used extensively in the cores of conventional power reactors because they absorb the slow thermal neutrons needed to maintain the nuclear chain reactions and they also become highly radioactive, which can impede maintenance. For CANDU reactors in particular, neutron economy is very important and having neutron-absorbing materials, such as Ni-alloys, in the core is not desirable. However, Ni-alloys have been used in specialized core components, especially springs, for many years. Those Ni-alloys most commonly used in the cores of power reactors are Inconel® 600, Inconel 625, Inconel 718 and Inconel X-750. The composition of these alloys is shown in Table 1.

Ni-alloy components in Boiling Water Reactors (BWR) and Pressurized Water Reactor (PWR) fuel assemblies are not subjected to very high neutron exposures because their residency times within the core are short (up to five years) relative to the operating life for many reactors (30-40 years). Other Ni-alloy components, such as tensioning springs for reactivity control systems in CANDU reactors, reside outside of the reactor core. These peripheral components are not part of the fuel assemblies, are an integral part of the reactor structure and therefore often operate for the life of the reactor. Some Ni-alloy components such as flux detector thimble tubes and cladding for absorber rods in some PWR reactors, and flux-detector assemblies and fuel-channel spacers in CANDU reactors, are subjected to high neutron exposures because they reside within the core, and for much longer periods than the PWR and BWR fuel assemblies.

Although Ni-alloys have been successfully used in nuclear reactors for many years, evidence is accruing that they are also subject to long-term radiation effects that are more severe than for reactor-core components made from other alloys, in particular Zr-alloys. Just as Zr is unusual in having a very low neutron absorption cross-section (the reason why it is the most commonly used core material), Ni also has certain unusual

TABLE 1: Major Elements (wt%) in Ni-alloys Commonly Used in Reactor Cores [1-4]

Inconel	Ni	Cr	Fe	Mo	Nb	Co	Mn	Cu	Al	Ti	Si	C
600	72.0	14.0-17.0	6.0-10.0				1.0	0.5			0.5	0.15
625	58.0	20.0-23.0	5.0	8.0-10.0	3.15-4.15	1.0	0.5		0.4	0.4	0.5	0.1
718	50.0-55.0	17.0-21.0	11.2-22.5	2.8-3.3	4.75-5.5	1.0	0.35	0.2-0.8	0.65-1.15	0.3	0.35	0.08
X-750	70.0	14.0-17.0	5.0-9.0		0.7-1.2	1.0	1.0	0.5	0.4-1.0	2.25-2.75	0.5	0.08

in structural alloys for nuclear reactor cores, although the effect of irradiation is less benign in this case [5-7].

Ni-alloy components are exposed to a range of conditions for varying times within, and around the periphery, of power-reactor cores. The neutron spectra can be different at each location and the spectrum, rather than the total neutron exposure, can have a profound impact on the properties and therefore function of the component.

The CANDU nuclear reactor contains different Ni-alloy components at various locations and is ideally suited for the study of the response of Ni-alloys to differences in temperature, neutron flux and neutron spectrum. The remainder of this review will therefore focus on the effects of irradiation on Ni-alloy components in a CANDU reactor, although the discussion is useful for all power-reactor systems. This review is mostly based on a compilation of results for CANDU reactors that have been reported elsewhere [8-12].

In a CANDU reactor, Ni-alloys are used as tensioning springs, fuel channel spacers (in the form of garter springs) and as cable sheathing and core wires in flux detector assemblies. Prediction of the irradiation processes that affect the functionality of these CANDU internals, such as irradiation embrittlement and irradiation creep, especially under conditions of extended operation, necessitates a consideration of the nuclear reactions between neutrons and Ni.

2. Radiation Damage
The unusual properties of Ni with respect to certain nuclear reactions are by now well known and established [13-19]. Ni-rich components in reactors that have a high thermal and epi-thermal neutron flux are particularly prone to degradation as a result of a two-stage process involving the transmutation of ^{58}Ni to ^{59}Ni, followed by various nuclear reactions involving ^{59}Ni.

Unlike materials test reactors such as EBR-II, which have been used in the past to generate much of the available data on mechanical properties and creep response to irradiation of Ni-rich alloys, the CANDU reactor contains an abundance of thermal and epi-thermal neutrons (Figure 1). For this reason, many of the effects of neutron irradiation that stem from transmutations of Ni in thermal-neutron power reactor environments have not been apparent until recent years. At this time, more and more data are accruing from Ni-alloy components removed from power reactors that have been subjected to high neutron doses that were hitherto restricted to materials tests in high-flux reactors such as EBR-2, HFIR or ATR.

The nuclear properties of Ni in a high thermal-neutron flux environment leads to enhanced production of displaced atoms, hydrogen and helium. In particular, ^{59}Ni (which does not exist in natural nickel) is generated by thermal neutron capture by ^{58}Ni, which is the most abundant isotope in Ni (about 68%). ^{59}Ni, in turn, has very high neutron capture cross-sections for (n,α), (n,p) and (n,γ) over a wide range of neutron energies and it is this fact that makes Ni unusual amongst the alloying elements that make up the structural core components of nuclear reactors. The two-stage transmutations of ^{58}Ni to ^{59}Ni with subsequent (n,γ), (n,p) and (n,α) reactions are illustrated below:

$$^{58}\text{Ni} + \text{n} \rightarrow {}^{59}\text{Ni} + \gamma$$
$$^{59}\text{Ni} + \text{n} \rightarrow {}^{56}\text{Fe} + {}^{4}\text{He}$$
$$^{59}\text{Ni} + \text{n} \rightarrow {}^{59}\text{Co} + \text{H}$$
$$^{59}\text{Ni} + \text{n} \rightarrow {}^{60}\text{Ni} + \gamma$$
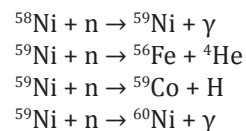
The ^{59}Ni (n, α) reaction releases 5.10 MeV, producing a 4.8 MeV α-particle, which loses most of its energy by electronic losses as it slows down over its trajectory of about 9 μm within the matrix, depositing thermal energy but producing only about 62 atomic displacements per each event [9]. However, the recoiling ^{56}Fe carries 340 keV, which

is large compared to most primary knock-on energies, and produces about 1701 displacements per event [13]. The thermal (n, p) reaction of ^{59}Ni produces about 1 proton per six helium atoms, reflecting the difference in thermal neutron cross sections of 2.0 and 12.3 barns, and is somewhat less energetic (1.85 MeV), producing a total of about 222 displacements per event [14]. Apart from the displacement damage and gas production, the nuclear heating rates in the material will also be augmented. All of these factors can have an impact on the behavior of components made from Ni-rich alloys in a nuclear reactor.

As a result of the reactions of ^{58}Ni (n,α) and ^{58}Ni (n,p) occurring at high neutron energies (E>1 MeV), there is additional production of helium and hydrogen due to Ni in most reactors. Other alloying elements present in Ni-alloys and steels, such as Cr and Fe, have (n,γ) reactions with thermal neutrons, E< 0.625 eV, and also (n,α) and (n,p) reactions with high neutron energies, E>1 M eV. The contribution from these other alloying elements to the overall radiation-induced damage and gas production is, of course, dependent on the spectrum. The impact of the high energy (n,α) and (n,p) reactions from elements other than Ni decreases with increasing thermal neutron dose as the ^{59}Ni concentration increases.

In general, care must be taken with the assessment of dose when variations in neutron spectra exist between the test environment and the environment of the application of interest. Greenwood and Smither [20] have developed an industry standard code (SPECTER) to calculate displacement damage and gas production rates in different materials for a given neutron spectrum. The SPECTER code also provides spectrum-averaged cross-sections for the (n,γ) reactions for ^{58}Ni and ^{59}Ni , and the (n,α) and (n,p) reactions for ^{59}Ni that are used, in conjunction with the formulae given in [13-14], to compute the ^{59}Ni concentration and the accumulated hydrogen and helium from ^{59}Ni. The formulae and cross-sections used to calculate the gas production from pure Ni have been assessed previously by Greenwood et al. [21]. They showed that He production was predicted well using the conventional high neutron energy (n,α) cross-sections for naturally occurring Ni isotopes in addition to the two-stage ^{58}Ni (n,γ)^{59}Ni(n,α) reaction after irradiation in the HFIR reactor over a thermal fluence range up to about 4 x 10^{26} n.m^{-2}, corresponding with about 10 years of full-power operation in a CANDU reactor core. In a similar validation exercise for the CANDU-reactor case, He measurements were obtained from Inconel X-750 spacers removed after about 14 full power years of service [12], and were shown to be slightly lower than predicted, i.e., He concentration measurements were about 90% of that predicted using the formulae reported by Greenwood [13].

In addition to validating equations and cross-sections, Greenwood et al. [21] also showed that surprisingly large quantities of hydrogen were retained in the material over a temperature range of 300 °C to 600 °C, although it was recognized that some of the retained hydrogen could have been picked up from the environment. Analysis of Inconel X-750 spacer material at CRL after irradiation in the CANDU core up to about 14 full-power years of operation has shown that hydrogen was not measurable in any statistically significant quantities and, although some hydrogen may be trapped within cavities, it seems that the majority of the hydrogen is not retained within the material [12]. For this reason, the possible effects of hydrogen will not be discussed in connection with the properties of irradiated CANDU reactor components in this paper.

Fast reactors were often used in the past to perform accelerated irradiation tests where the emphasis was on the production of radiation damage in the form of displaced atoms. Because fast reactors have very high fast neutron fluxes, the displacement damage is generally significantly higher than a conventional power reactor (by a factor of ten) and, therefore, it is instructive to examine the ^{59}Ni production as a function of displacement damage to understand the relative contribution of ^{59}Ni when simulating radiation damage of power reactor components in a fast reactor. The ^{59}Ni production as a function of displacement damage in a fast reactor materials irradiation location (8D5 in EBR-2) compared with a CANDU reactor core is plotted in Figure 2. This plot corresponds with the spectra shown in Figure 1. It is clear that the amount of ^{59}Ni reaches a peak value of about 0.04^{58}Ni$_o$, where ^{58}Ni$_o$ refers to the original ^{58}Ni concentration of the alloy prior to any
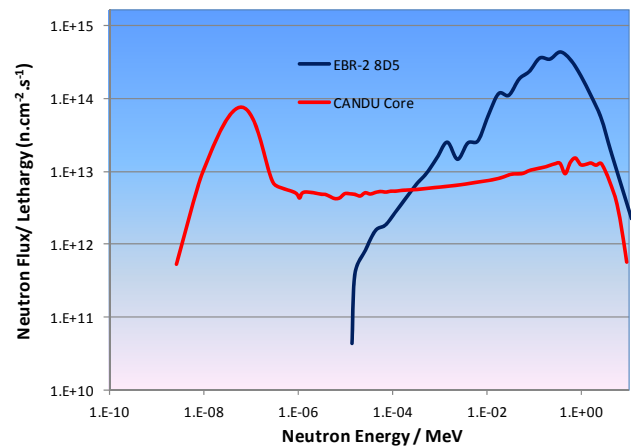

FIGURE 1: Comparison of neutron spectra for the one location in a fast-breeder reactor (EBR-2, row 8) compared with a typical power reactor (CANDU) [12].
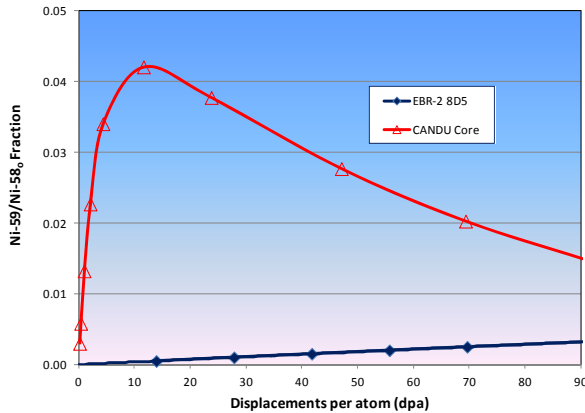
FIGURE 2: ^{59}Ni concentration as a fraction of the original ^{58}Ni concentration for the core region of a fast-breeder reactor (EBR-2) compared with a typical power reactor (CANDU) as a function of displacement damage dose [12].
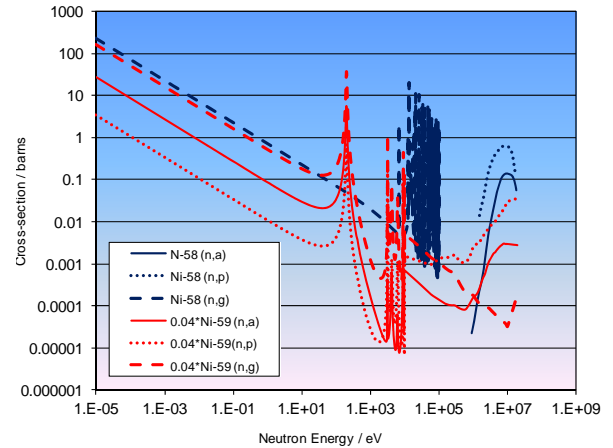

FIGURE 3: Reaction cross-section for (n,α), (n,p) and (n,γ) reactions of ^{58}Ni and ^{59}Ni as a function of neutron energy. The ^{59}Ni cross-sections have been weighted by a factor of 4% for comparison with the reaction rates of ^{58}Ni at the point where the ^{59}Ni is at its highest concentration [22].

irradiation, at substantially lower displacement damage doses in the CANDU compared with the fast reactor. The peak in ^{59}Ni concentration occurs after about five years of full-power operation in a high-power location in a CANDU reactor core. When ^{59}Ni is close to its peak concentration, a fast-reactor simulation based on displacement damage will not accurately reflect the substantial effects of gas production from ^{59}Ni in a power-reactor environment. Eventually, because of the high thermal neutron reaction cross-sections of ^{59}Ni and the finite supply of ^{58}Ni, the ^{59}Ni concentration will reduce due to burn-up. The relative reaction rate constants (cross-sections) for each nuclear reaction with the ^{58}Ni and ^{59}Ni are illustrated in Figure 3 [22]. In order to compare the reaction rates for (n,γ), (n,p) and (n,α) for ^{59}Ni relative to ^{58}Ni, the ^{59}Ni cross-sections have been reduced by a factor of 0.04 to give a sense of the magnitude of the ^{59}Ni effect on both dpa and gas production when the concentration of ^{59}Ni is at its highest.

Typical spectra for Inconel X-750 tensioning springs in the CANDU-6 periphery and Inconel X-750 garter springs in a high-power channel in the CANDU-6 reactor core are shown in Figure 4. The group structures for the spectra from the two regions differ, with the core having 89 groups and the periphery 19, with all thermal neutrons comprising one group with energies E < 0.625 eV. The lower resolution of the spectrum in the peripheral case will result in some errors in the calculated dpa and gas production, but for the purpose of this paper, the resolution is sufficient to illustrate the spectral effect. The calculated H, He and dpa generation as a function of time for two locations within the CANDU-6 core and periphery regions are shown in Figures 5 and 6. Although

the total neutron flux in the periphery region is only about 4% of the in-core value, the dpa and gas production after approximately 30 years of service is in the range of 25% to 50% of the in-core dpa and gas production. The thermal neutron flux is 5% higher in the periphery region compared to the core location where Inconel X-750 garter spring spacers are located; the non-thermal neutron flux in the periphery is only 0.3% of the in-core value. Averaged over the CANDU-6 core after about five years exposure the displacement damage rate in Inconel X-750 due to collisions with fast neutrons is about the same as the displacement damage rate due to the recoil effects experienced by ^{59}Ni, both averaging about 1 dpa/year.

There is no natural ^{59}Ni at the beginning of irradiation. However, as the ^{59}Ni concentration increases in the presence of thermal neutrons, via the ^{58}Ni (n, γ) reaction, the effect of ^{59}Ni increases from zero to substantial in a relatively short period of time. For the core and reflector (periphery) locations, the relative contribution is illustrated in Figure 7.

The point defects and gaseous atoms created by nuclear collisions and transmutations in nuclear reactor core components have a profound effect on their physical properties. The clustering of the point defects in the form of dislocation loops, cavities, precipitates and other vacancy clusters increases the strength of the components [7]. The migration of the point defects to various sinks also affects the dimensions of the components, resulting in swelling for materials such as steels and various Ni-alloys, or irradiation growth for the case of Zr-alloys. In the presence of a stress, there is often an increase in the creep rate due to the
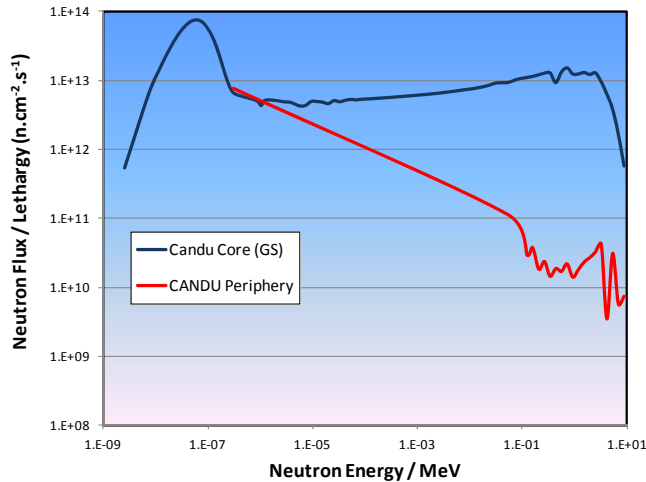
FIGURE 4: Comparison of neutron spectra for the core and reflector regions of a CANDU-6 reactor [12].

FIGURE 5: Calculated helium, hydrogen and displacements per atom for an Inconel X-750 garter spring in a high-power channel of a CANDU-6 reactor at 100% power assuming a mid-burn-up flux spectrum [12].

enhanced diffusional mass-transport. Although swelling can occur due to void formation in the absence of gaseous atoms, such as He, the production of He, in particular, has been shown to enhance swelling [7, 23-26]. More importantly, He can segregate at grain boundaries and stabilize cavities where otherwise vacancy point defects would simply be absorbed. The accumulation of He-stabilized cavities at grain boundaries is one way in which an alloy can become embrittled [27-30].

There have been few observations of cavities reported in power-reactor components until the past 10-15 years [26]. Most notably, cavities have been reported in a 316 stainless-steel PWR flux thimble and, more importantly, segregation of cavities at grain boundaries has been observed [31]. In the PWR flux thimble, the cavities were described as bubbles containing high levels of hydrogen and helium. The segregation of the bubbles at grain boundaries was linked with decreased ductility and a propensity for intergranular failure. The He and H were primarily generated from the 13.3wt% Ni present in the 316 stainless steel. More recently, data on the in-reactor performance of Ni-alloys from CANDU reactors has been accrued. The effect of irradiation on Ni-alloy CANDU reactor components (tensioning springs, fuel-channel garter spring spacers and flux detector assemblies) will now be described.

3. Inconel-600 Flux Detectors

The early design of flux detectors in use in CANDU reactors consisted of multiple-paired-coiled detectors sheathed in Inconel-600 and wrapped around a Zircaloy-2 carrier rod. The signal from these detectors was carried by Inconel-600 co-axial cables that were threaded through the carrier-rod and fed back to instrumentation outside of the reactor core. Failures occurred in early applications that were related to the environment in which the detectors operated (moist air leading to the formation of nitric acid in a radiation environment). These failures were mitigated by ensuring that the detectors operated with a He cover gas that acted both to limit corrosion and as an efficient conductor of heat (generated by nuclear heating). An improved design was introduced consisting of single-individual-replaceable (SIR) detectors with improved performance by eliminating brazed joints that were susceptible to nitric acid attack, but also limited the degree of localized nuclear heating that existed in the early coiled design. As a result, the SIR detectors survive for longer periods before they need to be replaced.

Post-irradiation examination of encapsulated Inconel-600 coiled flux detectors that had failed after several years of service (between five and 10) in a CANDU reactor showed that many of the detector wires inside the carrier rod were broken. The failures were brittle and intergranular [32]. It
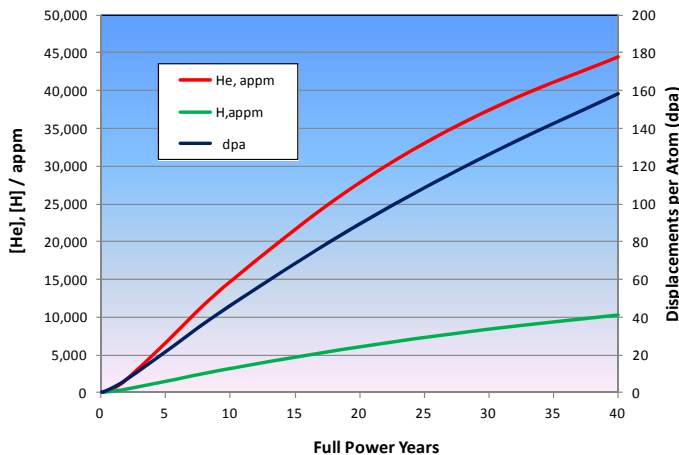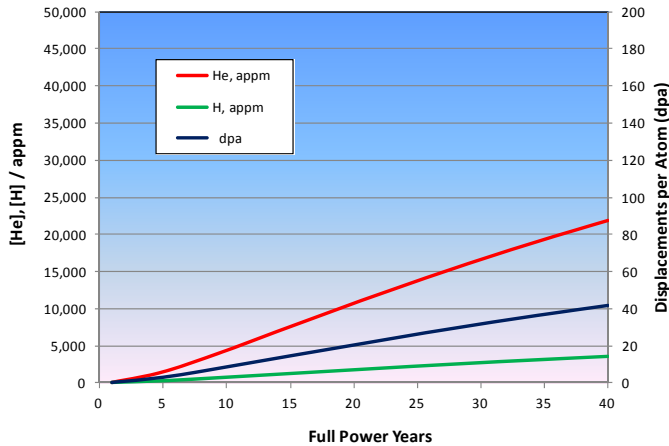
FIGURE 6: Helium, hydrogen and displacements per atom for an Inconel X-750 tensioning spring in the reflector region of a CANDU-6 reactor [12].

was concluded that failure occurred because the He cover gas was lost and replaced by air. The examination also showed that those parts of the Inconel-600 detector wires that had operated at the highest temperature, as evidenced by the degree of localized corrosion on the Inconel and Zircaloy-2 carrier rod, were the most severely embrittled. Estimates of the temperature in the assembly from the oxide layer on the Zircaloy-2 carrier rod ranged between 250 °C and 350 °C, assuming that the component was operating in an air environment for most of the residency time in the reactor [10, 32]. Different sections of the assembly were clearly operating at various temperatures based on the varying degrees of corrosion observed. The temperature variation in different parts of the assembly was attributed to nuclear heating and a variable mass concentration as the number of lead wires inside the carrier rod increased from one end to the other [10, 32].
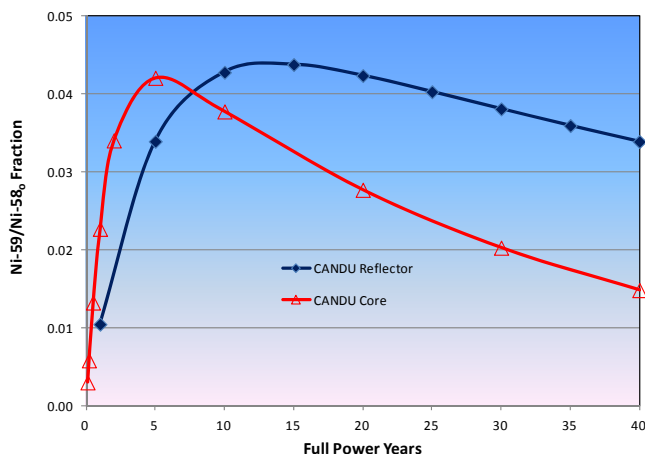
FIGURE 7: ^{59}Ni production as a fraction of the original ^{58}Ni concentration for the central core and reflector regions of a CANDU-6 reactor [12].

Bend tests on sections of lead wire showed that those parts of detector wires that were clearly operating at the lowest temperatures (because they were un-corroded and shiny) were ductile (Figure 8(a)). The wire shown in Figure 8(a) was located at the centre of the detector assembly (but on the outside of the carrier rod) and was therefore exposed to the highest neutron fluxes but not elevated temperatures. The same wire from a different section of the assembly and inside the carrier rod showed evidence of corrosion and therefore higher temperature operation, and was very brittle (Figure 8(b)).

One explanation for the embrittlement was that corrosion of the Inconel-600 in an oxygen-reduced atmosphere (due to the gettering effect of the Zircaloy-2 carrier rod) led to excessive nitrogen pick-up of the sheath at the highest temperatures [32]. There was a brittle nitrogen and carbon-rich layer on the surface of the most severely embrittled sheathing (Figure 9). Cracks were evident in the surface layer that sometimes were arrested at the interface between the surface layer and the base metal and sometimes
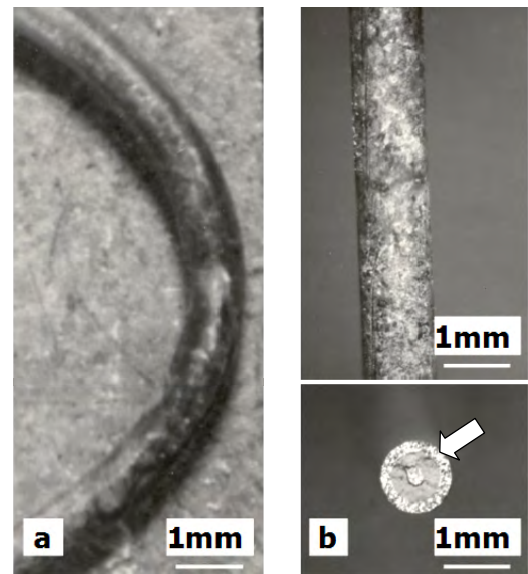
FIGURE 8: Comparison of detector signal wires removed from outside (a), and inside (b) the carrier-rod assembly: (a) section of wire taken from a section corresponding with the peak neutron flux following bend-testing; (b) section of wire taken from a section at about 80% peak neutron flux but high mass concentration (high nuclear heating) following bend-testing. The sample in (a) was relatively shiny, indicating that it was operating at a low temperature and was ductile. The sample in (b) showed evidence of corrosion (creating a thin nitrogen/carbide-rich surface layer), indicating that it had operated at a high temperature; both the outer sheath and inner core wire were brittle, exhibiting brittle failure with no signs of necking (arrowed in (b)) [32].
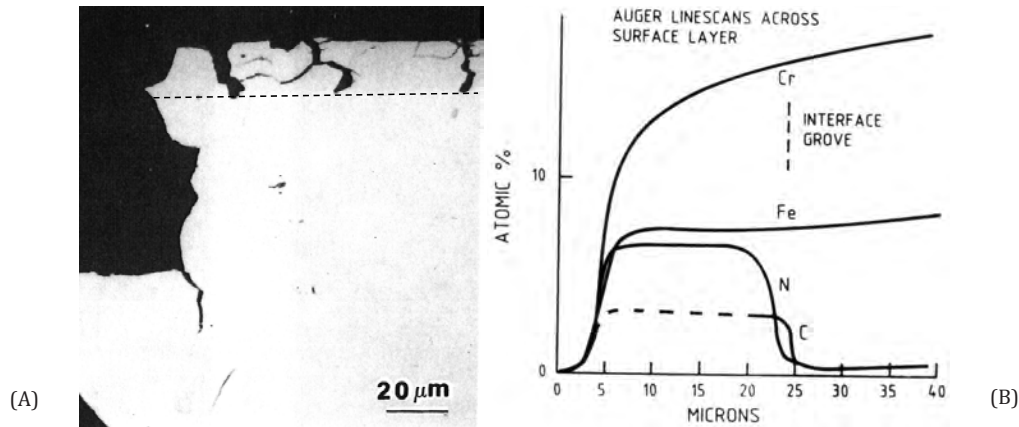
FIGURE 9: Image of nitrogen-rich layer (dotted line interface) at a broken section of Inconel-600 sheath and concentration profiles at surface of Inconel-600 flux detector wire following service for about nine years in a CANDU reactor [32].

progressed into the metal as an intergranular crack (Figure 4(b) of [32]). The cracks in the nitrogen rich surface layer act as stress raisers; however, the material itself had to have been embrittled also (either due to irradiation or some other factor). The fact that some cracks in the nitrogen-rich layer arrested at the interface and some continued into the matrix as intergranular cracks [32] suggests that those cracks that progressed from the surface layer did so because they intersected a grain boundary.

One can conclude that the failures of the Inconel-600 flux detector signal wires were the result of having a brittle nitrogen-rich surface layer (which cracked easily) and an embrittled substrate. Carbon was also present in the surface layer (Figure 9) and, whereas the nitrogen likely originated from the air in the assembly, the source of the carbon is unknown. There are three possible sources of carbon: (i) from hydrocarbons present on the surface, (ii) diffusion from the matrix, (iii) transmutation of the nitrogen within the surface layer.

In light of the advances in understanding of the production of He, and the effects of He on embrittlement, coupled with the fact that these assemblies are operating in a neutron environment producing substantial amounts of He (Figure 10), it is possible that the Inconel-600 signal wires were embrittled by He. The high temperature embrittlement (high in this case being >250 ℃), could be linked with the mobility of He and/or vacancy point defects. The temperature dependence of the flux detector embrittlement bears similarities with observations of Inconel X-750 garter spring spacers within the CANDU reactor core [11-12], where corrosion in air is not a factor, and this will be described next.

4. Inconel X-750 Spacers (Garter Springs)

4.1 Mechanical Properties
Garter spring-type spacers are used in the fuel channels of CANDU reactors to separate each pressure tube from a concentric calandria tube and thus maintain an insulating gas gap between the cold moderator and the hot pressure tube (Figure 11). The tight-fitting spacers, as the name implies, are required to remain tight on the pressure tubes at least until the tubes have sagged sufficiently that the springs become pinched between the hot pressure tube (operating at 260 ℃ - 310 ℃) and relatively cold calandria tube (operating at 60 ℃- 80 ℃). The temperature of the spacer in the pinched region (about 4 cm long) is somewhere intermediate between the pressure tube and calandria tube and there will also be a temperature gradient between the points on the spacer coil in contact with

FIGURE 10: Helium, hydrogen and displacements per atom for Inconel 600 flux-detector components in the core of a CANDU reactor [10].
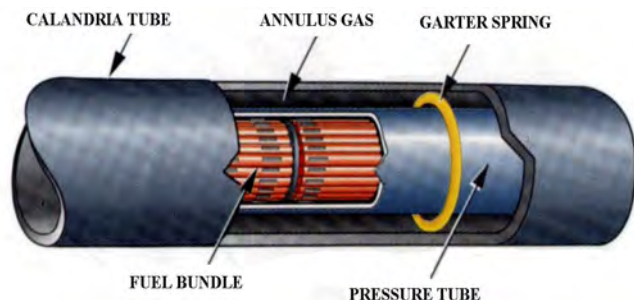
FIGURE 11: Schematic diagram showing an Inconel X-750 spacers (also known as garter springs) in a fuel channel of a CANDU reactor. The spacers fit tightly around the pressure tube containing the primary coolant and fuel and maintain in an insulating gas gap, containing CO_2, between the hot pressure tube and the cold calandria tube.

each tube. The temperature in the remainder of the spacer (about 32 cm) is at or above the pressure tube temperature due to nuclear heating. There are four spacers spread over the 6 metre span of the fuel channel. For the two central spacers, the pinching occurs very early in the operating life of the fuel channel (<1000 hours). For the outboard spacers, pinching could occur after much longer operating times depending on the tilt of the pressure tube relative to the calandria tube, and the channel power.

The spacers reside in the reactor core for the duration of the reactor life and are subject to similar radiation fields as the zirconium alloy pressure tubes and calandria tubes. They maintain the gas gap (carbon dioxide) between the pressure tube and calandria tube and thus minimize heat loss from the primary coolant to the moderator, and also prevent

direct contact between the two tubes that could lead to hydride blister formation. In addition, the spacers support the pressure tube and effectively transfer the weight of fuel channel from the faster-sagging pressure tube to the slower sagging calandria tube.

Post-irradiation examination of spacers removed from CANDU reactors have indicated that they exhibit embrittlement, and lower ultimate tensile strength, compared with unirradiated material [11-12, 33]. The embrittlement is characterized by intergranular failure (Figure 12).

Recent studies have shown that the non-pinched sections of spacers, in particular, are more embrittled by irradiation and have lower strength compared with pinched sections, Figure 13 [12, 33]. Transmission electron microscopy (TEM) shows that the radiation damage microstructure consists of small defect clusters. The density of defects giving rise to diffraction contrast (dislocation loops, stacking-fault tetrahedra and small precipitates) appears to be higher for the unpinched sections of spacer, but more significantly, the cavity density and distribution is different. The differences in cavity size and density between a pinched and non-pinched section of spacer are illustrated in Figure 14 [11].

In general, the pinched sections of spacers have smaller cavity sizes (1-2 nm diameter) compared with the unpinched sections, having cavity sizes ranging from 2-8 nm in diameter [11-12]. The densities of bubbles are of the order of 10^{24} m^{-3} [12]. Although dose and dose rate are also likely to have an effect on the microstructure [7, 34], the main effect, which is apparent for any given spacer, is that due to the temperature in the pinched compared with non-
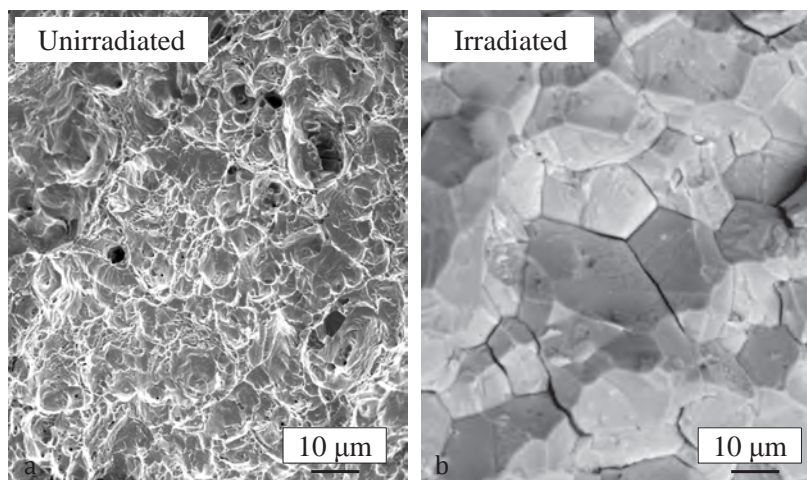
FIGURE 12: Comparison of fracture surfaces for unirradiated and irradiated (23 dpa) spacers after mechanical testing to breakage at room temperature. The unirradiated sample (a) exhibits ductile failure compared with the irradiated sample (b) that exhibits brittle intergranular failure [12].
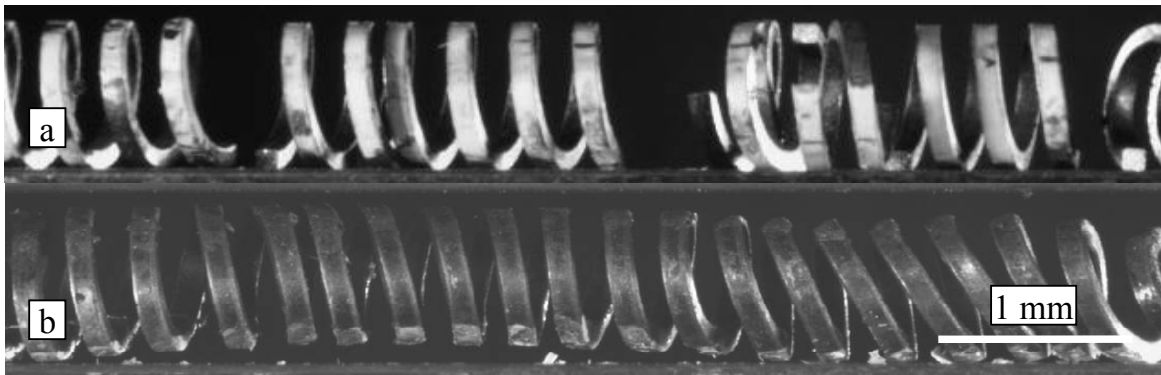
FIGURE 13: Comparison of (a) unpinched and (b) pinched sections of irradiated spacers removed after about 14 EFPY of service and after mechanical testing at ambient temperature (about 25 °C). The unpinched sample exhibited brittle intergranular failure while the pinched sample deformed without failure when subjected to the same load [33].
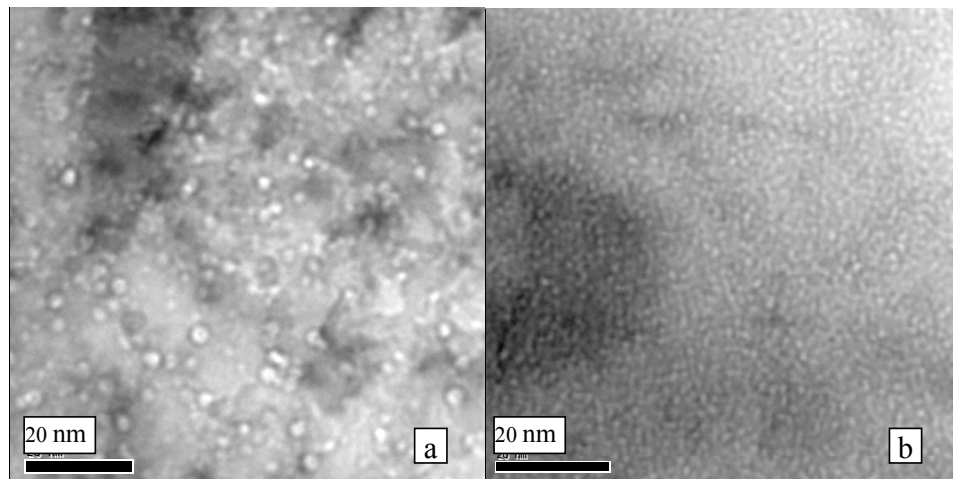
FIGURE 14: TEM micrographs illustrating cavity sizes as a function of irradiation temperature: (a) un-pinched (about 9 EFPY, 23 dpa), (b) pinched (about 11 EFPY, 43 dpa). The cavities are smaller in (b) even though the dose is higher [11].
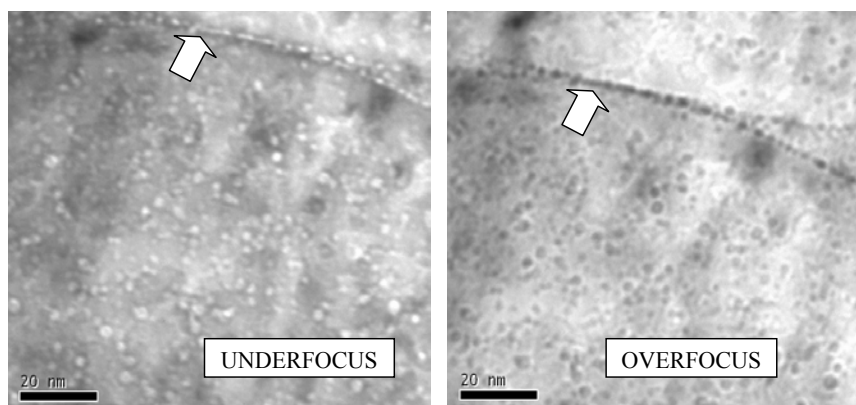
FIGURE 15: TEM micrographs illustrating cavity distribution on and near a grain boundary (arrowed) in an un-pinched spacer after about 9 EFPY, 23 dpa [11].
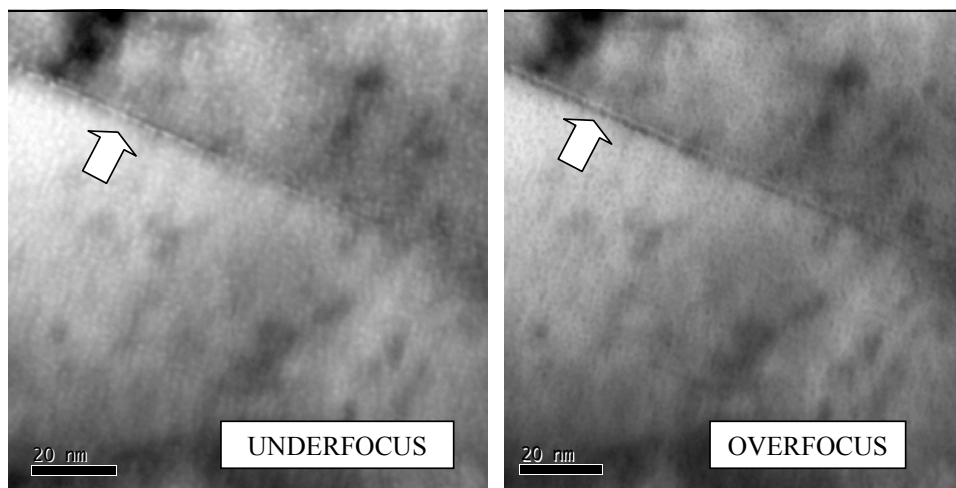
FIGURE 16: TEM micrographs illustrating cavity distribution on and near a grain boundary (arrowed) in a pinched spacer after about 11 EFPY, 43 dpa [11].

pinched regions. In particular, the cavity distribution on and near grain boundaries reflects the differences in operating temperature. The cavities at the boundaries are typically <10 nm in diameter and do not show up when imaging fracture surfaces with a Scanning Electron Microscope (SEM). For the non-pinched sections, there is often a zone that is partially denuded of cavities adjacent to the grain boundary (Figure 15 [11]). As this zone indicates that He-induced cavities have not formed adjacent to the boundary, it is safe to assume that the missing He has segregated to the boundary, consistent with the reasoning of Dai *et al*. [28]. The boundary segregation and concomitant denuded zone are less apparent in the pinched regions (Figure 16, [11]) and this, together with other differences in microstructure, correlates with the mechanical property differences [33]. The non-pinched sections of garter spring spacer tend to be weaker and more brittle than the pinched sections of spring. This is likely to be because more He is segregated at the grain boundary due to the higher operating temperature, as evidenced by the cavity sizes and the observations of a measurable denuded zone adjacent to the boundary. Ultimately, failures are intergranular in nature whether the material is from a pinched or a non-pinched section of spring [11-12], and this is likely to be because there is a higher density of cavities on grain boundaries compared with the matrix in each case.

When considering the intergranular failure, one has to consider that the cohesive strength of grain boundaries far exceeds the yield strength of the material, requiring stress levels about 10^4 to 10^5 MPa to simply pull apart the atoms [35]. Slip, on the other hand, occurs at stresses substantially less (about 10^2 to 10^3 MPa). Although irradiation increases the yield and ultimate tensile strength of any material, it is never sufficient to exceed the strength of the boundary. However, if the boundary is perforated by an array of cavities, any local stress in the grain will be intensified in the ligaments between the cavities. Yielding can then occur between the cavities provided the bulk stress is sufficiently high. The cavities can simply coalesce, thus enhancing the stress intensification further in the same way that necking and porosity increases the stress in a tensile specimen, Figure 17. The presence of a crack will also give rise to stress intensity and one would anticipate that any cracking would follow the weakest links, i.e., the perforated boundary. A similar argument and derivation based on inter-cavity stress concentration has been proposed to explain for void-induced embrittlement by Neustroev *et al*. [27].

In the absence of any other contrary evidence, the segregation of He-induced cavities at grain boundaries is likely to be the main cause of embrittlement in CANDU reactor garter spring spacers. In this respect, the He segregation is likely to increase non-linearly with increasing temperature [36]. When boundaries also contain precipitates of a different phase there may be an additional impact due to the so-called "interfacial energy credit" that favours cavity formation at a two-phase interface [37]. Temperature is important because it affects the defect clustering as evidenced by the denuded zone observed in the non-pinched sections of spacer material.

4.2 Creep Properties

Irradiation creep is important for tight-fitting Inconel X-750 spacers (garter springs) because, as the name implies, they are expected to remain tight on the pressure tube until such time that it is pinched between the pressure tube and the calandria tube as the pressure tube sags after the commencement of reactor operation (Figure 11). It is important to know the rate at which the springs relax and become de-tensioned. Although the springs are designed to roll as the fuel channel elongates and contracts due to thermal cycles experienced during startups and shutdowns, they have to remain within a prescribed length of the pressure tube. To be assured that the springs will remain in a particular location, the time to de-tension due to creep and swelling has to be greater than the time for the fuel channel to sag and cause pinching. The tight-fitting design differs from an earlier (mid-1980s) design in that the earlier design (made from Zr-Nb-Cu) was meant to sit tightly against the inside diameter of the calandria tube and consequently was a loose fit relative to the pressure tube. There are two main aspects of assessing spacer de-tensioning: (i) whether the garter spring spacer can become loose prior to being pinched between the pressure tube and calandria tube due to pressure tube sag; (ii) whether the garter spring spacer can become loose after long periods of operation even when pinched. Loose in this context is defined as the condition when there is zero tension in the spring. This condition cannot occur by stress relaxation alone and must be accompanied by swelling.

FIGURE 17: Schematic description of one postulated grain boundary failure mechanism. The grain boundary fails when the yield strength between the cavities is exceeded [14].

There are a number of factors that need to be taken into account to determine the rate of spacer de-tensioning: (i) the initial tension in the spacer is determined by the extension that is imposed as it is stretched onto the pressure tube and is determined by the spring rate (2.48 N.cm^{-1} or 5 N.cm^{-1} for the two designs applicable to operating CANDU reactors); (ii) creep reduces the spring tension with time but is partially balanced by the diametral expansion of the pressure tube; (iii) swelling of the spacer increases its stress-free diameter and counters the effect of the pressure tube diametral expansion.

The rate of stress relaxation as a function of displacement damage (dpa) has been determined from stress relaxation tests in NRU at 300 °C and 60 °C [38]. When these tests were originally carried out, the creep rate was determined as a function of fast neutron fluence, or displacement damage due to fast neutrons only. With the advent of more rigorous damage calculations involving Ni transmutation effects (Section 2), a re-assessment of the creep rate has been performed [8-9, 12]. The new creep rates as a function of fast neutron dose and dpa at two different temperatures are shown in Figure 18. There is no way to measure the temperature of the operating garter spring spacer and therefore all one can do is assume that the temperature, for the most part, coincides with the temperature of the pressure tube and that the data obtained at 300 °C are applicable.

The factors dictating the tension in the garter spring have been incorporated into a de-tensioning algorithm (Figure 19). The tension of the spacer relaxes over time due to irradiation creep. At the same time, the pressure tube expands and therefore stretches the spring. The two processes act against one another so that the end result, in the absence of any other factors, would be that the spring would simply conform to the shape of the pressure tube. However, swelling in the garter spring will result in an increased diameter that counters the effect of the diametral expansion of the tube. At the point where the spacer tension is negligible, if the expansion rate of the spring due to swelling exceeds the diametral expansion rate of the pressure tube, loosening could result.

The results of the calculated tension for the outboard springs of a CANDU reactor fuel channel are illustrated in Figure 20 [12]. Even if the conditions were such that loosening could occur, eventual tightening is inevitable and this is seen at longer exposures in Figure 20. Any swelling of the spacer is non-linear and slows down with increasing neutron dose (because of the burn-out of the ^{59}Ni), whereas expansion of the pressure tube due to creep is linear with increasing neutron exposure [12].
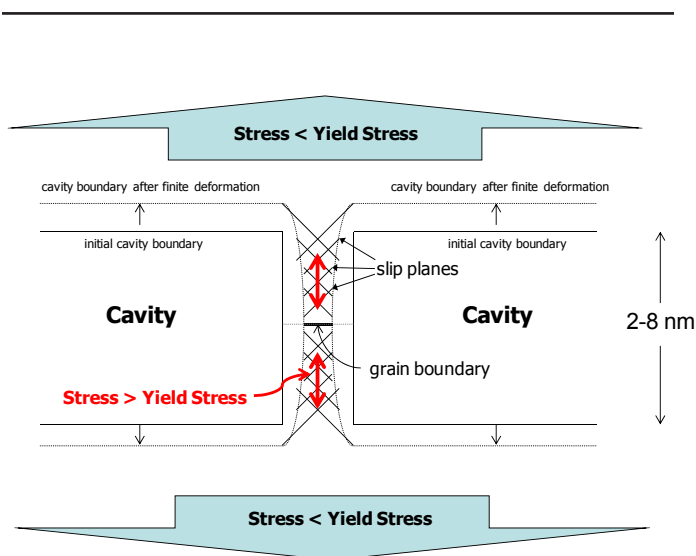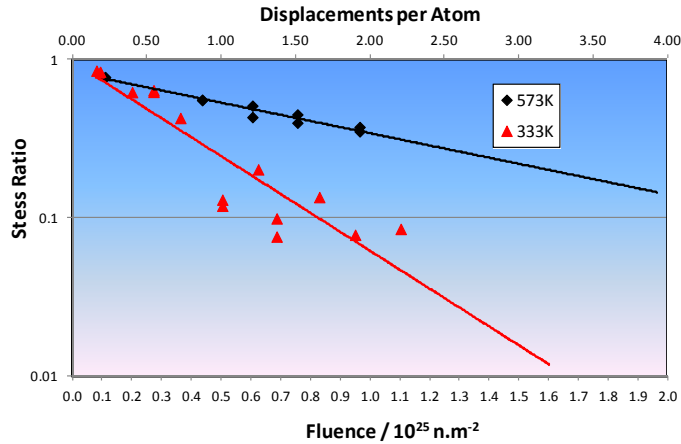
FIGURE 18: Stress-relaxation data from samples of Inconel X-750 irradiated in NRU irradiated at about 60 °C (333 K) and about 300 °C (573 K). The samples had been hot-finished and aged for 24 hours at 700 °C to simulate the final aging treatment for the Inconel X-750 garter spring. Fluence values are for neutron energies E>1 MeV [12].

FIGURE 19: Algorithm used to calculate the rate of de-tensioning of an optimised Inconel X-750 spacer. To simplify the analysis, the initial stress at time 0 is assumed to be the intercept of the steady-state stress relaxation data with the stress ratio axis and is 81% of the initial stress (3.65 N) [12].

5. Inconel X-750 Reactivity Mechanism Tensioning Springs

As for PWR and BWR reactors, CANDU reactor guide tubes surround and position the reactivity control mechanisms. In the case of the liquid zone control assemblies in CANDU reactors, to reduce possible flow-induced vibration of the guide tube, Inconel X-750 tensioning springs attach the guide tube to the base of the calandria vessel that is in the reflector region of the reactor (Figure 21). At the location of the reactivity mechanism tensioning spring (residing between 20 cm and 40 cm from the bottom of the core for a CANDU-6 reactor), the neutron flux is very low and the temperature is about 60 °C-80 °C. On installation, the springs are adjusted to produce an initial axial load of 1400 pounds in compression.

Inspection after 18.5 effective full power years (EFPY) of service in one CANDU-6 reactor showed that the springs lost most, if not all, of their installed tension. The extent to which the springs had relaxed was unexpected based on assessments of relaxation rates as a function of fast neutron flux on Inconel X-750 material tested in the National Research Universal (NRU) reactor [38]. For Zr-alloys in particular the fast neutron flux scales approximately linearly with displacement damage rate because Zr has very low absorption cross-sections for thermal neutrons, but this is not the case for other alloys containing substantial amounts of Fe, Cr and Ni. Ultimately it is the fraction of displaced atoms, or displacements per atom (dpa), that dictate the extent of stress relaxation (due to irradiation creep) that occurs in reactor components. In the core of the reactor, where there is a high fast neutron flux (E>1MeV), most of the damage is caused by direct displacements with neutrons. As the concentration of ^{59}Ni increases the proportion of atomic displacements caused by the (n,γ), (n,p) and (n,α) reactions increases to the point where it eventually exceeds that produced by direct collisions with energetic neutrons. However, in the peripheral regions of the CANDU reactor, the fast neutron flux drops much more rapidly than the flux of neutrons with lower energies. In these regions, the contribution to displacement damage by processes other than direct collisions are important and what is known as spectral effects predominate [8-9]. If the alloy has a high nickel concentration, then the spectral effects are very much enhanced due to the two-stage reactions that occur in nickel (see Section 2).

Earlier studies have shown that under some circumstances (e.g., HFIR pressure vessel embrittlement) gamma-induced atomic displacements could contribute between 10% - 90% of the total atomic displacement damage [39]. In light of this prior experience, the influence of gamma production on displacement damage rates was investigated and found to be a small contribution over the length of the spring. However, when the contribution of prompt gamma recoil, after capture of thermal neutrons, for the main isotopes in Inconel X-750 (nickel, iron and chromium) was examined the thermal neutron reactions were found to contribute much more to production of displacements than that of direct collisions with fast neutrons. The relative contributions to the atomic displacement rate from direct collisions with neutrons, (n,γ)-reactions, and displacement from gamma ray, for the
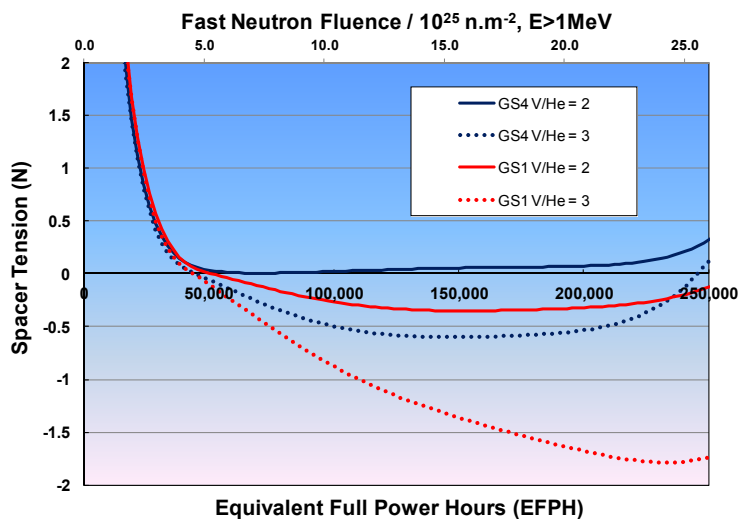
FIGURE 20: Spacer tension as a function of equivalent full-power operating time for Inconel X-750 garter spring in a high power channel. The time to de-tensioning is given by the point at which each curve passes through the horizontal tension axis, i.e., zero tension. GS1 and GS4 refer to the inlet-outboard and outlet-outboard garter springs respectively. V/He refer to hypothetical vacancy to helium ratios assuming that the cavities in the material are equilibrium bubbles [12].
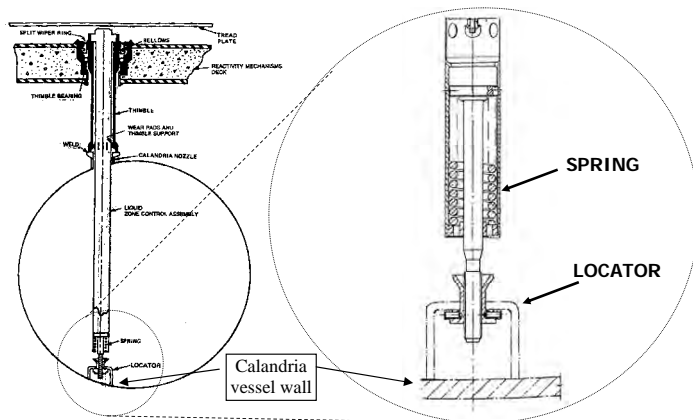
FIGURE 21: Schematic diagram (not to scale) indicating the location of guide-tube tensioning springs in CANDU reactors [9].

range of positions in the CANDU-6 reactor occupied by the springs is shown in Figure 22. Note that the relative contribution of thermal recoil events becomes larger as the distance from the core increases.

The stress-relaxation-rate data from NRU at the same temperature as the tensioning spring location (approximately 60 °C-80 °C) is shown in Figure 18. Using dpa as the (appropriate) measure of dose, calculations performed for the mid-point of the springs showed that including the thermal neutron contribution to production of displacements in the spring reduces the time to reach about 2 dpa and 90% relaxation from about 640 years to only about 30 years of operation. However, after including the calculated dpa from the ^{59}Ni reactions, this duration is reduced to about three years at the centre of the spring (Figure 23). Of course, the relaxation is complicated by the varying flux and spectrum along the spring. Although detailed calculations involving ^{59}Ni have not been performed at each location, it is safe to say that those parts of the spring closer to the core than the centre location will have relaxed >90% in less than three years of operation, and those parts of the spring further from the core than the centre location will have relaxed >90% in greater than three years of operation.

The major conclusion from this study was that not only can the influence of ^{59}Ni dominate damage production under some conditions, but that great care must be taken when using fast neutron flux as the measure of dose. In all circumstances, radiation-damage calculations need to be performed in order to compare the effects of irradiation in the different nuclear-reactor environments.

6. Discussion
In order to understand the irradiation creep and changes in mechanical properties of Ni-rich alloys such as Inconel X-750 during power-reactor operation, one has to consider the situation that arises when dealing with an alloy containing a large amount of nickel irradiated in a reactor with a spectrum that promotes large changes in the material due to enhanced atomic displacement damage and gas-atom production. Inconel X-750 contains about 70 wt% nickel. Of this, approximately 68% is the isotope ^{58}Ni. This isotope transforms to ^{59}Ni when irradiated with thermal neutrons. This reaction itself creates atomic displacement damage that is over and above what one would normally see in a fast-reactor test but, more significantly, the ^{59}Ni that is produced has very high cross-sections for interactions with a wide range of neutron energies, and this can have dramatic effects on the irradiation response of the material. There is no natural ^{59}Ni, but the latter is formed from ^{58}Ni via thermal neutron absorption, eventually peaking at a ^{59}Ni /^{58}Ni ratio of about 4%. The ^{59}Ni undergoes three main reactions with thermal neutrons that create
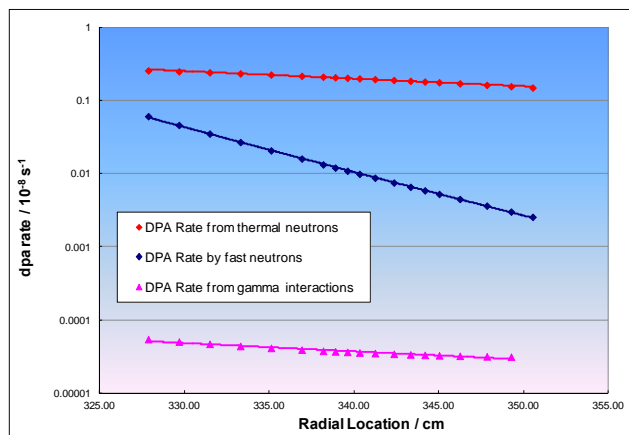
FIGURE 22: Displacement rates arising from various contributions calculated for Inconel X-750 as a function of radial mid-plane location in the CANDU-6 reactor core based on the natural stable isotope distribution and therefore not accounting for the ^{59}Ni effect. The calculations span the radial distance from the core centre (327 cm – 349 cm) occupied by the tensioning spring. The edge of the reactor core in the radial mid-plane is at about 308 cm [9]. The springs are located in the reflector region between about 20cm and 40 cm from the edge of the reactor core
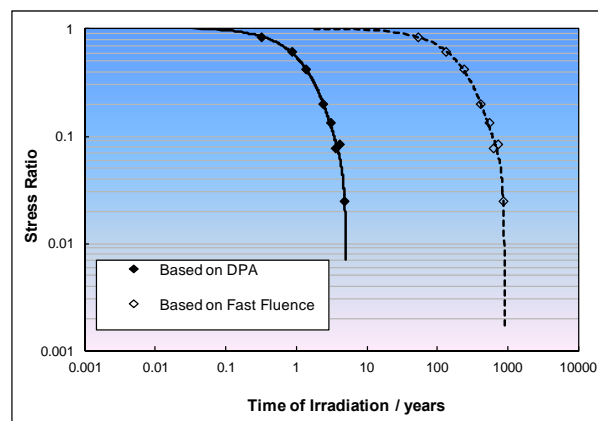
FIGURE 23: Stress relaxation of Inconel X-750 at the centre of the tensioning spring in the reflector region of a CANDU-6 reactor based on dpa and fast fluence as the measure of dose. The time to relax based on the dpa value is substantially less (20 times less) due to the contributions from the thermal neutron (n,γ) reactions with naturally occurring Fe, Cr and Ni and is another factor of 10 smaller (i.e., 200 times less) when the contribution from ^{59}Ni is included [9].

atomic displacements: (n, γ), (n, p) and (n, α). The latter two reactions release very large amounts of energy and thereby cause a very high level of atomic displacement, as well as producing very high levels of hydrogen and helium.

6.1 Embrittlement

There is incontrovertible evidence that components such as flux detectors and garter-spring spacers in CANDU reactors and flux detector thimble tubes in PWR reactors can become embrittled during service. In the case of thimble tubes made from 316 stainless steel [31], TEM examinations have been performed showing cavities segregated at grain boundaries, and this segregation was identified as a contributing factor in the tendency for intergranular failure with increasing dose.

Considering cavity effects alone, the most likely mechanism by which CANDU reactor Inconel X-750 garter spring spacers lose strength and become embrittled is one which involves the intensification of stress at boundaries due to the perforation by the segregated cavities. Trinkaus *et al.* [29-30] have proposed a mechanism whereby the embrittlement due to He bubbles segregated at grain boundaries is the result of stress intensification in the ligament between the bubbles. Their case was directed at high-temperature creep and the higher stress between the bubbles on the boundary resulted in enhanced vacancy diffusion, merging of the bubbles and therefore softening of the boundary as the load-bearing area was reduced. In the current case, where embrittlement is observed at room temperature, one cannot invoke exactly the same reasoning as Trinkaus *et al.* [29-30]. However, the presence of a higher density of cavities on the boundary and intergranular failure are correlated. If the underlying cause is the same, stress intensification due to perforation of the boundary, the mechanism is probably different. Given that the embrittlement exists during room-temperature testing (Figure 13), failure could simply initiate when the ultimate tensile strength (UTS) in the ligaments between the cavities is exceeded. In the case of unpinched sections of Inconel X-750 spacers, there is clearly a larger zone denuded of cavities adjacent to the grain boundaries in addition to segregation at existing dislocations (compare Figures 15 and 16). The implied increase in segregation of He at the higher temperature could then lead to a higher degree of boundary perforation and weaker boundaries. In principle, the higher density of cavities segregated at a boundary will result in higher stress concentrations in the ligaments between the bubbles and shorter distances for cracking and coalescence of neighbouring bubbles. The distance between cavities may be smaller for the unpinched sections of spacer because of the increased He segregation, as evidenced by the measurable zone denuded of cavities. Unfortunately, detailed quantitative measurements of bubble spacing are not yet available. If the density is high enough (i.e., if the load bearing area is small enough), and the applied stress is high enough, such that the UTS in the ligament is exceeded, then mechanical failure of the ligament between the bubbles can occur (Figure 17). This very localised yielding could then be the reason for the reduced ductility observed in Inconel X-750 spacers following irradiation (see Section 4.1).

The same mechanism leading to inter-granular failure of garter spring spacers could apply in the case of the irradiated Inconel-600 flux detectors (Section 3), except the dose rate for atomic displacement damage and He production is a factor of two lower (compare Figures 5 and 10), and the time in the reactor is relatively short (about nine years in this case). For the flux detectors, however, there may be synergy between the effect of corrosion at high temperatures and irradiation at high temperatures. There is evidence to indicate that cracks created in the nitrogen-rich surface layer are either arrested at the interface with the matrix or propagate inter-granularly. If a crack happens to intersect a grain boundary that is weakened by irradiation and He segregation, it is conceivable that the stress raised by the crack is sufficient to cause failure in the weakened grain boundary and easy propagation will result leading to brittle failure.

6.2 Creep
It is clear from Section 2 that CANDU-specific conditions, particularly the high thermal neutron flux, could result in different responses to irradiation compared to conditions in low thermal flux (high fast flux) test reactors. Thermal-neutron-induced transmutations of Ni create measurable quantities of helium that are commensurate with the calculated amount [12, 21]. Measurement of hydrogen in garter-spring material did not show any statistically significant quantities and, although some may be trapped within cavities, as has been reported for ion irradiated steels [40], there is insufficient evidence to indicate that sufficient hydrogen is retained to contribute to the swelling, and therefore de-tensioning, or embrittlement, of spacers [12]. Attempts to measure hydrogen have not been made for other CANDU reactor components.

In addition to enhancing the displacement damage rate, which largely controls irradiation creep, the accumulation of gaseous elements in the material, especially helium, will induce and/or stabilize gas bubbles or cavities that give rise to swelling. It has been shown (Section 4.2) how swelling can contribute to the de-tensioning of garter-spring spacers. However, in addition to the effect of swelling, the creep will be modified as the microstructure evolves as a natural consequence of balancing the flow of point defects to the different sinks in the evolving microstructure [7, 41]. The increase in the vacancy sink strength from cavity evolution, which is manifested as increased swelling, has been shown to give rise to enhanced creep rates [26, 42].

One peculiarity of the creep data for Inconel X-750 is that the creep is faster at low temperatures compared with high temperatures (Figure 18). There are numerous possible explanations for this phenomenon that necessitate a knowledge of the microstructure in the creep specimens

during irradiation, which is currently unknown. Models have been developed to explain the phenomenon in terms of a prolonged transient effect [43-45].

7. Conclusions
1) For peripheral locations in power reactors like the CANDU reactor, thermal-neutron reactions can be important and should be included in any assessment of radiation-damage effects on materials. The spectral effect is especially important for Ni-rich alloys because radiation damage is substantially enhanced for Ni alloys in a reactor environment with a high thermal-neutron flux.

2) Apart from the elevated atomic displacement damage that occurs in Ni-rich alloys, the production of H and He in a high thermal-neutron flux environment can affect the integrity of reactor-core components. The segregation of He-induced bubbles at grain boundaries and precipitate interfaces, in particular, results in a loss of strength and toughness for Ni-alloy reactor-core components.

REFERENCES
[1] "INCONEL® Alloy 600", Special Metals Corporation, SMC-027, September 2008, Available at: http://www.specialmetals.com/products/inconelalloy600.php.
[2] "INCONEL® Alloy 625", Special Metals Corporation, SMC-063, January 2006, Available at: http://www.specialmetals.com/products/inconelalloy625.php.
[3] "INCONEL® Alloy 718", Special Metals Corporation, SMC-045, September 2007, Available at: http://www.specialmetals.com/products/inconelalloy718.php.
[4] "INCONEL® Alloy X-750", Special Metals Corporation, SMC-067, September 2004, Available at: http://www.specialmetals.com/products/inconelalloyx750.php.
[5] R.M Boothby, 2012, "Radiation Effects in Nickel-Based Alloys", Comprehensive Nuclear Materials, Elsevier, Amsterdam, Vol. 4, pp.123-150.
[6] A.F. Rowcliffe, L.K. Mansur, D.T. Hoelzer, R.K. Nanstad, 2009, "Perspectives on Radiation Effects in Nickel-Base Alloys For Applications In Advanced Reactors", J. Nucl. Mater., Vol. 392(2), pp. 341-352.
[7] L.K. Mansur and M.L. Grossbeck, 1988, "Mechanical Property Changes Induced in Structural Alloys by Neutron Irradiations with Different Helium to Displacement Ratios", J. Nucl. Mater., Vol. 155-157, Part 1, pp.130-147.
[8] M. Griffiths, F.J. Butcher, I. Ariani, S. Douglas, F. Garner and L. Greenwood, 2008, "Spectral Effects on Stress Relaxation of Inconel X-750 Springs in CANDU Reactors", 8th Intl. Conference on CANDU Maintenance, Toronto, Ontario, Canada, November 16-18, 2008, Paper 93.
[9] F.A. Garner, L.R. Greenwood, E.R. Gilbert, M. Griffiths, 2009, "Impact of Ni-59 (n, α) and (n, p) Reactions on Dpa Rate, Heating Rate, Gas Generation and Stress Relaxation in LMR, LWR and CANDU reactors", Proc. Fourteenth Intern. Conf. on Environmental Degradation of Materials in Nuclear Power Systems Water Reactors, Virginia Beach, Virginia, USA, August 23-27, 2009, pp.1344-1354.

[10] M. Griffiths, G.A. Bickel and S.R. Douglas, 2010, "Irradiation-Induced Embrittlement of Inconel 600 Flux Detectors in CANDU Reactors", Proceedings of the 18th International Conference on Nuclear Engineering (ICONE18), Xi'an, China, May 17-21, 2010, Paper ICONE18-30121.

[11] C.D. Judge, M. Griffiths, L. Walters, M. Wright, G.A. Bickel, O.T. Woo, M. Stewart, S.R. Douglas and F.A. Garner, 2013, "Embrittlement of Nickel Alloys in a CANDU Reactor Environment", 25th Int. Symposium on Radiation Effects in Materials, ASTM, Anaheim, California, USA, ASTM STP 1547, pp.161-175.

[12] M. Griffiths, G.A. Bickel, S.A. Donohue, P. Feenstra, C.D. Judge, L. Walters, M.D. Wright, 2013, "Degradation of Ni-alloy Components in CANDU Reactor Cores", submitted to 16th Int. Conference on Environmental Degradation of Materials in Nuclear Power Systems – Water Reactors, Asheville, North Carolina, USA, August 11-15, 2013.

[13] L. R. Greenwood, 1983, "A New Calculation of Thermal Neutron Damage and Helium Production in Nickel", J. Nucl. Mater., Vol. 115(2-3), pp. 137-142.

[14] L.R. Greenwood, F.A. Garner, 1996, "Hydrogen Generation arising from the ^{59}Ni (n,p) Reaction and its Impact on Fission-Fusion Correlations", J. Nucl. Mater., Vol. 233-237 Part 2, pp. 1530-1534.

[15] F. A. Garner, E. P. Simonen, B. M. Oliver, L. R. Greenwood, M. L. Grossbeck, W. G. Wolfer, and P. M. Scott, 2006,"Retention of Hydrogen in FCC Metals Irradiated at Temperatures Leading to High Densities of Bubbles or Voids", J. Nucl. Mater. Vol. 356(1-3), pp.122-135.

[16] F. A. Garner, M. L. Hamilton, L. R. Greenwood, J. F. Stubbins and B. M. Oliver, 1994, "Isotopic Tailoring with 59Ni to Study the Effect of Helium Generation Rates and their Effect on Tensile Properties of Neutron-Irradiated Fe-Cr-Ni Alloys", Proceedings of 16th ASTM International Symposium on Effects of Radiation on Materials, ASTM STP 1175, Aurora, CO, June 22-24, 1992 pp. 921-939.

[17] L. R. Greenwood, F. A. Garner, and B. M. Oliver, 1994, "An Assessment of the ^{59}Ni Isotopic Tailoring Technique to Study the Influence of Helium/Dpa Ratio," J. of Nucl. Mater., Vol. 212-215, Part A, pp. 492-497.

[18] F. A. Garner, L. R. Greenwood and B. M. Oliver, 1999, "A Reevaluation of Helium/dpa and Hydrogen/dpa Ratios for Fast Reactor and Thermal Reactor Data Used in Fission-Fusion Correlations", Effects of Radiation on Materials: 18th International Symposium, R. K. Nanstad, M. L. Hamilton, F. A. Garner and A. S. Kumar, Eds., American Society of Testing and Materials, ASTM STP 1325, pp. 794-807.

[19] F. A. Garner, B. M. Oliver and L. R. Greenwood, 1998, "The Dependence of Helium Generation Rate on Nickel Content of Fe-Cr-Ni Alloys Irradiated at High Dpa Levels in EBR-II", J. of Nucl. Mater., Vol. 258-263, Part B, pp. 1740-1744.

[20] L.R. Greenwood, R.K. Smither, 1985, "SPECTER: Neutron Damage Calculations for Materials Irradiations," Argonne National Laboratory, Report ANL/FPP/TM-197.

[21] L.R. Greenwood, F.A. Garner, B.M. Oliver, M.L. Grossbeck and W.G. Wolfer, 2004, "Surprisingly Large Generation and Retention of Helium and Hydrogen in Pure Nickel Irradiated at High Temperatures and High Neutron Exposures", Journal of ASTM International., Vol. 1, No. 4, Paper ID: JAI11365.

[22] ENDF/B-VI nuclear library, T-2 Nuclear Information Service, Los Alamos National Laboratory, Available at URL: http://t2.lanl.gov/nis/data.shtml

[23] F.A. Garner, 2012, "Radiation Damage in Austenitic Steels", Comprehensive Nuclear Materials, Elsevier, Amsterdam, Vol. 4, pp. 33-95.

[24] F.A. Garner, L.R. Greenwood, 2003, "Survey of Recent Developments Concerning the Understanding of Radiation Effects on Stainless Steels used in the LWR Power Industry", Eleventh Int. Conference on Environmental Degradation of Materials in Nuclear Power Systems – Water Reactors, Stevenson, WA, August 10-14, 2003 pp. 887-910.

[25] F.A. Garner, 1994, "Irradiation Performance of Cladding and Structural Steels in Liquid Metal Reactors", in Nuclear Materials, Vol. 10A, Part 1 of Materials Science and Technology: A Comprehensive Treatment, VCH Publishers, Chapter 6, pp. 419-543.

[26] F. A. Garner, 2010, "Void Swelling and Irradiation Creep in Light Water Reactor Environments", Understanding and Mitigating Ageing in Nuclear Power Plants: Materials and Operational Aspects of Plant Life Management (PLiM), edited by Philip G. Tipping, Woodhead Publishing Limited, Chapter 10, pp. 308-356.

[27] V.S. Neustroev, V.K. Shamardin, 1997, "Medium-Temperature Radiation Embrittlement of Austenitic Steels and Alloys Irradiated in Fast-Neutron Reactors", Physics of Metals and Metallography, Vol. 83, Issue 5, pp. 555-560.

[28] Y. Dai, G.R. Odette, T. Yamamoto, 2012, "The Effects of Helium in Irradiated Structural Alloys", Comprehensive Nuclear Materials, Elsevier, Amsterdam, Vol. 1, pp.141-193.

[29] H. Trinkaus, H. Ullmaier, 1994, "High Temperature Embrittlement of Metals due to Helium: Is the Lifetime Dominated by Cavity Growth or Crack Growth?", J. Nucl. Mater., Vol. 212-215, Part 1, pp. 303-309.

[30] H. Trinkaus, B.N. Singh, 2003, "Helium Accumulation in Metals during Irradiation – Where Do We Stand?", J. Nucl. Mater., Vol. 323(2-3), pp. 229-242.

[31] D.J. Edwards, F.A. Garner, S.M. Bruemmer, P. Efsing, 2009, "Nano-Cavities Observed in a 316SS PWR Flux Thimble Tube Irradiated to 33 and 70 dpa", J. Nucl. Mater., Vol. 384, Issue 3, pp. 249-255.

[32] M. Griffiths, J.P. Slade and A.M. McDonald, 1988, "Failure of Inconel-600 Thin-Walled Tubes due to Nitriding Embrittlement", Proc. of International Metallographic Society Conf., Microstructural Science, Vol. 17, p.321-330.

[33] M. Griffiths, D. Poff, Z. Yao and K. Huang, 2013, "Performance of Ni-alloy Components in CANDU Reactors", to be published in Proceedings of Int. Conf. on Materials Science & Technology(MS&T'13), Montreal, Quebec, Canada, October 27-31, 2013.

[34] S.I. Golubov, A.V. Barashev and R.E. Stoller, 2012, "Radiation Damage Theory", Comprehensive Nuclear Materials, Elsevier, Amsterdam, The Netherlands, Vol. 1, pp.357-391.

[35] A. Kelly and N.H. Macmillan, 1987, "Strong Solids (Monographs on the Physics and Chemistry of Materials)", 3rd edition, Oxford University Press, Cary, North Carolina, USA.

[36] B.N.Singh and A.J.E. Foreman, 1989, "Nucleation of Helium Bubbles at Grain Boundaries During Irradiation", 14th International Symposium on Effects of Radiation on Materials; ASTM STP 1046; Volume 1, pp 555-571.

[37] L.K. Mansur, W.A. Coghlan, 1983, "Mechanisms of Helium Interaction with Radiation Effects in Metals and Alloys: A Review", J. Nucl. Mater., Vol. 119(1), pp.1-25.

[38] A.R. Causey, G.J.C. Carpenter and S.R. MacEwen, 1980, "In-Reactor Stress Relaxation of Selected Metals and Alloys at Low Temperatures", J. Nucl. Mater., Vol. 90(1-3) pp. 216-223.

[39] I. Remec, J.A. Wang, F.B.K. Kam, 1996, "HFIR Steels Embrittlement: The Possible Effect of Gamma Field Contribution", Effects of Radiation on Materials: 17th International Symposium, ASTM STP 1270, pp. 591-605.

[40] G.D. Tolstolutskaya, V.V. Ruzhytskiy, I. E. Kopanets, S.A. Karpov, V.V. Bryk, V.N. Voyevodin and F.A. . Garner, 2006, "Displacement and Helium-Induced Enhancement of Hydrogen and Deuterium Retention in Ion-Irradiated ^{18}Cr^{10}NiTi Stainless Steel," J. Nucl. Mater. Vol. 356(1-3), pp. 136-147.

[41] L.K. Mansur, E.H. Lee, P.J. Maziasz and A.P. Rowcliffe, 1986, "Control of Helium Effects in Irradiated Materials Based on Theory and Experiment", J. Nucl. Mater., Vol. 141-143, Part 2, pp. 633-646.

[42] C. H. Woo and F. A. Garner, 1999, "Contribution to Irradiation Creep Arising from Gas-Driven Bubble Growth", J. of Nucl. Mater. Vol. 271-272, pp. 78-83.

[43] M.L. Grossbeck, L.K. Mansur, 1991, "Low-Temperature Irradiation Creep of Fusion Reactor Structural Materials", J. Nucl. Mater. Vol. 179-181, Part 1, pp. 130-134.

[44] R.E. Stoller, M.L. Grossbeck, L.K. Mansur, 1992, "A Theoretical Model of Accelerated Irradiation Creep at Low Temperatures by Transient Interstitial Absorption", 15th International Symposium on Effects of Radiation on Materials; ASTM STP 1125; pp 517-529.

[45] M.L. Grossbeck, L.T. Gibson, S. Jitsukawa, L.K. Mansur, L.J. Turner, 1999, "Irradiation Creep at Temperatures of 400 °C and Below for Application to Near-Term Fusion Devices", 18th International Symposium on Effects of Radiation on Materials; ASTM STP 1325; pp 725-741.

INVITED ARTICLE

In 2009 May, the National Research Universal (NRU) calandria leaked. During the next year, the calandria was inspected with six new Non-Destructive Evaluation (NDE) techniques to determine the extent of the corrosion, repaired, and finally the repair was inspected with four additional new NDE techniques before the reactor was returned to service.

The calandria is surrounded by a light-water reflector vessel fabricated from the same material as the calandria vessel. Concerns that the same corrosion mechanism had damaged the reflector vessel led to the development of a system to inspect the full circumference of the reflector wall for corrosion damage. The inspection region could only be accessed through 64 mm diameter ports, was 10 m below the port, and had to be inspected from the corroded surface. The ultrasonic technique was designed to produce a closely spaced wall thickness (WT) grid over an area of approximately 5 m^2 on the corroded surface using a very small probe holder.

This paper describes the Reflector Wall Inspection (RWI) development project and the system that resulted.

DEVELOPMENT OF NRU REFLECTOR WALL INSPECTION SYSTEM

R.H. Lumsden*, B. V. Luloff, N. Zahn and N. Simpson

Atomic Energy of Canada Limited, Chalk River Laboratories, Chalk River, Ontario, Canada K0J 1J0

*Corresponding author: (613) 584-3311, lumsdenr@aecl.ca

Nomenclature
AECL   Atomic Energy of Canada Limited
ASME   American Society of Mechanical Engineers
ASTM   American Society for Testing and Materials
CANDU® CANada Deuterium Uranium
CGSB   Canadian General Standards Board
CIQB   CANDU Inspection Qualification Bureau
COG   CANDU Owners Group
ET   Eddy Current Testing
FAATS   Feeder Automated Analysis Trending Software
ICP-MS Inductively Coupled Plasma – Mass Spectrometry
IMD   Inspection, Monitoring & Dynamics
NDE   Non-Destructive Evaluation
NRU   National Research Universal
PEEK   PolyEther Ether Ketone
RWI   Reflector Wall Inspection
UT   Ultrasonic Testing
VLRP   Vessel Leak Repair Project
WT   Wall Thickness

1. Introduction

The NRU reactor first went critical on 1957 November 3. It has been used for production of isotopes for cancer diagnosis and treatment, research activities conducted at the Canadian Neutron Beam Centre, and CANDU® reactor research and development. The NRU includes a vertically oriented cylindrically shaped vessel that contains the fuel and heavy water (calandria), and a second vessel that contains the light water (reflector) that surrounds the calandria. These two vessels are separated by a 149 mm gap (approximately half the annulus is 149 mm wide; the width over the rest of the annulus varies from 149 mm to 187 mm) called the gas annulus space (Figure 1).

In 2009 May, a heavy-water leak was found in the calandria vessel, and visual inspections from the gas annulus space indicated that the leak was likely due to corrosion of the calandria vessel wall from the gas annulus space side [1]. The Vessel Leak Repair Project (VLRP) was conducted to assess the extent of condition (corrosion), repair the vessel, and inspect the repair. In 2010, the RWI project was initiated to inspect the inner wall of the water reflector vessel due to concern that the corrosion in the gas annulus space may have also affected the water reflector vessel.
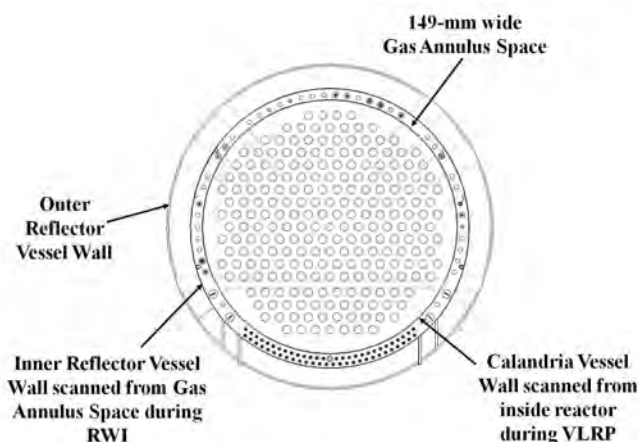
FIGURE 1: Cross-section of NRU calandria and reflector vessels, viewed from above.

The evolution of inspection systems from the VLRP to RWI is discussed herein. Similarities and differences between these inspection systems are discussed and organizational tools that helped both the development and the inspections are presented. The VLRP and RWI results will be presented in a future paper.

1.1 VLRP Inspections
The NDE used in the VLRP was predominantly performed from inside the calandria vessel on the un-corroded surface. The NDE included: eddy current testing (ET), ultrasonic testing (UT), visual inspection, radiography testing support and laser profilometry of repair locations. Six different NDE probe holders were employed during the extent-of-condition inspections and four more probe holders were used during the repair.

The reactor was still fuelled and filled with heavy water when the first inspection occurred about one month after the leak. AECL-Chalk River Laboratories developed the Mark I axial scanning tool for this inspection, which delivered a combined UT/ET probe holder (Figure 2). The bottom 300 mm of about half of the circumference (full circumference is 11 m) of the calandria vessel was inspected with this tool.

By three months after discovery of the leak, the calandria had been defueled and emptied of heavy water to reduce radiological hazards. The Mark II circumferential scanning tool (Figure 3) was developed with new UT and ET probe holders to perform a dry inspection (ET operates under both wet and dry conditions, UT requires a liquid to transmit sound into the material) that included both the

calandria vessel wall and a lower angular flange. The Mark II tool was able to inspect areas that could not be reached with the Mark I tool due to obstructions. The Mark II tool delivered eight different probe holders: phased array UT, high resolution ET, shear wave UT, ET marking (repeat ET technique used to locate the repair positions and make visual markings for the welders), as well as one ET and three UT probe holders used during inspection of the repair.

In addition, a previously used inspection tool was refurbished to perform full-height vertical scans of the calandria and water reflector vessel walls. These inspections were done to verify that the vertical extent of the corrosion was limited to the bottom 300 mm of the vessel.

In all, nine NDE techniques were developed and implemented in NRU by 300 staff over a period of seven months. At the time, and with the agreement of the regulator, only four of these NDE techniques were required to be CANDU Inspection Qualification Bureau (CIQB) qualified since they related to inspection of the repairs.

FIGURE 2: Mark I tool with combined UT/ET probe holder.

FIGURE 3: Mark II tool with probe holder.

1.2 Reflector Wall Inspection

The calandria vessel is housed inside a water-reflector vessel. Between the walls of these vessels is a gas-annulus space, which is filled with carbon-dioxide cover gas. Based on visual inspections and chemical analysis [1], it was determined that the corrosion mechanism that affected the calandria wall may have also affected the water-reflector wall.

The outer diameter of the calandria vessel is 3.5 m and the inside diameter of the inner reflector vessel wall is 3.8 m, nominally. The inner reflector wall is 3.2 m tall within the gas annulus space.

The RWI was different from the VLRP inspections in that it was constrained to be conducted in stages during planned reactor maintenance outages. The RWI faced the same complexities as the VLRP, including inspecting a region located 10 m below the access port. However, there were also additional difficulties related to a reduction in the entry port diameter (64 mm versus the previous 120 mm) and inspection on a corroded surface. In addition, the RWI tool (Figure 4) had to scan large areas of the water reflector wall and cover at least the bottom 300 mm from within a 149 mm wide gas annulus space, with many protruding obstructions.

2. RWI Project Development

The key to quick development of many inspection systems and techniques during the RWI and VLRP, and their rapid implementation into the field, was having the same development and inspection teams throughout and having the implementation team work on development. Furthermore, the UT inspections during the VLRP were based upon prior experience with similar inspections. The UT inspection team had previously developed key system components, including a phased array UT probe holder and the FAATS-COG (Feeder Automated Analysis Trending Software – CANDU Owners Group) analysis software, used to successfully measure WT through the complex surfaces of CANDU feeder Grayloc hub welds and header nozzle welds. Knowledge gained was readily transferrable to the design of the VLRP and RWI UT probe holders. The analysis software developed for CANDU inspections was used throughout the VLRP project. This previously developed technology and experience enabled the inspection team to quickly develop the VLRP and RWI techniques.

The RWI development and implementation team included staff who worked on VLRP tasks such as: technique/technology development, procedure writing, testing, training, implementation in NRU, data analysis, and reporting of results. Having a consistent and experienced team that worked on both the VLRP and RWI ensured that lessons learned from the VLRP inspections were considered during development of the RWI.
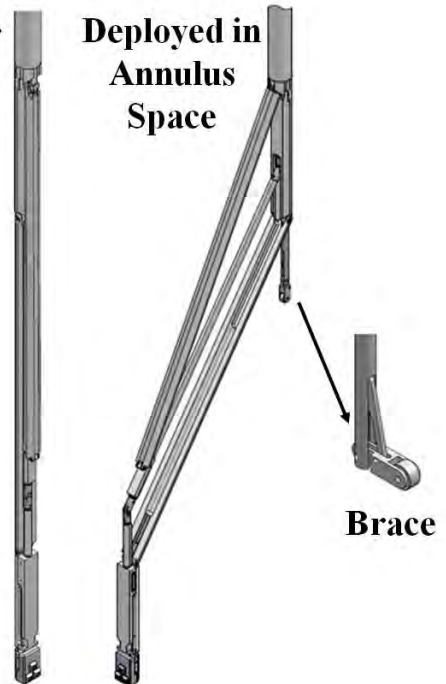
FIGURE 4: RWI tool, tool on insertion (left), tool deployed (centre), brace deployed (right).
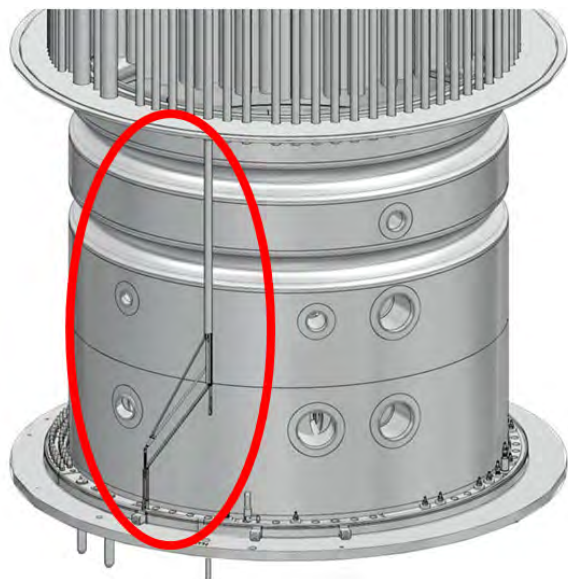
FIGURE 5   RWI tool deployed against the water reflector vessel wall (not shown) for inspection.
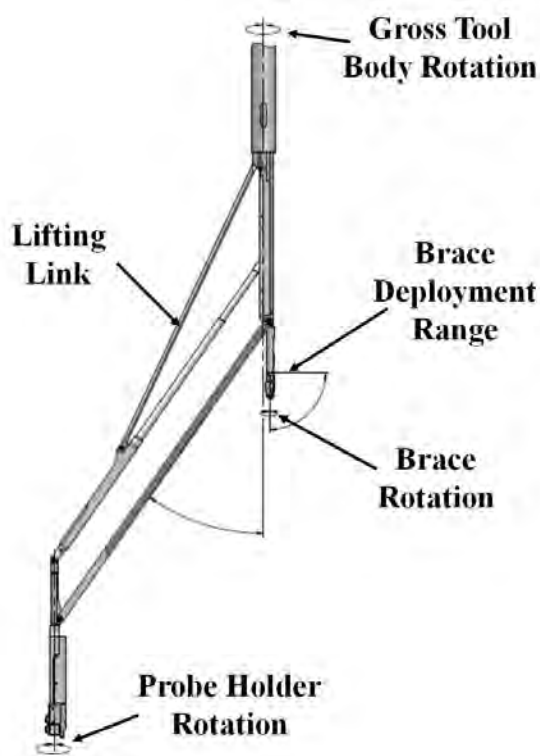
FIGURE 6: RWI tool mechanics.

WT inspections of the NRU calandria and water reflector walls had been previously performed in 2004. During these previous inspections, the UT instrument triggered on WT signals, automatically produced the WT results, but did not record the UT signals. Consequently, the data could not be analyzed after the inspection. In contrast, the UT signal was digitally captured during the VLRP and RWI to allow post-acquisition analysis with FAATS-COG by trained and qualified UT inspectors (inspection team was composed of UT Canadian General Standards Board (CGSB) certified inspectors who had been specially trained and tested to be qualified for this inspection) to calculate the WT [2]. This radically improved approach enabled UT inspectors, with the aid of the analysis software, to produce WT maps over large regions of the calandria and water reflector vessel walls. Furthermore, collection of the UT signals and post-acquisition analysis allowed WT measurements to be obtained even when the surface condition produced low amplitude, noisy signals. This fundamental inspection approach was used during all NRU inspections and led to consistent results.

The VLRP inspections had major challenges: a very aggressive schedule over a sixteen-month unscheduled outage as described earlier. The RWI, which is on-going, has different challenges: the inspections occur over two-day periods in five-day scheduled outages, only one technique has been developed, more time was available for development (one year to prepare), a smaller group of staff are involved (~50 people), and the costs are significantly lower.

Despite the differences between the VLRP and RWI, experience was carried over from one project to the other. The VLRP inspection techniques, procedure, testing, training and staff qualification used for the inspections of the repair sites in the calandria were qualified by the CIQB. The experience from this extensive qualification process helped prepare for the RWI. Furthermore, lessons learned from the sixteen-month VLRP outage were implemented in all aspects of the RWI project.

2.1 Comparison of the VLRP and RWI Tools
The VLRP and RWI were performed in locations with very restricted access, which led to development of custom made tools that were 10 m long and delivered custom probe holders to the inspection sites. The Mark I and II tools (Figures 2 and 3, respectively), which allowed vertical and circumferential scanning, respectively, were developed and inserted through a 120 mm diameter entry port into the calandria vessel. The RWI tool is also 10 m long, but had to be smaller because it enters the gas-annulus space through 64 mm diameter ports. During inspection, the Mark I and II tools were seated in emptied fuel-cup locations in

the bottom of the calandria. The RWI tool has a brace to make contact with the calandria vessel wall, enabling the probe holder to make contact with the reflector vessel wall without sitting in a cup, as shown in Figures 4, 5 and 6. The Mark I and II tools were deployed to scan the calandria vessel wall from within the largely emptied calandria vessel, whereas the RWI tool is deployed to scan segments of a wall from within a 149 mm wide annulus space, at its narrowest locations.

The VLRP tools (Mark I and II) were manually operated and, therefore, exposed operators to radiation during inspection. The load to the inspection surface was limited by calibrated break-away control bars. The Mark I tool used a drill to control scanning speed. In contrast, the RWI tool is remotely controlled to reduce radiation dose to the worker. The RWI tool contains six motorized drives, three of which include torque limiters (clutches). These clutches maintain and limit the load applied to the calandria and water reflector vessel walls. All of the drives are encoded and have manual back-up if the motors fail.

During the VLRP development, a scale mock-up was fabricated from the original calandria vessel drawings, including nominal wall thickness and geometry. This mock-up was used to perform final probe and tool testing and to confirm that contact could be maintained during scanning. During the RWI tool development, another mock-up was built to accept replaceable test plates. Different test plates were used during commissioning of the tool and training of the tool operators. Several plates were machined with a ball-nose end mill to contain simulated corrosion patterns based upon the NDE results of the VLRP (sample shown in Figure 7). One of the plates was used for qualification of UT operators and was quarantined before, during, and after the operators' use, in order to keep the UT operator's acquisition or analysis tests unbiased.

2.2 Tool Mechanics, Drive Mechanisms and Clutches
The RWI system is comprised of the RWI tool, instrumentation and data-acquisition system, procedures and documentation, analysis software and computers, drive system controls that allow the tool operator to remotely operate the five motorized drives, and the modified elevator. The RWI tool features a probe holder with independently sprung probe modules (discussed further in Section 2.4), a parallelogram linkage arm with actuating lifting link, a brace arm, a long, tube-shaped body, see Figures 4, 5 and 6, and the drive core, which houses the motors and drive mechanisms required to deploy the arm, see Figures 8 and 9. The elevator allows the tool to be moved vertically during an inspection and features three main components: the frame, a long screw with motor, and the carriage to which the tool mounts. An existing elevator

FIGURE 7: Simulated corrosion pattern from VLRP WT results, used for RWI mock-up testing.
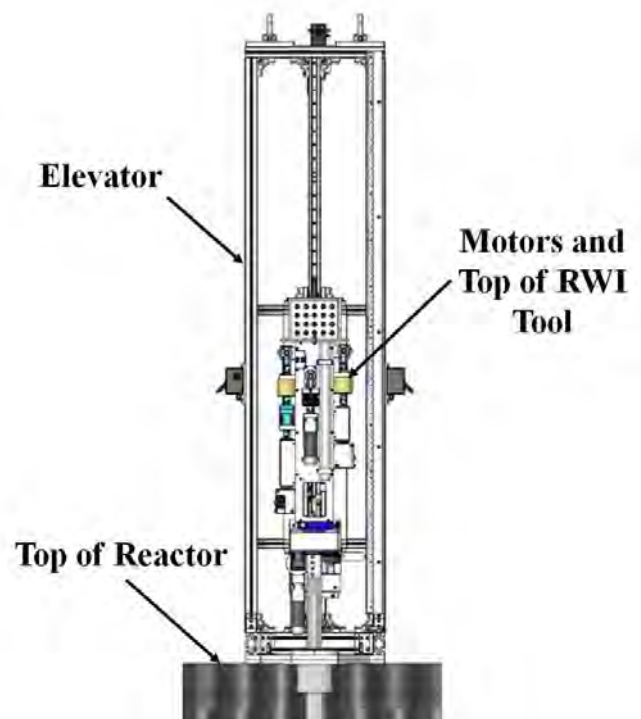
FIGURE 8: RWI tool and elevator above deck plate.
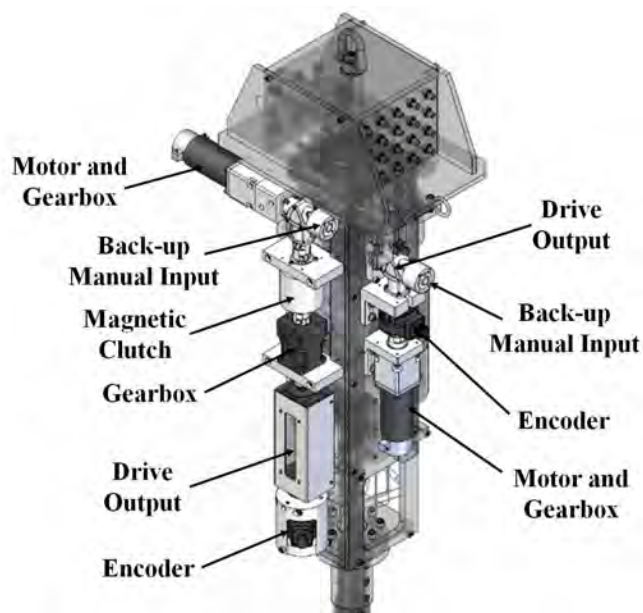
FIGURE 9: RWI tool drive mechanisms, with magnetic clutch on left and without on right; these are both duplicated on the other side of the tool.

design for a camera tool was modified to support both the RWI tool and its associated camera tool. For the purpose of the RWI, a carriage adaptor was installed to provide gross tool rotation.

In essence, the RWI tool is similar to the Mark I NDE Inspection tool. However, the key differences are that all tool movements are motorized and can be controlled remotely, the diameter of the tool is smaller (60 mm) and a second arm, the brace, is included to reduce tool deflection by pushing off the calandria wall. The linkage arm is deployed by lifting the actuating lifting link, which is connected to the top link of the parallelogram linkage. Once a desired arm extension is reached, the probe holder and entire tool can be independently rotated to orient the probe holder normal to and against the reflector wall, with a limited load on the wall. The brace is then deployed and rotated to contact against the calandria vessel wall. Vertical scanning is achieved by positioning the entire tool at its intended scanning position and then turning the screw on the modified elevator with the motor. A series of arm configurations are required to ensure complete circumferential coverage from the target J-Rod position into which the tool has been inserted. Note that although there are 50 J-Rod positions around the circumference of the annulus, not all of the positions are accessible for entry, so the tool was designed to inspect the reflector wall circumference from 13 J-Rod positions.

A number of critical features were incorporated into the design of the RWI system: a limit switch below the probe holder, clutches in the gear train for drives that apply the majority of load on the vessel walls, and design features that assure fail-safe operation. The limit switch trigger is directed downwards and has the same footprint as the probe holder (and collapsed tool), so that the elevator axial drive is immediately stopped upon probe holder contact with any reactor component below. This radiation-hardened limit switch is also used to provide a vertical reference for the lowest reachable elevation of the probe holder in any given arm configuration. The following three drives have magnetic particle clutches: the linkage drive (left side of Figure 9) that extends the arm, the brace deployment drive (on the back side of the tool, but having a configuration similar to the linkage drive) that extends the brace arm, and the tool rotation drive that is part of the modified elevator. As these drives actuate tool components that contact the calandria and reflector walls, a means to limit the applied force was required. The amount of torque transmitted by the clutch is linearly proportional to the power supplied to it. Limiting the load applied to the calandria and reflector vessel walls was an NRU requirement. Finally, potential failure modes were carefully scrutinized during the design phase of the tool. As a result, the tool can be recovered from the annulus in the event of any drive system failure. The motors were located above deck and manual inputs downstream of the clutches were included (but not normally accessible) to facilitate troubleshooting. The brace rotation drive (depicted on the right side of Figure 9) and probe holder rotation drive (on the back side of the tool, but having a configuration similar to the brace rotation drive) do not require magnetic clutches for use during tool operation.

2.3 Material Selection and Irradiation Testing
The use of metals in inspection tooling within the core of a reactor typically leads to the use of aluminum over steel due to neutron activation. Aluminum has a half life of 2.3 minutes [3] (note that the quoted values from [3] are "... the half-lives of the activities formed ..."), so waiting 15 minutes leads to an appreciable drop in dose, which is of great benefit compared to the longer periods that would be required if steel were used. For fasteners and members that require higher strength, stainless steel is the typical choice for the following reasons: the isotope of iron typically produced by activation has a half life of 45 days [3, 4], which is relatively short compared to other activated metals; the use of carbon steel can lead to the generation of loose contamination as it corrodes; and stainless steel is readily available from most suppliers. Certain stainless steels contain cobalt that becomes activated with a high-energy decay and a half-life of 5.26 years [3]. Titanium has a half-life of 5.8 minutes [3], but the cost of material,

and more importantly, the greater challenges in machining have limited its use within tooling. It is expected that titanium will be used in place of stainless steel in the future for higher strength material applications within this type of tooling to reduce dose to workers.

For the VLRP and RWI tooling, the use of copper was avoided due to the potential for galvanic reaction between the aluminum vessel walls and copper components.

Qualification of new materials for use in reactor can be a complex task. During the VLRP Delrin® had been used in tools. Delrin has a radiation tolerance of only 104 Gy with embrittlement and colour changes [5]. Thus, Delrin would not last long in typical CANDU fuel channel inspections and so engineered plastics such as PEEK (polyether ether ketone) have been used for such purposes. The RWI tool probe holder modules, Figure 10, were made of plastic to reduce damage to the aluminum wall, but PEEK had not been qualified for use in the annulus, so early RWI probe holders used Delrin. This was only a short-term solution and another plastic had to be qualified. DuPont™ was contacted to obtain other engineered plastics with radiation tolerance similar to PEEK (107 Gy, "PEEK shows excellent resistance to hard (gamma) irradiation, absorbing over 1000 Mrad of radiation without suffering significant damage and showing no embrittlement of the polymer. It is believed that PEEK will resist dose levels of well over 10,000 Mrad of particle (alpha or beta) irradiation without significant degradation of properties." [5]). DuPont Vespel® SP-1 (unfilled grade) was suggested as a comparable plastic to 30% glass filled or unfilled PEEK, mechanically and for radiation tolerance (for Vespel "radiation resistance is excellent with no property changes observed up to 1000 Mrad" [6]). Vespel is part of the polyimide family of plastics, not to be confused with the polyamide family, such as Nylon® by DuPont, which does not have adequate mechanical performance or radiation tolerance. These two plastics were sent to McMaster University's nuclear reactor for neutron activation (for testing: neutron flux $\sim 6 \times 10^{12}$ neutrons/(cm^2 × s), pure neutron (no gamma source), irradiation time was 120 seconds), and Inductively Coupled Plasma - Mass Spectrometry (ICP-MS) analyses. The analyses were completed for a number of specific chemicals including sulfates, phosphates and halides, as per the strict requirements of NRU chemistry. Vespel's sulphur and phosphorus concentrations, captured from ICP-MS, post neutron activation, were much lower than PEEK. The glass-filled version of PEEK was tested but its elevated aluminum content, likely as a result of its silicon (glass) content, did not allow for reliable fluorine or sulphur neutron activation analysis results. Additional irradiation testing of these plastics, and other RWI tooling components, was completed in the NRU annulus to examine the effects of radiation on dimensional stability and hardness under

the actual radiation fields for these inspections. As a result of this testing, Vespel SP-1 was qualified for RWI tooling and the Delrin components were replaced with Vespel.

2.4 Probe Holders
The VLRP inspections were performed from the non-corroded side of the calandria wall. The surface was very smooth prior to the repair, and consisted of various irregular surfaces (repair plates, weld overlay, etc) after the repair. Nevertheless, the inspection surface was relatively smooth. Obtaining valid ultrasonic data in the RWI was technically more complex because it was performed on the corroded surface of the reflector wall. This required development of a modular probe holder design, shown in Figure 10, which could adapt to changing inspection surfaces using three independently sprung modules. Each module contains five small (3 mm diameter case) probes and water irrigation ports.

A very rough surface was inspected during testing of the RWI tool in a mock-up. The rough surface was machined using VLRP WT data from the calandria vessel and, hence, similar to the surface that was expected during the RWI. The amount of valid WT measurements collected over this very rough surface met the inspection requirements. Data collected on the rough surface in mock-up confirmed that the modular probe holder collected more data than the single sprung module, but also showed the inadequacy of the on-module irrigation holes (Figure 10). Note that most UT techniques require a liquid couplant between the probes and the inspection surface to keep air or other lower acoustic impedance fluids from attenuating the signal. Moving the irrigation holes to above the probe holder modules (Figure 11) resolved this irrigation inadequacy.

2.5 Procedures and Demonstration
The RWI procedure was written based on VLRP experience and American Society of Mechanical Engineers (ASME) [7-9], American Society for Testing and Materials (ASTM) [10, 11], and CGSB [2] code requirements. The format and details of the RWI procedure are consistent with the VLRP procedures because the same group of UT experts was involved in developing procedures for both inspections. The RWI procedure and training plan were written to comply with CIQB requirements, based on experience gained during the CIQB qualification of the VLRP repair inspection procedures. During RWI operator training and testing, the inspection procedure and tool were demonstrated to, and subsequently approved by, the Ontario Technical Standards and Safety Authority.

The inspection and analysis procedure for the RWI describes details such as: capabilities and limitations of the inspection, position conventions, data acquisition system checks,

---

® A registered trademark of DuPont, Delrin is also known as acetal or by its chemical name polyoxymethylene.

examination sequence, rescan criteria, analysis, and reporting, all of which are required to meet best-practice principles. The RWI procedure also incorporated lessons learned from the VLRP inspections.

2.6 Software
The same data acquisition software was used for both the VLRP and RWI. It was developed in-house as an extension of software previously developed for the AECL Fuel Channel Inspection System. The acquisition software and related hardware allows data collection based on either time or position and is able to collect data from up to 20 UT probes simultaneously. Figure 12 shows a single probe from a calibration file using this software. FAATS-COG is used for data analysis. FAATS-COG creates two-dimensional WT maps based on the position of the collected data and enables very detailed analysis of the UT signals post acquisition. Figure 13 shows how the 15 probes are displayed for the same calibration file using the FAATS-COG software.

3. Discussion
Development, implementation, analysis, and reporting of the RWI project were performed in a similar manner to the VLRP. Some of the similarities are listed below:

- A small group of inspection experts, with relevant previous experience, defined the methodology and technology. Several aspects of the approach and technology were used for both projects. Capture of the entire UT signal and its post-acquisition analysis is an example.
- The inspection procedures were developed and written by this small group of experts. Consistent approaches, wording, format, and technology were used whenever possible.
- Work plans, training plans, and support documents on software verification were written to facilitate uniform operation.
- The delivery tools are similar. The Mark I VLRP tool evolved into the RWI tool.
- Mark I and II tool instrumentation cables are routed externally on the tools. This allows for easy changeover between different NDE cabling, but also caused cabling to be severed on occasion during tool entry. Due to space limitations, the RWI tool cabling runs from the top of the tool, inside the tool body and down the linkage arm to the probe holder.
- The calibration fixture from the Mark II tool was used for the RWI. Use of a similar fixture helped inspection staff perform calibrations quickly, reducing radiation dose.
- The same support staff, including shift supervisors, tool designers, software developers, tool operators, and equipment maintainers were involved in the RWI
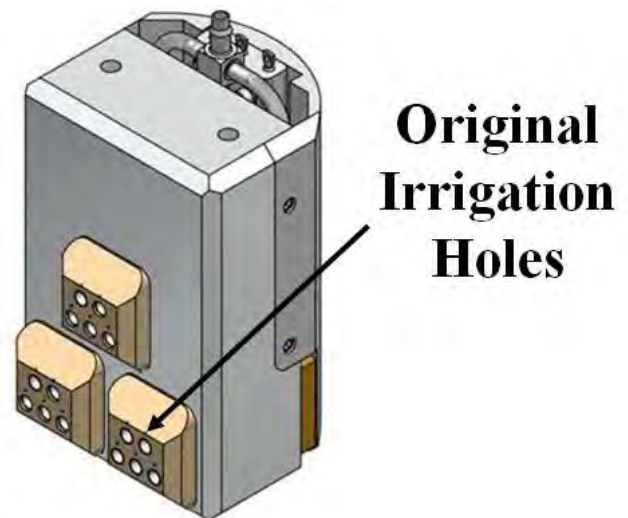
FIGURE 10: RWI probe holder, original design.
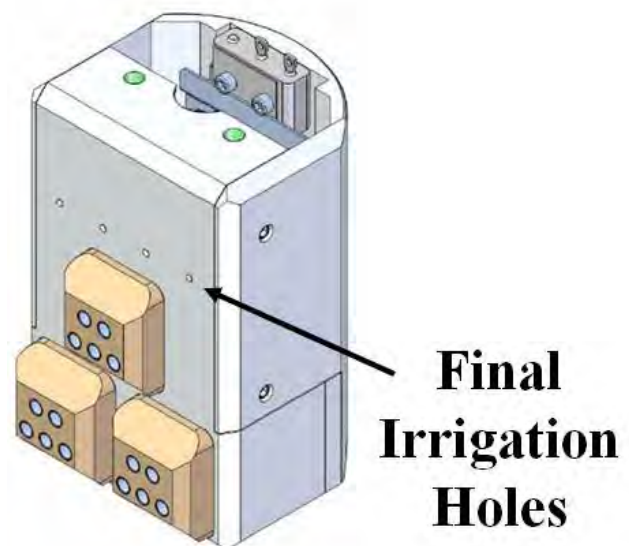
FIGURE 11: RWI probe holder, final design.

project. Use of a consistent group of people helped ensure that lessons learned were passed on.
- Training of staff on tool operation, communication, and inspection procedures was performed in a realistic mock-up for both the VLRP and RWI projects. The mock-ups and staff training were in the same location.
- The RWI pre-job briefings and post-job reviews were performed in the same manner as the VLRP inspections. As a shift was nearing its end, the incoming shift would observe the final actions of the outgoing shift. Then work was paused and a post-job review and pre-job
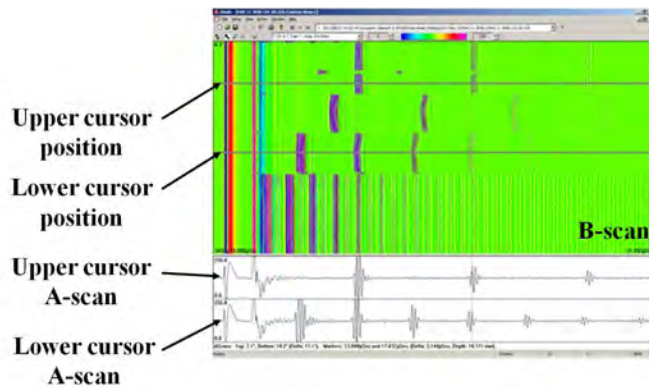
FIGURE 12: Acquisition software screen of a single probe from system calibration.

FIGURE 13: FAATS-COG software screen for all probes from system calibration (same data as Figure 12).

briefing was performed. After, each team member met with their counterpart on the other shift to discuss specific details prior to continuing the inspection.

- Experience with collected and analyzed data, inspection shift logs, training, and video captured from inspections and repairs, were used to improve inspection performance.
- The VLRP used a small number of probe designs, instruments, and support technologies for consistency. The RWI used a UT probe from the VLRP. Prior experience with this technology helped ensure success.
- Multiple people analyzed each inspection file. Two analysts with prior relevant experience in VLRP were responsible for final analysis and release of the data. Use of two, and often three, analysts per file helped ensure that data were properly analyzed and ensured consistency in results. This analysis strategy was similar to what was done during the VLRP analysis.

4. Conclusions

Prior experience with similar inspections in the NRU calandria vessel and CANDU inspections was an important factor in the success of the RWI project. Prior experience includes measuring WT through weld caps on feeders and using FAATS-COG analysis software. Operational experience gained in the VLRP inspections was incorporated into the development and implementation of the RWI project. Experience gained from the CIQB procedure qualification process during the VLRP strengthened the RWI procedures and training. Experience with shift turnover meetings led to improvements in how the inspection team captured lessons learned, trended issues, and eliminated reoccurring design and procedure problems. Experience with collecting and analyzing data, inspection shift logs, training, and video captured from inspections and repairs,
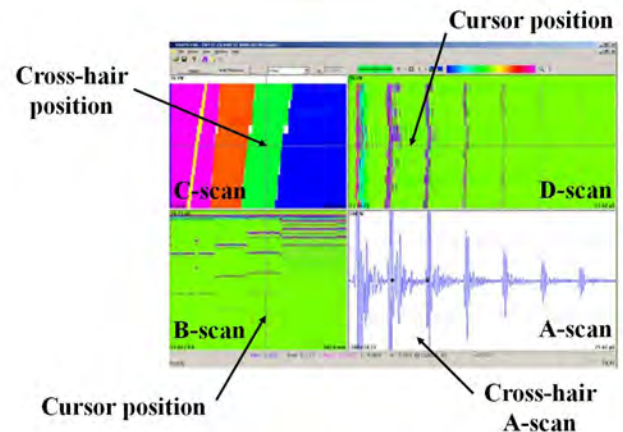
was used to improve the RWI project performance. Finally, tool-mechanism design, material selection and irradiation testing reduced dose to tool operators and improved tool performance.

References

[1] C.R. Stuart, D.S. Mancey, M.D. Wright, "Corrosion Control for the NRU Reactor Vessel", Nuclear Plant Chemistry Conference (International Conference on Water Chemistry of Nuclear Reactor Systems), Quebec City, QC, Canada, 2010 October 3-7, Paper 4.04.

[2] Canadian General Standards Board, 2006, "Non-destructive Testing - Qualification and Certification of Personnel", Standard CAN/CGSB-48.9712-2006.

[3] R. Sher, 1974, "2200 m/s Neutron Activation Cross-Sections", Handbook on Nuclear Activation Cross-Sections, IAEA Technical Reports Series No. 156, Vienna, Austria, pp. 1-14

[4] G. Audi, O. Bersillon, J. Blachot and A.H. Wapstra, 2003, "The NUBASE Evaluation of Nuclear and Decay Properties", Nuclear Physics A, 729(1), pp. 3-128.

[5] L.K. Massey, 2005, "The Effect of Sterilization Methods on Plastics and Elastomers", William Andrew Inc., 2nd Edition, Norwich, NY, USA.

[6] D.J. Kemmish, 1995, "High Performance Engineering Plastics", Smithers-Rapra Publishing, Akron, OH, USA.

[7] American Society of Mechanical Engineers, 2010, "SE-797, Standard Practice for Measuring Thickness by Manual Ultrasonic Pulse-Echo Contact Method", ASME Boiler & Pressure Vessel Code 2010 (with 2011 Addendum), Section V, Subsection B, Article 23.

[8] American Society of Mechanical Engineers, 2010, "Ultrasonic Examination Methods for Materials", ASME Boiler and Pressure Vessel Code, Section V, Subsection A, Article 5.

[9] American Society of Mechanical Engineers, 2010, "Examination System Qualification", ASME Boiler & Pressure Vessel Code, Section V, Subsection A, Article 14.

[10] American Society for Testing and Materials, 2010, "Standard Terminology for Nondestructive Examinations", ASTM E1316-10a.

Analytical Representation of ZED-2 Reactor Geometry by Means of the R-Function Method

D. Altiparmakov*

Atomic Energy of Canada Limited, Chalk River Laboratories, Chalk River, Ontario, Canada
K0J 1J0

*Corresponding author: (613) 584-3311, altiparmakovd@aecl.ca

The R-function method is applied to model the geometry of the critical facility ZED-2 as an illustrative example. Each material region is represented by a real, continuous and differentiable function of spatial coordinates that is referred to as the domain function. Instead of using particular functions for individual elements, a single function is constructed to represent all spatial domains that contain the same material, for instance all fuel pins, etc. Owing to continuity and differentiability, the domain functions can be used to construct a basis for approximate solution of the related boundary-value problems. A study of the approximation ability of the domain functions is carried out using the two-group spatial neutron flux distribution in the ZED-2 facility as a model problem. The least squares method is used to determine the unknown coefficients by minimizing the discrepancy between the reference MCNP solution and a power series of domain functions. The results show that a modest number of terms in the series is able to produce a good approximation of the neutron flux distribution specified on a mesh grid of 500 x 500 points.

1. Introduction

A mathematical description of the geometry is required in a wide range of scientific and engineering problems, such as approximate solution of boundary values problems, solid modeling, computer-aided design and manufacturing, etc. By the introduction of the Cartesian coordinate system in 1637, the French philosopher René Descartes is credited with conceiving the analytical geometry, which allows algebraic equations to be expressed as geometric shapes. For instance, quadric surfaces (cylinder, cone, ellipsoid, paraboloid and hyperboloid), which are largely used in solid modeling and Monte Carlo calculations, represent sets of points at which a quadratic polynomial of spatial coordinates is equal to zero. Over the past centuries, remarkable progress was made in understanding and classifying the properties of analytic and algebraic equations. The efforts were focussed mainly on what is termed as the direct problem of the analytical geometry, i.e., to determine the geometric shape or the locus (set of points) for a given equation. The inverse problem that consists of determining an equation for a given geometric shape was not treated until recently. Despite a very large class of geometric shapes that have been considered, analytical geometry is unable to describe some very simple geometric shapes such as triangle and square, for instance. Instead of a single equation, the mathematical description of such shapes, which are usually referred to as semi-analytic domains, consists of a set of equalities and inequalities.

A solution of the inverse problem of the analytical geometry was given in the 1960's [1] by the R-function Theory [2, 3] developed by Ukrainian mathematician V.L. Rvachev. It is a powerful tool to address the geometric part of the problem in various scientific and engineering disciplines. Using R-functions, one can easily construct an analytical, continuous and differentiable function that describes the boundary of a semi-analytic object, i.e., a complex spatial domain the boundary of which consist of parts of analytic surfaces. In this way, the geometric information can be *a priori* and analytically incorporated in the approximate solution of a boundary problem. Accordingly, the R-function method has been efficiently applied to approximate solution of heat transfer, electrostatics, theory of plates, and other elliptic boundary-value problems [3], including

the neutron diffusion [4, 5]. It has been shown [6] that in dealing with some complicated geometric shapes, the R-function method allows an efficient approximate solution of the Laplace equation with a radical reduction of the number of unknowns. In addition to boundary-value problems, the method has been also applied as solid modeller for Monte Carlo calculations [9].

There are numerous publications (15 monographs and more than 500 articles) [10] on the R-function method covering both the theoretical aspects and applications. However, a great majority of these publications are in Russian so that the R-function theory is still little known in the Western world. The interested reader can find references to a number of papers in English in the reference list of reference [10], including an English translation [11] of the reference [3]. The goal of this paper is to present some of the potentials of the R-function method applied to an analytical description of the geometry in nuclear reactor simulations. To this end, the ZED-2 critical facility is considered as an illustrative example. To facilitate the reader's understanding of the matter presented herein, a review of some of the basic elements from the R-function theory is given in Section 2.1. Based on this formalism, the analytical modeling of the geometric shape of characteristic material regions of the ZED-2 facility is presented in Section 2.2. The resulting functions are continuous and differentiable, so that, in addition to geometric modeling, they can be used to specify an approximation basis for the related boundary value problem. A study of approximation abilities of domain functions is presented in Section 3.

2. Analytical Modeling of the ZED-2 Critical Facility

The ZED-2 critical facility is a zero-power heavy-water moderated reactor, in which experiments are done to provide a broad experimental background for lattices of heavy-water reactors. Fuel channels are vertically suspended into the heavy-water moderator and reactivity is controlled by fine adjustments of the moderator level. Measurements are made for various lattice arrangements, at different lattice pitches, different fuel conditions, and different coolants. Figure 1 shows the top view of a typical reactor configuration in which 52 fuel channels are arranged in a square lattice of 24 cm lattice pitch. Each fuel channel consists of aluminum pressure and calandria tubes that are separated from each other by an air gap. Fuel bundles and the coolant, light water in this case, are accommodated within the pressure tube. Figure 2 shows the cross-sectional view of a fuel channel with 43-element CANFLEX[1] fuel bundles. Geometry data of the bundle can be found elsewhere [12].
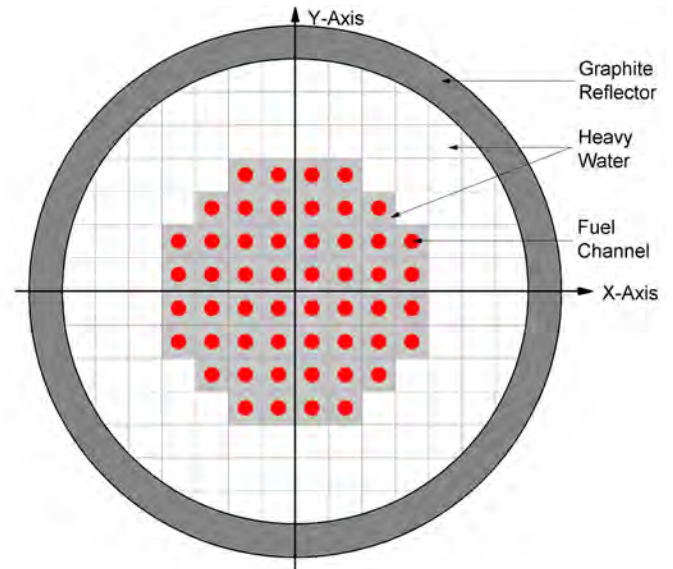
FIGURE 1: Top view of a ZED-2 configuration with square reactor lattice.
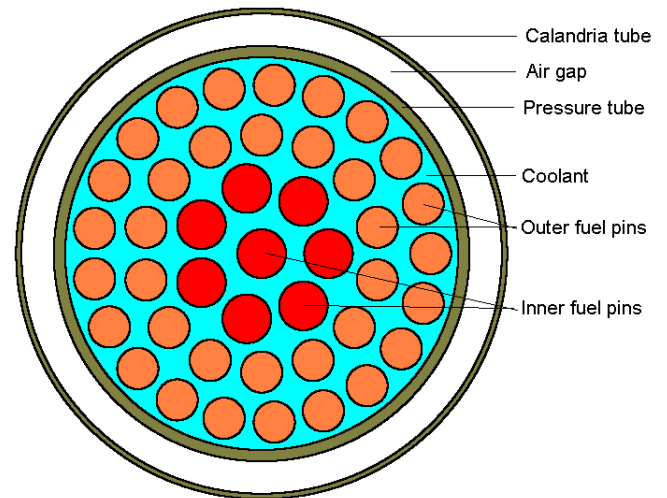
FIGURE 2: Cross-sectional view of a fuel channel with CANFLEX fuel bundle.

[1] CANFLEX is a registered trademark of Atomic Energy of Canada Limited (AECL) and the Korea Atomic Energy Research Institute (KAERI).

2.1 A Review of Relevant Terms

2.1.1 Domain Functions

The above two figures specify a two-dimensional model of the ZED-2 facility. In such a simplified representation, it consists of the following material regions: fuel, cladding, light water as a coolant, pressure tubes, calandria tubes, air gap between pressure and calandria tubes, heavy water (moderator and reflector), and graphite reflector. Each of these regions occupies a spatial domain V_i bounded by a boundary ∂V_i. The goal is to construct for each material region a real, continuous, and differentiable function $\omega_i(r)$ of spatial coordinates $\mathbf{r}=\{x, y, z\}$ that is greater than zero inside the domain V_i, equal to zero at its boundary ∂V_i, and smaller than zero everywhere else, i.e.,

$$\omega_i(\mathbf{r}) \begin{cases} > 0\,, & \mathbf{r} \in V_i \\ = 0\,, & \mathbf{r} \in \partial V_i \\ < 0\,, & \mathbf{r} \notin V_i \cup \partial V_i \end{cases} \quad (1)$$

Owing to the above properties, the function $\omega_i(r)$ can be used to describe the related domain and, as such, it is referred to as the domain function. A boundary point $r \in \partial V$, at which a unique normal $\mathbf{n}$ to the boundary ∂V exists, is referred to as a regular boundary point. A domain function is normalized to the order m if the inward directed normal derivative at the regular points of the boundary ∂V is equal to unity, while normal derivatives above order 1 and up to order m are equal to zero, i.e.,

$$\frac{\partial \omega_i(\mathbf{r})}{\partial n} = 1, \quad \frac{\partial^k \omega_i(\mathbf{r})}{\partial n^k} = 0, \quad k = 2, 3, \dots m; \quad \mathbf{r} \in \partial V_i \quad (2)$$

Accordingly, near the boundary, the domain function behaves as a linear distance from the boundary, i.e.,

$$\omega_i(\mathbf{r}) = |\mathbf{r} - \mathbf{r}_0| + \varepsilon(|\mathbf{r} - \mathbf{r}_0|^{m+1})\,, \quad \mathbf{r}_0 \in \partial V_i \quad (3)$$

where ε denotes a small quantity. As a consequence, at regular boundary points, the inward normal can be expressed as the gradient of the domain function, i.e., $\mathbf{n} = \nabla \omega_i(r)$. Thus, the normal derivative $n\nabla$ of a given function f at the boundary takes the following form:

$$\frac{\partial f(\mathbf{r})}{\partial n} = \frac{\partial \omega_i}{\partial x}\frac{\partial f}{\partial x} + \frac{\partial \omega_i}{\partial y}\frac{\partial f}{\partial y} + \frac{\partial \omega_i}{\partial z}\frac{\partial f}{\partial z}, \quad \mathbf{r} \in \partial V_i \quad (4)$$

The above equation simplifies the mathematical apparatus of a boundary value problem. Instead of various case dependent expressions, the normal derivative at a boundary can be easily specified in a general form using the derivatives of the related domain function.

The material regions of the ZED-2 model considered here are bounded by cylindrical surfaces. Starting from the analytical equation of a cylindrical surface, a variety of functions can be constructed to describe a spatial domain bounded by a cylindrical surface. For instance, the following function satisfies the properties of Equation (1) and is normalized to the first order as specified by Equation (2):

$$\omega(x, y) = 2R - \sqrt{2[R^2 + (x - x_0)^2 + (y - y_0)^2]} \quad (5)$$

where R denotes the cylinder radius, while x_0 and y_0 are the coordinates of the cylinder axis.

In the case of an annular region (pressure tube, calandria tube, etc.), the product of two functions of the type (5) would satisfy the properties of Equation (1). However, difficulties may arise if the resulting function needs to be normalized in the sense of Equation (2). A general method of constructing domain functions for arbitrary semi-analytic domains has been given by the R-function theory as presented in what follows.

2.1.2 R-Functions

In order to explain the main idea in the development of the R-function method, it is useful to consider two sets V_1 and V_2 and the set operations intersection $V_1 \cap V_2$ and union $V_1 \cup V_2$. Suppose the sets V_1 and V_2 represent spatial domains bounded by analytic surfaces ∂V_1 and ∂V_2, respectively. Consequently, they can be represented by corresponding domain functions $\omega_1(r)$ and $\omega_2(r)$. The basic idea of the R-function approach is to specify such operators $\wedge_*$ and $\vee_*$ (analogous to set operators $\cap$ and $\cup$) that acting on the real functions $\omega_1(r)$ and $\omega_2(r)$ will produce domain functions of the resulting sets $V_1 \cap V_1$ and $V_1 \cup V_1$, i.e.,

$$\omega_1(\mathbf{r}) \wedge_* \omega_2(\mathbf{r}) = \omega_{inter}(\mathbf{r}) \begin{cases} > 0\,, & \mathbf{r} \in (V_1 \cap V_2) \\ = 0\,, & \mathbf{r} \in \partial(V_1 \cap V_2) \\ < 0\,, & \mathbf{r} \notin (V_1 \cap V_2) \cup \partial(V_1 \cap V_2) \end{cases} \quad (6.\text{a})$$

$$\omega_1(\mathbf{r}) \vee_* \omega_2(\mathbf{r}) = \omega_{union}(\mathbf{r}) \begin{cases} > 0\,, & \mathbf{r} \in (V_1 \cup V_2) \\ = 0\,, & \mathbf{r} \in \partial(V_1 \cup V_2) \\ < 0\,, & \mathbf{r} \notin (V_1 \cup V_2) \cup \partial(V_1 \cup V_2) \end{cases} \quad (6.\text{b})$$

By analogy with the corresponding logical operators of conjunction ($\wedge$) and disjunction ($\vee$), the operators $\wedge_*$ and $\vee_*$ are referred to as R-conjunction and R-disjunction, respectively. By the development of the R-function theory, several complete systems of R-functions have been specified. The explicit forms of R-conjunction and R-disjunction in three such systems are given in what follows.

R_α-system:

$$\omega_1 \wedge_\alpha \omega_2 \equiv \frac{1}{1+\alpha}\left(\omega_1 + \omega_2 - \sqrt{\omega_1^2 + \omega_2^2 - 2\alpha\omega_1\omega_2}\right) \qquad (7.\text{a})$$

$$\omega_1 \vee_\alpha \omega_2 \equiv \frac{1}{1+\alpha}\left(\omega_1 + \omega_2 + \sqrt{\omega_1^2 + \omega_2^2 - 2\alpha\omega_1\omega_2}\right) \qquad (7.\text{b})$$

where α is an arbitrary function that satisfies $-1 < \alpha \leq 1$.

R_1-system as a special case of R_α using $\alpha = 1$:

$$\omega_1 \wedge_1 \omega_2 \equiv \frac{1}{2}(\omega_1 + \omega_2 - |\omega_1 - \omega_2|) \equiv \min(\omega_1, \omega_2) \qquad (8.\text{a})$$

$$\omega_1 \vee_1 \omega_2 \equiv \frac{1}{2}(\omega_1 + \omega_2 + |\omega_1 - \omega_2|) \equiv \max(\omega_1, \omega_2) \qquad (8.\text{b})$$

R_0-system as a special case of R_α using $\alpha = 0$:

$$\omega_1 \wedge_0 \omega_2 \equiv \omega_1 + \omega_2 - \sqrt{\omega_1^2 + \omega_2^2} \qquad (9.\text{a})$$

$$\omega_1 \vee_0 \omega_2 \equiv \omega_1 + \omega_2 + \sqrt{\omega_1^2 + \omega_2^2} \qquad (9.\text{b})$$

The complement $\overline{V}_i$ of a set V_i is another set operation that is important for solid modeling purposes. The analogous R-operation is termed as R-negation and is equal to the sign inversion in all R-systems.

Depending on the R-system, the functions may have different differential and logical properties. It is appropriate to select the R-system according to the properties of the problem being solved. For solid modeling purposes, the R_1-system is the most attractive one due to the very simple mathematical form that results in very fast computation. However, it is inadequate for approximate solution of boundary value problems because there is a discontinuity of the first derivative when $\omega_1 = \omega_2$ or $\omega_1 = -\omega_2$. In such cases, it is necessary that the R-functions be differentiable, so that the R_0-system, which has a simpler mathematical form than the generic R_α-system, is more convenient. Another important feature is that Equations (9), as well as Equations (8) and (10), preserve the normalisation, i.e., if the functions ω_1 and ω_2 are normalized, then the resulting functions $\omega_1 \wedge_* \omega_2$ and $\omega_1 \vee_* \omega_2$ are normalized as well. A drawback is that the R_0-system does not obey the law of associativity, i.e.,

$$\omega_1 \wedge_0 (\omega_2 \wedge_0 \omega_3) \neq (\omega_1 \wedge_0 \omega_2) \wedge_0 \omega_3 \qquad (10.\text{a})$$

$$\omega_1 \vee_0 (\omega_2 \vee_0 \omega_3) \neq (\omega_1 \vee_0 \omega_2) \vee_0 \omega_3 \qquad (10.\text{b})$$

Suppose, for instance, that each function ω_i (i=1,2,3) represents a planar half-space so that the functions $\omega_1 \wedge_0 (\omega_2 \wedge_0 \omega_3)$ and $(\omega_1 \wedge_0 \omega_2) \wedge_0 \omega_3$ describe a triangle in two-dimensional geometry. Assuming that it is an equilateral triangle, one would expect that the domain function is symmetric with respect to triangle sides. However, if the associativity law is not satisfied, as is the case with the inequalities (10), the resulting domain functions would not be symmetric. Therefore, particular attention should be paid to symmetrise the domain function, if necessary. This can be done by averaging,

$$\omega = \frac{1}{3}[\omega_1 \wedge_0 (\omega_2 \wedge_0 \omega_3) + \omega_2 \wedge_0 (\omega_1 \wedge_0 \omega_3) + \omega_3 \wedge_0 (\omega_1 \wedge_0 \omega_2)] \qquad (11)$$

or by using R-functions of three or more arguments. For instance, three-argument R_0-conjunction can be represented as follows:

$$\omega_1 \wedge_0 \omega_2 \wedge_0 \omega_3 \equiv \omega_1 + \omega_2 + \omega_3 - \sqrt{\omega_1^2 + \omega_2^2} - \sqrt{\omega_1^2 + \omega_3^2} - \sqrt{\omega_2^2 + \omega_3^2}$$
$$+ \sqrt{\omega_1^2 + \omega_2^2 + \omega_3^2} \qquad (12)$$

Henceforth, the R_0-system will be used throughout this paper. For the sake of simplicity, the related operators $\wedge_0$ and $\vee_0$ will be denoted as $\wedge$ and $\vee$ without any confusion with the corresponding logical operators.

2.1.3 Transformation of Translational Symmetry

In many applications, including the ZED-2 modeling presented here, one needs a mathematical description of periodically repeating domains. In such cases, it is convenient to transform spatial coordinates into variables that obey the required periodicity. To achieve this, the following transformation can be applied:

$$t(x, h, a) = \frac{h}{\pi} arcsin \frac{sin(\pi x/h)}{1 - \tau(x) \cdot (1 - 1/c)} \qquad (13)$$

where x is a spatial coordinate, h is the repetition period, while the parameter c and the interval of linearity a are explained in what follows. The function $\tau(x)$ allows a smooth and n-times differentiable transition from one repetition period to another.

$$\tau(x) = \left\{ \frac{q - cos(px - \pi) + |q - cos(px - \pi)|}{2(1 - q)} \right\}^{n+1} \qquad (14)$$

The parameters c, p and q are specified as follows, where the quantity a denotes the interval of linearity:

$$c = sin\left[\frac{\pi}{4}\left(1 - \frac{a}{h}\right)\right], \quad p = 2\frac{\pi}{h}, \quad q = cos\left[\pi\left(1 - \frac{a}{h}\right)\right] \qquad (15)$$

The function $t(x, h, a)$ is continuous and takes linear values $t = (-1)^k (x - kh)$ on the intervals $(kh- a/2, kh+ a/2)$, $k = 0, \pm 1, \pm 2,...$ According to Equation (14), it is n-times differentiable and the first derivative is constant and equal to $(-1)^k$ within the intervals of linearity.

2.2 Modeling of Characteristic Geometric Regions

2.2.1 Fuel Channels

A fuel channel on a whole occupies a cylindrical spatial domain encompassed by the outer radius R of the calandria tube. The related domain function can be described by Equation (5), in which the coordinates (x_0, y_0) of the cylinder axis vary according to the channel position in the lattice. In this way, one can get a domain function for each particular channel. However, this approach may be cumbersome and time-consuming in the case of a large number of channels.

A more elegant way of modeling with less computing effort is to model the entire lattice on a whole by using the transformation of translational symmetry specified by Equation (13). As shown in Figure 1, the fuel channels are arranged in a square lattice that is shifted from the reactor centre by half a lattice pitch. Accordingly, the following transformation of spatial coordinates should be applied:

$$x \to x' = t(x - h/2, h, a) \qquad (16.a)$$

$$y \to y' = t(y - h/2, h, a) \qquad (16.b)$$

where the repetition period h is equal to the lattice pitch, while the interval of linearity a is greater than the outer diameter of the calandria tube ($2R < a < h$). Substituting Equations (16) into Equation (5), one gets a domain function ω_{arr} (x, y) that describes an infinite array of cylindrical domains arranged in a square lattice. To select only a desired number of channels it is necessary to specify a spatial domain that encompasses them. For the particular case here, such a domain can be constructed as a union of two rectangles and a square (the gray shaded area in Figure 1). To construct the related domain function, consider first the following two functions:

$$\omega_{x,1}(\boldsymbol{r}) = d + x \qquad (17.a)$$

$$\omega_{x,2}(\boldsymbol{r}) = d - x \qquad (17.b)$$

Each of them represents a half-space bounded by a planar surface that is parallel to the y-z plane and encompasses the coordinate origin at a normal distance d. The intersection of these two half-spaces represents an infinite slab, the spatial domain of which can be represented as an R-conjunction of the functions specified by Equations (17), i.e., $\omega_{x,slab} = \omega_{x,1} \wedge \omega_{x,2}$. Another function $\omega_{y,slab}$ can be constructed in a similar manner to specify an infinite slab in the y-direction. Then, the function $\omega_{square} = \omega_{x,slab} \wedge \omega_{y,slab}$ represents a square of side-length size d. The domain functions $\omega_{rect,1}$ and $\omega_{rect,2}$ of the rectangles that form the shaded area in Figure 1 can be constructed in the same manner by a proper choice of the parameter d. As a final result, the domain function of the shaded area can be cast in the following form:

$$\omega_{mask} = \omega_{square} \vee \left(\omega_{rect,1} \vee \omega_{rect,2}\right) \qquad (18)$$

Hence, the function $\omega_{chan} = \omega_{mask} \wedge \omega_{arr}$ describes only the desired number of channels as shown in Figure 3. For the sake of visual clarity, the figure presents only the positive part $\omega^+_{chan} = (\omega_{chan} + |\omega_{chan}|)/2$ of the considered domain

function. The negative part describes the rest of the space including the heavy-water region.

Varying the cylinder radius R in Equation (5), the same procedure can be applied to produce functions that describe finite arrays of the same number of cylindrical domains but with different cylinder radii. Denote by ω_{cinn}, for instance, the domain function of the array in which the cylinder radius is equal to the inner radius of the calandria tube. Then, taking into account that ω_{chan} was specified for the outer radius of the calandria tube, the function $\omega_{ctube} = \omega_{chan} \wedge (-\omega_{cinn})$ will describe all calandria tubes in the ZED-2 model considered here. The same procedure can be used to construct a domain function for all pressure tubes as well as all air gaps between calandria and pressure tubes.

The extension to three-dimensional geometry is straightforward. Suppose, for instance, that the fuel channels have a finite length L in axial direction. A domain function $\omega_{z,slab}$, which represents an infinite z-dependent slab of thickness L, can be constructed using Equations (17) with a proper change of spatial coordinates, x→z, and the parameter $d = L/2$. Then the function $\omega_{chan} \wedge \omega_{z,slab}$ represents 52 channels of axial length L arranged in a square lattice as shown in Figure 1.

2.2.2 Heavy-Water Region
In the reactor model considered here, the heavy water plays a twofold role, as a moderator within the lattice of fuel channels and as a reflector around them. It occupies the entire space inside the reactor tank but outside calandria tubes. Denoted by ω_{tank} the function that describes a cylindrical

FIGURE 3: Positive part of the domain function representing fuel channels.

domain the radius of which is equal to the inner radius of reactor tank. Having already specified the function ω_{chan} for all fuel channels, the domain function of the heavy water region can be easily constructed as $\omega_{D_2O} = \omega_{tank} \wedge (-\omega_{chan})$.

However, the above function may suffer from non-linearity effects due to non-linearity of the transformation (13) over the intervals *(kh + a/2, (k+1) h - a/2)*. In order to reduce these effects to an acceptable level, one may specify a translational transformation with twice as large repetition period, i.e., *t(x, 2h, a)*. Applied to Equation (5), it will produce a function that describes every second cylinder in x and y directions. Four such transformations are necessary to cover the entire array as follows:

$$x \rightarrow x_1 = t(x + h/2, 2h, a), \quad y \rightarrow y_1 = t(y + h/2, 2h, a) \quad \Rightarrow \quad \omega_{arr}^{1,1}$$

(19.a)

$$x \rightarrow x_1 = t(x + h/2, 2h, a), \quad y \rightarrow y_2 = t(y - h/2, 2h, a) \quad \Rightarrow \quad \omega_{arr}^{1,2}$$

(19.b)

$$x \rightarrow x_2 = t(x - h/2, 2h, a), \quad y \rightarrow y_1 = t(y + h/2, 2h, a) \quad \Rightarrow \quad \omega_{arr}^{2,1}$$

(19.c)

$$x \rightarrow x_2 = t(x - h/2, 2h, a), \quad y \rightarrow y_2 = t(y - h/2, 2h, a) \quad \Rightarrow \quad \omega_{arr}^{2,2}$$

(19.d)

For each transformation, a finite number of channels can be selected using the R-conjunction with the domain function of the encompassing region, i.e., $\omega_{chan}^{i,j} = \omega_{arr}^{i,j} \wedge \omega_{mask}$. For all channels of interest, the domain function with reduced non-linearity effects can be cast as follows:

$$\omega_{chan}^* = \left(\omega_{chan}^{1,1} \wedge \omega_{chan}^{2,2}\right) \wedge \left(\omega_{chan}^{1,2} \wedge \omega_{chan}^{2,1}\right) \qquad (20)$$

Accordingly, the heavy water region can be represented by $\omega_{D_2O} = \omega_{tank} \wedge (-\omega_{chan}^*)$, the positive part of which is shown in Figure 4.

FIGURE 4: Positive part of the domain function representing the heavy water region.

2.2.3 Fuel and Coolant Regions

The CANFLEX fuel bundle consists of a central fuel pin, inner ring of 7 pins, middle ring of 14 pins, and outer ring of 21 pins. The spatial domain of each particular pin can be modeled by Equation (5) with properly chosen values of the radius R and cylinder axis coordinates (x_0, y_0).

However, as mentioned in the previous section, it may be a cumbersome and time-consuming process to deal with a large number of repeating spatial domains. Similar to the square array of cylinders, the transformation of translational symmetry can be applied to specify a ring of rotationally repeating domains. Consider the inner ring of seven fuel pins of radius R_{pin1}. The first pin in the ring is specified by Equation (5), in which $R=R_{pin1}$, $x_0=R_{ring1}$ and $y_0=0$, where R_{ring1} denotes the radius of the inner ring of pins. Replace the transformed Cartesian coordinates (x', y') as given in Equation (16) with polar coordinates (r, θ):

$$x' = r \cos \theta, \ \ y' = r \sin \theta \tag{21}$$

$$r = \sqrt{x'^2 + y'^2}, \ \ \theta = \arctan \frac{y'}{x'} \tag{22}$$

The inner ring of pins represents a seven-fold rotational repetition of the first pin with a repetition period $h=2\pi/7$. In order to apply the transformation (13) to the coordinate θ, select the parameter a so that the interval of linearity encompasses the entire pin, i.e., $a=2\arctan(R_{pin1}/R_{ring1})$. Replace the coordinate θ with the translational symmetry transformation (13), i.e., $\theta \rightarrow \theta'=t(\theta,h,a)$, and transform Cartesian coordinates accordingly:

$$x'' = r' \cos \theta', \ \ y'' = r' \sin \theta' \tag{23}$$

Equation (5) with the above coordinate transformation produces a domain function ω_{ring1} that represents all seven pins in the inner ring of pins. The same procedure can be applied to construct domain functions ω_{ring2} and ω_{ring3} of the middle and outer rings of pins, respectively. Of course, in this case, the repletion periods h as well as the linearity interval a need to be specified according to the number of pins in the ring considered. The domain function ω_{cpin} of the central pin can be constructed directly from Equation (5) using $x_0=0$ and $y_0=0$ without any coordinate transformation. Then, all fuel regions in the cluster can be described by the following function:

$$\omega_{fuel} = \left(\omega_{cpin} \lor \omega_{ring2}\right) \lor \left(\omega_{ring1} \lor \omega_{ring3}\right) \tag{24}$$

The same procedure can be repeated using the outer cladding radius in Equation (5) to get a function ω_{clus} that describes all fuel pins on a whole. Assuming that there is no gap between the fuel and the cladding, the function that describes only the cladding can be constructed as follows:

$$\omega_{clad} = \omega_{clus} \land \left(-\omega_{fuel}\right) \tag{25}$$

Denoting by ω_{ptin} the function that represents the interior of the pressure tube, the domain function of the coolant region takes the following form:

$$\omega_{cool} = \omega_{ptin} \land \left(-\omega_{clus}\right) \tag{26}$$

As a visual illustration, Figures 5 and 6 show the positive parts of functions ω_{fuel} and ω_{cool}, respectively. They were constructed by transformed spatial coordinates according to Equation (16), so that the corresponding spatial domains repeat periodically in an infinite square lattice. To select only the spatial domains within the actual fuel channels, an R-conjunction with the function ω_{mask} should be applied. As mentioned earlier, an extension to three-dimensional models of the fuel, cladding and coolant is straightforward.

It is worth repeating here that each of the Figures 3 to 6 represents the shape of a single real analytic function that is continuous, differentiable and normalized to the first order, i.e., the first derivative along the inward normal at the boundary is equal to unity.
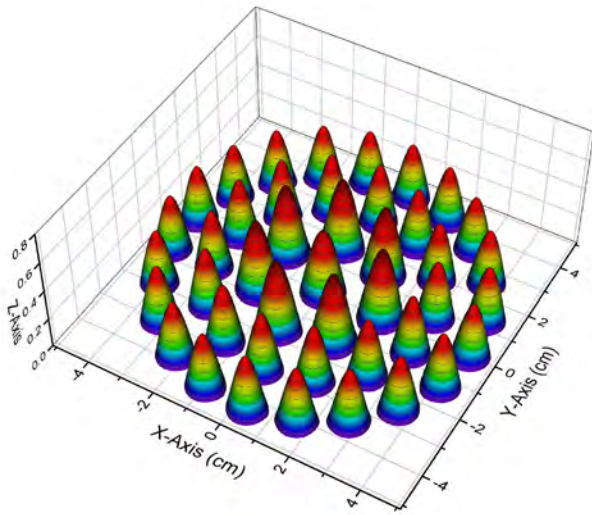
FIGURE 5: Positive part of the domain function representing the fuel pins in the CANFLEX bundle.
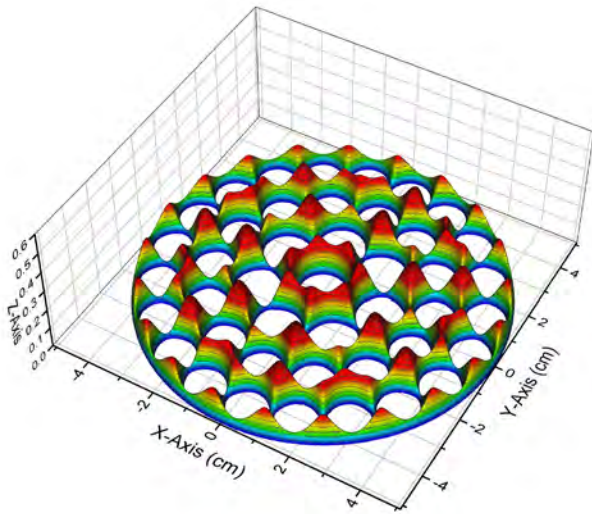
FIGURE 6: Positive part of domain function representing the coolant region.

3. Approximation Abilities of Domain Functions

The scalar neutron flux as the solution of the neutron transport equation belongs to the class of continuous functions that are differentiable everywhere except at material interfaces. A common approach of the current deterministic transport methods is to approximate the solution with a set of trial functions from a less restrictive class of functions than the class to which the exact solution belongs. This is mainly due to the inability of conventional numerical mathematics to handle complex spatial domains on a whole. Instead, such a complex domain needs to be subdivided into a number of subdomains of simple geometric shapes (triangles, rectangles, etc.), to each of which a classical approximation (finite difference, finite element, etc.) could be applied. By lessening the requirements on the trial functions, however, the number of degrees of freedom (unknown coefficients) of the approximate solution may increase significantly.

To construct an approximation basis that satisfies both the continuity and differentiability, each material region needs to be considered as a distinct spatial domain V_i represented mathematically by a continuous and differentiable function ω_i®. Since the R-function method is able to handle arbitrary semi-analytic domains, a mesh-free approximation of finite element type can be specified so that a finite element is associated with each material region without any need for subdivision into simpler shapes. By a proper choice of the R-system, the neutron flux approximation inside the region would be approximated by a continuous and differentiable function. At interface boundaries, the flux continuity can be achieved by a proper coupling of boundary specified functions and the related unknown coefficients.

Another possible approach is to approximate the solution as a linear combination of the positive parts of the domain functions themselves. Consider for instance a two-region reactor that consists of a homogenous core surrounded by a reflector. Denote by ω_{core} (r), ω_{refl} (r), and ω_{reac} (r) the domain functions that represent the core, reflector, and the reactor on a whole, respectively. The approximate solution in region i can be represented as a linear combination of the positive parts of the domain functions:

$$\varphi_i(\boldsymbol{r}) = a_0\omega_{reac}^+(\boldsymbol{r}) + a_1\omega_{core}^+(\boldsymbol{r}) + a_2\omega_{refl}^+(\boldsymbol{r}) \tag{27}$$

where the region index i denotes either the core or reflector, and a_0, a_1, and a_2 are unknown coefficients to be determined. The function ω^+_{reac} (r) specifies the global shape of the reactor flux, while the functions ω^+_{core} (r) and ω^+_{refl}(r) introduce local perturbations that are due both to material properties and the geometric shape of the related material region. Since both of them vanish at their boundary, the

flux at the interface boundary is continuous and equal to a_0 ω^+_{reac} (r). To increase the order of approximation, if necessary, higher order terms $(\omega^+_j)^k$ can be used, as well as mutual products of some of the domain functions, i.e., $\omega^+_{reac} \cdot \omega^+_{core}$ and $\omega^+_{reac} \cdot \omega^+_{refl}$.

The above approach can be extended to reactor models that consist of an arbitrary number of material regions. Starting from material regions as the lowest-level domains, one can specify a number of higher-level domains as unions of two and more material regions, up to the highest level, the spatial domain of the entire reactor. Each of these domains can be represented by a domain function ω_j(r).

Owing to the properties specified by Equation (1), the function $\omega^+=(\omega+|\omega|)/2$ represents the positive part of ω(r) inside the related domain V and vanishes everywhere else. Thus, the neutron flux φ_i (r) in a material region V_i can be approximated as a superposition of ω_i^+(r) and higher level functions ω_j^+(r) of all domains in which this region is nested, i.e.,

$$\varphi_i(\boldsymbol{r}) = a_i\omega_i^+(\boldsymbol{r}) + \sum_{j:\, V_i \subset V_j} b_j\, \omega_j^+(\boldsymbol{r}), \quad \boldsymbol{r} \in V_i \tag{28}$$

where a_i and b_j are unknown coefficients to be determined.

Before embarking on a code-development adventure, which may require significant time and efforts, it is useful to investigate the ability of the domain functions to approximate the actual solution of the neutron-transport equation. To this end, a feasibility study was carried out using the spatial flux distribution in ZED-2 as a model problem and a reference solution obtained by the Monte Carlo code MCNP5 [13] Version 1.40. For the sake of simplicity, the consideration is restricted to two-dimensional geometry as presented in Figures 1 and 2. To get a virtually continuous flux distribution, flux tallies were calculated on a square mesh of 500 x 500 grids of about 0.33 mm step size. The mesh covers a square region the side length size of which is equal to the outer radius of the heavy water region of the ZED-2 model. Only two energy groups were considered because of restrictions in the MCNP input. The fast group covers the neutron energy range from 4 eV to 20 MeV, and the thermal group the range below 4 eV. Figures 7 and 8 show three-dimensional plots of the fast- and thermal-neutron flux, respectively. The granular structure of flux surfaces is due to the statistical uncertainty in flux tallies that were calculated with 100 millions active histories. The relative error of the tallies in the central core region is about 0.65% and 0.35% for the fast and thermal groups, respectively. Increasing the distance from the centre, the neutron flux decreases while the tally error increases, so that at a distance of 100 cm, the tally error

reaches the magnitudes of 1.5% and 0.5% for the fast and thermal groups, respectively. At the reactor periphery, the neutron flux takes very small magnitude, even zero values in many meshes in the reflector and end moderator region. Therefore, in these regions, the code reports tally errors of 100%.

For each energy group considered, an approximate flux distribution is constructed according to Equation (27) using a power series of domain functions and their products. Unknown coefficients of the series were determined by the least square method applied to the discrepancy between the reference flux distribution and the approximate one. Afterwards, the root mean square (RMS) value of the absolute error is calculated for each energy group over the space of the considered square region. As explained above, due to large tally errors at the reactor periphery, it is inadequate to use the relative error as a measure of agreement between the reference solution and approximate flux distribution. Instead, the RMS value of the absolute error is divided by the RMS value of the flux distribution to give an average relative error over the region of interest. Increasing the number of terms in the series, the relative error decreases so that, for a total number of about 50 unknowns, a reasonable error level of 2.0% is achieved. As a visual illustration of the agreement between the reference solution and the domain function series, Figures 9 and 10 compare, respectively, the fast- and thermal-neutron flux distribution along the diagonal line of the ZED-2 model. The results of the reference solution and the approximate series almost coincide with each other.

The results show that a set of domain functions, applied as an approximation basis, is able to produce a good approximation of the spatial flux distribution in the ZED-2 reactor model with a modest number of unknowns. It is to be expected that similar results can be obtained if the least-square method, which is used here to minimize the discrepancy between the reference and approximate solution, is replaced with another minimization procedure (the method of moments for instance) intended for approximate solution of the neutron transport equation. If successful, such an approach would result in a significant reduction of the number of unknowns compared to the standard transport methods. To get an impression about potential benefits, it is worth mentioning that a standard method, such as the collision probability method, requires more than ten thousand unknowns for a sufficiently accurate solution of the ZED-2 problem considered here. Thus, by using the domain function approach presented here, a significant reduction may be expected in both the number of unknowns and computing time.
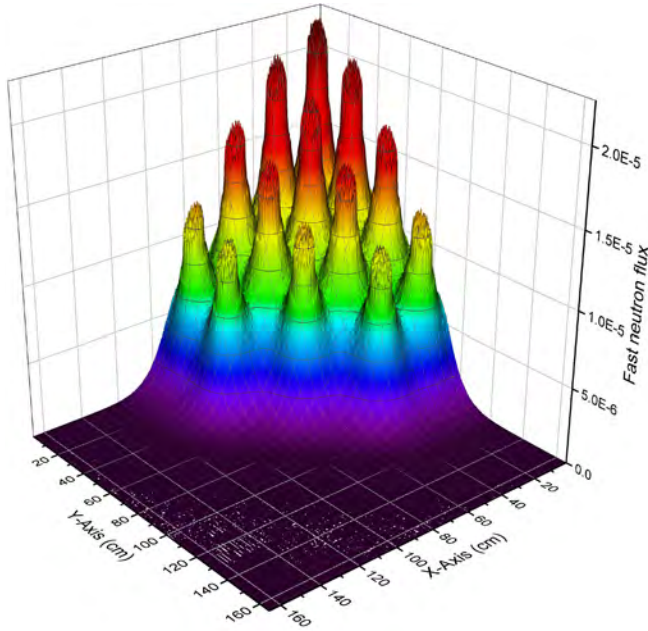
FIGURE 7: Spatial distribution of fast neutron flux in ZED-2 reactor.
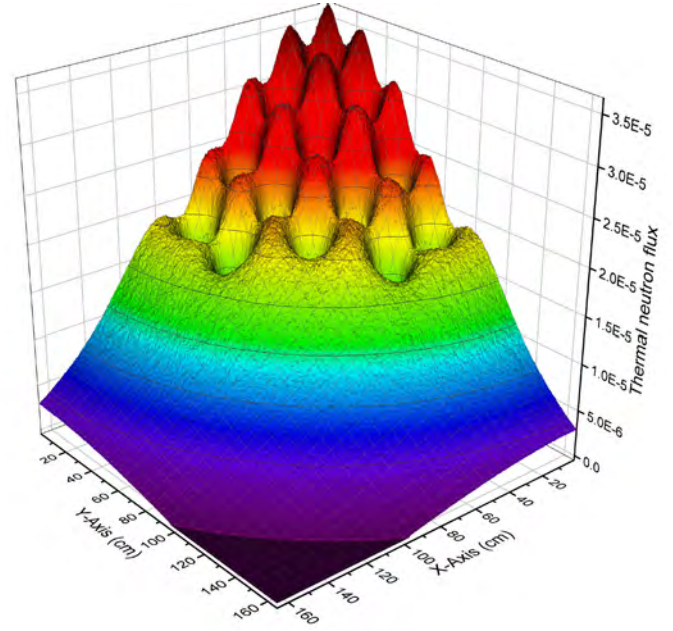
FIGURE 8: Spatial distribution of thermal neutron flux in ZED-2 reactor.
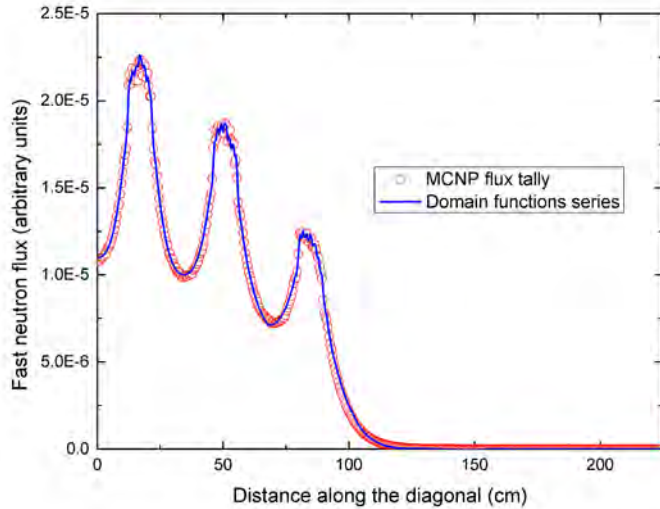
FIGURE 9: Spatial distribution of fast neutron flux along diagonal line.
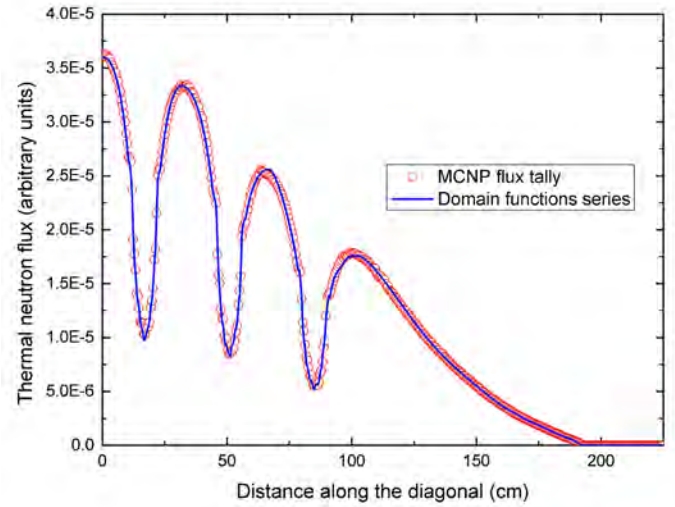
FIGURE 10: Spatial distribution of thermal neutron flux along diagonal line.

4. Conclusion

The potentials of the R-function method are illustrated by modeling of reactor specific material regions using the ZED-2 reactor as a characteristic example. Spatial domains of complex geometric shape, such as the domain of all fuel elements in the reactor, are mathematically described by a single continuous function. Depending on the R-system applied, the resulting functions can be used in a variety of applications. They offer an easy solution of the point inclusion (set membership classification) problem, which is a central issue in solid modeling techniques. On the other hand, owing to continuity and differentiability, they can be directly used to specify a basis for approximate solution of the related boundary value problems. The spatial neutron flux distribution in ZED-2 is used as a model problem to study the approximation abilities of domain functions. The results show that a power series of domain functions is able to give a good approximation of the reference solution obtained by MCNP.

References

[1] V.L. Rvachev, 1963, "On Analytical Description Of Some Geometric Objects", Reports (Doklady) Of Academy Of Sciences, USSR 153, pp. 765–768.

[2] V.L. Rvachev and V.A. Rvachev, 1979), Nonclassical Methods of Approximation Theory in Boundary-Values Problems, Naukova Dumka, Kiev. In Russian.

[3] V.L. Rvachev, 1982, R-Function Theory and Some of Its Applications, Naukova Dumka, Kiev. In Russian.

[4] D.V. Altiparmakov, 1983, "Nested Element Method in Multidimensional Neutron Diffusion Calculations", Proc. CNS/ANS Int. Conference on Numerical Methods in Nuclear Engineering, Montreal, Canada, September 6-9, 1983, Canadian Nuclear Society, Vol. 1, pp. 327-347.

[5] D.V. Altiparmakov, 1986, "On Trial Functions in the Nested Element Method", Nucl. Sci. Eng., 92(2): pp. 330-337.

[6] P. Belicev and D.V. Altiparmakov, 2001, "An Efficient Electric Field Approximation for Spiral Inflector Calculations", Nuclear Instruments and Methods in Physics Research A, 456(3):pp. 177-189.

[7] Stoyan, G. Yu, V.S. Procenko and G.P. Man'ko, I.V. Goncharyuk, L.V. Kurpa, V.A. Rvachev, N.S. Sinekop, I.B. Sirodza, A.N. Shevchenko and T. L. Sheyko, 1986, R-Function Theory and Actual Problems of Applied Mathematics, Naukova Dumka, Kiev, In Russian.

[8] V.L. Rvachev and L.V. Kurpa, 1987, R-Functions in Problems of Theory of Plates, Naukova Dumka, Kiev. In Russian.

[9] D.V. Altiparmakov and P. Beliccev, 1990, "An Efficiency Study of the R-Function Method Applied as Solid Modeler for Monte Carlo Calculations", Progress in Nuclear Energy, 24(1-3): pp. 77-88.

[10] V. Shapiro, 2007, "Semi-Analytic Geometry with R-Functions", Acta Numerica, 16:239-303.

[11] V. Shapiro, 1991, "Theory of R-Functions and Applications: A Primer", Cornell University, Technical Report: pp. 91-1219.

[12] M.A. Lone, 2001, "Fuel Temperature Reactivity Coefficient of a CANDU Lattice – Numerical Benchmark on WIMS-AECL (2-5d) Against MCNP", Proc. 22nd Annual Conference of the Canadian Nuclear Society, June 10-13, 2001, Toronto, Canada.

[13] X-5 Monte Carlo Team, 2008, "MCNP – A General Monte Carlo N-Particle Transport Code, Version 5. Volume 1: Overview and Theory," Los Alamos National Laboratory, Report LA-UR-03-1987.

Implementation of a Gibbs Energy Minimizer in a Fission-Product Release Computer Program

D.H. Barber[*,1,2]

[1] Atomic Energy of Canada Limited, Chalk River, Laboratories, Chalk River, Ontario, Canada, K0J 1J0
[2] Royal Military College of Canada, Kingston, Ontario, Canada, K7K 7B4

*Corresponding author: (613) 584-3311, barberdh@aecl.ca

SOURCE 2.0 is the Canadian computer program for calculating fractional release of fission products from the UO$_2$ fuel matrix. In nuclear accidents, fission-product release from fuel is one of the physical steps required before radiation dose from fission products can affect the public. Fission-product release calculations are a step in the analysis path to calculating dose consequences to the public from postulated nuclear accidents. SOURCE 2.0 contains a 1997 model of fission-product vaporization by B.J. Corse et al. based on lookup tables generated with the FACT computer program. That model was tractable on computers of that day. However, the understanding of fuel thermochemistry has advanced since that time. Additionally, computational resources have significantly improved since the time of the development of the Corse model and now allow incorporation of the more-rigorous thermodynamic treatment. Combining the newer Royal Military College of Canada (RMC) thermodynamic model of irradiated uranium dioxide fuel, a new model for fission-product vaporization from the fuel surface, a commercial user-callable thermodynamics subroutine library (ChemApp), an updated nuclide list, and updated nuclear physics data, a prototype computer program based on SOURCE IST 2.0P11 has been created that performs thermodynamic calculations internally. The resulting prototype code (with updated and revised data) provides estimates of ^{140}La releases that are in better agreement with experiments than the original code version and data. The improvement can be quantified by a reduction in the mean difference between experimental and calculated release fractions from 0.70 to 0.07. ^{140}La is taken to be representative of "low-volatile" fission products. To ensure that the existing acceptable performance for noble gases and volatile fission products is not adversely affected by the changes, comparisons were also made for a representative noble gas, ^{85}Kr, and a representative volatile fission-product, ^{134}Cs. These nuclides have the largest dataset in the SOURCE 2.0 validation test suite. This improvement provides increased confidence in the safety margin for equipment qualification in Loss-of-Coolant Accidents with Loss of Emergency Core Cooling.

®CANDU is a registered trademark of Atomic Energy of Canada Limited.

Nomenclature

AECL	Atomic Energy of Canada Limited
CANDU®	The Canadian deuterium uranium reactor.
ChemApp	A commercial thermodynamics subroutine library containing the chemical solver from FactSage
FACT	Facility for the Analysis of Chemical Thermodynamics, a computer program for chemical thermodynamics
FactSage	A successor computer program to FACT
IST	Industry Standard Toolset
LOCA	Loss-of-coolant accident
LOECC	Loss-of-emergency core cooling
MFPR	Mechanistic Fission-Product Release, a computer program
ORIGEN	Oak Ridge isotope generation and depletion program
PHW(R)	Pressurized Heavy Water (Reactor)
RMC	Royal Military College of Canada
SC11	A prototype computer program, based SOURCE IST 2.0P11, that calculates the radioactive source term with an internal chemical solver
SOURCE 2.0	A generic designation, includes multiple versions
SOURCE IST 2.0	The Canadian IST computer program for calculating fission-product release fractions from the matrix of nuclear fuel.
SOURCE IST 2.0P11 2.0	A specific production version of SOURCE 2.0 developed as part of the Industry Standard Toolset and released by Ontario Power Generation to the Canadian nuclear industry in 2008 January
STAR	Steady-state and Transient Activity Release, a computer programṁing
TQCE	A ChemApp subroutine for calculating equilibrium

Symbol Meaning

$(H^t)_{in}$	The quantity of hydrogen atoms (moles) entering the system in a time interval
$\dot{m}_{H_2}$	The molar flow rate of molecular hydrogen (moles/s)
$\dot{m}_{H_2^0}$	The molar flow rate of steam (moles/s)
$\dot{m}_{Inert}$	The molar flow rate of inert gas molecules (moles/s)
$\dot{m}_{O_2}$	The molar flow rate of molecular oxygen (moles/s)
$(O^t)_{in}$	The quantity of oxygen atoms (moles) entering the system in a time interval
Δt	A time interval (seconds)

1. Introduction

Within Industry Standard Toolset (IST), which is the Canadian nuclear industry's suite of computer program for safety analysis, the computer program SOURCE 2.0 is the computer program for calculating fractional release of fission products from the fuel [1-3]. The fuel matrix and fuel sheath provide the first two barriers to fission-product release to the environment and potential radiation dose to the public. Fission-product release from the fuel matrix is a precursor to potential radiation dose to the public. Fission-product release calculations are a step in the analysis path for calculating dose consequences to the public from postulated nuclear accidents. The motivation for the work is to provide improved accuracy in nuclear safety analyses that calculate radiation dose to plant equipment, workers and the public.

SOURCE 2.0 contains models for the following physical phenomena: actinide fission, transmutation and decay [4-6], fission-product diffusion within fuel grains [7-10] coupled to fission-product yield, decay and transmutation; equi-axed and columnar grain growth, grain-boundary sweeping, grain-boundary bubble growth and interlinkage [11]; fission-product vaporization from the fuel surface [12-14]; and grain-boundary separation. The phenomena not modelled directly by the code include: UO_{2+x} formation; U_4O_9-U_3O_8 formation; UO_{2-x} formation; UO_2/Zircaloy interaction; UO_2 dissolution by molten Zircaloy; matrix stripping; fuel melting; and fission-product leaching; these phenomena are modelled based on user-specified input values. This treatment is unaltered in SC11.

SOURCE 2.0 [1-3] contained a 1997 model of fission-product vaporization by B.J. Corse, M.H. Kaye, B.J. Lewis and W.T. Thompson [12-14]. That model was based on lookup tables generated with the FACT (Facility for the Analysis of Chemical Thermodynamics) computer program [15-17] and was tractable on computers of that day. The Royal Military College of Canada (RMC) model of irradiated uranium dioxide fuel, its fission and activation products has been expanded [18], as most recently documented by Corcoran [19] and Piro [20]. The advantage of the new model is that many of the chemical elements produced as activation or fission products during irradiation of UO_2 fuel are treated. Additionally, the inclusion of solid solution phases that can be formed in the irradiated fuel allows a more rigorous description of the phases that can exist in the irradiated fuel. FACT [15-17] has evolved into FactSage [21] and the thermodynamic solver is available as ChemApp [22], which consists of a library of subroutines that can be called from users' computer programs.

The new prototype computer program [23] is designated SC11, as a shorthand for source term determination

(based on SOURCE IST 2.0P11) with internal chemical solver. SC11 differs from SOURCE IST 2.0P11 primarily by the replacement of the model for fission-product vaporization from the fuel surface in SOURCE IST 2.0P11 with a new model. The new model incorporates the newer RMC thermodynamic model of irradiated uranium dioxide fuel [18-20], the commercial ChemApp user-callable thermodynamics subroutine library [22] and supporting subroutines and modules. Incidental changes were required to support this work. Minor modifications were made to the SOURCE 2.0 model for radionuclide generation and depletion in order support an expanded list of nuclides to be modelled. Some revisions and additions were made to nuclear data used by the computer program.

In both SOURCE 2.0 and SC11, the sheath failure time is a user-specified value. After sheath failure, a calculation of fission-product vaporization from the fuel surface is performed at each time step. At the end of the time step, the resulting gas phase, including noble-gas fission-product inventory is released.

2. Literature Review

There is overlap between the models in SOURCE 2.0 (and SC11) and those in two other modern computer programs, STAR [24, 25] and MFPR [26].

2.1 STAR, Steady-state and Transient Activity Release Code

The STAR code [24, 25] was developed, at the Royal Military College of Canada, for analysis of on-power fission-product activity in the Heat Transport System of a CANDU-PHW reactor. It has two modes of operation. The first mode allows interpretation of on-line coolant-activity monitoring data to give radioactivity release rates into the coolant, track evolution of defect size, predict future coolant activity, and estimate the linear power of a defected fuel element. In the second mode, STAR can be used to predict future coolant activity during steady-state operation and during operational transients (e.g., startup, shutdown and online refuelling). In order to use the predictive mode, constants need to be derived for a given reactor design from existing coolant activity data.

The STAR model uses a single fuel grain to represent the fuel element. The latest version accounts for fission-product chains of two nuclides coupled by decay or neutronic transformations. The fuel temperature is not calculated internally, but is an input parameter. Internally, STAR uses a five-point order finite-difference scheme on a moving spatial grid to convert partial differential equations into set of ordinary differential equations in time. STAR is not intended to model accident transients.

2.2 MFPR, Mechanistic Fission-Product Release Code

MFPR [26] is a joint development between IBRAE (Moscow, Russia) and IRSN (Cadarache, France). It has a very detailed treatment of fuel grains. It models four types of bubbles: intragranular bubbles within fuel grains, grain boundary bubbles on the surface of fuel grains, grain-edge bubbles where grain edges meet and grain corner bubbles where grain edges meet. Grain-face bubbles grow until the bubbles interconnect. Grain-edge and grain-corner bubbles grow and can form release paths to the fuel-to-sheath gap. Rather than use an "effective" diffusion coefficient for material within fuel grains MFPR models intragranular bubbles diffusion as well as atomic diffusion within the fuel grains. MFPR contains a fission-product chemistry model that partitions fission-products based on chemical stability among the fuel matrix, metallic inclusions, solid ternary oxides (e.g., $BaUO_4$), the gas phase, and a separate CsI(c) phase [26]. MFPR includes the elements niobium, antimony and europium which, while present in relatively small molar quantities, have measurable contribution to activity release. MFPR models the change in fuel stoichiometry due to fuel oxidation and/or reduction.

3. Background

3.1 Gibbs Energy Minimization Software

The theory of Gibbs energy minimization was originally developed by J. Willard Gibbs [27, 28] and can be found in a thermodynamics textbook, e.g., Butler [29]. The commercial thermodynamics software ChemApp [21, 22] has a subroutine TQCE[1] that calculates the equilibrium composition of a system at a given temperature, pressure, and containing specified quantities of initial component elements. The subroutine requires a data file that contains the functions for the molar Gibbs energy of each possible constituent of the equilibrium as described. The possible constituents of the multiple phases in the RMC thermochemical model of irradiated uranium dioxide fuel are the chemical compounds that can be formed from the component chemical elements. A data file was prepared that contains a list of components and constituents along with sufficient thermodynamic data to calculate the molar Gibbs energy of the constituents and the phases in the system. The phases include pure substances, ideal solutions and non-ideal solutions. The data file used to describe the RMC thermochemical model is based on earlier work by a large number of contributors at the Royal Military College of Canada [18-20].

3.2 RMC Thermochemical Model of Irradiated Uranium Dioxide

The RMC thermochemical treatment incorporated into SC11 contains 17 solution phases and 279 pure compound phases

[23]. The component chemical elements of the model are hydrogen, oxygen, rubidium, strontium, yttrium, zirconium, molybdenum, technetium, ruthenium, rhodium, palladium, lurium, iodine, xenon, caesium, barium, lanthanum, cerium, praseodymium, neodymium, uranium, neptunium and plutonium. These chemical elements were selected based on elemental abundances [19]. An ideal gas phase contains gases and vapours. A fluorite lattice phase contains uranium dioxide (with the possibility of non-stoichiometry) and soluble activation products (e.g., neptunium and plutonium) and fission-products (typically as oxides). A liquid uranium oxide phase includes activation and some fission products. Five noble-metal phases (face-centred cubic, body-centred cubic, hexagonal close-packed, a tetragonal molybdenum-technetium phase, and a liquid noble metal phase) contain molybdenum, technetium, ruthenium, rhodium and palladium. Additional mixed-oxide phases are modelled for alkali-metal zirconates, alkali-earth zirconates, alkali-metal molybdates, alkali-earth molybdates, alkali-metal uranates and alkali-earth uranates. These phases contain alkali-metal fission-product elements (caesium and rubidium), alkali-earth fission-product elements (strontium and barium) with a tetravalent cation (zirconium, molybdenum and uranium) with oxygen. These additional oxide phases are not modelled as mixing with each other. A metallic uranium/noble-metal phase models an ideal solution of URu_3, URh_3 and UPd_3. A rhombohedral uranium/rare-earth oxide phase models ULa_6O_{12}, UCe_6O_{12} and UNd_6O_{12} as an ideal solution. The models of the liquid uranium oxide phase, the face-centred cubic noble-metal phase and the hexagonal close-packed noble-metal phase include treatment of a miscibility gap that permits the formation of two immiscible phases.

4. Theory of Fission-Product Vaporization

In the types of accidents analysed by SOURCE 2.0, there has been a loss of liquid coolant from the reactor. The fuel is cooled to a limited extent by steam, air, or hydrogen (or a mixture thereof). The hydrogen is typically produced from the reaction of steam with the Zircaloy fuel sheath. The fuel sheath is assumed to have ruptured (at a user-specified time) and to provide no barrier between the fuel and the gas phase. In the case of fission-product vaporization from the fuel surface, there are three sets of phases in contact: a user-specified fraction of the gas-phase of the coolant plus the gas in the pellet-to-sheath gap; the actinides and oxygen in the condensed fuel phase or phases; and the fission products that have been transported to the fuel surface and exist as liquid or solid inclusions on the grain-boundary.

In both the old (SOURCE IST 2.0P11) model from Corse [12-14] and in SC11 chemical equilibrium is assumed to exist at the fuel surface. The target scenarios for the computer programs are those with higher fuel temperatures than normal operating conditions and it is likely that kinetic limits are not as prevalent as at lower temperatures. Chemical

---

[1] ChemApp subroutine names usually begin with "TQ". CE presumably stands for "Calculate" or "Compute" "Equilibrium".
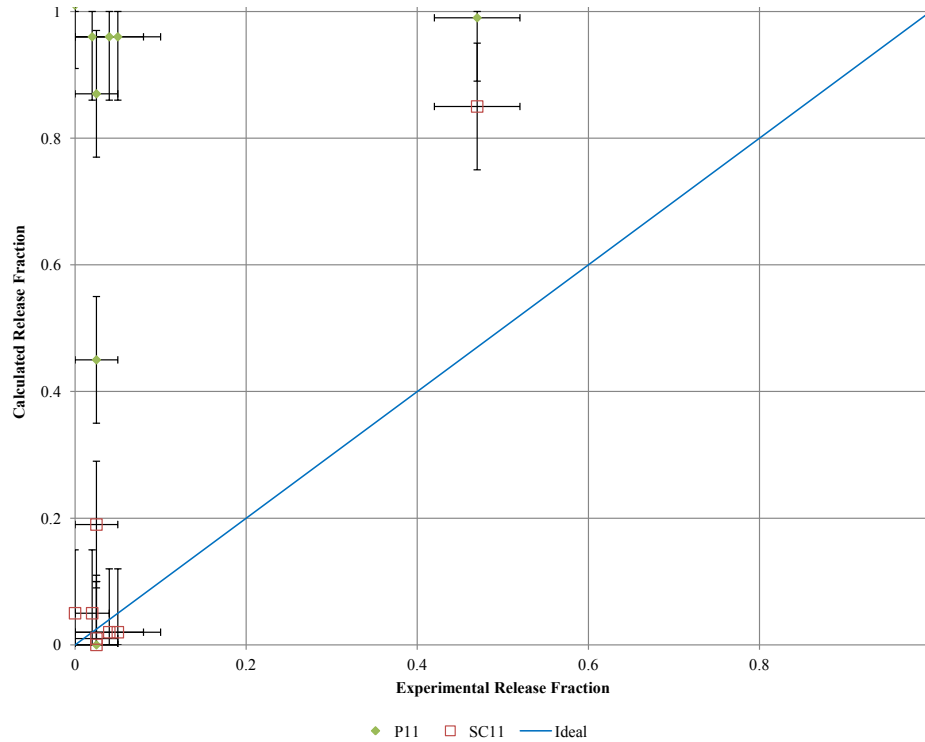
FIGURE 1: Comparison of calculated to experimental release fractions for ^{140}La.

equilibrium is also an assumption that makes the tractable. A fully kinetic model would require far more chemical data than an equilibrium model.

4.1 Existing Model in SOURCE 2.0

In order to obtain information on the equilibrium concentration of fission products and actinides in a postulated reactor accident, the initial elemental composition of the system needs to be specified. In the 1997 model by Corse [12-14], that composition was fixed by two user-specified factors and by the pre-calculated composition of CANDU fuel at a burnup[2] of 100 MW·h·kg^{-1}. The user-specified equilibrium ratio of molar hydrogen, $H_2(g)$, to steam, $H_2O(g)$, fixed the initial oxygen potential of the system. The user-specified molar ratio of caesium to hydrogen plus steam $(Cs/(H_2O+H_2))$ fixed the relative molar quantity of the fuel material and the gas phase. The hydrogen to steam ratio (or oxygen to steam ratio) ensures that the portion of the chemical lookup tables for an appropriate oxygen potential are used. The inert gas assumed in the thermodynamic calculations was the total molar quantity of krypton and xenon fission products per mole of caesium. The thermodynamic results were summarized in tables of vapour pressure as a function of the ratio of hydrogen to steam, the ratio of caesium to hydrogen plus steam, pressure and temperature. The range of this model was extended to consider more-oxidizing conditions using the ratio of oxygen to steam in place of the ratio of

[2] Burnup values in the paper are per kilogram of uranium in the initial fuel.

hydrogen to steam. Additional lookup tables are based on calculations performed at Atomic Energy of Canada Limited, Chalk River Laboratories, by Lemire, Colins and Szpunar [23].

4.2 New Model in SC11

In the new model, there is no need for the safety analyst to pre-calculate the equilibrium hydrogen to steam ratio in the incoming gas stream, or the ratio of caesium to hydrogen plus steam. The quantities of hydrogen atoms, $(H^t)_{in}$ and oxygen atoms, $(O^t)_{in}$ entering the system from the gas phase in a time interval are calculated from the molar gas flow rates $(\dot{m}_i)$ and the duration of the time interval (Δt). For sheathed fuel samples, the molar flow rates are the estimated flow rates in the fuel-to-sheath gap. These quantities are input values specified by the analyst.

$$(H^t)_{in} = 2(\dot{m}_{H_2} + \dot{m}_{H_2O})\Delta t \qquad (1)$$

$$(O^t)_{in} = (2\,\dot{m}_{O_2} + \dot{m}_{H_2O})\,\Delta t \qquad (2)$$

The quantity of inert gas contributed by the coolant is calculated similarly.

$$(InertGas)_{in} = \dot{m}_{Inert}\,\Delta t \qquad (3)$$

The molar quantity of hydrogen atoms in the coolant that flows in the gap is used as the hydrogen inventory for the equilibrium calculation. This quantity is an input from the analyst. The molar quantity of oxygen atoms in

the gap is added to the molar inventory of oxygen atoms in the fuel surface. The inert gas is treated as an extra mole of xenon for each mole of inert gas molecules. Since the RMC model does not treat krypton separately, the quantity of fission-product krypton in the fuel-to-sheath gap is replaced on a molar basis with additional xenon. Krypton and xenon are both chemically inert. Xenon exists in the RMC model only as a gas and xenon in the gap must exist in the gas phase. A similar situation would occur for krypton, if it were modelled independently. To ensure that the fuel surface composition is in equilibrium with the fuel, the actinide and associated oxygen inventory of the fuel grain is added to the system. In this way, the equilibrium solver establishes the equilibrium of three heterogeneous phases in contact: the fuel, the fuel surface inventory of fission products outside the grains, and the gas stream within the sheath. The equilibrium calculation is performed internally by the prototype program using the calculated inventories. The lookup tables of the previous model are eliminated.

4.3 Completeness of Molar Inventories
SOURCE 2.0 was originally intended to calculate release fractions for radiologically-significant radionuclides. Given that the fuel composition for the fission-product vaporization model was fixed by an ORIGEN-S 4.2 [30] calculation, there was no perceived need to track the

temporal evolution of the inventories of stable fission products with SOURCE 2.0. However, the prototype program uses a burnup-dependent inventory, so there is now a need to track a more complete list of nuclides of the modelled chemical elements. For example, ^{140}La (already modelled by SOURCE IST 2.0P11) represents only about 1 to 3 % of the fission-product lanthanum in irradiated CANDU fuel at burnups between 50 MW·h·kg^{-1} and 300 MW·h·kg^{-1}. The stable ^{139}La which accounts for most of the molar inventory of lanthanum is not modelled in SOURCE IST 2.0P11. ^{139}La is one of forty-four fission product nuclides or nuclear isomers proposed to be added to the nuclide set to allow SOURCE 2.0 to calculate a more complete initial molar inventory of the fission product elements for which the chemistry is modelled. Three fission-product nuclides and two actinide nuclides have been identified to be deleted from the nuclide set due to their small contributions to the chemical and radiochemical inventories (see Appendix A). In one case (^{132}Sb), there is additional uncertainty as to decay scheme for two nuclear isomers. Three actinides have been identified to be added. The revised nuclide set consists of 18 actinides and 174 fission products (see Table 1 in Appendix A), in place of the 17 actinides and 133 fission products in SOURCE IST 2.0P11. The agreement between ORIGEN-S 6.0 [31] calculations and SC11 [23] calculations of the molar inventory of the chemical
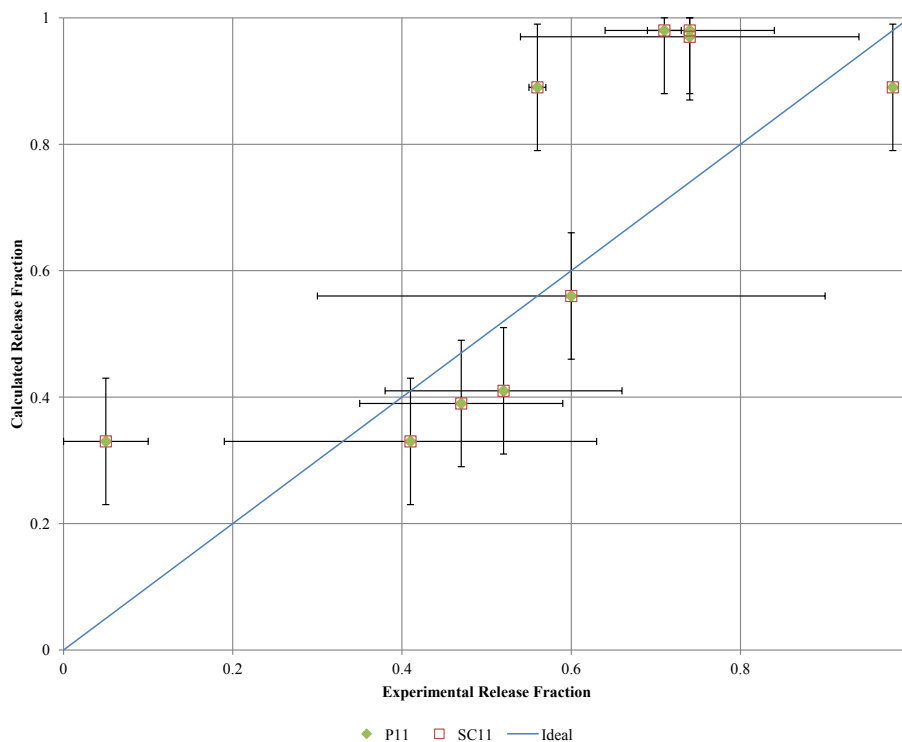
FIGURE 2: Comparison of calculated to experimental release fractions for ^{85}Kr.
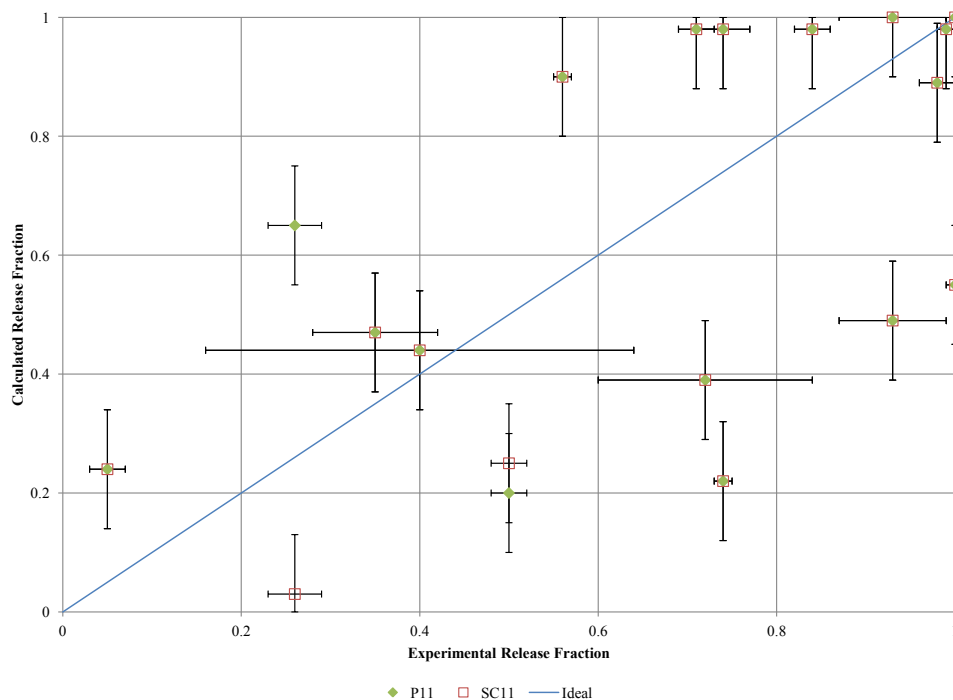
FIGURE 3: Comparison of calculated to experimental release fractions for [134]Cs.

elements modelled in the RMC thermochemical model [18-20] is within 20% for all chemical elements, and is frequently much better. This comparison is documented in [23]. Comparisons of individual nuclides have not been performed for the entire SC11 nuclide list.

5. Benchmarking

The validation approach for SOURCE 2.0 was described by Barber *et al.* [32]. It consists of simulating 18 fission-product release experiments with the computer program and comparing calculated fission-product release fractions with the final release fraction calculated from measurements during the tests. The benchmarking exercise used the same set of tests. Validation is a formal process used for as part of the code qualification process. The benchmarking, described here, was performed by the author as part of a development process. The 18 tests used are six AECL-Chalk River tests in steam; one CEA-Grenoble (France) hot cell test in steam; three AECL-Chalk River hot cell tests in air; three AECL-Chalk River hot cell tests in an inert (argon or argon/2% hydrogen) environment; one CEA-Grenoble hot cell test in hydrogen; one Oak Ridge (USA) hot cell test in hydrogen; two AECL-Chalk River in-reactor tests performed in the Blowdown Test Facility at Chalk River and one in-reactor performed in the French Phébus test facility.

For each test case, SC11 prints the calculated elemental inventory that is provided to the thermodynamic solver

and the calculated equilibrium. These values can be examined to look for anomalies. The benchmarking exercise itself provides a check that the key output parameters (the release fractions for radiologically-significant nuclides) are in agreement with experimental results. This agreement increases confidence in the computation of fission-product vapour pressures. However, even with that agreement it is still possible that some species that do not contribute to fission-product releases are in error. One advantage of the compatibility of ChemApp [21, 22] and FactSage [22] is that the RMC database can be used with FactSage to calculate phase diagrams for subsystems of the treatment (e.g., noble metals, or $UO_{2\pm x}$). Agreement of the calculated phase diagrams with published diagrams adds further confidence of the correctness of that aspect of the model. Finally, the consistency of the calculated equilibrium with the thermochemical database can be verified as reported by Piro *et al.* [33].

In Figure 1 through Figure 3, the vertical axis corresponds to calculated release fractions, the horizontal axis corresponds to experimentally-derived release fractions, and the diagonal line represents the calculated release fraction equal to the experimental release fraction. Experimental release fractions (X) reported as <X (with no "best" values or error intervals) are plotted against the x-axis as X/2 with horizontal error bars extending from 0 to X. The vertical error bars

represent the smaller of the target code accuracy of +/- 0.1 in absolute release fraction, or the difference between the calculated release fraction and the limits of 0 and 1.

5.1 Benchmarking ^{140}La

One issue with the existing SOURCE 2.0 results is that the calculated release fractions from the fuel to the coolant for lanthanides are larger than the experimentally-measured fractions. The mean difference between the calculated release (with SOURCE IST 2.0P11) and the experimentally-derived release fractions for ^{140}La is 0.70. Calculated release fractions for other lanthanides are similar. While the code predictions are conservative for the purpose of dose to the public, improved accuracy is desirable. ^{140}La is taken as representative of other lanthanides. If, as is the frequent analysis practice, retention of fission products in the primary heat transport piping is not credited, the calculated releases to containment are also higher than expected in reality. The lanthanides are not particularly volatile under expected containment conditions and would be calculated to settle or be deposited in containment. This situation would lead to calculated doses to equipment and personnel in containment that are higher than would be expected in reality. As such, a reduction in release fractions to values closer to measured values is desirable. A comparison of release fractions for the existing code (labelled P11) and the SC11 prototype code (labelled SC11) is shown in Figure 1. The prototype results represent an improvement in all cases. In particular, the cluster of points from SOURCE IST 2.0P11 in the upper left corner, representing a near-zero release fraction experimentally, but almost complete release by calculation, is now eliminated. This change results from the incorporation of the RMC thermodynamic model of irradiated uranium dioxide fuel matrix with lanthanum oxide in solid solution. The mean difference in release fractions for SC11 is 0.07.

5.2 Benchmarking ^{85}Kr

The existing code version had performed adequately for calculating release fractions of ^{85}Kr, a long-lived noble gas. ^{85}Kr is taken as representative of long-lived noble gases and due to its long half-life has the largest dataset within the SOURCE 2.0 validation test suite. Since the noble gas elements are modelled only as noble gases, and not as compounds that could accumulate on the fuel surface, the expectation is that noble gas releases are unaffected by the inclusion of a more rigorous fuel surface thermochemistry model. A comparison of the results of the existing SOURCE IST 2.0P11 code version with the prototype is shown in Figure 2. As expected, these results are unchanged.

5.3 Benchmarking ^{134}Cs

Caesium is modelled in the RMC Fuel Thermochemistry model as an element that participates in compound formation. The compounds range from the simplest gaseous species ($Cs(g)$) to polymeric mixed oxides (e.g., $Cs_2U_{15}O_{46}$). A comparison of caesium release fractions from various fission product release experiments as calculated with SOURCE IST 2.0P11 and the prototype indicates where the modelled chemistry has altered final release fractions. These data are plotted in Figure 3. ^{134}Cs is taken as a representative volatile fission product. Differences are seen in the final release for a test case in air at 1313 K with SOURCE IST 2.0P11 results of (0.26 Experimental, 0.65 Calculated) and prototype results of (0.26 Experimental, 0.03 Calculated). In the output from the SC11 prototype, the speciation of the caesium is primarily $Cs_2Zr_3O_7(s)$. This compound was introduced to the RMC database from the FACT data base after the FACT calculations used for SOURCE IST 2.0P11 were performed. In the FACT database, the thermodynamic data for $Cs_2Zr_3O_7(s)$ is referenced to a document by Heames $et\ al.$ [34] related to the VICTORIA code. Bixler [35] in a later VICTORIA code document references unpublished work by D.A. Powers. No original reference to thermodynamic data for this compound has been located. It may be prudent to delete it from the RMC fuel thermochemistry model.

As with SOURCE IST 2.0P11, the fuel vaporization model is called by the prototype for each time interval after sheath failure for which the fuel temperature (at either the beginning or end of the time) is greater than or equal to 600 K. The prototype prints the composition of the system for each vaporization calculation. The data for the first call to the vaporization model in this test case were entered into FactSage. The RMC fuel database in FactSage format was used to calculate an equilibrium composition. The same $Cs_2Zr_3O_7(s)$ solid was the dominant caesium-containing in the FactSage-calculated equilibrium, as expected. When $Cs_2Zr_3O_7(s)$ was removed from the possible products, the vapour pressure of caesium gas ($Cs(g)$) increased by four orders of magnitude, and became the dominant caesium-containing species.

The other difference seen in Figure 3 is the release fraction from a test in steam at 1373 K. The experimentally-observed release fraction was 0.50 ± 0.02. The calculated quantities were 0.20 from SOURCE IST 2.0P11 and 0.25 from the prototype. In the SOURCE IST 2.0P11 base case, the final distribution table shows ^{134}Cs remaining on the fuel surface at the end of the test. In the results of the prototype, no ^{134}Cs remains on the fuel surface. In keeping with the calculated chemical speciation, it has all vaporized. The new calculated result is in closer agreement with the experimental data. Because there is no caesium left on the fuel surface (in the calculated results), the remaining difference between the experimental and the computations must relate to transport of caesium from the fuel grains by diffusion to the grain-boundary bubbles (the grain surfaces) or to the transport of

caesium from the grain-boundary bubbles to the fuel pellet surface. These models are unchanged in the prototype computer program.

5.4 Benchmarking Summary

Preliminary benchmarking was performed for three radionuclides. The benchmarking has used 36 data pairs (8 for ^{140}La, 11 for ^{85}Kr and 17 for ^{134}Cs).

The first nuclide, ^{140}La, is a lanthanide for which the current production version, SOURCE IST 2.0P11, produces higher release fractions than are experimentally observed. The results with the prototype code are significantly better than the results from the existing production version.

The second nuclide, ^{85}Kr, is a noble gas that is not explicitly modelled in the model for fission-product release from the fuel surface. The expectation was that the new model would not alter the predicted releases of this nuclide from those of production code version. This expectation was confirmed by the benchmarking.

The third nuclide, ^{134}Cs, is a volatile activated fission product. Its release behaviour at elevated temperatures is expected to be diffusion-limited, rather than limited by vaporization at the fuel pellet surface. As such, the expectation was that the revised model for fission-product vaporization from the fuel surface would not affect the release fraction of ^{134}Cs in most cases. This was the behaviour observed in 15 of 17 test cases. In one of the other cases, the release fraction increases with the new model into better agreement with the experimental observation, and the ^{134}Cs calculated to remain on the fuel surface by the production code has vaporized. In the remaining case, the prototype code is predicting the retention of $Cs_2Zr_3O_7$(s) on the fuel surface. This case had the lowest temperature of all of the tests and was conducted in air. Neither of the two open-literature references located for the compound $Cs_2Zr_3O_7$(s) has any thermodynamic data [36, 37]. There is little basis for adjusting the thermodynamic data for this compound. A recent study of the caesium-zirconium-oxygen system by Dash *et al*. [38] does not include this compound. Because the computed presence of a solid compound decreases the releases of ^{134}Cs, introducing a non-conservatism into the analysis, elimination of this compound from the database may be prudent from a safety analysis perspective.

5.5 Implications of Lower Lanthanide Release

Current analyses of some cases of Loss of Coolant Accidents (LOCA) with Loss of Emergency Core Cooling (LOECC) have relied on expert judgments (based on experimental data) to bound the release fraction of lanthanides. The computer programs used at that time did not explicitly model lanthanide solubility in uranium dioxide. The present prototype computer program contains models of

lanthanide solubility in uranium dioxide. The calculated results are in better agreement with experimental results, and add confidence to the safety analysis.

6. Conclusions

This work has produced a prototype computer program SC11 (based on SOURCE IST 2.0P11) that incorporates an internal Gibbs energy minimizer into a revised model for fission-product vaporization from the fuel surface. The preliminary benchmarking for three nuclides (^{140}La, ^{85}Kr, and ^{134}Cs) indicates improved predictions for ^{140}La. The improvement can be quantified by a reduction in the mean difference between experimental and calculated release fractions from 0.70 to 0.07. Earlier bounding models had presented challenges to the equipment qualification in analysis of some accident scenarios. The improved results with the prototype would result in lower calculated doses to equipment in containment, and would improve the safety case for those power reactors. The benchmarking of ^{85}Kr demonstrates that this nuclide, which should be unaffected by the simulation of thermochemistry, is unaffected. The benchmarking of ^{134}Cs found unchanged behaviour in fifteen cases, improved behaviour in one case, and worse behaviour resulting from unexpected formation of $Cs_2Zr_3O_7$(s) on the fuel surface in one case. Further work is ongoing to benchmark more nuclides and to perform further benchmarking.

APPENDIX A:

The nuclides modeled in the prototype code SC11 are listed in Table 1. The 47 nuclides shown in bold font are additions to the set modelled by SOURCE IST 2.0P11. The five deletions from the list modelled in SOURCE IST 2.0P11 are ^{77}As, ^{79}As, ^{132}Sb, ^{240m}Np and ^{240}Np.

TABLE 1 Nuclides Modelled in SC11

234U	84Br	92Y	102Mo	112Pd	130I	**134Ba**	142Ba
235U	84Kr	**92Zr**	**102mTc**	112Ag	130Xe	135I	142La
236U	85mKr	93Y	102Tc	113Ag	130mSb	135mXe	**142Ce**
237U	85Kr	**93Zr**	**102Ru**	113mCd	130Sb	135Xe	143Ce
237Np	85Rb	94Y	103Ru	115mCd	**130Te**	135Cs	143Pr
238Np	86Rb	**94Zr**	103mRh	115Cd	131Sb	136Xe	**143Nd**
238U	86Kr	95Y	**103Rh**	121Sb	131mTe	136Cs	144Ce
239U	87Kr	95Zr	**104Rh**	122Sb	131Te	137Xe	**144mPr**
239Np	**87Rb**	95Nb	**104Pd**	123Sb	131I	137Cs	144Pr
239Pu	88Kr	**95Mo**	104Tc	124Sb	131mXe	137mBa	**144Nd**
240Pu	88Rb	**96Zr**	**104Ru**	125Sb	131Xe	**137Ba**	**145Nd**
241Pu	**88Sr**	97Zr	105Tc	**126Sn**	132Te	138Xe	**146Nd**
241Am	89Kr	97mNb	105Ru	126Sb	132I	138Cs	147Nd
242mAm	89Rb	97Nb	105Rh	127Sb	132Xe	**138Ba**	147Pm
242Am	89Sr	**97Mo**	105Pd	127mTe	133mTe	139Cs	148mPm
242Pu	**89Y**	**98Mo**	106Ru	127Te	133Te	139Ba	148Pm
242Cm	90mRb	99Mo	106Rh	**127I**	133I	**139La**	**148Nd**
238Pu	90Sr	99mTc	**106Pd**	128mSb	133mXe	140Ba	**150Nd**
81Br	90Y	**99Tc**	**107Pd**	128Sb	133Xe	140La	153Sm
82Br	91Sr	**100Ru**	**108Pd**	**128Te**	133Cs	**140Ce**	153Eu
83Se	91mY	**100Mo**	109Pd	129Sb	134Te	141Ba	154Eu
83Br	91Y	101Mo	109Ag	129mTe	134I	141La	155Eu
83mKr	**91Zr**	101Tc	110mAg	129Te	134Cs	141Ce	156Eu
83Kr	92Sr	**101Ru**	111Ag	129I	134Xe	**141Pr**	157Eu

REFERENCES

[1] A.C. Brito, F.C. Iglesias, Y. Liu, M.A. Petrilli, M.J. Richards, R.A. Gibbs and P.J. Reid, 1995, "SOURCE 2.0: A Computer Program to Calculate Fission Product Release from Multiple Fuel Elements for Accident Scenarios", 4th International Conference on CANDU Fuel, Pembroke, Ontario, Canada, October 1-4, 1995, Vol. 2, pp. 5B-45-5B-56.

[2] D.H. Barber, F.C. Iglesias, Y. Hoang, L.W. Dickson, R.S. Dickson, M.J. Richards and R.A. Gibbs, 1999, "SOURCE IST 2.0: Development and Beta Testing", Sixth International Conference on CANDU Fuel, Niagara Falls, Ontario, Canada, September 26-30, 1999, Vol. 1, pp. 393-402.

[3] D.H. Barber, F.C. Iglesias, L.W. Dickson, M.J. Richards and P.J. Reid, 2001, "SOURCE IST 2.0: Phenomena Modelling", Seventh International Conference on CANDU Fuel, Kingston, Ontario, Canada, September 23-27, 2001, Vol. 2, pp. 5C-21 - 5C-30.

[4] E. Rutherford, 1905, "Radio-activity", 2nd Edition, Cambridge University Press, Cambridge, Great Britain.

[5] H. Bateman, 1910, "The Solution of a System of Differential Equations Occurring in the Theory of Radio-active Transformations", Proceedings of the Cambridge Philosophical Society, Vol. 15, pp. 423-427.

[6] G.F. Thomas, D.H. Barber, 1994, "Stiffness in Radioactive Decay Chains", Annals of Nuclear Energy, Vol. 21(5), pp. 309-320.

[7] P.J. Reid, B.J. Lewis, F.C. Iglesias, D.H. Barber, 1999, "Modelling of Intra-Granular Diffusion, Production and Removal in SOURCE 2.0", Sixth International Conference on CANDU Fuel, Niagara Falls, Ontario, Canada, September 26-30, 1999, Vol. 2, pp. 249-257.

[8] G.V. Kidson, 1980, "A Generalized Analysis of the Cumulative Diffusional Release of Fission Product Gases from an "Equivalent Sphere" of UO2", Journal of Nuclear Materials, Vol. 88(2-3), pp. 299-308.

[9] J.A. Turnbull, C.A. Friskney, J.R. Findlay, F.A. Johnson, A.J. Walter, 1982, "The Diffusion Coefficients of Gaseous and Volatile Species during the Irradiation of Uranium Dioxide", Journal of Nuclear Materials, Vol. 107(2-3), pp. 168-184.

[10] J.A. Turnbull, R.J. White, C. Wise, 1988, "The Diffusion Coefficient for Fission Gas Atoms in Uranium Dioxide", Proceedings of the International Atomic Energy Agency Technical Committee Meeting on Water Reactor Fuel Element Computer Modelling in Steady State, Transient and Accident Conditions, Preston, England, September 18-22,1988, pp. 174-181.

[11] L.D. Macdonald, D.B. Duncan, B.J. Lewis, and F.C. Iglesias, 1988, "FREEDOM: A Transient Fission Product Release Model for Radioactive and Stable Species", Presented at the International Atomic Energy Agency Technical Committee Meeting on Water Reactor Fuel Element Computer Modelling in Steady-State, Transient and Accident Conditions, Preston, England, September 18-22,1988, pp. 203-208 (also available as Report AECL-9810, 1989 May).

[12] B.J. Corse, 1997, "FORM 2.0: Fuel Oxidation and Release Model: a Computer Code to Predict the Low Volatile Fission-Product Release and Fuel Volatilization from Uranium Dioxide Fuel Under Severe Reactor Accident Conditions", M. Eng. Thesis, Royal Military College of Canada, Kingston, Ontario, Canada.

[13] B.J. Lewis, B.J. Corse, W.T. Thompson, M.H. Kaye, F.C. Iglesias, P. Elder, R.S. Dickson and Z. Liu, 1997, "Vaporization of Low-Volatile Fission Products Under Severe CANDU Reactor Accident Conditions", Fifth International Conference on CANDU Fuel, Toronto, Ontario, Canada, September 21-25, 1997, Vol. 1, pp. 145-159.

[14] B.J. Lewis, B.J. Corse, W.T. Thompson, M.H. Kaye, F.C. Iglesias, P. Elder, R.S. Dickson and Z. Liu, 1998, "Low Volatile Fission-Product Release and Fuel Volatilization During Severe Reactor Accident Conditions", Journal of Nuclear Materials, Vol. 252 (3), pp. 235-256.

[15] W.T. Thompson, C.W. Bale and A.D. Pelton, 1979, "Teaching Chemical Thermodynamics Applications with the FACT Interactive Computing System", Engineering Education, Vol. 70(2), pp. 201-205

[16] W.T. Thompson, C.W. Bale and A.D. Pelton, 1980, "Interactive Computer Tabulation of Thermodynamic Properties with the F*A*C*T System", Journal of Metals, Vol. 32(12), pp. 18-22.

[17] W.T. Thompson, A.D. Pelton and C.W. Bale, 1985, "Facility for the Analysis of Chemical Thermodynamics Guide to Operations", Royal Military College of Canada and École Polytechnique, Kingston, Ontario and Montreal, Quebec, Canada.

[18] W.T. Thompson, B.J. Lewis, E.C. Corcoran, M.H. Kaye, S.J. White, F. Akbari, Z. He, R. Verrall, J.D. Higgs, D.M. Thompson, T.M. Besmann and S.C. Vogel, 2007, "Thermodynamic Treatment of Uranium Dioxide Based Nuclear Fuel", International Journal of Materials Research, Vol. 98(10), pp. 1004-1011.

[19] E.C. Corcoran, 2009, "Thermochemical Modelling of Advanced CANDU Reactor Fuel", Ph.D. Thesis, Royal Military College of Canada, Kingston, Ontario, Canada.

[20] M.H.A. Piro, 2011, "Computation of Thermodynamic Equilibria Pertinent to Nuclear Materials in Multi-Physics Codes", Ph.D. Thesis, Royal Military College of Canada, Kingston, Ontario, Canada.

[21] G. Eriksson and E. Königsberger, 2008, "FactSage and ChemApp: Two Tools for the Prediction of Multiphase Chemical Equilibria in Solutions", Pure and Applied Chemistry, Vol. 80(6), pp. 1293-1302.

[22] S. Petersen, 2010, "ChemApp© - The Thermochemistry Library for your Software, Programmer's Manual Edition 3.13 for ChemApp Versions 2.0.2 through 6.1.3", GTT-Technologies, Herzogenrath, Germany

[23] D.H. Barber, 2013, "Implementation of a Thermodynamic Solver within a Computer Program for Calculating Fission Product Release Fractions", Ph.D. Thesis, Royal Military College of Canada, Kingston, Ontario, Canada.

[24] A. El-Jaby, B.J. Lewis, W.T. Thompson and F. Iglesias, M. Ip, 2010, "A General Model for Predicting Coolant Activity Behaviour for Fuel-Failure Monitoring Analysis", Journal of Nuclear Materials, 399(1), pp. 87-100.

[25] A. El-Jaby, 2009, A Model for Predicting Coolant Activity Behaviour for Fuel-Failure Monitoring Analysis", Ph.D. Thesis, Royal Military College of Canada, Kingston, Ontario, Canada.

[26] M.S. Veshchunov, V.D. Ozrin, V.E. Shestak, V.I. Tarasov, R. Dubourg, and G. Nicaise, 2006, "Development of the Mechanistic Code MFPR for Modelling Fission-Product Release from Irradiated UO2 Fuel", Nuclear Engineering and Design, Vol. 236(2), pp. 179-200.

[27] J.W. Gibbs, 1873, "A Method of Geometrical Representation of the Thermodynamic Properties of Substances by Means of Surfaces", Transactions of the Connecticut Academy of Arts and Science, Vol. 2, Part 2, pp 382-404.

[28] J.W. Gibbs, 1876, "On the Equilibrium of Heterogeneous Substances", Transactions of the Connecticut Academy of Arts and Science, Vol. 3, pp. 108-248 and 343-524.

[29] J.A.V. Butler, 1951, "Chemical Thermodynamics", 4th edition (with corrections), MacMillan and Company, London, England.

[30] O.W. Hermann and R.M. Westfall, 1995, "ORIGEN-S – SCALE System Module to Calculate Fuel Depletion, Actinide Transmutation, Fission Product Buildup and Decay, and Associated Radiation Source Terms, in SCALE: A Modular Code System for Performing Standardized Computer Analysis for Licensing Evaluations", Report NUREG/CR-0200, Rev. 4 (ORNL/NUREG/CSD-2/R4), Vol. II, Part I.

[31] I.C. Gauld, O.W. Hermann and R.M. Westfall, 2009, "ORIGEN-S: SCALE Module to Calculate Fuel Depletion, Actinide Transmutation, Fission Product Buildup and Decay, and Associated Radiation Source Terms", Oak Ridge National Laboratory, Report ORNL/TM-2005/39, Version 6, Vol. II, Sect. F7.

[32] D.H. Barber, L.W. Dickson, R.S. Dickson and M. Audette-Stuart, 2001, "SOURCE IST 2.0 Validation Approach", Seventh International Conference on CANDU Fuel, Kingston, Ontario, Canada, September 23-27, 2001,Vol. 2, pp. 5C-31-5C-37.

[33] M.H.A. Piro, T.M. Besmann, S. Simunovic, B.J. Lewis and W.T. Thompson, 2011, "Numerical Verification of Equilibrium Thermodynamic Computations in Nuclear Fuel Performance Codes", Journal of Nuclear Materials, Vol. 414(3), pp. 399-407.

[34] T.J. Heames, D.A. Williams, N.E. Bixler, A.J. Grimley, C.J. Wheatley, N. A. Johns, M.D. Vine, P. Domagala, L.W. Dickson, C.A. Alexander, I. Osborn-Lee, S. Zawadzki, J. Rest and H.S. Bond, 1992, "VICTORIA: A Mechanistic Model of Radionuclide Behavior in the Reactor Coolant System Under Severe Accident Conditions", Rev. 1, Report SAND90-0756, NUREG/CR-5545, Sandia National Laboratories.

[35] N.E. Bixler, 1998, "VICTORIA 2.0: A Mechanistic Model for Radionuclide Behaviour in a Nuclear Reactor Coolant System Under Severe Accident Conditions", Sandia National Laboratories, Report NUREG/CR-6131, SAND93-2301 R3.

[36] V.E. Plyushchev, A.A. Grizik, 1967, "Alkali Metal Zirconates and Hafnates", Redkie Shchelochnye Elementy; Sbornik Dokladov Vsesoyunogo Soveshchanii po Redkim Shchelochnym Elementam, 2nd (1964), Novosibirsk, Soviet Union, pp. 201-218 (In Russian).

[37] A.A. Grizik, V.E. Plyushchev, 1968, "Existence of Caesium Zirconates and Hafnates", Izvestiya Vysshikh Uchebnykh Zavedenii, Tsvetnaya Metallurgiya, Vol. 11(5), pp. 53-59 (In Russian)

[38] S. Dash, D.D. Sood, R. Prasad, 1996, "Phase Diagram and Thermodynamic Calculations of Alkali and Alkali Earth Metal Zirconates", Journal of Nuclear Materials, Vol. 228(1), pp. 83-116.

Hydrogen co-production from subcritical water–cooled nuclear power plants in Canada

N. Gnanapragasam*, D. Ryland and S. Suppiah

Atomic Energy of Canada Limited, Chalk River Laboratories, Chalk River, Ontario, Canada K0J 1J0

*Corresponding author: (613) 584-3311, gnanapragasamn@aecl.ca

Subcritical water-cooled nuclear reactors (Sub-WCR) operate in several countries including Canada providing electricity to the civilian population. The high-temperature-steam-electrolysis process (HTSEP) is a feasible and laboratory-demonstrated large-scale hydrogen-production process. The thermal and electrical integration of the HTSEP with Sub-WCR-based nuclear-power plants (NPPs) is compared for best integration point, HTSEP operating condition and hydrogen production rate based on thermal energy efficiency. Analysis on integrated thermal efficiency suggests that the Sub-WCR NPP is ideal for hydrogen co-production with a combined efficiency of 36%. HTSEP operation analysis suggests that higher product hydrogen pressure reduces hydrogen and integrated efficiencies. The best integration point for the HTSEP with Sub-WCR NPP is upstream of the high-pressure turbine.

Nomenclature

ACR	Advanced CANDU® Reactor
AECL	Atomic Energy of Canada Limited
BOP	balance of plant
CEP	condensate extraction pump
$\dot{E}_{cell}$	electrical energy required by the e-cell to split water (W)
$\dot{E}_{HTSEP}$	total electrical energy for e-cell and supplementary heaters in HTSEP (W)
e-cell	electrolysis cell
F	Faraday constant (96485 C•mol^{-1})
FWH	feed water heater
FWP	feed water pump
GSC	gland seal condenser
LHV	lower heating value of hydrogen (119.96 MJ•kg^{-1})
HPT	high pressure steam turbine
HTGR	high temperature gas-cooled nuclear reactor
HTSEP	high temperature steam electrolysis plant or process
IPT	intermediate pressure steam turbine
LPT	low pressure steam turbine
$\dot{m}_{H2}$	product hydrogen mass flow rate (kg•h^{-1})
MPa	Mega Pascal
MSR	moisture separator reheater
MW	mega Watt
$\dot{n}_{mol}$	molar flow rate of hydrogen from the e-cell (mol•h^{-1})
NPP	nuclear power plant
$\dot{Q}_{in.HTSEP}$	thermal energy demand by the HTSEP (W)
$\dot{Q}_{in.NPP}$	total thermal energy input to the NPP from the nuclear reactor (W)
Sub-WCR	subcritical water-cooled nuclear reactor
V_{el}	voltage required for electrolysis (volts)
$\dot{W}_{in.NPP}$	total work input to pumps in NPP (W)
$\dot{W}_{in.HTSEP}$	total work input to pumps and compressor in HTSEP (W)
$\dot{W}_{out.NPP}$	total work output from steam turbine stages in NPP (W)
X	steam quality

Greek Symbols

η_{el}	efficiency, thermal-to-electrical or electrical
η_{H2}	efficiency, thermal-to-hydrogen or hydrogen
$\eta_{el.H2}$	efficiency, thermal-to-electrical+hydrogen or integrated

AECL NUCLEAR REVIEW
VOL 2, NUMBER 1, JUNE 2013

HYDROGEN CO-PRODUCTION FROM SUBCRITICAL WATER-COOLED NUCLEAR POWER PLANTS IN
CANADA - N. GNANAPRAGASAM, D. RYLAND AND S. SUPPIAH

1. Introduction

Hydrogen is abundant in nature, but is typically bound with other species so must be manufactured for commercial and industrial use. While parts of a hydrogen economy infrastructure still require development, AECL has pursued the design of a suitable large-scale hydrogen-production process using energy from nuclear-power plants is being pursued [1-3].

Utility-scale energy storage is one possible application for hydrogen produced from nuclear-power plants. Production of hydrogen using electricity when grid demand is low and using hydrogen to produce electricity (either through combustion or fuel cells) during high-demand periods is a potential market for large-scale advanced electrolysis processes. The work reported in this paper targets such an application, where hydrogen is co-produced using off-peak nuclear electricity for large-scale storage. The efficiency and economics of large-scale energy storage have been assessed [4, 5] with consideration given to renewable energy technologies as the electricity source for hydrogen produced using water electrolysis. From these assessments, compared to battery storage of electricity, hydrogen storage has lower energy transfer efficiency in the electricity-to-hydrogen-to-electricity route and higher costs due to the involvement of higher number of energy intensive processes. But the advantage with hydrogen for energy storage is that it provides higher volumetric energy density than batteries, thus the cost of storing electricity in large capacities is lower.

Enbridge Inc. and Hydrogenics Corp. have announced a joint venture to develop utility-scale energy storage in North America [6]. Hydrogen produced using water electrolysis during periods of excess electricity generation will be injected into Enbridge's natural gas pipeline network. The existing natural gas pipelines can manage between 5 to 15% hydrogen by volume without pipeline material deterioration and without increasing risks associated with the gas blend in the end-use devices such as household appliances [7].

New demand for hydrogen is emerging from the transportation sector in Canada and elsewhere. Hydrogen is used in cars and buses either through direct injection into internal combustion engines with maximum efficiencies between 30 and 40% [8] or in fuel cells (with maximum efficiencies between 50 and 60% [9]) that produce electricity to run an electric motor that drives the vehicle. There are more than 600 such cars in California alone with more than 20 hydrogen-fuelling stations [10]. In comparison to vehicles using battery-electricity, hydrogen-electric vehicles have some practical advantages: refuelling takes minutes instead of hours; the travel range of the vehicle is much longer; and

replacement and maintenance costs are much lower [9, 11]. Both technological and economic challenges still remain in large-scale clean hydrogen production, distribution of hydrogen for refuelling and long-term large-scale storage to utilize off-peak electricity.

In Canada, hydrogen is produced in large quantities for heavy oil upgrading and for producing chemicals such as ammonia and methanol. Hydrogen is produced mainly through two processes: (i) steam methane reforming, and (ii) partial oxidation (gasification) of heavy hydrocarbons. These processes produce CO_2 as a by-product. Since CO_2 is a greenhouse gas (GHG), such hydrogen production processes will be discouraged in the long term.

Only a few processes are available to produce hydrogen without generating *additional* GHGs. One of these is electrolysis of water, where water or steam is split into hydrogen and oxygen using electrical energy in an electrochemical cell. Depending on the operating temperature of the process there are two types of water electrolysis processes: (i) low temperature water electrolysis (between 25 and 80 °C) and (ii) high temperature steam electrolysis (over 800 °C).

The high-temperature steam electrolysis (HTSE) is a water-electrolysis process where high-temperature steam is split into hydrogen and oxygen. The HTSE process has higher thermal-to-hydrogen efficiency than low-temperature electrolysis since, at higher temperatures, less electricity is needed (from thermal energy conversion) and more of the energy required to split the water comes from process heat [2]. HTSE uses ceramic as an electrolyte as opposed to the caustic solution used in conventional water electrolysis. A laboratory-scale experiment of hydrogen production using the HTSE process was operated at the Idaho National Laboratories [12] for about 1000 hours to demonstrate its long-term viability. One of the key stages in the HTSE process is to convert water into steam at a pressure of about 5 MPa. The reason to operate the HTSE process at pressure is to remove the requirement to compress the product hydrogen at the end. Thermal energy from an existing steam power cycle, standalone steam plant or renewable energy plant can be used for water splitting in order to reduce the amount of electricity required by the electrolysis cell.

Currently, there are no large-scale electrolysis-based hydrogen production plants in Canada. But there is sufficient expertise available to model, design and implement such plants especially in producing nuclear hydrogen. The term "nuclear hydrogen" describes hydrogen produced by electrolysis of water using heat and electricity from the steam-power cycle of a nuclear power plant (NPP) [13].

AECL NUCLEAR REVIEW
VOL 2, NUMBER 1, JUNE 2013

HYDROGEN CO-PRODUCTION FROM SUBCRITICAL WATER-COOLED NUCLEAR POWER PLANTS IN
CANADA - N. GNANAPRAGASAM, D. RYLAND AND S. SUPPIAH

In Canada, all of the existing NPPs operate with various CANDU (CANada Deuterium and Uranium) designs that are heavy-water cooled and moderated, at subcritical conditions. This paper compares the overall performance when the HTSE process is integrated with the power cycle of an ACR-1000 power reactor - an advanced concept of CANDU nuclear reactors [14]. Some of the electricity and a small portion of the heat produced from the NPP will be used in the HTSE process to convert steam into hydrogen and oxygen, while the rest of the electricity will be sent to the electrical grid.

A comparison is done through balance of plant (BOP) process model of a given NPP concept. A balance of plant involves only the steam cycle of the NPP, to maintain consistency the BOP of an NPP will be referred to simply as NPP in the rest of the paper. Process models were built using Aspen HYSYS [15], a commercial process simulation software package, for the following systems based on existing conceptual designs:

*   An ACR-1000 based steam cycle (NPP)
*   An HTSE plant/process (HTSEP)
*   A plant integrating an NPP and HTSEP

By analysing these models for a number of different integration points, the integrated NPP-HTSEP plant has been assessed for thermal efficiency of individual systems and the integrated system.

2. Subcritical Water-cooled Reactor (Sub-WCR) based Nuclear Power Plant and Model
The ACR-1000 is one of the subcritical reactor concepts designed by AECL. The schematic shown in Figure 1 is of an optimized indirect steam cycle concept of the NPP for an ACR-1000 reactor based design. An indirect steam cycle is

one where the heat from the primary loop (reactor cycle) is transferred to the subcritical steam power cycle through a steam generator as shown in Figure 1. The water and steam of the power cycle do not come in direct contact with the fuel in the reactor.

Key stream conditions are given in Figure 1. In this work, only the steam-power cycle (secondary loop in Figure 1) is modeled and analyzed. Such a dual-cycle process has a major disadvantage in that the large surface area required for heat transfer in the steam generator between the two cycles increases the cost while decreasing thermal-to-electrical efficiency (defined in section 4.1).

The Sub-WCR NPP system is a preliminary optimized design whose balance of plant was modeled with some adaptive changes in HYSYS. When the HTSE plant is integrated, the system optimization is changed so the integrated process was re-optimized in HYSYS. There is an adjust function in the NPP model that adjusts the mass flow rates for changes in integration points with HTSEP. Thus values of some streams in the HYSYS flow sheet for the NPP are slightly different from that designed originally for the ACR-1000 NPP.

The steam turbines in the power cycle are pressure staged from 5.8 MPa (HPT) to 0.954 MPa (LPT) turbines. The feed-water heaters are pressure-staged according to the bleed streams from each turbine stage. The moisture separator and reheater (MSR) is used instead of a reheat cycle for improving the steam quality from the exhaust of HPTs entering the LPTs. This requires that the operating parameters for the MSR be carefully selected to maintain control of the moisture content of the steam in LPT stages [16]. In turbine stages where the outlet pressure is such that there is liquid in steam, a knockout tank is required to separate liquid water from the steam.
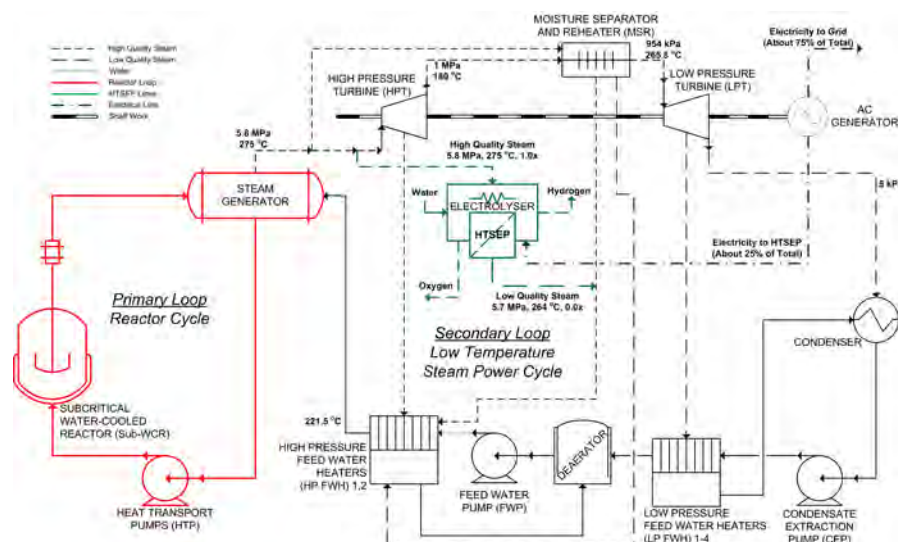
FIGURE 1: Simplified schematic of Indirect Steam Cycle concept with an MSR in an Sub-WCR Nuclear Power Plant (NPP), integrated with an HTSEP.

AECL NUCLEAR REVIEW
VOL 2, NUMBER 1, JUNE 2013

HYDROGEN CO-PRODUCTION FROM SUBCRITICAL WATER-COOLED NUCLEAR POWER PLANTS IN
CANADA - N. GNANAPRAGASAM, D. RYLAND AND S. SUPPIAH

2.1 NPP Model Assumptions and Conditions

The following assumptions are made to model a NPP in HYSYS:

1. The thermal energy from Sub-WCR core is modeled as a heater and the heat input is fixed at about 3295 MW$_{th}$.
2. Only steady-state simulations are performed.
3. Efficiencies for the steam generator, feed water heaters and coolers are not directly specified in the respective models. Default performance parameter values are used for each of these heat transfer models in HYSYS.
4. Fixed adiabatic efficiency of 85% is assumed for feed water pumps (FWP) and condensate extraction pump (CEP).
5. The steam turbine stages and bleed points are modeled as independent turbines. Fixed polytropic efficiency of 90% is assumed for high pressure steam turbines (HPT) and 91% is assumed for low pressure steam turbines (LPT).
6. An efficiency of 98% is assumed for the electricity generator.
7. The pressure drop across the steam generator is set at 160 kPa [14].
8. Pressure drop across LP FWHs are set at 15 kPa; pressure drops across HP FWHs are set at 25 kPa.
9. The condenser operates at a pressure of 4.9 kPa.
10. Properties for water, hydrogen and oxygen are estimated within HYSYS by using Peng-Robinson equation of state and the related property database. The reason for using Peng-Robinson equation of state is that within HYSYS it is compatible for processes in both the steam cycle model (NPP) and the electrolysis plant model (HTSEP) described below. Based on a comparison of values of the NPP-only HYSYS models using ASME steam tables and Peng-Robinson, the Peng-Robinson over-predicted some of the stream values by 3%.

3. High Temperature Steam Electrolysis Plant (HTSEP) Model

The design and process model of HTSEP as shown in Figure 2 was originally proposed by Idaho National Laboratories (INL) without the hydrogen compressor [2]. Detailed models of HTSEP have also been simulated by the group at INL for standalone hydrogen production purposes using a high temperature gas-cooled reactor (HTGR). A similar HTSEP is modelled here to integrate with ACR-1000 NPP model within HYSYS. The HTSEP model is done without steam sweep for the oxygen stream from the e-cell. Steam sweep (sometimes nitrogen or air is used) is to remove excess oxygen [12] in the oxygen outlet stream from the HTSE cell.

In the schematic of HTSEP shown in Figure 2, JN refers to a junction of material streams; LTHX is a low temperature heat exchanger; IHE is the intermediate heat exchanger; STM/H$_2$RG is the steam/hydrogen regenerator; SWRG is the sweep regenerator; and SUPHT is a supplemental heater, with stream ELEC HT representing an external heat source such as electrical heating. Streams "From NPP" and "To NPP" are the streams from the NPP that form the integration points. The point of integration of thermal energy transport from the NPP into the HTSEP is the IHE.

In Figure 2, the feed water enters the plant at atmospheric pressure and temperature and then is pressurized to 5.4 MPa. The high pressure water mixes with water removed from the product hydrogen in the JN1 process unit and then is warmed by heat exchange with the hydrogen stream in the LTHX process unit. The thermal energy from the NPP is used to increase temperature of stream E3 from 149 ºC to 274 ºC in stream E4. These conditions were derived based on optimization of the configuration given in Figure 2 such
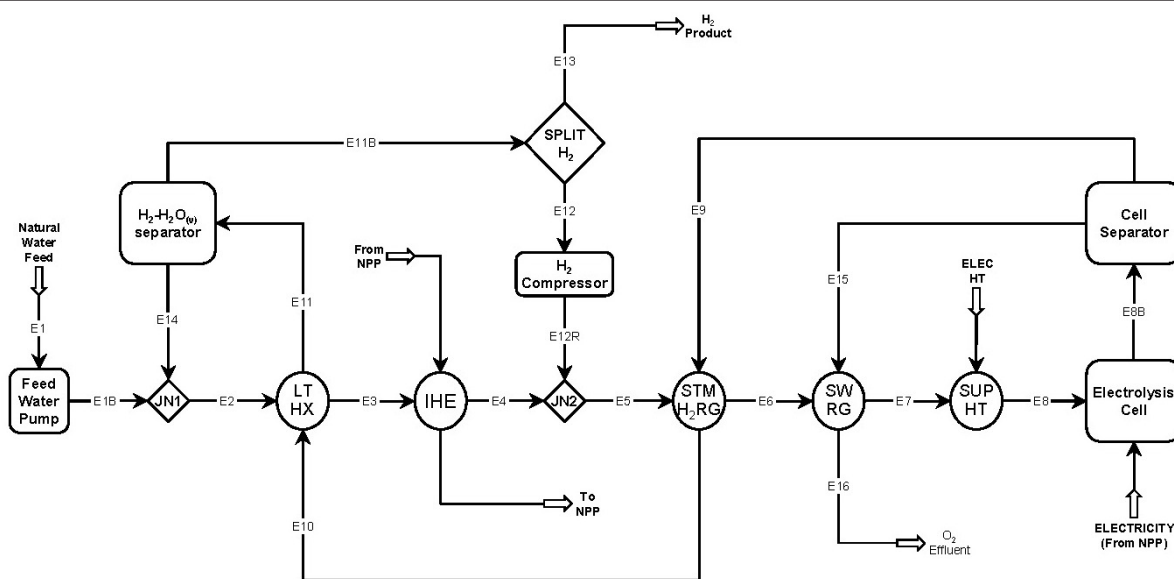
FIGURE 2: Schematic of high temperature steam electrolysis plant.

AECL NUCLEAR REVIEW
VOL 2, NUMBER 1, JUNE 2013

HYDROGEN CO-PRODUCTION FROM SUBCRITICAL WATER-COOLED NUCLEAR POWER PLANTS IN
CANADA - N. GNANAPRAGASAM, D. RYLAND AND S. SUPPIAH

that the HTSEP provides the best thermal-to-hydrogen efficiency within the confines of the available heat from the NPP.

The electrolysis cell was modeled as a combination of a conversion reactor and separator without using a specific electrolytic model. The Electrolysis Cell process unit (e-cell) in Figure 2 is the conversion reactor that converts water into hydrogen and oxygen using electrical energy input (stream ELECTRICITY in Figure 2). The gas products are separated in Cell Separator process unit. An additional heater is added (SUP HT in Figure 2) to provide the required heat to raise the temperature of steam to 826 °C, the cell operating temperature. This temperature is chosen based on similar temperatures (1100 K) tested in the lab-scale cells by the group at Idaho National Labs [12]. For the purposes of this study, it is assumed that the heat is provided by electricity from the NPP through resistive heating. All of the water vapour that is not converted into hydrogen is assumed to be carried by the hydrogen stream. In reality, both hydrogen and oxygen streams carry water vapour. The aim is to recover that water from both these streams and recycle it back to the cell.

The mass flow rate of steam from the NPP is varied depending on the integration case. Note that the stream ELECTRICITY in Figure 2 for the electrolysis cell (e-cell) is assumed to be provided by the NPP at the plant thermal-to-electrical efficiency. The stream ELEC HT in Figure 2 is electricity provided by the NPP to the supplementary electrical heater SUP HT.

A hydrogen compressor was added for the recycle stream at E12 in Figure 2. This is done so that the pressure at E5 is balanced between E12 and E4 and thus will allow the Cell Separator process unit to function properly. This situation arose to account for pressure drop across the heat exchangers. The heat exchangers shown in Figure 2 are modeled as shell and tube heat exchangers.

3.1 HTSEP Model Assumptions and Conditions
The following assumptions are made to model HTSEP in HYSYS:
1. Only steady-state simulations are performed.
2. Fixed adiabatic efficiency of 90% is assumed for feed water pump.
3. Fixed polytropic efficiency of 85% is assumed for the hydrogen compressor.
4. Pressure drop of 20 kPa is assumed across all the heat exchangers on both tube and shell sides, except for the IHE. In the IHE, the shell side pressure drop is set at 100 kPa.
5. Water is split completely by the e-cell (i.e., it operates at full theoretical efficiency).

6. No impurities or losses are associated with the e-cell.
7. Thermal energy conversion to electricity for input to the e-cell was calculated at NPP efficiency.
8. 10% of product hydrogen is recycled to maintain reducing conditions at the cathode of the electrolysis cell.
9. Hydrogen plant capacity is set at about 190 tonnes per day.

The electrical energy needed for the e-cell in the HTSEP to split water is calculated based on the power requirement for the steam electrolysis process. This is summarized in equation (1),

$$\dot{E}_{cell} = 2FV_{el}\dot{n}_{mol} \qquad (1)$$

Within the HTSEP, the e-cell voltage (V_{el}) is calculated by balancing Equation (1) using the electric power required by the cell $\dot{E}_{cell}$ (which is about 269 MW for 190 tonne per day hydrogen plant) and is found to be 1.28 volts. If the conversion reactor (electrolysis cell) and cell separator combination, in Figure 2, is replaced with an actual e-cell, it must operate at this voltage to obtain the thermal-to-hydrogen efficiencies predicted by the model.

4. NPP and HTSEP Integration
Process integration of an HTSEP with an NPP was sought here only from the prospect of co-producing hydrogen and did not consider standalone production of hydrogen. The production capacity of the plant modelled (190 tonnes per day) is the same as that proposed by INL for integration with the 600 MW$_{th}$ HGTR [2]. This provides a means to compare their plant with what would be required if a Canadian reactor design were used. For comparison, a typical Steam-Methane Reformer (SMR) plant could produce about 500 tonnes per day, while a standalone hydrogen production facility could produce about 1000 tonnes per day. Process integration of an NPP with an HTSEP was done by determining possible points within the NPP that are suitable for integration from a list of several integration points. An integration point begins with a high enthalpy stream "From NPP," passes through the IHE in Figure 2, and returns as a low enthalpy stream "To NPP".

The criteria for choosing the integration points for an HTSEP with an NPP were:

- The highest enthalpy stream from the NPP would provide better heat exchange at the IHE in an HTSEP and the return stream (To NPP) will still retain enough enthalpy to reheat feed water in one of the feed water heaters (FWH).
- Returning low quality steam to any of the low pressure turbine stages is not useful, since the steam quality of return stream from HTSEP is always less than half ($x < 0.5$).

AECL NUCLEAR REVIEW
VOL 2, NUMBER 1, JUNE 2013

HYDROGEN CO-PRODUCTION FROM SUBCRITICAL WATER-COOLED NUCLEAR POWER PLANTS IN
CANADA - N. GNANAPRAGASAM, D. RYLAND AND S. SUPPIAH

- The feed going into the FWP (feed water pump) should be liquid (x = 0). Thus, connecting the return stream to first two of the low pressure FWH would not improve the thermal energy conditions required by these FWHs and would increase the rejected heat at the condenser.

The stream from NPP that provided the best thermal efficiency for both NPP and HTSEP is chosen by calculating enthalpies of streams. Starting from the stream with highest enthalpy several combinations of integration were tested. The best of them are listed below.

The four integration cases/points considered are:

Case 1: HTSEP in Figure 2 is connected between S2 and L1 in Figure 3. Stream S2 is the inlet to the high pressure turbine, which is the highest enthalpy point within the NPP. Stream L1 is the exit stream from the first stage MSR, and feeds heat exchanger number 5 (JN-HX5) as shown in Figure 3. The HYSYS flow sheet shown in Figure 3 is for Case 1. The HX5 is a high pressure feed water heater which in reality has three feeds as it is divided into three subsections, namely: desuperheater, condenser and drains cooler. In this work, the models for high pressure FWHs were simplified by mixing all the feeds into one inlet stream. This destroys some of the available energy from high quality steam. But is left as an opportunity to improve the model performance in simulating the ACR-1000 BOP. The stream temperature, pressure and vapour content for "From NPP" are 275 °C, 5.8 MPa and 1, respectively, and for "To NPP" are 264 °C, 5.7 MPa and 0, respectively.

Case 2: HTSEP in Figure 2 is connected between S6 and L1 in Figure 3. Stream S6 is the inlet stream to the second stage high pressure turbine. S6 is split into three streams - From NPP, S6A and S6B. The stream temperature, pressure and vapour content for "From NPP" are 233 °C, 2.95 MPa and 1, respectively, and for "To NPP" are 232 °C, 2.85 MPa and 0.84, respectively.

Case 3: HTSEP in Figure 2 is connected between S8 and L1 in Figure 3. Stream S8 is the inlet stream to the third stage high pressure turbine. S8 is split into three streams - From NPP, S8A and S8B. The stream temperature, pressure and vapour content for "From NPP" are 222 °C, 2.4 MPa and 1, respectively, and for "To NPP" are 220 °C, 2.3 MPa and 0.86, respectively.

Case 4: HTSEP in Figure 2 is connected between S7 and S13B in Figure 3. Stream S7 is the outlet stream from the third stage high pressure turbine. The stream temperature, pressure and vapour content for "From NPP" are 180 °C, 1 MPa and 0.955. respectively. and for "To NPP" are 175 °C, 0.9 MPa and 0.91, respectively.

4.1 Thermal Efficiency Definitions

There are a number of different expressions that can be used to calculate the thermal efficiency of integrated systems such as NPP and HTSEP [17]. There are efficiency expressions found in the literature that consider the distinction between electrical and thermal energy while others ignore it [17, 18]. Thus, it is critical to clearly define the efficiency values quoted. This work considers three possible definitions for thermal energy conversion efficiency.
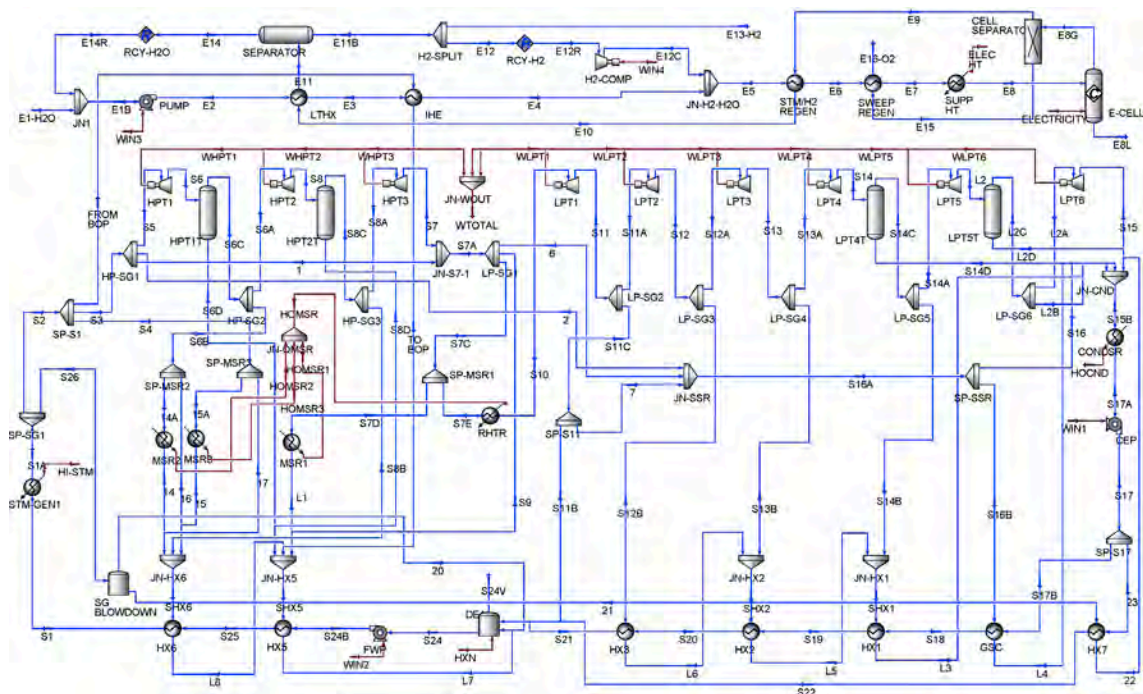
FIGURE 3: HYSYS flow sheet model of the NPP integration with an HTSEP (Case 1).

AECL NUCLEAR REVIEW
VOL 2, NUMBER 1, JUNE 2013

HYDROGEN CO-PRODUCTION FROM SUBCRITICAL WATER-COOLED NUCLEAR POWER PLANTS IN
CANADA - N. GNANAPRAGASAM, D. RYLAND AND S. SUPPIAH

Electrical efficiency (NPP only): This is the thermal-to-electrical efficiency and is the ratio of total amount of work produced at the turbines to the total thermal energy available at the steam generator and accounting for any other energy inputs. This scenario assumes that all the turbine work output is converted into electricity and sent to the electrical grid. This is the thermal efficiency of the NPP alone.

$$\eta_{el} = \frac{\dot{W}_{out.NPP} - \dot{W}_{in.NPP}}{\dot{Q}_{in.NPP}} = \frac{Output}{Input}$$

(2)

In the above equation, $\dot{W}_{out.NPP}$ is the total work output from all the turbines in the NPP, $\dot{W}_{in.NPP}$ is the total work input to the pumps in NPP and $\dot{Q}_{in.NPP}$ is the thermal energy input for the NPP available from the nuclear reactor loop.

Hydrogen efficiency (HTSEP only): This is the thermal-to-hydrogen efficiency and is the ratio of thermal energy of product hydrogen to the total thermal and electrical energy transferred to the HTSEP. The thermal energy from product hydrogen is calculated based on the lower heating value (LHV) of hydrogen. The total energy input to HTSEP includes the thermal equivalent of electrical energy to the e-cell and the heater along with any thermal energy transferred from the NPP. This is the thermal efficiency of the HTSEP alone.

$$\eta_{H2} = \frac{LHV \dot{m}_{H2}}{\dot{E}_{HTSEP}/\eta_{el} + \dot{Q}_{inHTSEP} + \dot{W}_{in.HTSEP}/\eta_{el}}$$

(3)

In the above equation, $\dot{m}_{H2}$ is the mass flowrate of hydrogen, LHV is the lower heating value of the hydrogen (119.96 MJ/kg), $\dot{E}_{HTSEP}$ is the electrical energy required by the electrolysis cell and supplementary heaters used in the HTSE process, and $\dot{Q}_{in.HTSEP}$ is the thermal energy provided by the NPP to the HTSEP. Note that the thermal energy conversion of electrical energy used by the HTSEP ($\dot{E}_{HTSEP}$) is calculated at the electrical efficiency of the NPP.

Integrated efficiency (NPP-HTSEP combined): This is the thermal efficiency of the integrated system that produces both electricity and hydrogen simultaneously. It is the ratio of total energy from both products (electricity and hydrogen) minus the electrical energy used by the HTSEP to the total thermal energy input for the integrated system and accounting for any other energy inputs. This scenario assumes that the integrated NPP-HTSEP system produces hydrogen by using both heat and electricity from the NPP and also sends electricity to the grid.

$$\eta_{el.H2} = \frac{Derived\ energy - Consumed\ energy}{Heat\ energy\ input}$$

$$\eta_{el.H2} = \frac{(\dot{W}_{out.NPP} + LHV \dot{m}_{h2}) - (\dot{E}_{HTSEP} + \dot{W}_{in.NPP} + \dot{W}_{in.HTSEP})}{\dot{Q}_{in.NPP}}$$

(4)

5. Results and Discussion

Results from HYSYS flow sheet models for each case have been analyzed for reactor NPP, HTSEP and integration of both. The results are discussed in four sections comparing NPP performance with and without integration to HTSEP. The last section compares this work's results with that of another work reporting similar integration of a next-generation nuclear reactor power cycle to a modified HTSEP.

5.1 Comparison of Integration Cases of NPP-HTSEP

Table 1 provides an energy summary of the NPP, HTSEP and NPP-HTSEP integration cases. The electrical efficiency of the NPP only is about 36%. This is typical for a subcritical water Rankine cycle, and there is very little that can be done to improve this efficiency. The turbines are the second-most-expensive component in NPP and thus are optimized to run at full capacity. When steam is diverted to the HTSEP from the existing NPP, less diversion is always better.

Harvego *et al.* [19] provided a comparison of advanced nuclear reactors capable of operating at reactor outlet temperatures of 600 to 900 °C and found that the hydrogen production efficiencies could range between 25 and 55%. For comparison, the best hydrogen-production efficiencies range from 60 to 80% [20] depending on the system design
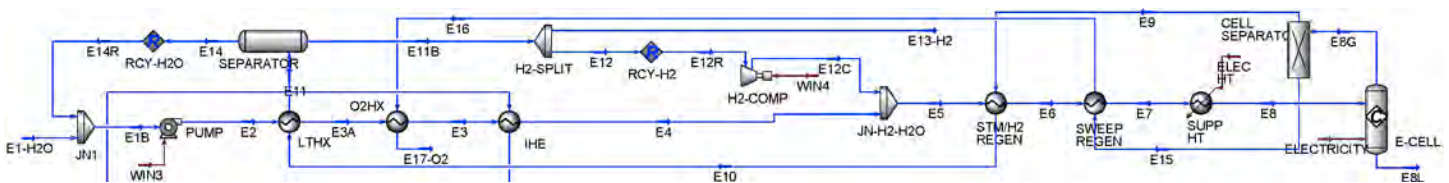
FIGURE 4: HYSYS flow sheet model of modified HTSEP that has additional heat recuperation.

AECL NUCLEAR REVIEW
VOL 2, NUMBER 1, JUNE 2013

HYDROGEN CO-PRODUCTION FROM SUBCRITICAL WATER-COOLED NUCLEAR POWER PLANTS IN
CANADA - N. GNANAPRAGASAM, D. RYLAND AND S. SUPPIAH

TABLE 1: Analysis of NPP-HTSEP Integration Points

NPP-HTSEP integration point cases	NPP	Case 1	Case 2	Case 3	Case 4
NPP energy summary					
Thermal Energy (MW)					
INPUT: from steam generator	3295	3295	3295	3295	3295
REJECTED: by the condenser	1879	1879	1844	1840	1876
Work (MW)					
INPUT: to CEP	1	1	1	1	1
INPUT: to FWP	13	13	13	13	13
OUTPUT: from all turbine stages	1234	1234	1215	1214	1234
Key Temperatures (C)					
High pressure turbine inlet	275	275	275	275	275
Low pressure turbine inlet	266	266	266	266	266
Electricity Efficiency	**36.3%**	**36.3%**	**35.7%**	**35.7%**	**36.3%**
HTSEP energy summary					
Thermal Energy (MW)					
INPUT: from NPP		46	8	7	3
INPUT: E-cell electricity (thermal equivalent)		740	752	753	740
INPUT: supplementary electrical heating (thermal equivalent)		14	121	124	134
OUTPUT: product hydrogen (LHV)		262	262	262	262
Work (MW)					
INPUT: to feed water pump		0.14	0.14	0.14	0.14
INPUT: to hydrogen compressor		0.29	0.29	0.29	0.29
Stream parameters for E4 in Figure 2					
Temperature (C)		274	233	222	180
Vapour fraction		1	0	0	0
Hydrogen Efficiency		**32.7%**	**29.7%**	**29.6%**	**29.8%**
NPP-HTSEP energy summary					
Thermal contribution from NPP to HTSEP		6.2%	1.0%	0.8%	0.3%
Electrical contribution from NPP to HTSEP		22%	26%	26%	26%
Integrated Efficiency		**35.9%**	**34.2%**	**34.1%**	**34.6%**

Based on hydrogen plant size of 190 tonne per day

TABLE 2: Stream Conditions for HTSEP
from HYSYS Model for Case 1

Streams in Figure 2	Vapor fraction	Temperature	Pressure	Mass flow rate
		°C	kPa	tonne·h⁻¹
E1 (H$_2$O)	0	20	101	70
E2	0	21	5401	74
E3	0	149	5381	74
E4	1	274	5361	74
E5	0.9945	262	5361	75
E6	1	675	5341	75
E7	1	730	5321	75
E8	1	826	5311	75
E9	1	826	5249	13
E10	1	265	5229	13
E11	0.9508	25	5209	13
E12	1	25	5199	1
E13 (H$_2$)	1	25	5199	8
E14	0	25	5199	4
E15	1	826	5249	62
E16 (O$_2$)	1	675	5229	62
From NPP	1	275	5800	100
To NPP	0	264	5700	100

prevalent in the steam-methane reforming industry. For a steam generator outlet temperature of 275 °C the Sub-WCR NPP-HTSEP has hydrogen efficiency of 37.8% which is in the middle of the range estimated by Harvego *et al*. [19]. Thus, energy storage using hydrogen is not simply an option for high-temperature plants, but could be an opportunity even for existing subcritical water-based NPPs including CANDU stations. The reason for this, as we shall see from the examinations below, is that most of the heat requirement stems from the absorption of latent heat, and not from the heating of steam to the higher temperatures needed for steam electrolysis.

When an HTSEP is integrated with a NPP, the electricity used by the electrolyser is up to 22% of the total electricity produced by the NPP (for Case 1 in Table 1). In contrast, the thermal energy contribution is a small fraction of this. The thermal contribution to the HTSEP in Table 1 is the ratio of thermal energy from the NPP to the total electrical energy input to the HTSEP. The electrical contribution from the NPP to the HTSEP in Table 1 is the ratio of electrical energy used by HTSEP to the total electrical energy output from the NPP. A 6% thermal contribution and 22% electrical contribution for Case 1 suggests that the electrical efficiency of the NPP is crucial for the integrated system as slight improvements in it can significantly improve the overall efficiency. For this reason, flow rate of diverted steam ("From NPP" in Table 2) has been kept to a minimum to maximize efficiency. Lower flow rates would affect the quality of stream entering the steam/hydrogen regenerator.

Among the four integration cases examined, Case 1 has the highest hydrogen production efficiency of 32.7% and the highest integrated efficiency of 35.9% (Table 1). Case 1 has an inherent advantage, in that the saturation temperature of the steam at E4 (in Figure 2) is just above the boiling point of the HTSEP feed water, allowing efficient heat transfer. The other three cases, in contrast, require electrical energy to boil the feed water. Unless the feed water pressure is reduced, which would require adding a compressor for the product hydrogen, these three integration points are inherently less efficient. Comparing the integration points, diverting steam before the first stage turbine (as shown in Figure 3) gives the best performance for HTSEP while slightly reducing the NPP efficiency. The supplementary electrical heating for Case 1 was 14 MW, while for the other three cases it was above 120 MW due to the absorption of latent heat. Thus, we have taken Case 1 as the base case.

AECL NUCLEAR REVIEW
VOL 2, NUMBER 1, JUNE 2013

HYDROGEN CO-PRODUCTION FROM SUBCRITICAL WATER-COOLED NUCLEAR POWER PLANTS IN
CANADA - N. GNANAPRAGASAM, D. RYLAND AND S. SUPPIAH

TABLE 3: Analysis of HTSEP Operating
Conditions on NPP-HTSEP Performance

HTSEP operating condition cases	A1	A2	A3	A4
A1: hydrogen production rate (tonne/day)	94	189	189	189
A2: product hydrogen pressure (MPa)	5.2	10.4	5.2	5.2
A3: additional recuperation from oxygen stream	None	None	Yes	None
A4: temperature of electrolysis cell (C)	826	826	826	60*
NPP energy summary				
Thermal Energy (MW)				
INPUT: from steam generator	3295	3295	3295	3295
REJECTED: by the condenser	1879	1879	1879	1879
Work (MW)				
INPUT: to CEP	1	1	1	1
INPUT: to FWP	13	13	13	13
OUTPUT: from all turbine stages	1234	1234	1234	1234
Electricity Efficiency	**36.3%**	**36.3%**	**36.3%**	**36.3%**
HTSEP energy summary				
Thermal Energy (MW)				
INPUT: from NPP	23	16	38	0
INPUT: E-cell electricity (thermal equivalent)	370	742	740	851
INPUT: supplementary electrical heating (thermal equivalent)	7	105	15	0
OUTPUT: product hydrogen (LHV)	131	262	262	262
Work (MW)				
INPUT: to feed water pump	0.07	0.29	0.14	0.14
INPUT: to hydrogen compressor	0.15	0.01	0.01	0.65
Stream parameters for E4 in Figure 2				
Temperature (C)	274	274	274	35
Vapour fraction	1	0	1	0
E-cell calculations				
Hydrogen flow rate (kmol/h)	1953	3902	3902	3904
E-cell electricity (MW)	134	269	269	309
Cell voltage (V)	1.28	1.29	1.28	1.48
Cell current (MA) - total cell size	105	209	209	209
Hydrogen Efficiency	**32.7%**	**30.3%**	**33.0%**	**30.7%**
NPP-HTSEP energy summary				
Thermal contribution from NPP to HTSEP	6.2%	1.9%	5.0%	0.0%
Electrical contribution from NPP to HTSEP	11%	25%	22%	25%
Integrated Efficiency	**36.1%**	**34.9%**	**35.9%**	**34.8%**

All modifications in this table are based on case 1 HYSYS flow sheet and conditions

*The e-cell in this case is a low pressure, low temperature cell

TABLE 4: Stream Conditions for HTSEP
from HYSYS Model for Case A3

Streams in Figure 4	Vapor fraction	Temperature °C	Pressure kPa	Mass flow rate tonne·h⁻¹
E1 (H₂O)	0	20	101	70
E2	0	21	5401	74
E3	0	234	5361	74
E4	1	274	5341	74
E5	0.99486	261	5341	75
E6	1	673	5321	75
E7	1	726	5301	75
E8	1	826	5291	75
E9	1	826	5249	13
E10	1	268	5229	13
E11	0.95084	25	5209	13
E12	1	25	5199	1
E13 (H₂)	1	25	5199	8
E14	0	25	5199	4
E15	1	826	5249	62
E16	1	680	5229	62
E17 (O₂)	1	220	5209	62
From NPP	1	275	5800	75
To NPP	0	236	5700	75

5.2 Effect of HTSEP Operating Conditions on NPP-HTSEP Performance

To compare the impact of HTSEP performance on the NPP-HTSEP performance, four cases (A1 to A4) were analysed. The cases are various operating and configuration changes to HTSEP starting from conditions in Case 1. The cases and their corresponding values are listed in Table 3.

Case A1: Since the HTSEP uses a significant amount of electricity from the NPP, if the production of hydrogen is reduced, the electrical contribution from the NPP will be reduced. This is seen in Table 3 for Case A1 with electrical contribution reduced by 50% for a reduction of hydrogen production by 50%. The integrated efficiency increased marginally from 35.9% in Case 1 to 36.1%.

Case A2: Product hydrogen pressure is important if hydrogen is to be stored in large volume in underground caverns and spent oil/gas fields. One way to increase the pressure is by increasing the feed water pump pressure. This in turn, however, increases the boiling temperature of the feed water, which can affect the ability to transfer heat from the NPP to the HTSEP. This is seen in Case A2 (Table 3) where the feed water pressure has been increased to 10 MPa at which the boiling temperature is 311 °C. Because the steam from the steam generator is saturated at 275 °C it is unable to boil the feed water. As a result, the thermal energy contribution to the HTSEP decreased from 6.2% in Case 1 to 1.9%. Thus, the electrical contribution to the supplementary heat exchanger increased from 14 MW in Case 1 to 105 MW. This decreased the hydrogen production efficiency for Case A2 by 8% and the integrated efficiency by 3%. Therefore, increasing the feed water pressure to get higher product pressure is not a realistic approach.

Case A3: The HTSEP shown in Figure 2 provides an idea of heat recuperation from the product hydrogen and oxygen streams after the e-cell through three heat exchangers – LTHX, STM/H2 REGEN and SWEEP REGEN. The product hydrogen comes out at 25 °C and 5.2 MPa. The product oxygen comes out at 675 °C and 5.2 MPa (E16 in Table 2). Recuperation of this heat was considered in Case A3.

Figure 4 shows the HYSYS flow sheet model of the modified HTSEP that includes one more heat exchanger O2HX in between LTHX and IHE. By adding this heat exchanger, the product oxygen temperature is now brought down to 220 °C (E17 in Table 4). The corresponding impact on NPP-HTSEP integration is shown in Table 3 in the Case A3 column. The integrated efficiency is the same while the hydrogen efficiency has gone up slightly to 33%. The significant change is the reduction in thermal energy contribution within HTSEP to 5% from 6% in Case 1. This is due to the reduction in steam flow rate in stream "From NPP" (Table 4) from 100 tonne/h in Case 1 to 75 tonne/h in Case A3.

AECL NUCLEAR REVIEW
VOL 2, NUMBER 1, JUNE 2013

HYDROGEN CO-PRODUCTION FROM SUBCRITICAL WATER-COOLED NUCLEAR POWER PLANTS IN
CANADA - N. GNANAPRAGASAM, D. RYLAND AND S. SUPPIAH

TABLE 5: Analysis of Hydrogen Production
Size on NPP-HTSEP Performance

Hydrogen production size cases	B1	B2	B3	B4
Hydrogen production rate (tonne/day)	20	40	80	160
Mass flow rate of steam from NPP to HTSEP (tonne/h)	8	16.5	31.5	63.3
NPP energy summary				
Thermal Energy (MW)				
INPUT: from steam generator	3295	3295	3295	3295
REJECTED: by the condenser	1879	1879	1879	1879
Work (MW)				
INPUT: to CEP	1	1	1	1
INPUT: to FWP	13	13	13	13
OUTPUT: from all turbine stages	1234	1234	1234	1234
Key Temperatures (C)				
High pressure turbine inlet	275	275	275	275
Low pressure turbine inlet	266	266	266	266
Electricity Efficiency	**36.3%**	**36.3%**	**36.3%**	**36.3%**
HTSEP energy summary				
Thermal Energy (MW)				
INPUT: from NPP	4	8	16	32
INPUT: E-cell electricity (thermal equivalent)	79	159	312	627
INPUT: supplementary electrical heating (thermal equivalent)	2	3	6	13
OUTPUT: product hydrogen (LHV)	28	56	111	222
Work (MW)				
INPUT: to feed water pump	0.02	0.03	0.06	0.12
INPUT: to hydrogen compressor	0.00	0.00	0.01	0.01
E-cell calculations				
Hydrogen flow rate (kmol/h)	419	837	1646	3305
E-cell electricity (MW)	29	58	113	227
E-cell voltage (V)	1.28	1.28	1.28	1.28
E-cell current (MA) - total cell size	22	45	88	177
Hydrogen Efficiency	**33.0%**	**33.0%**	**33.0%**	**33.0%**
NPP-HTSEP summary				
Thermal contribution from NPP to HTSEP	5.1%	5.0%	5.0%	5.0%
Electrical contribution from NPP to HTSEP	2%	5%	9%	19%
Integrated Efficiency	**36.2%**	**36.2%**	**36.1%**	**36.0%**

All modifications in this table are based on case A3 HYSYS flow sheet and conditions

Case A4: The high temperature electrolysis has a major electrical advantage over low temperature electrolysis in that the thermo-neutral potential (the potential at which the cell operates adiabatically) is lower. This is seen in the "E-cell voltage" row in Table 3. The low pressure (1 MPa) and low temperature (60 °C) cell in Case A4 requires 1.48 volts which is about 15% higher than the HTSE cell in cases A1 to A3. Another advantage of an HTSE cell is the utility of the resistive heat produced by the passage of electrical current through the cell; in a low temperature cell this resistive heat is not very usable. Thus the hydrogen efficiency of the low temperature cell is about 6.5% lower and the integrated efficiency is about 3% lower than Case 1.

5.3 Effect of Hydrogen Production Size on NPP-HTSEP Performance
To compare the impact of HTSEP performance on the NPP-HTSEP performance, four cases (B1 to B4) of increasing hydrogen production rate were analysed starting from the conditions in Case A3. The cases and their corresponding values are listed in Table 5.

Earlier in Case A1 the effect of lower hydrogen production rate gave an improved integrated efficiency. Table 5 with

values of cases B1 to B4 provides an extended assessment of Case A1. The lowest hydrogen production (20 tonnes per day, arbitrarily chosen to show the effect of incrementally increasing the production size) gives the best integrated efficiency (only slightly better than A3) since it only consumes 2% of electrical energy produced by the NPP. By doubling the hydrogen production size, the integrated efficiency was reduced proportionately and the electrical consumption more than doubled. It should be noted that the stream flow rate "From NPP" increased with hydrogen production (in cases B1 to B4 in Table 5) as required to maintain the steam conditions at stream E4.

The hydrogen production using HTSEP provides a compelling opportunity for using off-peak electricity mainly from nuclear power plants. To obtain the maximum power output and ensure full utilization of the fissile material, nuclear power plants need to operate at full capacity. In a demand-sensitive electrical grid, it is ideal to implement energy storage technologies when the demand is lower at certain hours of the day. The electrical storage can be done at scale by producing hydrogen using the HTSE process and storing it until demand arises. Hydrogen can be produced by diverting small amounts of electricity (2% as in Case B1) and heat (5% as in Case B1) from the NPP to the HTSEP during periods of less demand from the grid. An economic analysis would be required to choose an ideal hydrogen production size.

From the integrated efficiency values in Table 5, it is clear that the operating cost of the HTSEP (if a cost is associated with electricity used by the HTSEP) will be lowest for Case B1. Hydrogen produced using HTSEP is a useful commodity in the energy market when combined with ideal short-term small-volume energy storage options such as tank farms or natural gas pipeline networks. When coupled with a fuel cell plant, hydrogen stored in the tank farms can be converted back to electricity. The hydrogen stored in natural gas pipeline networks [21] would be consumed along with natural gas in industrial and residential applications. Thus, the NPP-HTSEP integration would be an asset for a smart

TABLE 6: Performance Comparison of HTSEP
Integration with Sub-WCR NPP and HTGR NPP

	Sub-WCR-HTSEP (this work)	HTGR-HTSEP [22]
Hydrogen production efficiency (%)	33	40.4
Rankine cycle power conversion efficiency (%)	36	40
Heat exchange point pressure (MPa)	5.1	5.8
Heat exchange point temperature (°C)	275	650
Reactor thermal energy output (MW)	3295	600
Dedicated to electricity/hydrogen	Both	Hydrogen
Possible location	In Canada	In USA

AECL NUCLEAR REVIEW
VOL 2, NUMBER 1, JUNE 2013

HYDROGEN CO-PRODUCTION FROM SUBCRITICAL WATER-COOLED NUCLEAR POWER PLANTS IN
CANADA - N. GNANAPRAGASAM, D. RYLAND AND S. SUPPIAH

electricity grid – one that balances electricity distribution from base-load power plants, off-peak sources and energy storage facilities.

Comparison with another Advanced NPP Concept with HTSEP Integration

Similar integration of a reference HTSEP into a high temperature gas-cooled nuclear reactor (HTGR) has been reported by Harvego et al. [22] from Idaho National Laboratory. This helium-cooled reactor, with 7 MPa pressure and 750 °C at the outlet, is linked to a subcritical steam power cycle. Integration of an HTGR with an HTSEP is done through an intermediate helium loop, between the primary helium loop and the Rankine cycle loop, linked by two steam generators. This is done as an added barrier to minimize potential tritium (a radioactive isotope of hydrogen formed within the reactor) migration from the primary helium loop and to avoid tritium contamination to the HTSEP product hydrogen. Tritium migration is not an issue for the Sub-WCR NPP as it is an indirect steam cycle. Key parameters are compared in Table 6.

The purpose of the present work was to assess process conditions for co-production of hydrogen using a CANDU reactor concept in Canada, while that of the HTGR-HTSEP model is to assess process conditions for producing hydrogen using Generation IV nuclear reactors [23] to be deployed in the USA. It should be noted that the HTSEP used by Harvego *et al.* [22] is a slightly different system, with more thermal recuperation from the oxygen stream and a sweep gas arrangement that permits mixing of the oxygen stream with inert gas to reduce fire hazards. The size of the HTGR in Table 6 is smaller than a typical CANDU power reactor because the HTGR is a reactor dedicated for hydrogen production, while the Sub-WCR NPP (with a minimum of four reactor units) considered in this work is intended for co-production of hydrogen with electricity being the main product.

6. Conclusions and Recommendations

Some useful conclusions drawn from this work toward hydrogen co-production using heat and electricity from subcritical water-cooled nuclear power plants include:

- Existing Sub-WCR NPPs with 36% electrical efficiency are suitable for hydrogen co-production. The production size is to be determined based on a given scenario and corresponding economic assessment.
- Integration of the HTSEP with higher-temperature NPPs having higher electrical efficiencies improves the HTSEP efficiency by increasing the thermal contribution and reducing the electrical contribution, while at the same time improving the efficiency for energy conversion to electricity. An extension of the analysis done in this work to a Generation IV Supercritical Water Reactor

will illustrate this effect more clearly.
- The efficiency of hydrogen production by the HTSEP is proportional to the thermal energy contribution from the NPP.
- Increasing feed-water pressure to obtain high-product hydrogen pressure will negatively impact the hydrogen production efficiency as the boiling temperature of water increases with pressure.

An economic analysis of the integration of a Sub-WCR NPP with an HTSEP considering off-peak electricity would provide further evidence that the HTSEP is a viable process in the long-term for effective energy storage.

REFERENCES

[1] G.F. Naterer, S. Suppiah, L. Stolberg, M. Lewis, Z. Wang, V. Daggupati, K. Gabriel, I. Dincer, M.A. Rosen, P. Spekkens, S.N. Lvov, M. Fowler, P. Tremaine, J. Mostaghimi, E.B. Easton, L. Trevani, G. Rizvi, B.M. Ikeda, M.H. Kaye, L. Lu, 2010, "Canada's Program On Nuclear Hydrogen Production And The Thermochemical Cu–Cl Cycle", International Journal of Hydrogen Energy 35(20), pp. 10905-10926.

[2] J.E. O'Brien, M.G. McKellar, E.A. Harvego and C.M. Stoots, 2010, "High-temperature electrolysis for large-scale hydrogen and syngas production from nuclear energy – summary of system simulation and economic analyses", International Journal of Hydrogen Energy 35(10), pp. 4808-4819.

[3] G. Cerri, C. Salvini, C. Corgnale, A. Giovannelli, D.L. Manzano, A.O. Martinez, A. Duigou, J-M. Borgard, and C. Mansilla, 2010, "Sulfur–Iodine Plant For Large Scale Hydrogen Production By Nuclear Power", International Journal Of Hydrogen Energy 35(9), pp. 4002-4014.

[4] D. Steward, G. Saur, M. Penev, and T. Ramsden, November 2009, "Lifecycle Cost Analysis Of Hydrogen Versus Other Technologies For Electrical Energy Storage", Technical Report, National Renewable Energy Laboratory, DOE. NREL/TP-560-46719.

[5] R. Peters and L. O'Malley, 2008, "Storing Renewable Power", the Pembina Institute, ISBN 1-897390-15-7. Available at URL: http://pubs.pembina.org/reports/StoringRenewablePower-jun17.pdf.

[6] Hydrogenics, "Hydrogenics Announces Agreement with Enbridge to Develop Utility Scale Energy Storage in North America" News release dated April 20, 2012. Available from URL: http://www.hydrogenics.com/about-the-company/news-updates/2012/04/20/hydrogenics-announces-agreement-with-enbridge-to-develop-utility-scale-energy-storage-in-north-america.

[7] M.W. Melaina, O. Antonia and M. Penev, March 2010, "Blending Hydrogen into Natural Gas Pipeline Networks: A Review of Key Issues" National Renewable Energy Laboratory, DOE, Technical report: NREL/TP-5600-51995.

[8] K. Gillingham, January 2007, "Hydrogen Internal Combustion Engine Vehicles: A Prudent Intermediate Step or a Step in the Wrong Direction?" Stanford University.

[9] US Department of Energy, November 2010, "Hydrogen and Fuel Cell Technologies Program: Fuel Cells", Fact sheet, EERE Information Center.

[10] S.D. Stephens-Romero, T.M. Brown, J.E. Kang, W.W. Recker and G.S. Samuelsen, 2010, "Systematic planning to optimize investments in hydrogen infrastructure deployment", International Journal of Hydrogen Energy 35(10), pp. 4652-4667.

[11] G.J. Offer, D. Howey, M. Contestabile, R. Clague and N.P. Brandon, 2010, "Comparative analysis of battery electric, hydrogen fuel cell and hybrid vehicles in a future sustainable road transport system", Energy Policy 38(1), pp. 24-29.

[12] C.M. Stoots, J.E. O'Brien, K.G. Condie and J.J. Hartvigsen, 2010, "High-temperature electrolysis for large-scale hydrogen production from nuclear energy - Experimental investigations", International Journal of Hydrogen Energy 35(10), pp. 4861-4870.

[13] D.K. Ryland, H. Li and R.R. Sadhankar, 2007, "Electrolytic Hydrogen Generation Using CANDU Nuclear Reactors", International Journal of Energy

AECL NUCLEAR REVIEW
VOL 2, NUMBER 1, JUNE 2013

HYDROGEN CO-PRODUCTION FROM SUBCRITICAL WATER-COOLED NUCLEAR POWER PLANTS IN
CANADA - N. GNANAPRAGASAM, D. RYLAND AND S. SUPPIAH

Research 31(12), pp. 1142-1155.

[14] Atomic Energy of Canada Limited, January 2010, "ACR-1000, Technical Description Summary, AECL report 10820-01372-230-002, Rev.1.

[15] Aspen HYSYS, 2009. Operations Guide. Aspen Technology Inc., Burlington MA.

[16] R.B. Duffey, I. Pioro, X. Zhou, U. Zirn, S. Kuran, H. Khartabil and M. Naidin, "Supercritical Water-Cooled Nuclear Reactors (Scwrs): Current And Future Concepts - Steam Cycle Options", 16th International Conference on Nuclear Engineering, ICONE-16, Orlando, Florida, USA, May 11-15, 2008, paper ICONE16-48869.

[17] H. Zhang, G. Lin and J. Chen, 2010, "Evaluation and Calculation on the Efficiency of a Water Electrolysis System for Hydrogen Production", International Journal of Hydrogen Energy 35(20), pp. 10851-10858.

[18] B. Yildiz and M.S. Kazimi, 2006, "Efficiency of Hydrogen Production Systems Using Alternative Nuclear Energy Technologies", International Journal of Hydrogen Energy 31(1), pp. 77-92.

[19] E.A. Harvego, M.G. McKellar, J.E. O'Brien and J.S. Herring, 2009, "Parametric Evaluation Of Large-Scale High-Temperature Electrolysis Hydrogen Production Using Different Advanced Nuclear Reactor Heat Sources", Nuclear Engineering and Design 239(9), pp. 1571-1580.

[20] J.C. Molburg and R.D. Doctor, "Hydrogen From Steam-Methane Reforming With CO_2 Capture", 20th Annual International Pittsburgh Coal Conference, Pittsburgh, Pennsylvania, USA, September 15-19, 2003.

[21] J. Cargnelli, "Bridging Power and Gas Grids", IPHE Roundtable Meeting, Berlin, Germany, 17 November 2011.

[22] E.A. Harvego, J.E. O'Brien and M.G. McKellar, "Analysis Of Improved Reference Design For A Nuclear-Driven High Temperature Electrolysis Hydrogen Production Plant", 2nd International Meeting of the Safety and Technology of Nuclear Hydrogen Production, Control and Management (2IST-NH2), June 2010.

[23] US Department of Energy's Nuclear Energy Research Advisory Committee, December 2002, "A technology Roadmap For Generation Iv Nuclear Energy Systems", Report GIF-002-00.

Fouling of Nuclear Steam Generators: Fundamental Studies, Operating Experience and Remedial Measures Using Chemical Additives

C.W. Turner*

Atomic Energy of Canada Limited, Chalk River Laboratories, Chalk River, Ontario, Canada, K0J 1J0

*Corresponding author: (613) 584-3311, turnerc@aecl.ca

Fouling remains a potentially serious issue that if left unchecked can lead to degradation of the safety and performance of nuclear steam generators (SGs). It has been demonstrated that the majority of the corrosion product transported with the feed water to the SGs accumulates in the SG on the tube-bundle. By increasing the risk of tube failure and acting as a barrier to heat transfer, deposit on the tube bundle has the potential to impair the ability of the SG to perform its two safety-critical roles: provision of a barrier to the release of radioactivity from the reactor coolant and removal of heat from the primary coolant during power operation and under certain post accident scenarios. Thus, it is imperative to develop improved ways to mitigate SG fouling for the long-term safe, reliable and economic performance of nuclear power plants (NPPs). This paper provides an overview of our current understanding of the mechanisms by which deposit accumulates on the secondary side of the SG, how this accumulation affects SG performance and how accumulation of deposit can be mitigated using chemical additives to the secondary heat-transport system. The paper concludes with some key questions that remain to be addressed to further advance our knowledge of deposit accumulation and how it can be controlled to maintain safe, economic performance of nuclear SGs.

Nomenclature

Upper Case

A	Surface area of SG tube-bundle (m^2)
A_{site}	Surface area of a bubble nucleation site (m^2)
BD	Blow down mass flow rate (kg/s)
C	Mass fraction of material in suspension (or solution) (kg/kg)
E	Activation energy (Joule/mole)
D	Pipe diameter (m)
D'	Particle diffusion coefficient (m^2/s)
F	Force (Nt)
K	Mass transfer velocity (m/s)
M	Mass of liquid in a Recirculating Steam Generator (kg)
N_{active}	Active nucleation site density (m^{-2})
R	Universal gas constant (Joule/mole K)
Re	Reynolds Number = (DU/v)
Sc	Schmidt Number = (v/D')
T	Temperature (K), (°C)
U	Velocity (m/s)
U*	Friction velocity (= $0.199U/Re0.125$) (m/s)

Lower Case

h	Heat-transfer coefficient (W/m^2 °C)
m	Deposit mass (kg/m^2)
m'	Number of turbulent bursts per unit area (m^{-2})
t	Time (s)

Subscript

a	Attachment
b	Bulk
d	Deposition (or deposit)
D	Drag
f	Fluid
L	Lift
p	Particle
r	Removal
s	Surface
t	Transport

Greek

ρ	Density (kg/m^3)
v	kinematic viscosity (m^2/s)

AECL NUCLEAR REVIEW
VOL 2, NUMBER 1, JUNE 2013

FOULING OF NUCLEAR STEAM GENERATORS: FUNDAMENTAL STUDIES, OPERATING
EXPERIENCE AND REMEDIAL MEASURES USING CHEMICAL ADDITIVES - C.W. TURNER

1. Introduction

The function of the steam generator (SG) in an indirect cycle nuclear-power plant (NPP) is to generate steam from the nuclear heat produced by fission reactions in the core during operation at power, and to act as a heat sink to remove decay-heat from fission products during both normal reactor shut down and for a post accident scenario in the event that reactor-core cooling has been impaired. Situated at the boundary between the nuclear (radioactive primary coolant system) and conventional (non-radioactive secondary coolant system) sides of the plant, the SG plays two safety-critical roles:

1. Provides a barrier to prevent the release of radioactivity from the primary reactor coolant to the secondary coolant where it can be released to the environment; and,
2. Removes heat from the primary coolant to the secondary coolant to maintain a safety margin during power operation and some post accident scenarios.

Thus, the integrity of the SG and its internal components is vital for assuring both the safety and the performance of the NPP [1, 2].

Despite improvements in materials, designs and water chemistry, degradation affecting the safety and performance of the SG continues to be a major concern within the nuclear industry [3, 4]. For example, perforation of the SG tube wall as the result of either outside-diameter stress corrosion cracking (ODSCC), fretting wear or high-cycle fatigue provides a leakage path for radioactive, primary coolant to the secondary side where it can subsequently be released to the environment. Additional inspection and repair activities to ensure the integrity of the SG tube-bundle have a negative economic impact on plant performance, and lead to additional radiation exposure to plant personnel. Every SG design has a multitude of crevices at the tube/tube-support intersections which, when partially filled with deposit, become concentration sites for impurities which, in turn, increases the risk of ODSCC. Understanding the relationships between deposit accumulation, the development of aggressive chemistry environments and the impact of these environments on the risk of ODSCC must remain a key focus area for the industry, especially in light of the 60-plus year lifetimes that are now expected for SGs to meet the economic needs of NPPs. Recent tube failures in some Electricité de France (EdF) plants were caused by high-cycle fatigue related to flow re-distribution and tube lock up in the tube-support structure of the SG. Remedial measures included chemical cleaning of all the affected SGs in the fleet at significant cost to the utility. The accumulation of deposit on the tube-bundle[1] and tube-support[2] structure is also a concern with respect to its impact on the thermal-hydraulic performance of the SG. Heavy deposit on the tube-bundle has contributed to a loss of thermal performance during power operation at some NPPs as well as other operational problems, such as density-wave oscillations in the SGs, which could only be remediated by chemical cleaning to remove the accumulated deposit.

Almost without exception, the degradation that affects the safety and performance of the SG is related in one way or another to the accumulation of deposit on various components on the secondary-side of the SG, e.g., the tube-bundle, tube-support structure, tube-sheet and steam separators. A corollary of this statement is that a properly designed SG should not fail by any of the above-mentioned degradation mechanisms provided that the SG remains clean, i.e., free of deposits. Thus, the key to mitigating degradation of the SG is the ability to mitigate the accumulation of unwanted deposit, or fouling, of the surfaces of critical components within the SG.

This paper provides an overview of the current understanding of the mechanisms by which deposit accumulates on the secondary side of the SG, how this accumulation affects SG performance and how accumulation of deposit can be mitigated using chemical additives to the secondary heat transport system. The paper concludes with some key questions that remain to be addressed to further advance our knowledge of deposit accumulation and how it can be controlled to maintain safe, economic performance of nuclear SGs.

2. Nuclear Steam Generators: Design and Operating Experience

2.1 Nuclear SG Design

The SGs used in pressurized-water reactors (PWRs) are large tube-in-shell heat exchangers that use heat from the primary reactor-coolant system to generate steam in the secondary system to drive the turbine generators. Two designs of SG in use at NPPs in Asia, Western Europe and the Americas are the vertical U-tube Recirculating Steam Generator (RSG) and the vertical Once-Through Steam Generator (OTSG) illustrated in Figures 1 and 2, respectively. Russian-designed pressurized water reactors use a horizontal SG design, as shown in Figure 3, which has been implemented in plants built in Russia and in Eastern Europe [5]. The SGs at AECL's Nuclear Power Demonstration (NPD) plant, which was commissioned in 1962, were also a horizontal design.

---

[1] Precipitation fouling on the inside surface of the tube bundle as a result of the use of carbon steel for the feeder pipes and reactor coolant piping also leads to a loss of thermal performance in CANDU SGs. Precipitation fouling from the primary coolant will not be reviewed in this report.

[2] The one obvious exception is fretting wear associated with an improperly designed tube support structure, which can cause high tube-failure rates resulting from an excessively high fretting wear rate early in the life of the SG.

AECL NUCLEAR REVIEW
VOL 2, NUMBER 1, JUNE 2013

FOULING OF NUCLEAR STEAM GENERATORS: FUNDAMENTAL STUDIES, OPERATING
EXPERIENCE AND REMEDIAL MEASURES USING CHEMICAL ADDITIVES - C.W. TURNER

For all nuclear SGs, the primary reactor coolant flows on the inside of the SG tubes and boils water, i.e., the secondary coolant, on the outer surface, or shell side, of the tubes. In the vertical RSG design, feed water enters the SG either through a feed ring at the top of the tube-bundle or via an integral preheater located at the base of the cold-leg, as shown in Figure 1. The feed water is mixed with separated water from the steam separators, and then flows up through the tube nest where steam is generated. About 25 wt.% of the water is converted to steam on a single pass through the tube nest. The remainder is separated from the steam-water mixture in the steam separators and recirculated through the tube nest via the down comer, while the separated steam is sent to the turbine generator. A small flow of water known as blow down, corresponding to 1% or less of the main steam mass flow rate, is removed from the SGs on a continuous basis to limit the build up of impurities in the recirculating water. In the OTSG design (see Figure 2), the secondary water enters the SG at about the tenth tube-support plate (TSP) and is heated while it drains via the down comer to the tube-sheet, where it enters the tube nest. The OTSG is divided into two regions: the boiling region between the tube-sheet and the tenth TSP where the feed water is converted entirely to steam, and the super-heater section above the tenth TSP, where the steam is superheated before being sent to the turbine generator. In both the RSG and OTSG designs, after passing through the turbine generator, the steam is condensed and returned to the SGs via a series of feed water heaters that are heated using steam extracted from the high-pressure and low-pressure turbines.

FIGURE 2: Illustration of a vertical Once Through SG (OTSG) (courtesy of Babcock and Wilcox).

For the horizontal SG (see Figure 3), primary coolant enters the SG via a vertical header, flows through the horizontal SG U-tube-bundle and exits via a second vertical header. The inlet and outlet primary-coolant headers perforate the SG shell near the middle of the shell. Feed water is supplied to the shell-side of the tube-bundle at the middle of the tube-bundle via perforated piping under a perforated sheet. The tube-bundle is entirely submerged in the secondary coolant.

2.2 Transport of Corrosion Products to the SGs
An illustration of a typical feed-water-heating system used at a CANDU pressurized heavy-water reactor (PHWR) is shown in Figure 4. The materials of construction for the feed-water-heating system are typically carbon steel for the piping, condenser and heater shells and tube-sheets, stainless steel or titanium for the condenser tubes, stainless steel for the low-pressure (LP) feed water heater tubes and carbon steel for the high-pressure (HP) feed water heater tubes. The condensate that drains from the heater shells is pumped back to either the deaerator storage tank (from the HP heaters and steam re-heater drains) or to the condenser (from the LP heaters) to maximize system thermal efficiency. While maximizing thermal efficiency, this design ensures that corrosion products that are removed from the

FIGURE 1: Illustration of a vertical U-tube Recirculating SG (RSG) for a CANDU 6 NPP.

AECL NUCLEAR REVIEW
VOL 2, NUMBER 1, JUNE 2013

FOULING OF NUCLEAR STEAM GENERATORS: FUNDAMENTAL STUDIES, OPERATING
EXPERIENCE AND REMEDIAL MEASURES USING CHEMICAL ADDITIVES - C.W. TURNER
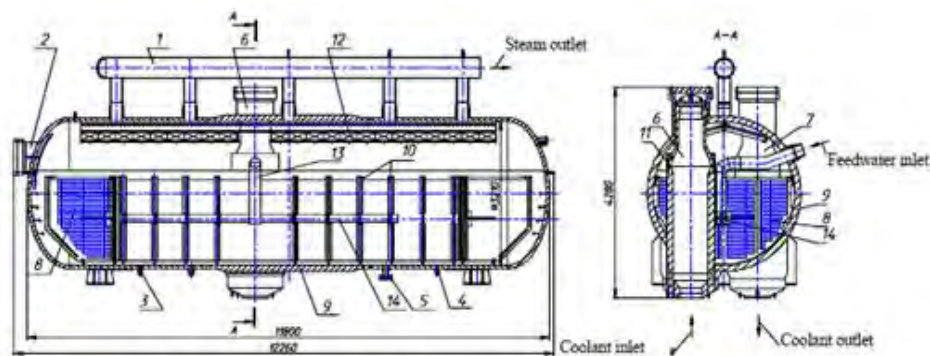
Structure of steam generator PGV-440:
1 – steam header, 2 – hatch-manhole; 3, 4 – blowdown pipe sleeves; 5 – drainage pipe
sleeve; 6, 7 – "hot" and "cold" collectors; 8 – heat exchanging tubes; 9 – steam
generator vessel; 10 – heat exchanging tube bundle supports; 11 – protective housing;
12 – separation blinds; 13 – feed water supply tube; 14 – feed water distribution
collector

FIGURE 3: Illustration of a horizontal SG (OKB Gidropress [5]).
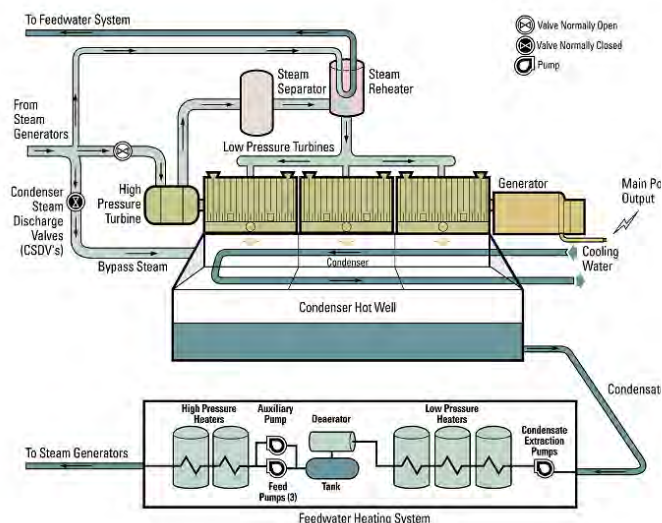
FIGURE 4: Illustration of a typical feedwater heating system in a CANDU pressurized heavy water reactor.

surfaces of carbon-steel piping and components during operation are ultimately transported with the feed water to the SGs where they can accumulate on internal structures such as the tube-bundle, tube-support structure and the tube-sheet. Experience has shown that unless otherwise removed, the accumulation of corrosion products on these internal surfaces will eventually lead to degradation of the safety and performance of the SGs [6].

The rates of iron transport at various locations of the feed water heating systems of PWRs have been thoroughly investigated by determining the quantity of corrosion product that accumulates on a filter with a nominal pore size of 0.45 μm followed by a cation exchange membrane. These studies have concluded that a majority of the iron (> 90% of the mass) is transported to the SGs in the form of suspended particulate material, with the remainder being a combination of dissolved iron and iron in colloidal form that passes through the 0.45 μm sample filter [7, 8].

Mossbauer analyses of the corrosion products in filtered water removed from various locations of the condensate/ feed water systems of PHWRs find primarily magnetite, hematite and lepidocrocite, with goethite appearing in some samples as a minor constituent [7, 9]. Similar analyses of the material filtered from the condensate/ feed water system of PWRs find magnetite and hematite as major constituents, with relatively less lepidocrocite and more goethite than is generally found at PHWRs [9, 10]. Iron transport investigations conducted at RBMK and VVER plants also report magnetite, hematite and lepidocrocite as being the major constituents of the corrosion products filtered from the hot-water systems at these plants [11].

AECL NUCLEAR REVIEW
VOL 2, NUMBER 1, JUNE 2013

FOULING OF NUCLEAR STEAM GENERATORS: FUNDAMENTAL STUDIES, OPERATING
EXPERIENCE AND REMEDIAL MEASURES USING CHEMICAL ADDITIVES - C.W. TURNER

FIGURE 5: Illustrations of different tube support designs used in nuclear SGs [31].

Although the results from corrosion product transport investigations at operating NPPs appear to be relatively consistent from one plant to another, how representative the samples are is still open to question. For example, long sample lines (up to 100 m in length) are used to deliver the sample stream to a centralized collection point, and almost invariably the sample is cooled before passing through the 0.45 μm filter to collect the suspended particles. Sampling nozzles have not necessarily been designed to ensure that the fluid entering the nozzle has the same velocity as the main stream, i.e., to ensure isokinetic sampling [12, 14, 15]. Thus, corrosion products sampled using existing sampling systems at NPPs are subject to the following uncertainties:

1. Precipitation of dissolved iron-on cooling will result in the concentration of dissolved iron in the system being under estimated and the concentration of suspended particulate being over-estimated. Precipitation on cooling may also affect the particle-size distribution of the filtered sample,

2. Anisokinetic sampling could influence the measured concentration and bias the particle size distribution of suspended material in the sample stream. Deposition and removal within the sample lines may affect the concentrations of both dissolved (by dissolution of existing deposit within the sample line) and suspended corrosion product.

Although the uncertainties introduced by anisokinetic sampling can be significant for an aerosol [13], the importance of matching the sample and fluid velocities diminishes when sampling for suspended material in a liquid because the higher viscosity of the fluid makes it more likely for the particle to follow the fluid streamline. For example, simulations of the particle collection efficiency for 1 μm particles of magnetite suspended in 300 °C water and in steam show that the sampling velocity has no discernable influence on the results for velocities ranging from 25% to 175% of the isokinetic velocity for the aqueous system, but results in errors of up to 25% when sampling for those same particles entrained in steam [16]. As expected, the deviat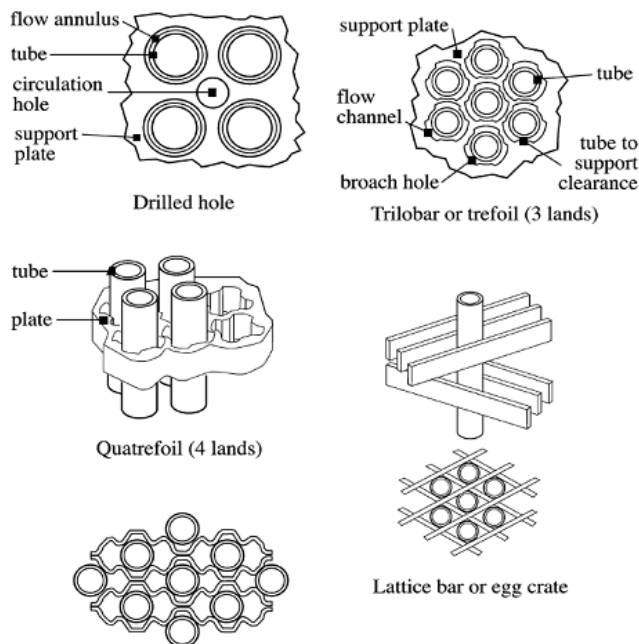ions become more significant with increasing particle size. Measurements of iron transport in the feed water at the Winfrith[3] experimental Steam Generating Heavy Water Reactor (SGHWR) using capillary lines and isokinetic sampling found that dissolved iron constituted only ~ 1 % of the mass of iron transported between the high-pressure feed-water heaters, and ~ 0.5 % of the mass of iron transported in the final feed water [14]. Measurements as a function of sample fluid velocity showed an absence of bias for fluid velocities between 75% and 125% of the isokinetic velocity. Deviations of +22% and -27% were reported for velocities of 30% and 200% of the isokinetic velocity, respectively. A study comparing hot filtration with filtration at ambient temperature using Ag and cellulose membrane filters, respectively, found no significant difference in particle size between the high-temperature and ambient-temperature samples [17]. Interestingly, the concentrations of dissolved iron were relatively consistent from one sample to the next[4], whereas the concentrations of filterable iron were three to six times lower in the samples filtered at ambient temperature compared to hot filtration. Although there are insufficient data to make a strong conclusion, particle deposition on the cooler may account for the lower concentration of filterable material in the sample filtered at ambient temperature[5].

A sampling system to permit isokinetic sampling and hot filtration of particulates in the reactor coolant system of a PWR has been designed and commissioned [18] to provide representative samples to estimate particulate concentrations in the reactor coolant system at Diablo Canyon. The technology does not look complicated, and it would be beneficial if a similar system were implemented to collect more representative samples of corrosion products suspended in the feed-water systems of NPPs.

Based on measurements of corrosion-product transport during steady operation at full power, it is estimated that from 25 to 50 kg of iron are transported to the SGs per

---

[3]The SGHWR was one of several experimental research reactors built at the Winfrith site in the United Kingdom.
[4]The data base from this study is small: three samples filtered hot, of which one was compromised by a torn membrane, and two samples filtered cold. The results from the torn membrane were not used for this analysis.
[5] Particle transport down a temperature gradient leading to deposition on a cold surface is known as thermophoresis, and is discussed later in this review.

AECL NUCLEAR REVIEW
VOL 2, NUMBER 1, JUNE 2013

FOULING OF NUCLEAR STEAM GENERATORS: FUNDAMENTAL STUDIES, OPERATING
EXPERIENCE AND REMEDIAL MEASURES USING CHEMICAL ADDITIVES - C.W. TURNER

year for a plant operating with between 1 and 2 µg/kg of iron in the feed water [6]. An equivalent amount of iron can be transported to the SGs during a single-crud burst during start-up, although this amount can be reduced by circulation and filtration of the secondary coolant prior to heat-up [19]. For comparison, chemical cleaning of the SGs at Point Lepreau Nuclear Generating Station (PLNGS) [20] resulted in the removal of 830 kg of iron from four SGs after 11.7 effective full power years (EFPY) of operation, which corresponds to an annual accumulation rate of 71 kg of iron per year of full-power operation. Chemical cleaning at Gentilly 2 NGS [21] removed 950 kg of iron from four SGs after approximately 18 EFPY of operation, corresponding to an annual accumulation rate of 53 kg iron per year of full-power operation. Most of this deposit would have been removed from the tube-bundle, since both plants water lance the tube-sheets of each SG about once every four years resulting in the removal of about 10 to 20 kg of tube-sheet deposit per campaign.[6]

2.3 Impact of Fouling on the Safety and Performance of Nuclear SGS

Fouling was originally a descriptive term used in the oil industry to refer to the accumulation of undesirable deposit on heat-exchanger surfaces that increases the resistance to heat transmission [22]. The accumulation of corrosion products on the internal surfaces of a nuclear SG can severely degrade SG performance and increase the risk of materials degradation as a result of:

1. Formation of a resistive layer of deposit on the tube surface that could reduce the rate of heat-transfer from the primary to the secondary coolant and decrease the safety margin,
2. Accumulation of ionic impurities to form-concentrated solutions that are aggressive to tube integrity under thick deposits or in deposit filled crevices between the tubes and the tube-support structure,
3. Restriction of the movement of the tubes caused by deposit build-up on the tube-support structure; tube "lock up" leading to high-cycle fatigue,
4. Blockage of the flow passages of the tube-support structure, resulting in several operational and materials degradation problems discussed below, and,
5. Accumulation of a thick sludge pile on the tube-sheet that becomes increasingly consolidated with time, with deleterious consequences for tube integrity.

The formation of a layer of corrosion product on the boiling-side of the SG tube has two separate effects on heat-transfer. The outer porous layer provides additional sites for bubble nucleation and, thus, reduces the wall superheat required for bubble nucleation. This is manifested by an improvement in heat-transfer as the bare tube surface

becomes covered with a thin layer of porous deposit. As deposits grow thicker, however, they develop a layered structure, with a dense inner layer that is resistive to heat-transfer and a porous outer layer that enhances heat-transfer [23]. The net result is that many RSGs show a net improvement in thermal performance during the first few years of operation, followed by a steady deterioration in thermal performance as thicker deposit grows onto the tube-bundle [24]. Other factors, such as changes in primary and secondary coolant flow rates, separator fouling and SG divider plate leakage to name a few, have also been shown to contribute to the degradation of SG thermal performance, and so a systematic approach must be taken to quantify all contributions to thermal performance degradation before taking any remedial action [25, 26].

The accumulation of deposit on the heat-transfer surface also raises the risk of under-deposit corrosion, especially in crevice regions at the tube-sheet, top of the sludge pile and at the tube/tube-support intersections [27] where high concentrations of impurities can accumulate during power operation through a process known as "hideout" [28, 29]. Hideout is driven by the evaporation of liquid within the pores of the deposit. As the liquid within the pores evaporates, it is replaced by fresh solution that is drawn into the deposit by capillarity. The fresh solution brings with it additional non-volatile ionic species, thus increasing the concentration of the solution in the pores. As the concentration of the solution increases, selected compounds will precipitate, depending on their solubility. The pH of the solution that remains in equilibrium with the precipitate is determined by the relative concentrations of ionic species that remain in solution. Thus, the pH in fouled crevice regions and within the pores of thick deposits is not determined by the amine that is added for pH control in the steam cycle. It is ultimately determined by the relative concentrations of soluble impurities that are transported to the SG with the feed water and by the solubilities and compositions of those compounds that precipitate in the crevices under boiling heat-transfer conditions. Electric Power Research Institute (EPRI) and AECL have developed codes to predict the high temperature crevice pH that results from hideout and precipitation of non volatile soluble ionic species based on equilibrium models of crevice chemistry.

This information, combined with measurements of the electrochemical corrosion potential (ECP) of SG tubes in various crevice environments, has been used to establish two-dimensional maps of pH and ECP at 25, 150 and 300 °C where the risk of localized crevice corrosion and pitting of SG tubes is at a minimum [30].

Accumulation of deposit on the SG tube-support structure can lead to both operational problems affecting the

---

[6] A pair of SGs are water lanced to remove tube-sheet deposit every two years, which means that the tube sheet of each SG is water lanced once every four years.

AECL NUCLEAR REVIEW
VOL 2, NUMBER 1, JUNE 2013

FOULING OF NUCLEAR STEAM GENERATORS: FUNDAMENTAL STUDIES, OPERATING
EXPERIENCE AND REMEDIAL MEASURES USING CHEMICAL ADDITIVES - C.W. TURNER

performance of the SG and to degradation of the support structure and the SG tubes. Examples of common tube-support designs used in nuclear SGs are shown in Figure 5 [31]. The trefoil and quatrefoil tube-support plate (TSP) design designs are particularly susceptible to deposit accumulation within the flow-holes of the TSP, which causes an increase in the pressure drop across the TSPs. Flow blockage tends to be higher on the hot-leg side of the SG compared to the cold-leg, and increases in the boiling zone with increasing steam quality. The increased pressure drop across the TSPs has led to flooding of the aspirator ports in OTSGs designed by Babcock and Wilcox [32, 33, 34] and to the onset of density wave oscillations in RSGs of both the Westinghouse [35] and the Babcock and Wilcox [36, 37] designs[7]. In both cases, the short-term remedial solution was to operate the plants at reduced power until such time as the deposit could be removed from the flow passages of the TSPs by either water-slap or chemical cleaning. The SGs at Gentilly-2 also showed early signs of level oscillations prior to chemical cleaning [21].

Blockage of the quatrefoil TSPs in SGs at the Cruas NPP did not lead to density-wave oscillations, but instead to a re-distribution of flow in the upper-bundle region that caused flow-induced vibration (FIV) that was outside of the design basis of the SG. FIV ultimately resulted in failure of some tight-radius SG tubes by high cycle fatigue [38], [39]. The problem was exacerbated somewhat by the SG design which included a tube-free region in the centre of the bundle. Interestingly, the heavy TSP blockage did not manifest itself in the onset of a density-wave oscillation, as observed in other RSGs with blocked trefoil or quatrefoil TSPs. However, thermal-hydraulic analyses concluded that the SGs were susceptible to the onset of a density-wave oscillation in response to certain transients, such as a 10% step in reactor power. A subsequent investigation concluded that the tube failures were caused by a combination of: 1) Blockage of the flow-holes of the quatrefoil TSPs that caused the steam/water mixture to be re-directed towards tubes near the centre of the bundle with small-radius bends, and 2) Tube lock-up, resulting from heavy fouling of the tube-TSP intersections, which increased the local stress intensity of the tubes.

Partial blockage of the trefoil TSPs on the hot-leg and extensive degradation of the carbon-steel TSPs on the cold-leg was identified in 2004 by a visual inspection of the SGs at the Embalse NPP [40, 41]. The degradation on the cold-leg was attributed to flow-accelerated corrosion (FAC) of the low chromium (0.07 to 0.08 wt. %) carbon steel TSPs. Partial blockage of the trefoil TSP on the hot leg, which led to a re-distribution of the riser flow and relatively high fluid velocity on the cold-leg, was identified as a contributing factor. FAC was also identified as the cause of extensive degradation of the carbon steel trefoil TSPs at

Unit 8 of the Bruce NPP, with the low chromium content of the carbon steel (0.03 to 0.04 wt. %) and relatively high local fluid velocity cited as exacerbating factors [42]. The highest damage rates at the Bruce Unit 8 SGs were found on the periphery of the hot leg. Although partial blockage of the TSPs at Bruce has been observed, it was not cited as a possible contributing factor.

3. Particulate fouling: Modelling and Experiments

3.1 Fouling – The Fundamental Steps
Epstein has outlined five fundamental steps involved in the process of fouling of a pipe wall or surface [43]:
1. Initiation (incubation period, surface conditioning, crystal nucleation),
2. Transport (mass transfer from the bulk to the surface),
3. Attachment (attachment of the foulant to the surface),
4. Removal (release, re-entrainment, detachment of the foulant from the surface), and,
5. Aging (dehydration, recrystallization, changes of physical or chemical properties of the accumulated deposit with time).

Each of these steps will be discussed in turn in the following sections. Please refer to the Nomenclature section for a complete listing of the symbols used in the equations.

3.1.1 Initiation
Initiation is associated with phenomena taking place on a wall or substrate that preclude a more rapid rate of fouling and is often but not always observed with precipitation fouling and biofouling, where the initiating phenomena could be nucleation of crystals and adsorption of polymeric substances important for the growth of microorganisms, respectively. There is no initiation step observed with particulate fouling, and so initiation will not be considered further in this report.

3.1.2 Transport
Transport is the best understood of the fundamental steps of the fouling process, where the mass flux of material transported from the bulk fluid to the wall is given by:

$$m_t = \rho_f \, K_t \, (C_b - C_s) \tag{1}$$

A thorough review of investigations into the mechanism of particle transport can be found in Reference [44].

For a suspension of colloidal particles in turbulent flow, Metzner and Friend derived an expression for the transport velocity of colloidal particles that simplifies to [45]:

$$K_t = U^* / (11.8 \cdot Sc^{2/3}) \tag{2}$$

---

[7]Density-wave oscillations can occur in a system if there is a higher pressure drop in the two-phase flow region than in the region where the flow is single-phase. Density-wave oscillations in an RSG manifest themselves as oscillations in the water level in the SG.

AECL NUCLEAR REVIEW
VOL 2, NUMBER 1, JUNE 2013

FOULING OF NUCLEAR STEAM GENERATORS: FUNDAMENTAL STUDIES, OPERATING
EXPERIENCE AND REMEDIAL MEASURES USING CHEMICAL ADDITIVES - C.W. TURNER

Using an entirely different approach, Cleaver and Yates [46] derived a similar expression with the factor 11.9 in the denominator instead of 11.8.

Equations (1) and (2) apply to particle sizes and fluid velocities that are low enough that inertial effects are not important, i.e., the particle dimensionless relaxation time, t_p^+, is < 0.1, where [46],

$$K_t = U^* / (11.8 \cdot Sc^{2/3}) \qquad (3)$$

A number of expressions and approaches have been developed to predict the transport velocity of particles in the inertial transport regime, i.e., for $t_p^+ > 0.1$ [46, 47, 48, 49, 50, 51]. Each of these methods predict a rapid increase in the dimensionless deposition velocity (K_t/U^*) in the range $0.1 < t_p^+ < 10$, followed by a region where the dimensionless deposition velocity is independent of t_p^+. Although the predicted deposition velocities are in reasonably good agreement with data for aerosols, they tend to overestimate the transport velocity by two to three orders of magnitude when compared to deposition data for aqueous suspensions of particles [44, 52].

3.1.3 Attachment

Under some circumstances, the rate at which particles deposit onto a wall in an aqueous medium is observed to be less than the rate at which particles are transported from the bulk to the wall region. This has been accounted for by the introduction of an additional step in the fouling process known as attachment, which acts in series with transport to determine the overall rate at which particles deposit onto a substrate from a flowing suspension [53, 54]. Treating transport and attachment as two steps in series, the deposition velocity, K_d, is written:

$$1/K_d = 1/K_t + 1/K_a \qquad (4)$$

where,

$$K_a = K_0 \exp(-E/RT) \qquad (5)$$

and the rate of particle deposition is given by:

$$\dot{m}_d(t) = \rho_f K_d (C_b - C_s) \qquad (6)$$

The rate of deposition can be limited by either the rate of particle transport from the bulk fluid to the wall or by the rate of attachment to the wall, whichever is smaller. Thus, for $K_t \ll K_a$, the rates of particle transport and attachment will be equal when $C_s \rightarrow 0$. In this case, the transport limited deposition rate will be given by:

$$\dot{m}_d \cong \rho_f K_t C_b \qquad (7)$$

Alternatively, for $K_t \gg K_a$, the rates of particle transport and attachment are balanced for $C_b \cong C_s$, and the attachment limited deposition rate will be given by:

$$\dot{m}_d \cong \rho_f K_a C_b \qquad (8)$$

The activation energy, E, in Equation (5) has its origin in the forces of interaction between the particle and the substrate, as discussed below. Examples of particle deposition limited by either transport or attachment are discussed in Section 3.3.1.

The surface interaction forces that come into play when a particle comes into close proximity to a substrate are described by the Derjaguin-Landau-Verwey-Overbeek theory of colloid stability, which is well described in numerous textbooks on colloid science [55], and so will not be discussed further in this paper. The net result of these forces of interaction is that once the particle has been transported to the vicinity of the substrate, it will be subjected to either a net force of attraction or a net force of repulsion, depending on the relative sign of the respective surface charges.[8]

Water has been called the "universal solvent", and it is well known that materials in an aqueous medium develop a surface charge as the result of chemical equilibria between ionic species in solution and the material itself. The surfaces of corrosion products and Fe-Cr-Ni alloys consist of hydrated metal oxides, which become charged as the result of preferential adsorption of H^+ and OH^- ions, which can be simply represented by the following reactions:

$$\rangle M(OH)_2 + H_2O \Leftrightarrow \rangle M(OH)(OH_2)^+ + OH^- \qquad (9)$$

$$\rangle M(OH)_2 + H_2O \Leftrightarrow \rangle M(OH)O^- + H_3O^+ \qquad (10)$$
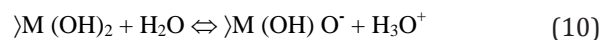
where $>M(OH)_2$ represents a hydrated oxide on the surface. It is clear from these equations that, in the absence of other equilibrium reactions, which may influence the surface

---

[8]The net force between a particle and substrate is equal to the sum of the van der Waals dipole-dipole interaction between the two bodies (which is always positive, or repulsive, in water) and a force of electrochemical origin which is positive (repulsive) if the two surfaces are of similar sign of charge, and negative (attractive) if the two surfaces are of opposite sign of charge.

AECL NUCLEAR REVIEW
VOL 2, NUMBER 1, JUNE 2013

FOULING OF NUCLEAR STEAM GENERATORS: FUNDAMENTAL STUDIES, OPERATING
EXPERIENCE AND REMEDIAL MEASURES USING CHEMICAL ADDITIVES - C.W. TURNER

charge, the sign of the surface charge of hydrated metal oxides will be determined by the pH. This dependence has been confirmed by numerous measurements reported in the literature [56]. The pH at which the net surface charge is zero is called the Point of Zero Charge (PZC), and the corresponding pH at which the potential at the plane of shear between a surface and the aqueous medium (the zeta potential) is zero is called the Isoelectric Point (IEP).[9]

For pH < PZC (IEP), the surface charge (zeta potential) will be positive. Correspondingly, for pH > PZC (IEP), the surface charge (zeta potential) will be negative. Therefore, if the pH of the medium is at a value that is between the PZCs (IEPs) of the particle and the substrate, the surfaces will be oppositely charged and the net force between them will be attractive. For pH outside of this regime, the surfaces will be similarly charged and the net force between the particle and the substrate will be repulsive.

3.1.4 Removal
Particles that have been transported to the wall and become attached do not necessarily remain there forever because they will continue to be acted upon by forces generated by the fluid flow. The hydrodynamics of particle removal in a turbulent flow have been thoroughly reviewed [57], and removal criteria based on particle size, wall-shear stress and the force of adhesion have been postulated.

Particles in steady shear flow are subjected to a drag force acting parallel to the direction of flow [58]:

$$F_D = 8\rho_f v^2 (d_p U^*/v)^2 \qquad (11)$$

and to a lift force acting normal to the direction of flow [59, 60]:

$$F_L = 0.81\rho_f v^2 (d_p U^*/v)^3 \qquad (12)$$

Starting with a flow model based on the theory of "turbulent bursts", Cleaver and Yates derived a similar expression for the lift force as that shown in Equation (12) except with a constant 0.076 [57] instead of 0.81. Regardless, for $(d_p U^*/v) < 1$, the particle will be buried deep within the so called "viscous", or laminar, sub-layer[10], and the lift force will be significantly smaller than the drag force. Although drag may cause a particle to roll or slide along the surface, it does not provide a component of force normal to the surface. Nor does it seem capable of moving a particle from the surface into the turbulent flow, as could be imagined for the case where $(d_p U^*/v) >> 1$. Thus, for small particles, i.e., $(d_p U^*/v) < 1$, the criteria for removal is that the lift force must exceed the force of adhesion holding the particle onto the

surface. Assuming that all adhesive forces are proportional to the particle diameter, the criteria for particle removal becomes [57]:

$$(\rho v^2/d_p) (d_p U^*/v)^3 > \beta \qquad (13)$$

where β is inversely proportional to the force of adhesion. For larger particles, i.e., $(d_p U^*/v) >> 1$, the drag force plays a more significant role in particle removal and the criteria for removal becomes:

$$(\rho v^2/\rho_p) (d_p U^*/v)^2 > \beta \qquad (14)$$

Cleaver and Yates developed a model of simultaneous deposition and removal of particles whereby particles are transported to a surface by a coherent downsweep of fluid turbulence and are either deposited in that downsweep (or subsequent downsweep) or transported back to the bulk by an outward turbulent burst [61]. The model provides a conceptual way to understand how particles can be simultaneously deposited and removed from a surface. The effect of removal on the overall rate of accumulation of particles onto a surface is given by:

$$N(t) \propto 100vm'/U^{*2}(1 - \exp(-U^{*2}t/(100vm'))) \qquad (15)$$

provided that the lift force generated by a burst is sufficient to overcome the force of adhesion and remove some fraction of the particles. In Equation (15), $100v/U^{*2}$ is the time between turbulent bursts and m' is the number of bursts per unit area.

Yung *et al.* compared the predictions of Cleaver and Yates' removal mechanism with measurements of the removal of particles from a substrate by turbulent burst activity, as recorded by high-speed photography [60]. For their investigation, the particle size was such that $0.5 < d_p U^*/v < 1.3$. Yung *et al.* found that the initial movement of a particle on a substrate under the influence of turbulent bursts is by rolling or possibly sliding along the surface. The rate of removal observed was not proportional to the rate of turbulent bursts, and the turbulent bursts were not very effective at removing particles buried deep within the laminar sub-layer. The cleaning efficiencies reported by Yung *et al.*, i.e., the fraction of the area under a turbulent burst that is cleaned of particles for a given burst, were very small, ranging from 0.013% to 0.58%.

Although the results of the investigations reported in this section provide good insights into the hydrodynamics of particle removal from substrates, there are too many

---

[9] The pH that corresponds to the PZC may be different from the pH at the IEP if there are charged species on the surface other than H^{+} and OH^{-}. Although it is important to distinguish between PZC and IEP, this topic is thoroughly discussed in the literature and is outside of the scope of this paper. The parameter of interest for particle deposition is the IEP, which determines whether the particle experiences a force of repulsion or attraction when it arrives within the vicinity of a substrate.

[10] The thickness of the laminar sub-layer in a turbulent flow, where turbulent eddies are rapidly damped by the fluid viscosity, is given by $v/U^* < 5$. Thus, for $(d_p U^*/v) < 1$, the particles are less than 20% of the thickness of the laminar sub-layer.

AECL NUCLEAR REVIEW
VOL 2, NUMBER 1, JUNE 2013

FOULING OF NUCLEAR STEAM GENERATORS: FUNDAMENTAL STUDIES, OPERATING
EXPERIENCE AND REMEDIAL MEASURES USING CHEMICAL ADDITIVES - C.W. TURNER

uncertainties in the parameters for this to form the basis for a useful predictive theory of particle removal for aqueous systems. Therefore, investigators must resort to an empirical model to take account of the effect of removal on the fouling rate. A common approach is to assume a rate of removal that is proportional to the deposited mass:

$$\dot{m}_r = - \lambda_r \, m_s \, (t) \tag{16}$$

Equation (16) is presumed to hold provided a critical threshold for particle removal is satisfied. For example, one could use the criterion that the dimensionless particle Reynolds number, $d_p U^*/v$, must be greater than 1 (i.e., the particle size must be greater than 20% of the thickness of the laminar sub layer) for a particle to be removed from the wall by the hydrodynamic forces.

The approximation that the rate of removal remains proportional to the deposited mass once the surface coverage of particles exceeds one monolayer is open to question. Only the outer layer of particles will be fully exposed to the hydrodynamic forces, therefore some adjustment must be made to Equation (16) to account for the fact that particles beneath the outer surface will not be subjected to the full hydrodynamic force. Thus, for $m(t) > m_{monolayer}$, a more realistic expression for the rate of removal once the surface is covered with at least one monolayer of particles is:

$$\dot{m}_r = - \lambda_r \, f \, m_{monolayer} \tag{17}$$

where f is a constant of proportionality (assumed to be $\geqq 1$) that depends on the degree to which the deposited particles are bound to one another.

3.1.5 Deposit Aging

Although much attention has been paid to modelling the contributions of transport, attachment and removal to particulate fouling, relatively little attention has been paid to the mechanism of deposit aging, or consolidation, and its effect on fouling behaviour. Consolidation is the process whereby particles become chemically bonded to both the heat-transfer surface and to pre-existing deposit, and is accompanied by an increase in deposit density and strength. It has been demonstrated that consolidation involves the precipitation or re-crystallization of material within the pores of existing deposit [62]. Processes that have been suggested to contribute to consolidation include Ostwald ripening, dissolution and re-precipitation of corrosion product in a temperature gradient and boiling-induced precipitation of dissolved species [63].

Ostwald ripening is the process whereby smaller particles or crystals dissolve and re-precipitate onto the surfaces of larger ones [64]. The process is thermodynamically favoured because it is accompanied by a reduction in surface area and, therefore, of surface energy. Consolidation by dissolution and re-precipitation takes place wherever a deposit resides in a temperature gradient. A gradient in temperature will be accompanied by a corresponding gradient in solubility across the deposit. The net result is that the deposit in the more soluble region will tend to dissolve and re-precipitate within the pores of regions of lower solubility. For deposit composed of material with a retrograde temperature-dependent solubility, the deposit will tend to dissolve at the deposit fluid interface and re precipitate at the heat-transfer surface. This phenomenon has been demonstrated with the precipitation of calcium carbonate from a flowing solution onto a heat-transfer surface [65] and with the precipitation fouling of magnetite onto the inside surface of SG tubes located in the preheater section of a CANDU SG [66], where the deposit porosity at the heat-transfer surface was estimated to be $\sim 5\%$. The third mechanism proposed for consolidation, boiling induced precipitation, will contribute to deposit consolidation on the secondary side of the SG for deposit on the tube-sheet, on the tube-bundle and at the entrance to the TSPs where flashing is proposed to cause localized boiling and precipitation onto the TSP [67, 68].

Consolidation of the deposit manifests itself by a reduction in the rate of particle removal from the deposit, as shown in Figure 6. The graphs in the Figure show Fe-59 radiotracing data for the deposition and removal of magnetite particles at a heat-transfer surface under flow-boiling conditions with the pH controlled by morpholine (top) and by dimethylamine (bottom) [63]. Clearly, the amine used for pH control has a significant effect on the rate of removal of particles from the surface. This phenomenon has been interpreted as evidence for the effect of the amine on the rate of deposit consolidation [69], as discussed further in Section 3.2.2.

3.2 Modeling Particulate Fouling

3.2.1 Fouling of an Un-heated Surface

A simple model of particulate fouling of an un-heated surface can be constructed by taking account of steps 2, 3, and 4 and the mechanisms discussed in Sections 3.1.2, 3.1.3 and 3.1.4. Starting with:

$$\dot{m}_s(t) = \dot{m}_d(t) - \dot{m}_r(t) \tag{18}$$

and substituting Equation (6) and Equation (16) for $m_d(t)$ and $m_r(t)$, respectively, one can solve to obtain:

$$m_s(t) = (K_d \, \rho_f/\lambda_r) \, (C_b - C_s) \, (1 - \exp \, (-\lambda_r \, t)) \tag{19}$$

Models of particulate fouling of the form shown in Equation (19) are called Kern-Seaton models after the investigators who first suggested modelling the rate of fouling as the difference between a rate of particle deposition and a rate of

AECL NUCLEAR REVIEW
VOL 2, NUMBER 1, JUNE 2013

FOULING OF NUCLEAR STEAM GENERATORS: FUNDAMENTAL STUDIES, OPERATING
EXPERIENCE AND REMEDIAL MEASURES USING CHEMICAL ADDITIVES - C.W. TURNER

TABLE 1: Recommended Fouling Models for Four Different Scenarios; with and without Removal, and Before and After Monolayer Coverage

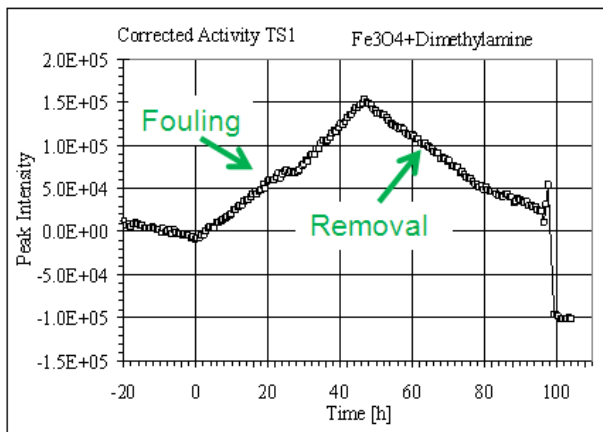|	Particle Removal $(d_p U^*/v) > 1$; $\lambda_r > 0$	No Particle Removal $(d_p U^*/v) < 1$; $\lambda_r \sim 0$
$m_s < m_{monolayer}$	$m_s(t) = (K_d \rho_f/\lambda_r)(C_b - C_s)(1 - \exp(-\lambda_r t))$	$m_s(t) = \rho_f K_d (C_b - C_s) t$
$m_s > m_{monolayer}$	$m_s(t) = (\rho_f K_a C_b - \lambda_r m_{monolayer}) t$ for pH $\neq$ IEP of the particle. Otherwise, $m_s(t) = (\rho_f K_t C_b - \lambda_r m_{monolayer}) t$	$m_s(t) = \rho_f K_a C_b t$ for pH $\neq$ IEP of the particle. Otherwise, $m_s(t) = \rho_f K_t C_b t$
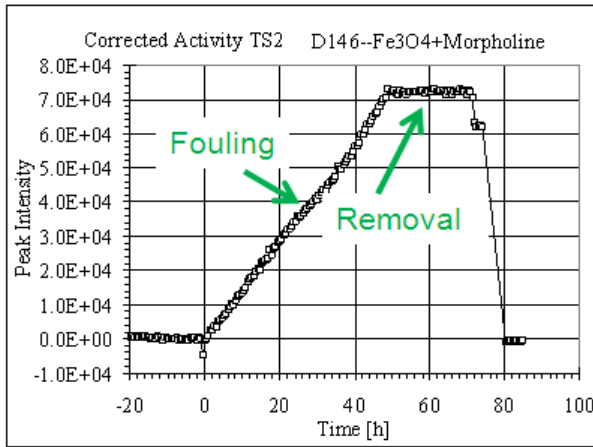
FIGURE 6: Illustration of the effect of consolidation on the rate of particle removal from a heat-transfer surface; top: high consolidation rate; bottom: low consolidation rate [63].

particle removal, with the removal rate being proportional to the deposit mass [70]. Equation (19) shows that the deposit mass will initially build up on the wall at a rate equal to $\rho_f K_d (C_b - C_s)$. Eventually, the rate of accumulation will be reduced as the rate of particle removal increases in proportion to the deposit mass until the deposit mass reaches the asymptotic value of $\rho_f K_d(C_b - C_s)/\lambda_r$. This, of course, presumes that the particles are large enough to be removed from the wall by the hydrodynamic forces, i.e., $(d_p U^*/v) > 1$, as suggested in Section 3.1.4. As noted in Section 3.1.4, it is not realistic to assume that the rate-of-deposit removal is proportional to the deposited mass once a monolayer coverage of particles on the wall has been exceeded. Thus, a more realistic approach to modeling would be to use Equation (18) for deposit loading less than one monolayer coverage, and for $m_s(t) > m_{monolayer,}$ use:

$$m_s(t) = (\rho_f K_d (C_b - C_s) - \lambda_r m_{monolayer}) t \qquad (20)$$

For $(d_p U^*/r) < 1$, the rate of removal is negligibly small, and so the rate of fouling of the wall can be approximated by Equation (20) with $\lambda r \approx 0$.

Note that for deposition under transport control, where the particle and the wall are of opposite sign of charge, once there is a monolayer of particles on the wall it is inevitable that an in-coming particle will now encounter a surface of the same sign of charge as the particle itself. Thus, one would expect that deposition under transport control would transition to control by attachment as deposit on the wall builds up to a monolayer, provided that the particle has a non-zero charge. For deposition of particles onto a wall of like sign of charge, deposition is already under attachment control, and so one would not expect to see a significant change in deposition rate once a monolayer of coverage has been attained. For deposition at pH = IEP of the particle, the deposition rate will always be under transport control. Models of particulate fouling for four different scenarios, with and without removal and before and after monolayer coverage, are listed in Table 1.

AECL NUCLEAR REVIEW
VOL 2, NUMBER 1, JUNE 2013

FOULING OF NUCLEAR STEAM GENERATORS: FUNDAMENTAL STUDIES, OPERATING
EXPERIENCE AND REMEDIAL MEASURES USING CHEMICAL ADDITIVES - C.W. TURNER
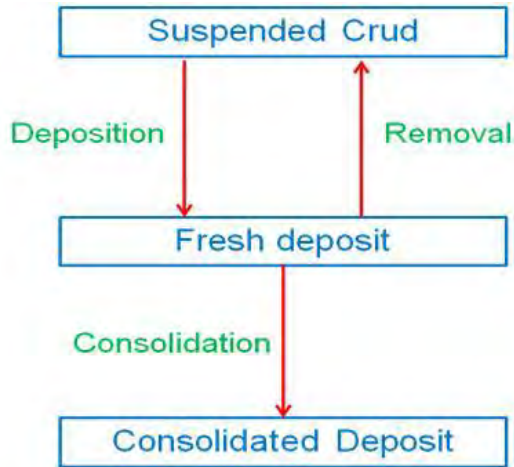
FIGURE 7: Model of particulate fouling onto a heated surface illustrating the rate processes of deposition, removal, and consolidation.

3.2.2 Fouling of a Heated Surface

A model of the fouling of a heated surface must take account of the effect of the temperature gradient on the rate of transport of the particle from the bulk fluid to the heated surface, as well as the effect of deposit aging, or consolidation, as discussed in Section 3.1.5.

Particles in a temperature gradient will tend to move from the hotter region to the cooler region of the fluid. This phenomenon can be understood as being the result of molecules in the hotter fluid having higher kinetic energy and, therefore, imparting more momentum when they collide with the particle than do molecules from the cooler region of the fluid. The migration of particles away from a heated surface and, by the same phenomenon, towards a cooled surface is called thermophoresis. The thermophoretic velocity of a particle down a temperature gradient has been calculated by McNab and Meisen [71]:

$$K_{th} = 0.26 \ h \ \nu \ \Delta T/((2 \ \kappa_f + \kappa_p) \ T_b)) \qquad (21)$$

The effect of the thermophoretic velocity on the overall rate of particle transport to a heated surface has been demonstrated by Turner and Smith [72] for the fouling of a heated surface of Alloy 600 by sub-micron particles of magnetite.

A model that takes account of the effect of deposit consolidation on the rate of deposit accumulation on a heated surface has been developed by Turner and Klimas [63], and is shown conceptually in Figure 7. Once a particle has been deposited onto the surface, it is subject simultaneously to the processes of removal and consolidation. Only the particles that have not yet been consolidated are subject to removal. Once they have become consolidated, they can no longer be removed.[11] Mathematically, this is expressed by two equations: one which calculates the time rate of change of the total deposit mass and the other that calculates the time rate of change of the removable (unconsolidated) portion of the deposit mass. Solving these two simultaneous equations and integrating, one obtains [63]:

$$m(t) = (\rho_f \ K_d \ C_b \ /\lambda) \cdot (t\lambda_c + (\lambda_r \ /\lambda) \cdot (1 - \exp(-\lambda \cdot t)) \qquad (22)$$

where $\lambda = \lambda_r + \lambda_c$

The model predicts the accumulation of a bi-layered deposit that consists of a dense (consolidated) inner layer overlain by a porous, un-consolidated outer layer. The predicted fouling kinetics can be linear, asymptotic or falling-rate, as illustrated in Figure 8, depending on the relative magnitudes of the rate constants for deposition, removal and consolidation.

A method for determining the ratios λ_r/λ and $\lambda_c \ /\lambda$ in Equation (22) from plots of fouling and removal data (see, for example, Figure 6) is described in Reference [63]. Because consolidation affects the rate of fouling itself, however, the magnitudes of the individual parameters λ_r and λ_c in Equation (22) could not be determined. From investigations of particulate fouling under sub-cooled and saturated flow-boiling in a loop operating at < 100 °C, Lister and Cussac proposed an expression for the consolidation rate constant, λ_c [73]:

$$\lambda_c \propto (1 - m_{labile}) \qquad (23)$$

where,

$$m_{labile} \propto A_{site} \cdot N_{active}/(q/L) \qquad (24)$$

The labile portion of the deposit defined in Equation (24) is equivalent to the fresh, unconsolidated deposit identified in Figure 7.

3.3 Experimental Investigations

3.3.1 Forced Convective Turbulent Flow: Deposition, Attachment and Removal

Investigations of particulate fouling in an aqueous, turbulent flow are based on several different methods for determining the mass of material that has accumulated on the wall of the test section as a function of time, including: thermal resistance [74, 75], absorption of X-rays [76, 77, 78, 79, 80] and radiotracer methods using neutron-activated particles [72, 81, 82, 83, 85]. Derivation of the deposit

---

[11] The model does not take account of spalling of larger pieces of consolidated deposit, but this would be an obvious extension of the model.

AECL NUCLEAR REVIEW
VOL 2, NUMBER 1, JUNE 2013

FOULING OF NUCLEAR STEAM GENERATORS: FUNDAMENTAL STUDIES, OPERATING
EXPERIENCE AND REMEDIAL MEASURES USING CHEMICAL ADDITIVES - C.W. TURNER

mass from a measurement of either thermal resistance or x-ray absorption is subject to uncertainty because the relationship between deposit mass and either of these quantities depends on the deposit density, which is generally not well known under the experimental conditions and can even change with time as the result of consolidation (see the discussion in Section 3.1.5).

Of the methods listed above, only radiotracing using neutron-activated particles that emit high-energy gamma rays provides a direct measure of the deposit mass independent of the deposit density. Experimental investigations of particulate fouling in a turbulent flow are inherently difficult because of the challenges associated with maintaining constant experimental conditions for a prolonged period of time, especially maintaining a constant concentration of particulates in the turbulent flow. In this respect, it is better to do experiments in small loops rather than large ones, and to use small, stirred tanks to maintain constant particle concentration rather than large tanks where particle agglomeration and settling can result in a major uncertainty regarding the concentration of suspended particulate during the test.

Investigations of magnetite particulate fouling from an aqueous turbulent flow onto aluminum tubes were conducted in a test loop at Harwell by Gudmundsson [76] and by Newson [77]. The suspension of particulates was maintained in a tank of volume 2,300 litres, which presented challenges with respect to the ability to maintain a constant concentration of suspended particles throughout each test. The deposit mass was calculated from measurements of the absorption of x-rays as a function of time as deposit built on the test section. The deposition/time curves were jagged, suggesting intermittent removal of parts of the deposit from the wall of the test section during the runs. Based on runs at two different flow velocities, it was deduced that the rate of particle deposition varied inversely with the fluid velocity [76]. An additional seven runs were subsequently performed on the same loop to do a more detailed investigation of the velocity dependence of the deposition rate. The runs were conducted at 40 ˚C using a suspension of magnetite particles of nominal particle size 2 μm. The results were fitted using a Kern-Seaton fouling asymptotic model. Based on these latter results, it was suggested that the deposition velocity increased with fluid velocity to the power 2.2 [77]. Neither of these two investigations resulted in a particle deposition velocity that is consistent with diffusion control, which is what would be expected for 2 μm particles under the test conditions.

The investigation of particulate fouling from flowing suspensions of magnetite in turbulent flow was continued by Newson et al. [78, 79] and by Hussain et al. [80] in a loop for which the suspension of particles was maintained in a stirred, 45 litre vessel. The runs were conducted at pH 6.8, and the deposit mass on the test section was determined by x-ray absorption, as before. It was later learned that spurious errors in measurement were due in part to the difficulty in maintaining constant strength of the x-ray beam. An analysis of the particles used for this investigation showed particle sizes ranging from 1 to 5 μm, with an average size of 1.5 μm. The data were analysed using an asymptotic Kern-Seaton model. Analysis showed that the initial deposition rate varied as fluid velocity to the exponent 0.73, which is in good agreement with a diffusion mechanism for particle transport. The authors also showed that correlations developed for particle transport in aerosol systems predict that interial transport should be the dominant mechanism for particle deposition under the test conditions. It appears, however, that the correlations developed for interial transport for aerosols over-predict the magnitude of intertial transport by several orders of magnitude when applied to aqueous systems [44, 52]. The asymptotic deposit mass determined from the fit of the Kern Seaton model to the fouling data showed a dependence on U raised to the exponent -0.66, which implies that a particle-removal mechanism could be limiting the build-up of deposit.[12]

The earliest investigation of particle deposition in an aqueous, turbulent flow using radiotracer techniques was made by Thomas and Grigull [81]. Using particles of magnetite with a mean size of 0.06 μm and radiotraced with Cr-51, which decays with the emission of a gamma ray, they found that the particle fouling rate in high-temperature neutral water increased linearly with the Reynold's number under single-phase isothermal conditions, which is consistent with particle transport from the bulk to the wall by a diffusion mechanism. Each test lasted only a few hours, and the deposition rate was observed to decrease about five-fold during this period of time. Thomas and Grigull observed that this behaviour is consistent with a falling "sticking probability".

Newson et al. [82] conducted an extensive investigation of fouling by 0.2 μm hematite particles suspended in a turbulent flow onto the surface of a 316 stainless-steel (SS) tube. The tests were conducted in a simple loop with a suspension of hematite particles maintained in a 50 litre vessel. There is no indication as to whether the suspension was stirred during each test. Runs were conducted as a function of pH, fluid temperature and fluid velocity using hematite particles that had been neutron-activated to produce Fe-59, an unstable isotope of Fe that decays with the emission of a gamma ray. The deposit mass on the test section was measured as a function of time using a sodium-iodide gamma ray detector. For a series of runs done at pH 6.8, the initial rates of

---

[12]The values of the exponent for the dependence of the deposition velocity and asymptotic deposit mass on U quoted in the text are from References [78] and [79]. The magnitudes, but not the signs, of the exponents are reversed in Reference [80] for the same body of work.

AECL NUCLEAR REVIEW
VOL 2, NUMBER 1, JUNE 2013

FOULING OF NUCLEAR STEAM GENERATORS: FUNDAMENTAL STUDIES, OPERATING
EXPERIENCE AND REMEDIAL MEASURES USING CHEMICAL ADDITIVES - C.W. TURNER

particle deposition increased with fluid velocity in a manner consistent with particle transport to the wall by a diffusion mechanism. The plot of deposition velocity versus pH went through a maximum at pH 6.2 [83]. No measurements were made of the IEPs of either the hematite particles or the 316 SS surface used in this investigation, and the effect of pH on the deposition velocity was interpreted in terms of a pH-dependent "sticking probability". The authors noted the similarity between their results and the results of Kuo and Matijevic, who observed that the mobility of hematite particles through a packed bed of stainless steel went through a maximum at a pH of 6.8 [84]. Measurements were also made of the particle-removal rate by switching from a suspension of active hematite particles to inactive particles, and measuring the deposit activity as a function of time. The authors reported no measurable removal of particles from the wall up to a Reynold's number of 140,000. Some of the experiments, however, indicated a falling deposition rate, which the investigators interpreted in terms of gradually decreasing "sticking probability". Even though many of the runs did not reach an asymptote, a Kern-Seaton model was fitted to the data and a relationship was established between the fitted asymptotic deposit mass and the fluid velocity.

A detailed investigation of fouling by magnetite particles suspended in a turbulent flow was conducted as a function of pH, fluid temperature, fluid velocity and temperature gradient [72, 85]. The neutron-activated particles of magnetite were nearly-monosized with a mean particle size of 0.26 μm, and the deposit mass was determined during each run as a function of time using a high-efficiency gamma ray detector. For each experiment, after establishing a fouling rate the suspension of active particles was switched out of the circuit and replaced with a solution of deionized water at the same pH as the suspension to measure the rate of particle removal from the wall. The fouling rate was observed to be a strong function of pH, going through a maximum near a pH of 7.5 and 7.1 for deposition onto

surfaces of Alloy 800 [85] and Alloy 600 [72], respectively. The effect of pH was interpreted in terms of the relative surface potentials of the magnetite particles and the substrates, with the surfaces being presumably oppositely charged in the pH-range of 6 to 8 (where the deposition rate goes through a maximum), and similarly charged for pH outside of this range. The measured rate of particle removal during the "release" phase of each test was very small, from which a removal rate constant, λ_r, was estimated to be $4 \cdot 10^{-7}$ s^{-1}. The deposition velocity at pH 7 showed an approximately linear dependence on fluid velocity raised to the power 0.5 for U* up to 0.15 m/s, whereupon the deposition velocity showed an abrupt decrease for U* > 0.15. A similar result was observed for fouling of a sand/water mixture where an abrupt decrease in deposition rate was observed for U* > 0.12 m/s [74]. This latter behaviour is interpreted as evidence for the onset of significant particle removal for a particle size greater than a critical value for a given fluid velocity [72] (see discussion of particle-removal criteria in Section 3.1.4).

Burrill conducted an investigation of the deposition of magnetite particles onto zirconium alloy and nickel surfaces at temperatures of 25 and 90 °C [86]. Fluid velocities between 5 and 100 m/s were achieved by forcing a suspension of magnetite particles to pass through small tubes under a high, applied pressure of air. The tests were very short, lasting only from 0.3 to 6 seconds. Deposits were removed after each test by acid dissolution, and this information was used along with the test duration to calculate a deposition velocity for each test. For tests at neutral pH and Re between ∼ 20,000 and ∼ 50,000, the fouling rate on the nickel tube increased as Re6, decreasing to a 0.8 power dependence for Re > 100,000. Burrill interpreted this behaviour as evidence for inertial deposition at lower Re, changing to a diffusion-controlled mechanism at the higher Re. In additional tests, the deposition rate constant was shown to increase with increasing concentration and with increasing temperature. Burrill also measured the pH dependence

TABLE 2: Comparisons of Key Parameters Related to Particle Transport and Removal Derived from Various Investigations of Particulate Fouling

Reference	d_p (μm)	t_p^+	U* (m/s)	(d_pU*/ν)	Initial Fouling Rate ∝ U$^\alpha$
[76]	∼ 2	-	-	-	$\alpha = -1$
[77]	∼ 2	$1.5 \cdot 10^{-3}$ to $1.5 \cdot 10^{-2}$	0.025 to 0.073	0.08 to 0.24	$\alpha = 2.3$
[78] [80]	∼ 1.5	$2 \cdot 10^{-4}$ to 0.11	0.062 to 0.16	0.05 to 0.55	$\alpha = 0.5$ to 1.0
[84]	∼ 0.06	$1.3 \cdot 10^{-4}$ to $6.4 \cdot 10^{-4}$	0.055 to 0.086	0.03 to 0.04	$\alpha \sim 1$
[85]	∼ 0.2	$1.2 \cdot 10^{-4}$ to $1.9 \cdot 10^{-3}$	0.072 to 0.17	0.02 to 0.08	$\alpha \sim 1$
[86]	∼ 0.25	$1.1 \cdot 10^{-4}$ to $6.4 \cdot 10^{-4}$	0.072 to 0.168	0.02 to 0.05	$\alpha \sim 0.5$
[87]	∼ 1	0.03 to 0.16 0.28 to 5.6	0.29 to 0.67 0.89 to 4.0	0.32 to 0.78 0.98 to 4.4	$\alpha \sim 6$ $\alpha \sim 1$

AECL NUCLEAR REVIEW
VOL 2, NUMBER 1, JUNE 2013

FOULING OF NUCLEAR STEAM GENERATORS: FUNDAMENTAL STUDIES, OPERATING
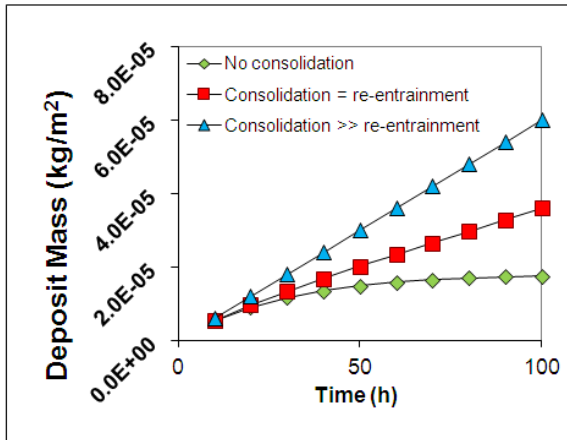EXPERIENCE AND REMEDIAL MEASURES USING CHEMICAL ADDITIVES - C.W. TURNER

FIGURE 8: Particulate fouling kinetics predicted by (22) for three different cases: i) no consolidation, ii) consolidation = removal, and iii) consolidation >> Removal [63].
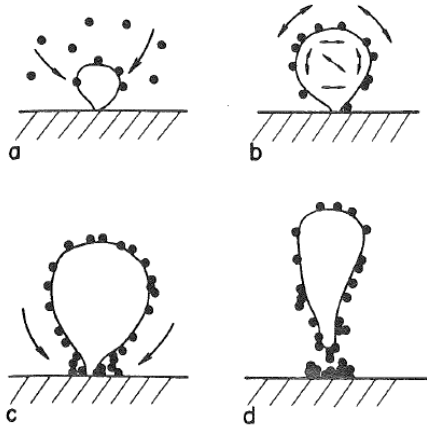

FIGURE 9: Illustration of the four stages leading to accumulation of hydrophobic particles at bubble nucleation sites on a surface under boiling heat-transfer; a) collection, b) surface migration, c) accumulation, and d) bubble departure [80].

of deposition onto a tube of Zircaloy-4 and found that the deposition rate was highest at pH 4 and lowest at pH 10, with an intermediate deposition rate constant at pH 7.

A comparison of the key parameters related to particle deposition and removal for the investigations discussed in Section 3.3.1 is listed in Table 2. For those studies that included deposition under both transport-limited and attachment-limited conditions, the U-dependence of the initial fouling rate listed in Table 2 is from the subset of tests that were done under transport limited conditions, i.e., for the pH-range for which the deposition rate goes through a

broad maximum with respect to pH. A comparison of the results from these investigations leads to the following conclusions:

1. The rate of removal of deposited particles from a wall in a turbulent flow is negligible when $d_p U^*/v < \sim 1$, i.e., the particle size is less than ∼20% of the thickness of the laminar sub-layer.
2. The deposition rate under transport-limited conditions is well described by a diffusion-limited process for $t_p^+ \le 0.1$.
3. Correlations for inertial transport, which show good agreement with particle transport behaviour in aerosol systems, over-estimate particle transport rates in aqueous systems by several orders of magnitude. The results from Reference [86] not withstanding, inertial transport may not be applicable to particle transport in aqueous systems.

3.3.2 Flow-boiling

3.3.2.1 Impact of Boiling on Rate of Particulate Fouling

The impact of boiling on the fouling of heat-transfer surfaces was of particular concern to the nuclear industry in the early days of the development of commercial nuclear power reactors. Some early studies suggested that the fouling rate under flow-boiling conditions was proportional to the product of the concentration of corrosion product with the square of the heat flux [87, 88, 89]. These investigations did not elucidate the relative contributions from fouling by soluble versus particulate corrosion products; therefore, they presented their results in terms of the total iron concentration.

Thomas and Grigull investigated fouling under flow-boiling conditions in a series of short (usually up to four hours) tests in a loop using magnetite particles radiotraced with Cr-51. They found that the particulate fouling rate increased with the onset of sub-cooled nucleate boiling, and that the fouling rate continued to increase as the degree of sub-cooling decreased [81]. They also showed that the fouling rate increased linearly with heat flux, which suggests that the enhancement of particulate fouling may be directly related to the rate of bubble nucleation on the heat-transfer surface. Thomas and Grigull, however, attributed the increase to a higher fluid turbulence and mass transport to the surface with the onset of boiling. Nicholson and Sarbutt conducted loop fouling tests under BWR conditions, and observed higher fouling rates of hematite particles on surfaces in boiling heat-transfer compared to heat-transfer without boiling [90]. Like Thomas and Grigull, they also observed an increase in deposition rate with decreased sub cooling. Iwahori *et al.* studied the effect of boiling on the fouling of heated wires of Zircaloy-2 and stainless steel by particles of hematite at 100 °C [91]. They, too, observed an enhancement of the rate of particulate fouling in the presence of boiling,
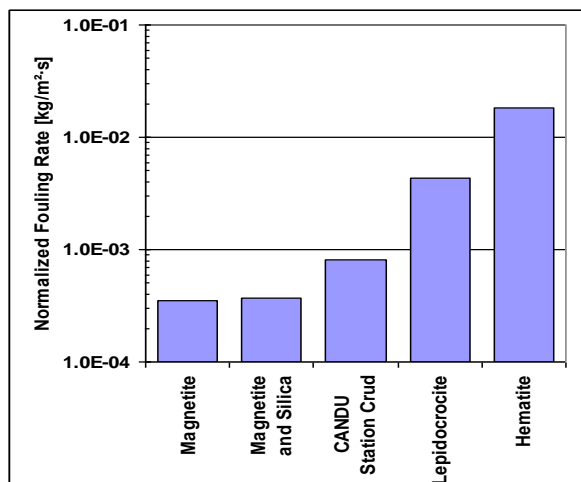
AECL NUCLEAR REVIEW
VOL 2, NUMBER 1, JUNE 2013

FOULING OF NUCLEAR STEAM GENERATORS: FUNDAMENTAL STUDIES, OPERATING
EXPERIENCE AND REMEDIAL MEASURES USING CHEMICAL ADDITIVES - C.W. TURNER

FIGURE 10: Measured particulate fouling rates for different corrosion products under flow-boiling conditions at a $pH_{T=270°C}$ of 6.2 adjusted using morpholine [63].

and observed that the deposits initially formed as rings around bubble nucleation sites. Significantly, they also showed that deposit of similar morphology was formed on un-heated surfaces around bubbles that were produced at the surface by a flow of air bubbles introduced from a capillary. These observations led Iwahori *et al.* to postulate that enhanced deposition under boiling heat-transfer was the result of metal oxide particles collecting on the surface of bubbles growing at the surface of the substrate. It was proposed that the particles move on the surface of the bubble and eventually collect in rings at the base of the bubble as the bubble detached from the surface. To support this hypothesis, the authors showed photographs of particles that had collected on the surfaces of bubbles that formed on the heat-transfer surface.

Figure 9, taken from the paper by Iwahori *et al.*, illustrates the various stages of the particle-bubble interaction that are proposed to lead to the accumulation of particles at the bubble nucleation site [91]. In the first step (a), particles collect on the surface of a growing bubble. The collected particles continue to move around the surface of the bubble as it grows (b). Particles also migrate towards the heat-transfer surface (c). Finally, the bubble grows large enough to depart from the surface (d), carrying some particles with it back to the bulk and leaving behind a ring of deposited particles on the surface.

Asakura *et al.* demonstrated a linear effect of particle concentration and heat flux on the rates of fouling by particles of hematite onto the heated surface of Zircaloy 2 under flow-boiling conditions at a pressure of 1 atm. [92]. Similar results were later obtained in a natural circulation

loop operating at a pressure of 10 atm. [93]. Asakura *et al.* also observed that the deposit formed at sites of bubble nucleation, and that the deposit morphology was circular. They invoked the theory of microlayer evaporation to develop a model of boiling-enhanced deposition to account for the observed deposit morphology and predict the boiling-enhanced deposition rate as a function of thermal-hydraulic conditions. More recently, Bassett *et al.* [94], Carpentier *et al.* [95], and Arbeau *et al.* [96] have all investigated particulate fouling of a heated surface in sub-cooled flow-boiling at 90 °C, and found linear relationships between the fouling rate and both heat flux and the concentration of particles in suspension.

3.3.2.2 Investigations of Particle-bubble Interactions

To further our understanding of the mechanism of boiling-enhanced fouling of heat-transfer surfaces, a number of investigations have been conducted at atmospheric pressure where high-speed photography can be used to interrogate the process of bubble nucleation and growth, and the interaction of the bubbles with particles in suspension.

For example, Wen and Melendres investigated fouling of a stainless-steel surface by hematite particles under nucleate boiling conditions at 100 °C [97]. The experiments were conducted in a glass cell with a heated steel disk at the bottom. The temperatures of the disk and suspension of particles were controlled separately to control the rate of bubble nucleation and bubble residence time on the surface. Formation and growth of individual bubbles was observed in real time, and the bubble size and residence time were correlated with the amount of deposit formed. Their investigation found that particles deposited primarily at the boundary of the gas/liquid/solid interface, consistent with the ring pattern of deposit reported by other investigators. The amount of deposit was correlated with the bubble size and its residence time on the heat-transfer surface. The authors conclude that their observations are not consistent with the microlayer evaporation theory, and that bubble-particle interactions play a dominant role in determining the boiling-enhanced fouling rate.

Basset *et al.* studied fouling by magnetite particles of Alloy-800 heated surfaces under sub-cooled nucleate boiling conditions in a loop operating at 90 °C [94]. The magnetite particles were radiotraced with Fe-59 so that fouling rates could be measured continuously using a gamma ray detector. A video camera was used to record bubble nucleation and growth as well as the particle-bubble interactions in sub-cooled nucleate boiling. Basset *et al.* proposed that when the fluid is highly sub-cooled and the bubble lifetime is relatively long, particle-bubble interactions dominate the deposition process resulting in ring-shaped deposits. As the

AECL NUCLEAR REVIEW
VOL 2, NUMBER 1, JUNE 2013

FOULING OF NUCLEAR STEAM GENERATORS: FUNDAMENTAL STUDIES, OPERATING
EXPERIENCE AND REMEDIAL MEASURES USING CHEMICAL ADDITIVES - C.W. TURNER

degree of sub-cooling decreases, bubble lifetimes decrease and microlayer evaporation is the dominant process, giving rise to disk-shaped deposits. This hypothesis may offer a means to reconcile the apparently divergent conclusions of Wen and Melandres [97] (who investigated bubble formation in a non-flowing system) with those of Asakura *et al*. [92, 93] regarding the relative importance of microlayer evaporation and particle-bubble interactions with respect to the mechanism of particle deposition in boiling water.

Lister and Cussac have proposed a model of particle fouling under sub-cooled and saturated flow-boiling conditions based on continuing studies of particle deposition at the University of New Brunswick [73]. The model is based on microlayer evaporation, and incorporates observations made of the process of bubble nucleation and growth and particle-bubble interactions observed using high-speed video photography. The model considers both deposition and removal at a single bubble nucleation site. In the early stages of deposit formation when the surface coverage is sparse, the deposition rate is governed by microlayer evaporation. As deposit accumulates on the surface, an additional deposition mechanism occurs whereby suspended particles are filtered by the deposit as liquid is drawn towards the heat-transfer surface and boiled. Turbulence created by collapsing and detaching particles affects particle removal. The model predictions agree well with the experimental data presented.

3.3.2.3 Effect of Water Chemistry: pH, Alternative Amines and Dispersants

The investigations described in the previous sections highlight the important role of surface interactions in determining the overall rate of particulate fouling under boiling heat-transfer conditions. Attachment of particles to a growing bubble and the migration of particles on the surface of the bubble during bubble growth are expected to be influenced by factors such as the surface tension of the steam/water interface, surface tension gradients across this interface, and the relative surface charges of the steam/water and the particle. Water-treatment chemicals added to control pH, for example, or to inhibit fouling, may influence the fouling rate through their effect on the surface tension, the surface tension gradient or surface potentials. All three of these factors influence the dynamics of the particle-bubble interaction, and therefore could play a dominant role in determining the rate of particulate-fouling under flow-boiling conditions. In this section, several investigations that illustrate the influence of water chemistry on the rate of particulate fouling under flow-boiling conditions are reviewed.

Iwahori *et al*. [91] investigated the effect of pH on fouling of heated wires by particles of hematite under both flowing and non-flowing conditions. Both sets of tests showed a pH-dependence of the fouling rate, although the pH dependence observed for the non-flowing tests was not the same as observed in the tests under flowing conditions. Under flowing conditions, the fouling rate was highest at pH 6, and decreased as the pH was either raised or lowered from this value. Under non-flowing conditions, the fouling rate was lowest in the range pH 8 to 9, and went through a maximum near pH 4 and near pH 11.5. The IEP of hematite at ambient temperature is reported to be at pH 9.1. The stability of colloidal suspensions is known to be at a minimum at the IEP [55], so it is possible that agglomeration and settling may have reduced the fouling rate in the tests under non-flowing conditions at pH values in the vicinity of the IEP.

Both Bassett *et al*. [94] and Arbeau *et al*. [96] measured the pH-dependence of the fouling rate of a heated surface of Alloy-800 by magnetite particles under sub-cooled flow-boiling conditions. Bassett *et al.* reported a maximum in the fouling rate centred at about pH 8, while Arbeau reported a similar dependence with a maximum at about pH 7.5. These results are in good agreement with measurements by Turner *et al*., who reported that the fouling rate of magnetite particles onto the surface of Alloy-800 under single phase forced convection was a strong function of pH, and went through a maximum at approximately pH 7.5 [85]. All three sets of investigators concluded that the pH-dependence of the fouling rate was related to the pH-dependences of the surface potentials on both magnetite and Alloy-800, and that the range of pH for which the fouling rate went through a broad maximum corresponds to the pH range where the respective surfaces are oppositely charged.

The effect of surface chemistry on the rate of particulate fouling was extensively investigated in a collaborative program by Atomic Energy of Canada Limited and the Electric Power Research Institute [63, 69, 98, 99, 100, 101, 102]. All tests were conducted in the B250 H3 high-temperature water chemistry loop at Chalk River Laboratories (CRL). The tests were conducted under flow-boiling conditions at a temperature of 270 °C and steam qualities ranging from -0.3 (sub-cooled) to > +0.50. The test program investigated the effect of the type of corrosion product (magnetite, hematite, lepidocrocite) and water-treatment chemical (various volatile amines, including ammonia, morpholine, ethanolamine, dimethylamine, and others) on the rate of particulate fouling as a function of steam quality. The concentrations of the amines used were adjusted so that all the tests were done at the same high-temperature pH (pH_T) of 6.2, calculated at zero steam quality.[13]

The tests demonstrated a strong influence of surface chemistry on the fouling rate. For example, it was shown

---

[13] Because the amines are volatile, one would expect a change in the concentration of amine and, therefore, pH_T with increasing steam quality. The deposition rates measured, however, were independent of steam quality in these tests for steam quality between 0 and 0.25. Therefore, the effect of any change in pH_T with increasing steam quality is not being reflected in the deposition rates measured in these experiments.

AECL NUCLEAR REVIEW
VOL 2, NUMBER 1, JUNE 2013

FOULING OF NUCLEAR STEAM GENERATORS: FUNDAMENTAL STUDIES, OPERATING
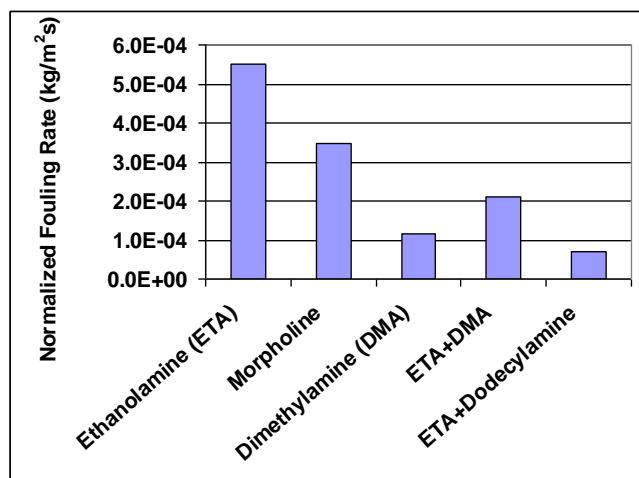EXPERIENCE AND REMEDIAL MEASURES USING CHEMICAL ADDITIVES - C.W. TURNER

FIGURE 11: Influence of amine used for pH control on the fouling rate of magnetite particles under flow-boiling conditions [63].
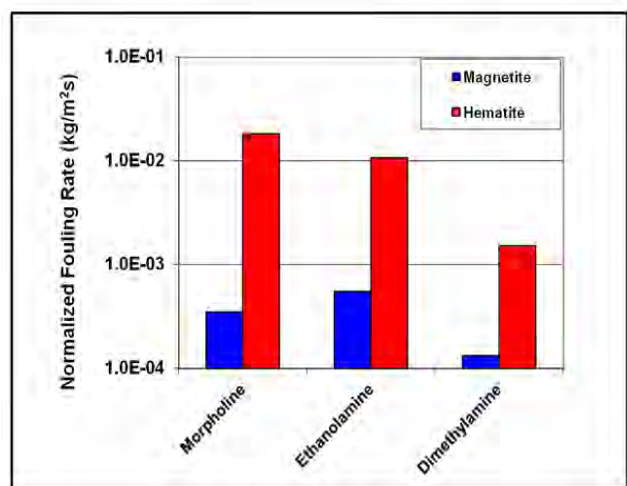

FIGURE 12: Influence of amine used for pH control on the fouling rate of particles of hematite and magnetite under flow-boiling conditions [100].

that the fouling rate by hematite particles is significantly higher than that of magnetite particles, with the fouling rate of lepidocrocite particles coming in between, as illustrated in Figure 10 [63].

The fouling rate of hematite relative to magnetite was explained in terms of the difference in the IEPs of the two oxides at 270 °C, i.e., magnetite particles are predicted to be negatively charged under the test conditions (i.e., $pH_T >$ IEP at 270 °C), while the hematite particles are predicted to be positively charged (i.e., $pH_T <$ IEP at 270 °C) [103]. The IEPs of Fe-Cr-Ni alloys have not been measured at high temperatures but based on measurements of the IEP of stainless steel at room temperature, one would expect the surface of Alloy 800 to be negatively charged under the test conditions, which is consistent with the relative fouling rates observed for hematite and magnetite particles. These results may be interpreted as illustrating the effect of surface potential on the rate of particle accumulation on a heat-transfer surface under flow-boiling conditions as a result of deposition from the evaporating microlayer at the bubble nucleation site.

The AECL EPRI collaborative investigation also showed evidence for a strong effect of the amine used for pH control on the overall fouling rate, as illustrated in Figures 11 and 12 for fouling by particles of magnetite and hematite, respectively, under flow-boiling conditions.

The origin of the effect of amines on the rate of particulate fouling under flow-boiling conditions was not fully elucidated during the course of these investigations. Several avenues of inquiry were followed, including investigations of the surface adsorption, atomic force microsocopy and surface-tension measurements to try to understand the mechanism by which the amine was affecting the fouling rate. Ultimately, however, no single phenomenon was able to account for the observed results.

The effect of using dodecylamine (DDA) in combination with ETA for pH control is particularly interesting because this combination resulted in the lowest fouling rates measured [104]. DDA is known as a filming amine, a group of aliphatic amines that have been added to the steam cycles of fossil-fired boilers to mitigate corrosion. There has recently been a renewed interest in the use of filming amines to mitigate fouling of nuclear SGs. If the results shown in Figure 11 are any indication, the use of filming amines to mitigate SG fouling may be well worth pursing.

Dispersants are a class of surface-active agent that have been used extensively to mitigate fouling of fossil-fired boilers in the utility and process industries. Investigations of the effect of chemical dispersants on particulate fouling under

AECL NUCLEAR REVIEW
VOL 2, NUMBER 1, JUNE 2013

FOULING OF NUCLEAR STEAM GENERATORS: FUNDAMENTAL STUDIES, OPERATING
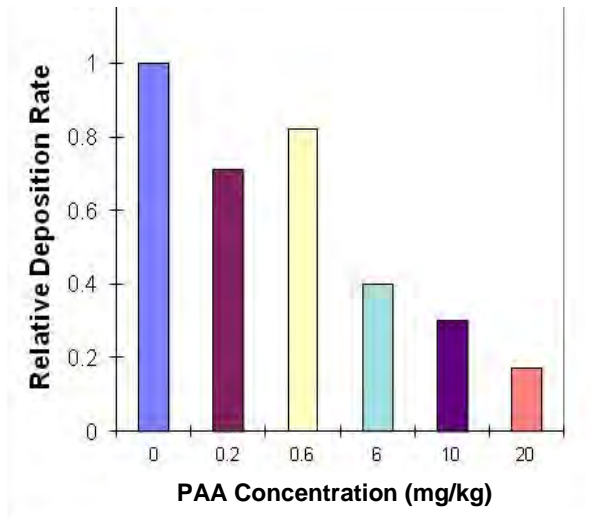EXPERIENCE AND REMEDIAL MEASURES USING CHEMICAL ADDITIVES - C.W. TURNER

FIGURE 13: Effect of the concentration of a low molecular weight polyacrylic acid on the rate of fouling by magnetite under flow-boiling conditions at a room temperature pH between 9.2 and 10.1 adjusted with morpholine.

flow-boiling conditions were conducted in the B250 H3 loop at CRL [105, 106]. These investigations identified several potential candidates that appeared to be suitable for use in a nuclear SG, including low molecular weight polyacrylic acid (PAA). The effectiveness of the concentration of PAA on the fouling rate under flow-boiling conditions is illustrated in Figure 13.

Interestingly enough, dispersants that were effective at mitigating fouling under flow-boiling conditions were often not effective when tested under single-phase forced convection. This implies that the effectiveness of dispersants is related to the particle-bubble interaction rather than through a surface repulsion mechanism.

3.3.3 Fouling of the Tube-support Structure
As discussed in Section 2.3, fouling of the tube-support structure has affected all nuclear SG designs that use either the trefoil or the quatrefoil TSP design. TSP fouling is characterized by the accumulation of very hard deposit at the inlet to the flow passages on the TSP itself. Deposit grows not from the heat-transfer surface, but from the surface of the TSP. As the deposit grows, the flow passage is increasingly blocked, leading to serious operational problems and materials degradation that challenge safe, economic reliable operation of the SGs.

With the trefoil and quatrefoil design, there is an abrupt reduction in the cross-sectional area to flow as the two-phase mixture on the secondary side of the SG enters the flow holes of the TSP. This abrupt reduction in flow cross-sectional area results in separation of the fluid boundary layer from the surface of the TSP, which causes the main flow to contract through a minimum cross-sectional area called the *vena contracta*. Associated with the *vena contracta* is a corresponding local maximum in fluid velocity, a local minimum in pressure and a local maximum in turbulence intensity. These localized phenomena at the entrance to the TSP have been verified by numerical modelling [107] and by measurements under single phase and two-phase flow conditions [68, 108]. The various phenomena that may contribute to the accumulation of deposit on the TSP surface at the entrance to the flow passages are identified in Figure 14 [68].

The separation of the boundary layer from the surface of the TSP at the entrance gives rise to three phenomena that act to promote the accumulation of deposit:

1. High-turbulence intensity and mass transfer coefficient increase the rate of particle transport from the bulk fluid to the wall,
2. Particles transported into the low-velocity circulation zone of the *vena contracta* will have little tendency to be removed because the hydrodynamic forces in this region will be very low, and,
3. Precipitation of dissolved iron caused by flashing of the two-phase mixture at the *vena contracta* will contribute to deposit consolidation at this location.

A detailed model based on the various hydrodynamic forces acting on a particle together with the phenomena described above has been developed to account for the fouling of TSPs in nuclear SGs [31, 68]. More recently, Prusek *et al*. developed a model of TSP fouling based on the studies of Rummens *et al.* [68] and used it in conjunction with a
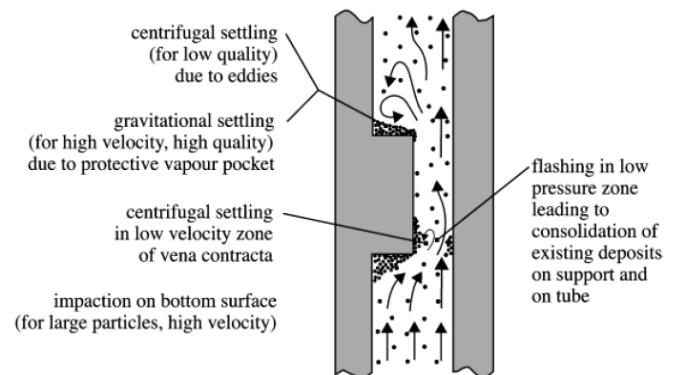

FIGURE 14: Illustration of potential contributing factors to fouling of orifices under flow-boiling conditions [68].

AECL NUCLEAR REVIEW
VOL 2, NUMBER 1, JUNE 2013

FOULING OF NUCLEAR STEAM GENERATORS: FUNDAMENTAL STUDIES, OPERATING
EXPERIENCE AND REMEDIAL MEASURES USING CHEMICAL ADDITIVES - C.W. TURNER

thermal-hydraulics code developed by EdF to compare to TSP blockage of quatrefoils in SGs in the French fleet [109]. The model takes account of changes in the fluid hydraulics as blockage of the TSPs progresses.

An alternative mechanism for TSP fouling has been proposed based on work by Beck *et al.* [110] and the investigations of the blockage of flow orifices used for boilers of Advanced Gas Reactors [111, 112]. The mechanism is based on the effect of the streaming potential that develops when a fluid flows past a charged surface. The streaming potential is one of four electrokinetic phenomena that are associated with the relative flow of a fluid with respect to a charged surface. These phenomena are well-described in the literature [113], and will not be discussed in detail here. Thus, for aqueous systems, uniform flow with respect to a pipe wall results in the formation of a streaming potential that causes a return current to flow through both the solution and the conducting walls of the pipe. These are steady-state currents that arise to maintain over-all charge balance, and are not involved with any net work being done. Under conditions where the flow is accelerating, however, it has been proposed that the localized divergence of fluid velocity where the flow is accelerating results in divergence of the current. In this case, charge balance is restored by an additional current arising from oxidation/reduction reactions taking place at the surface. This phenomenon was proposed by Beck *et al*. [110] to account for pitting of aircraft slide and sleeve hydraulic servo valves in a phosphate ester base hydraulic fluid, where the acceleration of the fluid through a gap at the interface of the slide and sleeve formed an anodic region on the surface of the sleeve and caused pitting of the sleeve. In the case of the fouling of flow orifices by magnetite, it is proposed that the acceleration of the fluid as it enters the orifice results in the formation of an anodic region at the entrance to the orifice and precipitation of magnetite via oxidation of ferrous ions [111, 112].

There has been a renewal of interest in the possible link between electrokinetic potentials and the accumulation of deposit in regions of accelerating flow in response to the experience of flow blockage of quatrefoils which lead to SG tube failures at some plants operated by EdF [38, 39]. Investigations by Guillodo *et al.* [114, 115] and Barale *et al*. [116, 117] conducted in fast-flowing water (fluid velocity ≈ 10 m/s) under secondary chemistry conditions have reproduced the previous results of Woolsey *et al*. [111]. Guillodo *et al.* considered three mechanisms that could potentially contribute to deposit formation [115]:

1) electrokinetic effects [110, 111, 112],
2) flashing [67, 68, 108], and
3) particle trapping [67, 68].

Mechanisms 1 and 2 were considered to be the most

TABLE 3: Approximate Distribution of Iron Transported with the Feed Water to an RSG

Tube-bundle deposit	~70%
Tube-sheet deposit	~15%
Removed by blow down	~15%

plausible, and were consistent with inspections of TSP blockage. Mechanism 3 was disregarded because it was not supported by inspection of the TSPs. Loop tests showed evidence for both precipitation fouling and deposition of fine particles within the orifice. The investigators proposed that pH and a redox potential were both important parameters, suggesting that a pH_T in the vicinity of 5.7 to 5.9 and a redox potential more positive than -570 mV relative to an Ag-AgCl electrode promoted fouling of the orifice. Although providing valuable data and information for understanding and controlling deposition in TSPs, their studies did not provide a definitive answer as to the extent to which electrokinetic potential contributed to deposition. Barale *et al.* also found that redox potential is a major parameter affecting deposit formation in a flow orifice. Their studies found that deposit accumulation occurred for a redox potential (relative to Ag-AgCl) more positive than -530 mV for nickel-base alloys and more positive than -450 mV for 410 stainless steel [117].   No definitive statement was made, however, regarding the contribution of electrokinetic potential to the deposition observed.

4. Plant Experience with Fouling Mitigation: Alternative Amines, Filming Amines and Chemical Dispersants

4.1 Criterion for Evaluating the Impact of Water Treatment Chemicals on the Rate of SG Fouling
Corrosion products that are transported to the SG with the feed water either accumulate within the SG by deposition onto an internal surface, e.g., primarily the tube-bundle, the tube-sheet and tube-support structure, or they remain suspended in the recirculating water where they are removed from the SG via blow down or moisture carry-over.[14] Table 3 lists the approximate distribution of corrosion products between various 'sinks' as a percentage of the total iron transported to the SGs with the feed water during operation. The estimated distribution listed in Table 3 is based on data from tube-sheet sludge lancing and chemical cleaning campaigns [118, 119, 120], and measurements of tube deposit loading [121] and corrosion product transport in the feed water and blow down [9, 122, 123].

It is clear from Table 3 that the fouling of internal surfaces

---

[14] Blow down is defined in Section 2.1. Moisture carry-over refers to the water content of the main steam exiting an RSG.

AECL NUCLEAR REVIEW
VOL 2, NUMBER 1, JUNE 2013

FOULING OF NUCLEAR STEAM GENERATORS: FUNDAMENTAL STUDIES, OPERATING
EXPERIENCE AND REMEDIAL MEASURES USING CHEMICAL ADDITIVES - C.W. TURNER

within the SG, and especially the accumulation of deposit on the tube-bundle, is a more effective removal mechanism for suspended corrosion product than removal from the SG by blow down. In other words, the fact that only 15% (on average) of the corrosion product that is transported to the SG during operation is removed by blow down is a direct consequence of the fact that the rate of removal of corrosion product via fouling of the tube-bundle is higher than the rate of removal by blow down. It follows that a water treatment chemical that results in a reduction in the tube-bundle fouling rate will lead to an increase in blow down efficiency and vice versa, as discussed below.

The fact that fouling of the internal surfaces of a SG is a more effective removal mechanism for corrosion products than blow down is related to the relative time scales on which the two processes occur. This is illustrated by comparing the half-mean-life for removal of corrosion product from the SG by blow down to the half-mean-life for removal of corrosion product from suspension by fouling, as shown by the following analysis [6].

The half-mean-life for removal of corrosion products from a SG via blow down is given by:

$$t_{1/2} = 0.5 * M / BD \qquad (25)$$

Equation (25) says that the half-mean-life for removal of suspended corrosion products from a SG by blow down is proportional to the total mass of fluid in the SG and inversely proportional to the blow down flow rate. For example, the half-mean-life for removal of suspended corrosion products from a CANDU 6 SG with a blow down flow rate of 1.3 kg/s, i.e., 0.5% of the steaming rate, and an inventory of 50 Mg of water during operation at power is 5.1 hours. Similarly, the half-mean-life for removal of corrosion products by fouling of the SG is given by:
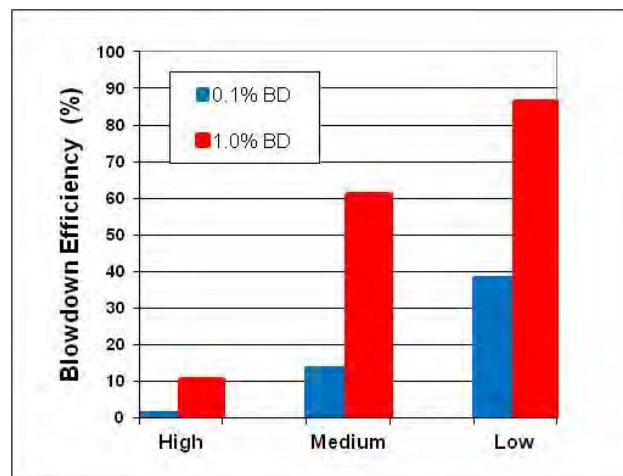
$$t_{1/2} = 0.5 * M / (\rho K_f * A) \qquad (26)$$

FIGURE 15: Effect of fouling rate on blow down efficiency (%) for two different blow down rates from simulations of fouling of an RSG using the SLUDGE code.

Thus, the fouling half-mean-life is inversely proportional to the product of the overall fouling rate constant and the surface area on which deposit accumulates. Considering only tube-bundle fouling, half-mean-lives for tube-bundle fouling for magnetite and hematite, calculated using the fouling rate constants shown in Figures 11 and 12, respectively, and a tube-bundle surface area of 3,500 m^2, are listed in Table 4 for selected amines.

For situations where $t_{1/2 \text{ fouling}} \approx t_{1/2 \text{ blow down}}$, i.e., fouling of magnetite in the presence of morpholine or ETA, the suspended corrosion products have approximately equal chances of being removed from the SG by blow down and being removed from suspension by fouling of the tube-bundle. Alternatively, if $t_{1/2 \text{ fouling}} \gg t_{1/2 \text{ blow down}}$, i.e., fouling of magnetite in the presence of DMA or a mixture of ETA

TABLE 4: Calculated Fouling Half-Mean-Lives for Magnetite and Hematite Based on Fouling Rates
Reported in Figure 11 and Figure 12

ρK_f (kg/m^{2}s)	Amine	$t_{1/2}$ (fouling) (hours)
Magnetite		
3.48×10^{-4}	Morpholine	5.7
5.52×10^{-4}	ETA	3.6
1.16×10^{-4}	DMA	17
0.7×10^{-4}	DDA/ETA	28
Hematite		
1.82×10^{-2}	Morpholine	0.11
1.08×10^{-2}	ETA	0.18
0.153×10^{-2}	DMA	1.29
-	DDA/ETA	-

AECL NUCLEAR REVIEW
VOL 2, NUMBER 1, JUNE 2013

FOULING OF NUCLEAR STEAM GENERATORS: FUNDAMENTAL STUDIES, OPERATING
EXPERIENCE AND REMEDIAL MEASURES USING CHEMICAL ADDITIVES - C.W. TURNER

and DDA, the particles will remain in suspension longer, which increases the likelihood of the corrosion products being removed from the SG by blow down. Conversely, if $t_{1/2\,fouling} << t_{1/2\,blow\,down}$, i.e., fouling by hematite in the presence of morpholine or ethanolamine, the rate of tube-bundle fouling is so high that the particles do not remain suspended long enough to have much chance of being removed from the SG by blow down.

The inverse relationship between tube-bundle fouling rate and blow down efficiency is illustrated by the results from modelling particulate fouling of an RSG shown in Figure 15. The figure shows the expected blow down efficiency versus fouling rate for two different blow down rates based on simulations of RSG fouling using a three-dimensional transient fouling code (SLUDGE) developed by Atomic Energy of Canada Limited (AECL). The fouling simulations were based on a CANDU 6 SG using a particle size of 1 μm. The blow-down flow rate is expressed as a percentage of the steaming rate. The concentration of suspended corrosion product in the SG recirculating water is a steady-state between the rate of input of corrosion product to the SG and the rates of removal by blow down and by fouling of the internal surfaces of the SG, as described elsewhere [121].

For the simulation results shown in Figure 15, a medium fouling rate corresponds to deposition of magnetite under flow-boiling conditions using morpholine to adjust the pH (see Figure 11). High and low fouling rates were arbitrarily selected to be 10-times higher and 10-times lower than the medium fouling rate, respectively. The results of the simulations show that a reduction in the tube-bundle fouling rate will be manifested by an increase in the blow down efficiency, a result that is consistent with the argument above based on the relative half-lives for blow down and tube-bundle fouling.

The discussion in this section has shown that the overall SG fouling rate is inversely proportional to the blow down efficiency. It follows, therefore, that a reduction in the SG fouling rate for a given rate of iron transport to the SG will be manifested by an increase in blow down efficiency and *vice versa*.

4.2 Alternative Amines
No systematic assessment has been published in the open literature on the effect of various alternative amines used for pH-control in the secondary systems of nuclear SGs on the rate of SG fouling using the criterion discussed in Section 4.1. There are numerous papers on the effect of alternative amines on the rate of iron transport to the SGs, and while this is of prime concern to power plant operators these reports tend not to include sufficient information to deduce an amine-specific effect on the rate of SG fouling, as might

be expected from the data shown in Figures 11 and 12.

One study has been published that looked for evidence from operating-plant data for a dimethylamine (DMA)-specific effect on both the rate of FAC and the rate of SG fouling [124]. This assessment focussed on nine plants operating in the U.S. that had initiated the addition of DMA after at least one cycle of operation. The evaluation of whether the addition of DMA to the feedwater system had any influence on the subsequent rate of SG fouling was based on an examination of trends of either the main-steam pressure or the SG fouling factor, as determined by a fouling factor analysis [26]. Unfortunately, the impact of the addition of DMA on blow-down efficiency was not included in the assessment.

Although the thermal fouling trend is important from the perspective of plant performance, it does not unambiguously provide a measure of the rate of accumulation of deposit on the SG tube-bundle. Several additional factors, including tube-deposit density and morphology, separator fouling, reactor power and primary coolant temperature, also influence the magnitude of the thermal fouling factor derived from plant-operating data, and care must be taken to separate these effects from the effect of deposit accumulation itself[15]. The methodology used to derive the thermal fouling factor is particularly important when comparing trends from one plant to another [25, 26]. The methodology used to calculate fouling factor trends was not described in the published report, and in only one case was it noted that the fouling factor was corrected for changes in reactor power level and the primary coolant temperature. Although the report concluded that no DMA-specific effect on the rate of SG fouling was apparent from the plant data, it is suggested here that the lack of rigour in comparing thermal performance trends from one plant to another and the absence of more definitive information on blow-down efficiency make the results of this assessment inconclusive.

4.3 Filming Amines
As noted in Section 3.3.2.3, there is increasing interest in the use of filming amines to mitigate corrosion in the steam cycle and fouling in nuclear SGs. Filming amines have used since the 1960s to mitigate corrosion in steam condensate systems in numerous industrial applications [125, 126], where their effectiveness is proposed to be related to the establishment of a non-wettable film on metal surfaces [126]. The film is proposed to be monolayer in thickness, and so its effectiveness does not increase with continued treatment beyond that required to maintain the monolayer coverage of the system surfaces. The most effective filming amines are those aliphatic amines with 10 to 18 carbon atoms in the chain. Octadecylamine (ODA) is a commonly used filming amine for the protection of industrial condensate systems.

The addition of ODA to mitigate corrosion in the secondary

---

[15] For CANDU plants that use carbon steel in the reactor-coolant circuit, the additional thermal resistance attributable to fouling of the inside surface of the SG tubes is a further complicating factor [25].

AECL NUCLEAR REVIEW
VOL 2, NUMBER 1, JUNE 2013

FOULING OF NUCLEAR STEAM GENERATORS: FUNDAMENTAL STUDIES, OPERATING
EXPERIENCE AND REMEDIAL MEASURES USING CHEMICAL ADDITIVES - C.W. TURNER

system and SGs of VVER plants is being investigated by a combination of experiments in autoclaves and tests in a pilot-scale SGs [127]. Its effectiveness is being evaluated with respect to its ability to mitigate FAC in the steam cycle to reduce the level of corrosion product transport to the SGs during power operation, as well as to reduce the risk of chloride cracking of the stainless steel SG tubes. The test program showed that ODA reduced the rate of chloride-cracking of stainless steel. It was postulated that its effectiveness was related to its adsorption onto the surface of the stainless steel, thus preventing access to the surface by chloride. Although the investigation was focussed on the effectiveness of ODA at mitigating corrosion, it was noted that the application of ODA to the Kola NPP increased the operating period between chemical cleanings. No other details were provided in the paper, so it is not clear whether the reduction in SG fouling was due to reduced corrosion product transport, reduced SG fouling or some combination of the two. In other testing in the pilot-scale SG, the application of ODA reduced tube deposits from an average loading of 48 g/m^2 to 17 g/m^2. Although few details were provided regarding deposit characterization, it appears that the application of ODA has been effective at removing deposit from the SG tube-bundle under SG operating conditions.

Results from field trials of the use of filming amines to mitigate corrosion in the steam cycles of PWR plants have been reported recently [128, 129]. As with the ODA trial reviewed above, the motivation for adding the filming amine was the reduction of FAC in the steam-cycle piping and, thereby, a reduction of the corresponding rate corrosion product transport to the SGs. Significantly, the field-trial results showed both a reduction in feed-water iron transport to the SGs and an increase in the concentration of corrosion product in the SG blow down, i.e., an increase in blow-down efficiency. This is a very important observation because it implies that the addition of the filming amine has reduced the rate of fouling of the SGs. Although it is possible that some of the increase in the concentration of corrosion product in the blow down arises from the removal of deposit from within the SG, it is more likely that the major contributing factor is a reduction in the rate of tube-bundle fouling.

4.4 Chemical Dispersants
While polymeric dispersants have been used for decades to mitigate deposit accumulation in fossil fuelled SGs, the nuclear industry has been reluctant to introduce dispersants to nuclear SGs to mitigate fouling because of the possibility of introducing inorganic impurities (left

over from the polymer synthesis) to the SGs, and concerns regarding the impact of polymer decomposition products on crevice chemistry and materials. The CANDU Owners Group funded research to investigate the feasibility of applying dispersants to CANDU SGs, and made preparations for a field trial of a low molecular weight PAA dispersant [105, 106]. The program was stopped, however, before a field trial could be launched. Betz Dearborn developed a high molecular weight PAA dispersant for application in nuclear SGs. Following rigorous qualification [130] the dispersant was approved for use, first in a short-term trial at ANO-2 [131] and subsequently at a longer-term trial at McGuire 2 [132].

The short-term trial at ANO-2 successfully demonstrated that PAA could mitigate deposition in nuclear SGs. PAA was added to the feedwater at a concentration of 2 μg/kg at the beginning of the trial, and the concentration was raised incrementally to 12 μg/kg by the end of the trial. Blowdown efficiencies for the two SGs increased from pre-trial values of 1 to 2% to average values of 20 to 60% during the trial. There were no unexpected changes in secondary system chemistry that were attributed to PAA addition to the feedwater. Changes in cation conductivity and total organic carbon were observed, but these correlated with changes in the concentration of ethanolamine, which is added for pH control at ANO-2. Analysis of the thermal-hydraulic performance of the plant suggested that the feedwater venturis de-fouled during the injection of dispersant while the steam venturis appear to have fouled. One apparently adverse effect of the dispersant addition was the sharp loss of thermal performance of the SGs during the last six weeks of the trial which was only partially recovered when dispersant injection was stopped at the end of the trial. Two plausible causes of the loss of thermal performance were suggested: fouling of the moisture separators and loss of the porous outer layer of deposit on the tube-bundle.[16] Of these two factors, loss of the porous outer layer was suggested to be the more likely [133], although this explanation does not account for the observation that the loss took place primarily during the last six weeks of the trial. Fouling of both the moisture separators and the steam venturis is consistent with the high moisture carry-over-rate of 1% at ANO-2. With blow-down iron concentrations averaging 14 to 32 times higher during the trial compared to pre-trial values[17], the fouling rates of any components exposed to high-pressure steam will be correspondingly higher during PAA injection. The rate of moisture carry-over at ANO-2 is anomalously high, and so the effect of elevated suspended iron concentration in the SG on the fouling of steam-cycle components down stream of the SGs will be significantly

---

[16] The outer porous layer reduces the wall superheat required for bubble nucleation, hence, acts to increase the rate of heat transfer. Only the dense inner layer offers a resistance to heat transfer.

[17] A log mean average is reported in Reference [131].

AECL NUCLEAR REVIEW
VOL 2, NUMBER 1, JUNE 2013

FOULING OF NUCLEAR STEAM GENERATORS: FUNDAMENTAL STUDIES, OPERATING
EXPERIENCE AND REMEDIAL MEASURES USING CHEMICAL ADDITIVES - C.W. TURNER

higher at ANO-2 than at other plants. Fouling of steam-cycle components is not expected to affect performance at plants where the rate of moisture carry-over is not an issue.[18]

The short term trial at ANO-2 was followed by a longer term trial at McGuire-2. PAA was injected into the feedwater to achieve a feedwater concentration ranging from 0.5 to 4 µg/kg. Blow-down efficiency increased from a pre-trial value of 5% to values in the range 45 to 50% when the PAA concentration was maintained between 2 and 4 µg/kg, i.e., roughly equivalent to the feed-water total iron concentration. It was reported that none of the secondary-system chemistry parameters were adversely affected during the trial. Exelon is implementing online PAA dispersant technology at Braidwood Units 1 and 2 and at Byron Units 1 and 2. Preliminary results are encouraging, with iron blow-down efficiencies at both Braidwood and Byron increasing to more than 50% [133, 134].

5. Summary and Conclusions

Fouling remains a potentially serious issue that if left unchecked can lead to degradation of the safety and performance of nuclear SGs. It has been demonstrated that the majority of the corrosion product transported with the feed water to the SGs accumulates in the SG on the tube-bundle. By increasing the risk of tube failure and acting as a barrier to heat-transfer, deposit on the tube-bundle has the potential to impair the ability of the SG to perform its two safety critical roles: provision of a barrier to the release of radioactivity from the reactor coolant and removal of heat from the primary coolant during power operation and under certain post accident scenarios. Thus, it is imperative to develop improved ways to mitigate SG fouling for the long-term safe, reliable and economic performance of NPPs.

Fifty years ago, the understanding of heat exchanger fouling was largely phenomenological, based on little or no mechanistic information. The impact of fouling on heat-exchanger performance was accounted for by adding a "fouling factor" to the heat-transfer calculation so the heat exchanger could be properly sized to take account of the impairment of heat-transfer by fouling. For the design of heat-exchanger equipment used in aqueous systems, the first edition of the Tubular Exchanger Manufacturers Association (TEMA) tables of fouling factors applicable to shell and tube heat exchanger equipment lists fouling factors for the following types of cooling water: sea water, brackish water, muddy water, river water, etc. [135]. Different fouling factors are suggested depending on whether the temperature is greater than or less than $\sim 50\,°C$ and whether the fluid velocity is greater than or less than ~ 1 m/s.

Significant progress has been made in developing a mechanistic understanding of the fouling of heat exchangers over the past five decades. As discussed in this paper,

particulate fouling is now understood in terms of a process involving particle transport, attachment, removal and consolidation on the heat-transfer surface. Correlations have been developed that have been shown to give good agreement with experimental data for the transport of fine particles (~ 1 µm) from the bulk to the heat-transfer surface in aqueous systems. The effect of water chemistry on the rate of particulate fouling by corrosion products is described by taking account of the effect of pH on the surface potentials of both the corrosion products and the surface on which they are depositing. Advances have been made in understanding the influence of boiling on the rate of particulate fouling by probing the nature of the particle-bubble interaction and how this interaction contributes to the accumulation of particles at bubble nucleation sites. Water chemistry has been shown to exert a strong influence on the rate of particulate fouling under flow-boiling conditions. For example, the amine used to control the pH has been shown to have a strong effect on the fouling rate, quite apart from any effect of pH. A class of amine known as filming amines appears to be particularly effective at reducing the particulate fouling rate under flow-boiling conditions, and, of course, dispersants have been used in industrial boilers for years to mitigate fouling. These latter chemicals are just starting to be introduced for use with nuclear SGs, and promise to be effective tools for the mitigation of the fouling of nuclear SGs.

Alternative amines, filming amines and dispersants all hold good promise for the development of improved water treatment strategies to mitigate the fouling of SGs, and especially fouling of the tube-bundle. How these reagents act to mitigate fouling, however, is not well understood. Further research is needed to better understand why some amines, for example, DMA, are effective at reducing the rate of deposit consolidation, thereby making it easier to remove particles that have already deposited and reducing the overall rate of fouling. The mechanism by which filming amines and dispersants act to reduce the fouling rate in boiling water is also not well understood. It is known from previous investigations that dispersants that are effective at mitigating fouling under flow-boiling heat-transfer are not necessarily effective when heat-transfer is by single-phase forced convection. This result focuses attention on the bubble-nucleation process itself, and how it affects the rate of particulate fouling. Further research into the influence of filming amines and dispersants on bubble-nucleation and growth, the particle-bubble interaction and subsequent accumulation of particles at bubble-nucleation sites should prove beneficial towards developing a better understanding of why these reagents are effective at mitigating particulate fouling in flow-boiling systems and how to develop new and improved water-treatment chemistries to mitigate the fouling of SGs.

---

[18] Moisture carry over rates at plants with properly functioning moisture separators are generally < 0.25%.

AECL NUCLEAR REVIEW
VOL 2, NUMBER 1, JUNE 2013

FOULING OF NUCLEAR STEAM GENERATORS: FUNDAMENTAL STUDIES, OPERATING
EXPERIENCE AND REMEDIAL MEASURES USING CHEMICAL ADDITIVES - C.W. TURNER

REFERENCES

[1] International Atomic Energy Agency, 1997, "Assessment and Management of Ageing of Major Nuclear Power Plant Components Important to Safety: Steam Generators", Report IAEA-TECDOC-981.

[2] J. Riznic and S. Milivojevic, 2006, "Some Performance Indicators of PWR Steam Generators", Proceedings of the 5th Canadian Nuclear Society International Steam Generator Conference, Toronto, Canada, 2006 November 26-29.

[3] R.L. Tapping, J. Nickerson, P. Spekkens, and C. Maruska, 2000, "CANDU Steam Generator Life Management", Nuclear Engineering and Design, 197(1), pp. 213-223.

[4] R.W. Staehle, J.A. Gorman, A. McIlree and R.L. Tapping, 2006, "Status and Future of Corrosion in PWR Steam Generators", Presented at Fontrevaud 6, Fontrevaud Royal Abbey, France, 2006 September 18-22, Paper A106-T06.

[5] B. Lukasevitch, N. Trunov, V. Sotskov and S. Harchenko, 2006, "The Past and the Future of Horizontal Steam Generators", Proceedings of the 5th Canadian Nuclear Society International Steam Generator Conference, Toronto, Ontario, Canada, 2006 November 26-29.

[6] C.W. Turner, 2011, "Implications of Steam Generator Fouling on the Degradation of Material and Thermal Performance", Proceedings of the 15th International Conference on the Environmental Degradation of Materials in Nuclear Reactor Systems, Colorado Springs, Colorado, USA, August 7-11, 2011, pp. 2287-2299.

[7] J.A. Sawicki and M.E. Brett, 1993, "Mossbauer Study of Corrosion Products from a CANDU Secondary System", Nuclear Instruments and Methods in Physics Research B76(1-4), pp. 254-257.

[8] "Pressurized Water Reactor Secondary Water Chemistry Guidelines-Revision 7", Electric Power Research Institute Final Report 1016555, February 2009.

[9] J.A. Sawicki, M.E. Brett and R.L. Tapping, 1998, "Corrosion-Product Transport, Oxidation State and Remedial Measures", Atomic Energy of Canada Report AECL-11959, COG-98-314-I, 1998 October.

[10] P.J. Millett and S.G. Sawochka, 1994, "Investigation of Redox Conditions in the Secondary System of PWRs", Proceedings of Chemistry in Water Reactors: Operating Experience and New Developments, Nice, France, April 24-27, 1994, pp. 618-622.

[11] A.A. Efimov, L.N. Moskvin, G.N. Belozerskii, M.I. Kazakov, B.A. Gusev, and A.V. Semenov, 1989, "Mössbauer Phase Analysis of Corrosion Products Dispersed in Nuclear Power Station Coolant", Atomnaya Energiya, 67(6), pp. 389-392.

[12] G.A. Sehmel, 1970, "Particle Sampling Bias Introduced by Anisokinetic Sampling and Deposition Within the Sampling Line", American Industrial Hygiene Association Journal, 31(6), pp. 758-771.

[13] V. Vitols, 1966, "Theoretical Limits of Errors due to Anisokinetic Sampling of Particulate Matter", Journal of the Air Pollution Control Association, 16(2), pp. 79-84.

[14] E.J. Bird, 1984, "Experience of Continuous Isokinetic Sampling on the Winfrith Reactor", Proceedings: Workshop on Corrosion Product Sampling From Hot Water Systems, Electric Power Research Institute Report EPRI NP-3402-SR, March 1984, pp.2-1 – 2-19.

[15] P. Srisukvatananan, D.H. Lister, R. Svoboda and K. Daucik, 2007, "Assessment of the Sate of the Art of Sampling of Corrosion Products from Water/Steam Cycles", Power Plant Chemistry, 9(10), pp. 613-626.

[16] P. Srisukvatananan, D.H. Lister, C.E. Ng, R. Svoboda, and K. Daucik, 2008, "Corrosion Product Sampling in Power Plants under Water/Steam Cycle Conditions", Proceedings on the 15th International Conference on the Properties of Water and Steam, Berlin, Germany.

[17] C.C. Stauffer, 1984, "Corrosion Product Sampling Experience at Babcock and Wilcox", Proceedings: Workshop on Corrosion Product Sampling From Hot Water Systems, Electric Power Research Institute Report EPRI NP-3402-SR, March 1984, pp. 7-1 – 7-23.

[18] G.F. Palino, D. McNea and W.R. Kassen, 2000, "Design of PWR Reactor Coolant Hot Sample Panel for Diablo Canyon", Electric Power Research Institute Report 1000990, December 2000.

[19] J. Sawicki, 1999, "Proceedings of the COG Workshop on Layup, Shutdown and Startup Chemistry Optimization", CANDU Owners Group Report COG-00-066-I, 1999 March

[20] K. Verma, S. Odar and D. Scott, 1996, "Steam Generator Secondary Side Chemical Cleaning at Point Lepreau using the Siemen's High Temperature Process", Presented at the 4th Technical Committee Meeting on the Exchange of Operational Safety Experience of Pressurized Heavy Water Reactors, Kyong-Ju, Korea, April 21-26, 1996.

[21] S. Plante, 2005, "Steam Generator Secondary Side Chemical Cleaning at Gentilly-2", Proceedings of the Seventh CNS International Conference on CANDU Maintenance, Toronto, Ontario, Canada, November 20-22, 2005.

[22] J. Taborek, T. Aoki, R.B. Ritter, and J.W. Palen, 1972, "Fouling: The Major Unresolved Problem in Heat-transfer", Chemical Engineering Progress, 68(2), pp. 59-67.

[23] C.W. Turner, S.J. Klimas, and M.G. Brideau, 2000,"Thermal Resistance of Steam-Generator Tube Deposits under Single-Phase Forced Convection and Flow-Boiling Heat-transfer", Canadian Journal of Chemical Engineering, 78(2), pp. 53-60.

[24] J.T. Lovett and B.L. Dow, 1991, "Steam Generator Performance Degradation", Electric Power Research Institute Report NP-7524.

[25] M. Yetisir, C.W. Turner and J. Pietralik, 2000, "Contribution of SG Degradation Mechanisms to RIHT Behaviour", Proceedings of the Fifth CANDU Maintenance Conference, Toronto, Ontario, Canada, November 19-21, 2000, pp. 319-326.

[26] M. Kreider, G.A. White, and R.D. Varrin, Jr., 1998, "A Global Fouling Factor Methodology for Analyzing Steam Generator Thermal Performance Degradation", Third International Steam Generator and Heat Exchanger Conference, Toronto, Ontario, Canada, June 1998, pp.191-208.

[27] 1994, Steam Generator Progress Report, Revision 10, Energy Management Services, Inc., Little Rock, Arkansas, November 1994.

[28] P.V. Balakrishnan, S.M. Pagan, S.M. McKay and F. Gonzalez, 1996, "Hideout and Hideout Return: Laboratory Studies and Plant Measurements", CANDU Owners Group Report COG-95-555-I, 1996 May.

[29] P.V. Balakrishnan, 1999, "Hideout, Hideout Return and Crevice Chemistry in Steam Generators", Proceedings of the Thirteenth International Conference on the Properties of Water and Steam, Toronto, Ontario, Canada, September 12-16, 1999, pp. 858-865.

[30] Y. Lu, 2007, "Define Optimal Conditions for Steam Generator Tube Integrity and an Extended Steam Generator Service Life", 15th International Conference on Nuclear Engineering ICONE-15, Nagoya, Japan, April 2007, Paper ICONE15-10854.

[31] H.E.C. Rummens, 1999, "The Thermalhydraulics of Tube-Support Fouling in Nuclear Steam Generators", PhD Thesis, Carleton University, Ottawa, Canada.

[32] L.E. Johnson, 1987, "Fouling in Nuclear Once-Through Steam Generators", Paper 87-WA/NE-12, ASME Winter Annual Meeting, Boston, Massachusetts, USA.

[33] R.H. Thompson and L.S. Lammana, 1986, "Video Inspection and Sampling of the Crystal River Unit-3 Once-Through Steam Generators", Proceedings of the Fourty-seventh International Water Conference, Pittsburgh, Pennsylvania, Paper IWC-86-3, pp.9-16.

[34] R.H. Thompson, 1992, "Fouling of the Crystal River-3 Once-Through Steam Generators After Switchover to Morpholine Water Chemistry", Proceedings of the 1992 International Joint Power Generation Conference, Atlanta, ASME NE-Volume 8, pp. 29-38.

[35] M.M. Stickel, E.P. Morgan, M.H. Hu, H.L. Miller and J.O. Eastwood, 1994, "Steam Generator Water Level Oscillations Resulting from Sludge Induced Flow Blockage", Proceedings: Steam Generator Sludge Management Workshop, Norfolk, Virginia, EPRI Report TR-104212, pp. 15-1 – 15-33.

[36] R. Dyck, P. Spekkens, K. Verma, and A. Marchand, 1990, "Operational Experience with Steam Generators in Canadian Nuclear Plants", Proceedings of the Steam Generator and Heat Exchanger Conference, Toronto, Ontario, Canada, April-May 1990, pp. 1-10 – 1-127.

[37] J. Malaugh and S. Ryder, 1990, "Bruce NGS-A Support Plate Inspection and Waterlancing", Proceedings of the Steam Generator and Heat Exchanger Conference, Toronto, Ontario, Canada, April-May 1990, pp. 3-51 – 3-76.

[38] H. Bodineau and T. Sollier, 2008, "Tube-support Plate Clogging Up of French PWR Steam Generators", Eurosafe 2008 Forum, Paris, France.

[39] G. Corredera, M. Alves-Vieira and O. De Bouvier, 2008, "Fouling and TSP Blockage of Steam Generators on EDF Fleet: Identified Correlation with Secondary Water Chemistry and Planned Remedies", International Conference on Water Chemistry of Nuclear Reactor Systems, Berlin, Germany, September 15-18, 2008.

[40] P. Luna, G. Diaz, H. Sveruga and R. Sainz, 2006, "Maintenance and Life

AECL NUCLEAR REVIEW
VOL 2, NUMBER 1, JUNE 2013

FOULING OF NUCLEAR STEAM GENERATORS: FUNDAMENTAL STUDIES, OPERATING
EXPERIENCE AND REMEDIAL MEASURES USING CHEMICAL ADDITIVES - C.W. TURNER

Assessment of Steam Generators at Embalse Nuclear Station", Proceedings of the 5th Canadian Nuclear Society International Steam Generator Conference, Toronto, Ontario, Canada, November 26-29, 2006.

[41] L. Obrutsky, R. Cassidy, M. Cazal and K. Sedman, 2006, "Eddy Current Assessment of Support Plate Structures Degradation in Nuclear Steam Generators", 5th Canadian Nuclear Society International Steam Generator Conference, Toronto, Ontario, Canada, November 26-29, 2006.

[42] K.G. Sedman, G.E. Galan and B. Dicks, 2005, "Boiler Tube-support Plate Degradation in Bruce Unit 8", Proceedings of the Seventh Canadian Nuclear Society International Conference on CANDU Maintenance, Toronto, Ontario, Canada, November 20-22, 2005.

[43] N. Epstein, 1983, "Thinking about Heat-transfer Fouling: A 5 x 5 Matrix", Heat-transfer Engineering, 4(1), pp. 43-56.

[44] J.S. Gudmundsson, 1981, "Particulate Fouling", Fouling of Heat-transfer Equipment, Editors E.F.C. Somerscales and J.G. Knudsen, Hemisphere, Washington D.C., pp. 357-387.

[45] A.B. Metzner and W.L. Friend, 1958, "Theoretical Analogies between Heat, Mass and Momentum Transfer and Modifications for Fluids of High Prandtl or Schmidt Numbers", The Canadian Journal of Chemical Engineering, 36(6), pp. 235-240.

[46] J.W. Cleaver and B. Yates, 1975, "A Sub Layer Model for the Deposition of Particles from a Turbulent Flow", Chemical Engineering Science, 30(8), pp. 983-992.

[47] S.K. Friedlander and H.F. Johnstone, 1957, "Deposition of Suspended Particles from Turbulent Gas Streams", Industrial & Engineering Chemistry, 49(7), pp. 1151-1156.

[48] M.W. Reeks and G. Skyrme, "The Dependence of Particle Deposition Velocity on Particle Inertia in Turbulent Pipe Flow", 1976, Journal of Aerosol Science, 7(6), pp. 485-495.

[49] A. Guha, 1997, "A Unified Eulerian Theory of Turbulent Deposition to Smooth and Rough Surfaces", Journal of Aerosol Science, 28(8), 1517-1537.

[50] P.G. Papavergos and A.B. Hedley, 1984, "Particle Deposition Behaviour from RidgeTurbulent Flows", Chemical Engineering Research and Design, 62(5), pp. 275-295.

[51] A.M. Reynolds, 1999, "A Lagrangian Stochastic Model for Heavy Particle Deposition", Journal of Colloid and Interface Science, 215(1), pp. 85-91.

[52] C.W. Turner, 1993, "Rates of Particle Deposition from Aqueous Suspensions in Turbulent Flow: A Comparison of Theory with Experiment", Chemical Engineering Science, 48(12), pp. 2189-2195.

[53] N. Epstein, 1981, "Fouling: Technical Aspects (Afterword to Fouling in Heat Exchangers)", Fouling of Heat-transfer Equipment, Editors E.F.C. Somerscales and J.G. Knudsen, Hemisphere, Washington D.C., pp. 31-53.

[54] E. Ruckenstein and D.C. Prieve, 1973, "Rate of Deposition of Brownian Particles Under the Action of London and Double-Layer Forces", Journal of the Chemical Society, Faraday Transactions II, 69, pp. 1522-1536.

[55] P.C. Hiemenz and R. Rajagopalan, 1997, "Principles of Colloid and Surface Chemistry", 3rd Rev. Ed., Marcel Dekker, Inc., New York.

[56] G.A. Parks and P.L. de Bruyn, 1962, "The Zero Point of Charge of Oxides", Journal of Physical Chemistry, 66(6), pp. 967-973.

[57] J.W. Cleaver and B. Yates, 1973, "Mechanism of Detachment of Colloidal Particles from a Flat Substrate in a Turbulent Flow", Journal of Colloid and Interface Science, 44(3), pp. 464-474.

[58] M.E O'Neill, 1968, "A Sphere in Contact with a Plane Wall in a Slow Linear Shear Flow", Chemical Engineering Science, 23(11), pp. 1293-1298.

[59] P.G. Saffman, 1965, "The Lift on a Small Sphere in a Slow Shear Flow", Journal of Fluid Mechanics, 22(2), pp. 385-400.

[60] B.P.K. Yung, H. Merry,and T.R. Bott, 1989, "The Role of Turbulent Bursts in Particle Re-Entrainment in Aqueous Systems", Chemical Engineering Science, 44(4), pp. 873-882.

[61] J.W. Cleaver and B. Yates, 1976, "The Effect of Re-Entrainment on Particle Deposition", Chemical Engineering Science, 31(2), pp. 147-151.

[62] C.W. Turner, M.E. Blimkie and P.A. Lavoie, 1997, "Physical and Chemical Factors Affecting Sludge Consolidation", Atomic Energy of Canada Report AECL-11674, COG-96-492-I, 1997 September.

[63] C.W. Turner and S.J. Klimas, 2001, "The Effect of Surface Chemistry on Particulate Fouling under Flow-Boiling Conditions", Proceedings of Heat Exchanger Fouling: Fundamental Approaches and Technical Solutions, Davos, Switzerland. AECL-12171.

[64] A.W. Adamson, 1982, "Physical Chemistry of Surfaces", Fourth Edition, John Wiley & Sons, New York.

[65] C.W. Turner and D.W. Smith, 1998, "Calcium Carbonate Scaling Kinetics Determined from Radiotracer Experiments with Calcium-47", Industrial & Engineering Chemistry Research, 37(2), pp. 439-448. AECL-11906

[66] S.J. Klimas, D.G. Miller, J. Semmler, and C.W. Turner, 1998, "The Effect of the Removal of Steam Generator Tube ID Deposits on Heat-transfer", Third International Heat Exchanger and Steam Generator Conference, Toronto, Ontario. AECL-11985.

[67] H.E.C. Rummens and C.W. Turner, 1994, "Experimental Studies of Flow Pattern Near Tube-support Structures", Proceedings of the 2nd International Steam Generator and Heat Exchanger Conference, Toronto, Ontario. AECL-11145, COG-94-361.

[68] H.E.C. Rummens, J.T. Rogers and C.W. Turner, 2004, "The Thermal Hydraulics of Tube-support Fouling in Nuclear Steam Generators", Nuclear Technology, 148(3), pp. 268-286.

[69] C.W. Turner, D.A. Guzonas and S.J. Klimas, 2004, "Surface Chemistry Interventions to Control Boiler Tube Fouling – Part II", Atomic Energy of Canada Limited Report AECL-12100, 2004 June.

[70] D.Q. Kern and R.E. Seaton, 1959, "A Theoretical Analysis of Thermal Surface Fouling", British Chemical Engineering, 4(5), pp. 258-262.

[71] G.S. McNab and A. Meisen, 1973, "Thermophoresis in Liquids", Journal of Colloid and Interface Science, 44(2), pp. 339-346.

[72] C.W. Turner and D.W. Smith, 1992, "A Study of Magnetite Particle Deposition onto Alloy-800 and Alloy-600 between 25 and 80 °C and predicted rates under steam generator operating conditions", Proceedings of Steam Generator Sludge Deposition in Recirculating and Once Through Steam Generator Upper Tube-bundle and Support Plates, Editors R.L. Baker and E.A. Harvego, Atlanta, ASME NE, 8, pp. 9-18. AECL-10754, COG-92-344.

[73] D.H. Lister and F.C. Cussac, 2007, "Modelling of Particulate Fouling on Heat Exchanger Surfaces: Influence of Bubbles on Iron Oxide Deposition", Proceedings of the Seventh International Conference on Heat Exchanger Fouling and Cleaning - Challenges and Opportunities 2007, Editors Hans Muller-Steinhagen, M. Reza Malayeri and A. Paul Watkinson, Engineering Conferences International, Tomar, Portugal, pp. 268-277.

[74] A.P. Watkinson and N. Epstein, 1970, "Particulate Fouling of Sensible Heat Exchangers", Proceedings of the Fourth International Heat-transfer Conference, Versailles, France, Volume 1, Paper HE1.6.

[75] R.M. Hopkins and N. Epstein, 1974, "Fouling of Heated Stainless Steel Tubes by a Flowing Suspension of Ferric Oxide in Water", Proceedings of the Fifth International Heat-transfer Conference, Tokyo, Japan, Volume 5, pp. 180-184.

[76] J.S. Gudmundsson, 1977, "Fouling of Surfaces", Ph.D. Thesis, University of Birmingham.

[77] I.H. Newson, 1979, "Studies of Particulate Deposition from Flowing Suspension", Fouling - Science or Art?, University of Surrey, pp. 35-81.

[78] I.H. Newson, T.R. Bott, and C. Hussain, 1981, "Studies of Magnetite Deposition from a Flowing Suspension", Fouling in Heat Exchange Equipment, ASME Heat-transfer Division, Publication HTD Volume 17, pp. 73-81.

[79] I.H. Newson, T.R. Bott and C.I. Hussain, 1983, "Studies of Magnetite Deposition from a Flowing Suspension", Chemical Engineering Communications, 20(5-6), pp. 335-353.

[80] C.I. Hussain, I.H. Newson, and T.R. Bott, 1986, "Diffusion Controlled Deposition of Particulate Matter from Flowing Slurries", Heat-transfer 1986: Proceedings of the Eighth International Heat-transfer Conference, San Francisco, California, Volume 5, pp. 2573-2579.

[81] D. Thomas and U. Grigull, 1974, "Experimental Investigation of the Deposition of Suspended Magnetite from the Fluid Flow in Steam Generating Boiler Tubes", Brennstoff-Warme-Kraft, 26(3), pp. 109-115.

[82] I.H. Newson, G.A. Miller, J.W. Haynes, T.R. Bott, and R.D. Williamson, 1988, "Particulate Fouling: Studies of Deposition, Removal and Sticking Mechanisms in a Hematite/Water System", Proceedings for the Second United Kingdom National Conference on Heat-Transfer, Glasgow, Volume 1, pp. 137-160.

[83] R. Williamson, I. Newson and T.R. Bott, 1988, "The Deposition of Haematite Particles from Flowing Water", Canadian Journal of Chemical Engineering, 66(1), pp. 51-54.

[84] R.J. Kuo and E. Matijevic,1981, "Particle Adhesion and Removal in Model Systems. III Monodispersed Ferric Oxide on Steel", Journal of Colloid Interface Science, 78(2), pp. 407-421.

AECL NUCLEAR REVIEW
VOL 2, NUMBER 1, JUNE 2013

FOULING OF NUCLEAR STEAM GENERATORS: FUNDAMENTAL STUDIES, OPERATING
EXPERIENCE AND REMEDIAL MEASURES USING CHEMICAL ADDITIVES - C.W. TURNER

[85] C.W. Turner, D.H. Lister and D.W. Smith, 1990, "The Deposition and Removal of Sub-Micron Particles of Magnetite at the Surface of Alloy 800", Proceedings of the Steam Generator and Heat Exchanger Conference, Toronto, Ontario, Volume 2, 6B-64-6B-76. AECL-10441.

[86] K.A. Burrill, 1977, "The Deposition of Magnetite Particles from High Velocity Water onto Isothermal Tubes", Atomic Energy of Canada Limited Report AECL-5308 1977 February.

[87] N.N. Mankina, 1961, "Formation of Iron Deposits in Recirculation Steam Boilers", British Power Engineering, 2(4), pp. 60-63.

[88] N.N. Mankina and B.L. Koktotv, 1973, "On the Problem of the Mechanism of Formation of Iron Oxide Deposits", Teploenergetika, 9, pp. 15-17.

[89] D.H. Charlesworth, 1970, "The Deposition of Corrrosion Products in Boiling Water Systems", Chemical Engineers Symposium Series 66, Number 104, pp. 21-30. AECL-3883.

[90] F.D. Nicholson and J.V. Sarbutt, 1980, "The Effect of Boiling on the Mass Transfer of Corrosion Products in High Temperature, High Pressure Water Circuits", Corrosion, 36(1), pp. 1-9.

[91] I. Iwahori, T. Mizun and H. Koyama, 1979, "Role of Surface Chemistry in Crud Deposition on Heat-transfer Surface", Corrosion, 35(8), pp. 345-350.

[92] Y. Asakura, M. Kikuchi, S. Uchida and H. Yusa, 1978, "Deposition of Iron Oxide on Heated Surfaces in Boiling Water", Nuclear Science and Engineering, 67(1), pp. 1-7.

[93] Y. Asakura, M. Kikuchi, S. Uchida and H. Yusa, 1979, "Iron Oxide Deposition on Heated Surfaces in Pressurized Boiling Water", Nuclear Science and Engineering, 72(1), pp. 117-120.

[94] M. Basset, J. McInerney, N. Arbeau and D.H. Lister, 2000, "The Fouling of Alloy-800 Heat Exchange Surfaces by Magnetite Particles", Canadian Journal of Chemical Engineering, 78(1), pp. 40-52.

[95] H. Carpentier, L. McCrea, and D.H. Lister, 2001, "Deposition of Corrosion Product Particles onto Heat Exchange Surfaces in Bulk Boiling", Proceedings of the International Conference On Heat Exchanger Fouling, Davos, Switzerland, July 8-13, 2001.

[96] N. Arbeau, W. Cook, and D. Lister, 2004, "The Early Stages of Deposition of Magnetite Particles onto Alloy-800 Heat Exchange Surfaces under Subcooled Boiling Conditions", Proceedings of the 2003 ECI Conference on Heat Exchanger Fouling and Cleaning: Fundamentals and Applications, Santa Fe, New Mexico, May 18-22, 2003, Paper 35, pp. 256-262.

[97] L. Wen and C.A. Melendres, 1998, "On the Mechanism of Hematite Deposition on a Metal Surface Under Nucleate Boiling Conditions", Colloids and Surfaces A: Physicochemical and Engineering Aspects, 132(2-3), pp. 315-319.

[98] C.W. Turner, S.J. Klimas and M.G. Brideau, 1997, "The Effect of Alternative Amines on the Rate of Boiler Tube Fouling", Atomic Energy of Canada Limited Report AECL-11848, 1997 October, Electric Power Research Institute Report EPRI TR-108004.

[99] C.W. Turner, S.J. Klimas and P.L. Frattini, 1988, "Reducing Tube-bundle Deposition with Alternative Amines", Proceedings of the Third International Steam Generator and Heat Exchanger Conference, Toronto, Ontario, Canada, June 1998, pp. 257-273.

[100] C.W. Turner, D.A. Guzonas, and S.J. Klimas, 1999, "Surface Chemistry Interventions to Control Boiler Tube Fouling", AECL-12036 (2000), EPRI Report TR-110083 (1999).

[101] S.J. Klimas, D.A. Guzonas and C.W. Turner, 2002, "Identification and Testing of Amines for Steam Generator Chemistry and Deposit Control", EPRI Report 1002773, December 2002.

[102] S.J. Klimas, K. Fruzzetti, C.W. Turner, P.V. Balakrishnan, G.L. Strati, and R.L. Tapping, 2003, "Identification and Testing of Amines for Steam Generator Corrosion and Fouling Control", 2003 ECI Conference on Heat Exchanger Fouling and Cleaning: Fundamentals and Applications, Santa Fe, New Mexico, May 18-22, 2003, Paper 37, pp. 271-278.

[103] M.A.A. Schoonen, 1994, "Calculation of the Point of Zero Charge of Metal Oxides Between 0 and 350 °C", Geochimica et Cosmochimica Acta, 58(13), pp. 2845-2851.

[104] S.J. Klimas, Y. Lu, and D. Beaton, 2004, "Identification and Testing of Amines for Steam Generator Chemistry and Deposit Control – Part 3: Qualification of Dodecylamine as an Amine Additive for Steam Generator Fouling Mitigation", EPRI 1011320, November 2004.

[105] P.V. Balakrishnen, S.J. Klimas L. Lepine, and C.W. Turner, 1999, "Polymeric Dispersants for Control of Steam Generator Fouling", Atomic Energy of Canada Limited Report AECL-11975, COG-99-165-I, 1999 May.

[106] P. Burgmayer, R. Crovetto, C. W. Turner and S.J. Klimas, 1999, "Effectiveness of Selected Dispersants on Magnetite Deposition at Simulated PWR Heat-Transfer Surfaces", AECL-11976, 1999 July.

[107] H. Hirano, M. Domae, K. Miyajima and K. Yoneda, 2010, "Study on the Mechanism of Flow-Hole Blockage of Steam Generator Tube-support Plates under PWR Secondary Conditions", Nuclear Plant Chemistry Conference 2010, Quebec City.

[108] H.E.C. Rummens, C.W. Turner and J.T. Rogers, 1997, "The Effect of Tube-Support Design on Steam Generator Fouling Susceptibility", Proceedings of Understanding Heat Exchanger Fouling and Mitigation, Lucca. AECL report FFC-FCT-079P.

[109] T. Prusek, E. Moleiro, F. Oukacine, O. Touazi, M. Grandotto, M. Jaeger and A. Adobes, 2011, "Deposit Model for Tube-support Plate Blockage in Steam Generators", Proceedings of the Fourteenth International Topical Meeting on Nuclear Reactor Thermalhydraulics, Toronto, Ontario.

[110] T.R. Beck, D.W. Mahaffey and J.H. Olsen, 1970, "Wear of Small Orifices by Streaming Current Driven Corrosion", Transactions of the ASME Journal of Basic Engineering, 92(4), pp. 782-788.

[111] I.S. Woolsey, D.M. Thomas, K. Garbett and G.J. Bignold, 1989, "Occurrence and Prevention of Enhanced Oxide Deposition in Boiler Flow Control Orifices", Water Chemistry of Nuclear Reactor Systems 5, Bournemouth, England, Volume 1, pp. 219-228.

[112] J. Robertson, 1986, "Corrosion and Deposition Due To Electrokinetic Currents", Central Electricity Generating Board Report TPRD/L/3030/R86, September.

[113] R.J. Hunter, 1981, "Zeta Potential in Colloid Science: Principles and Applications", Academic Press, New York.

[114] M. Guillodo, P. Combrade, B. dos Santos, T. Muller, G. Berthollon, N. Engler, C. Brun and G. Turluer, 2005, "Formation of Deposits in HT Water Under High Velocity Conditions: A Parametric Study", Proceedings of the International Conference on Water Chemistry of Nuclear Reactor Systems, San Francisco, California, October 2004, EPRI 1011579, pp. 1941-1949.

[115] M. Guillodo, T. Muller, M. Barale, M. Foucault, M-H. Clinard, C. Brun, F. Chahma, G. Corredera and O. de Bouvier, 2009, "Singular Deposit Formation in PWR Due to Electrokinetic Phenomena-Application to SG Clogging", 6th CNS International Steam Generator Conference, Toronto, Ontario, November 8-11, 2009, Paper 4.05.

[116] M. Barale, M. Guillodo, C. Brun, M-H. Clinard, G. Corredera and O. De Bouvier, 2008, "Preliminary Laboratory Tests of Investigation on the Blockage Phenomena Observed on TSP of French SGs", Proceedings of the International Conference on Water Chemistry of Nuclear Reactor Systems, Berlin, Germany, Paper P2-41.

[117] M. Guillodo, M. Barale, M. Foucault, N. Ryckelynck, M-H. Clinard, F. Chahma, C. Brun, and G. Corredera, 2010, "Secondary Side TSP Deposit Buildup: Lab Test Investigation Focus on Electrokinetic Considerations", Nuclear Plant Chemistry Conference 2010 (NPC 2010), Quebec City, Quebec, October 3-7, 2010.

[118] R. Roofthooft, 1990, "Belgian Steam Generator Chemical Cleaning and Related Waste Management", Proceedings of the Steam Generator Sludge Management Workshop, Nashville, Tennessee.

[119] B.L.Dow, 1994, "Overview of Steam Generator Chemical Cleaning Experience", Proceedings: Steam Generator Sludge Management Workshop, Norfolk, Virginia, May 10-12, 1994, EPRI TR-104212, Paper 36.

[120] S. Evans, S. Watson, J. Remark, and C. Hengge, 2002, "Review of Steam Generator Chemical Cleaning Experiences from 1998–2002", Proceedings of the 4th Canadian Nuclear Society International Steam Generator Conference, Toronto, Ontario, Canada, May 5-8, 2002.

[121] C.W. Turner, Y Liner, and M.B. Carver, 1994, "Modelling Magnetite Particle Deposition in Nuclear Steam Generators and Comparisons with Plant Data", Second International Steam Generator and Heat Exchanger Conference, Toronto, Ontario, Canada, June 1994, pp. 4.51-4.64.

[122] C. Welty, 1984, "Steam Generator Needs and Practices: Uses of Data", Proceedings: Workshop on Corrosion Product Sampling From Hot Water Systems, Blacksburg, Virginia, August 18-19, 1983, Electric Power Research Institute Report EPRI NP-3402-SR, pp. 5-1 – 5-11.

AECL NUCLEAR REVIEW
VOL 2, NUMBER 1, JUNE 2013

FOULING OF NUCLEAR STEAM GENERATORS: FUNDAMENTAL STUDIES, OPERATING
EXPERIENCE AND REMEDIAL MEASURES USING CHEMICAL ADDITIVES - C.W. TURNER

[123] M. Chocron, N. Fernandez and J.A. Sawicki, 1999, "Crud Transport and Sludge Control at Embalse", Proceedings: Steam Generator Sludge Management Workshop, Scottsdale, Arizona, September 30-October 1, 1999, EPRI TR-114854, Paper 5-1.

[124] C. Marks, 2009, "Steam Generator Management Program: Effects of Different pH Control Agents on Pressurized Water Reactor Plant Systems and Components", Electric Power Research Institute Report 1019042.

[125] J.J. Schuck, C.C. Nathan and J.R. Metcalf, 1973, "Corrosion Inhibitors for Steam Condensate Systems", Materials Protection and Performance, 12(10), pp. 42-47.

[126] M.F. Obrecht, 1964, "Steam and Condensate Return Line Corrosion – How to Employ Filming Amines for its Control", Heating, Piping and Air Conditioning, pp. 116-122.

[127] A.A. Avdeev, A.N. Kukushkin, D.A. Repin, V.V. Omelchuk, L.F. Barmin, V.A. Yurmanov and E. Czempik, 2010, "The Impact of ODA Microadditions into Secondary System on Corrosion Rate Reduction in VVER Steam Generators", Nuclear Plant Chemistry Conference 2010 (NPC 2010), Quebec City, Quebec, October 3-7, 2010.

[128] J. Fandrich, S. Hoffmann-Wankel, U. Ramminger, and B. Stellwag, 2012, "pH Optimization Strategy and Application of Film Forming Amines in the Secondary Side Chemistry Treatment of NPPs", Proceedings: Steam Generator Management Program, 2012 Steam Generator Secondary Side Management Conference, Atlanta, Georgia, EPRI 1026545, pp. 2-344 – 2-386.

[129] U. Ramminger, S. Hoffmann-Wankel, and J. Fandrich, 2012, "The Application of Film Forming Amines in Secondary Side Chemistry Treatment of NPPs", Nuclear Plant Chemistry Conference 2012 (NPC 2012), Paris, France. (Also published in: Revue Generale Nucleaire, no.6, 2012, pp. .68-73)

[130] K. Fruzzetti, P. Frattini, P. Robbins, A. Miller, R. Varrin and M. Kreider, 2002, "Dispersant Trial at ANO-2: Results from a Short-Term Trial Prior to SG Replacement", International Conference on Water Chemistry in Nuclear Reactor Systems, Avignon, France, April 2002.

[131] K. Fruzzetti, P. Frattini, P. Robbins, A. Miller, R. Varrin, and M. Kreider, 2002, "Dispersant Trial at ANO-2: Results From a Short-Term Trial Prior to SG Replacement", International Conference on Water Chemistry in Nuclear Reactor Systems, Avignon, France, April 2002.

[132] K. Fruzzetti, D. Rochester, L. Wilson, M. Kreider and A. Miller, 2008, "Dispersant Application for Mitigation of Steam Generator Fouling: Final Results from the McGuire 2 Long-Term Trial and an Industry Update and EPRI Perspective for Long-Term Use", International Conference on Water Chemistry of Nuclear Reactor Systems, Berlin, Germany, September 15-18, 2008.

[133] K. Fruzzetti, S. Choi, C. Haas, M. Pender and D. Perkins, 2010, "PWR Chemistry Controls: A Perspective on Industry Initiatives and Trends Relative to Operating Experience and the EPRI PWR Water Chemistry Guidelines", Nuclear Plant Chemistry Conference 2010 (NPC 2010), Quebec City, Quebec, October 3-7, 2010.

[134] K. Fruzzetti, C. Anderson, C. Marks, M. Kreider, B. Walton, W. Reecher and D. Morey, 2010, "Dispersant Application: (1) During Steam Generator Wet Layup for Removal of Existing Deposits, and (2) During the Long-Path Recirculation Cleanup Process of the Condensate/Feedwater System to Reduce Startup Corrosion Product Transport to the Steam Generators", Nuclear Plant Chemistry Conference 2010 (NPC 2010), Quebec City, Quebec, October 3-7, 2010.

[135] "Standards of the Tubular Exchanger Manufacturers Association", First Edition, TEMA, New York (1941).

Using Function Approximation to Determine Neural Network Accuracy

R.F. Wichman* and J. Alexander

* Atomic Energy of Canada Limited, Chalk River Laboratories, Chalk River, Ontario, Canada, K0J 1J0

*Corresponding author: (613) 584-3311, wichmanr@aecl.ca

Many, if not most, control processes demonstrate non-linear behavior in some portion of their operating range and the ability of neural networks to model non-linear dynamics makes them very appealing for control. Control of high reliability safety systems, and autonomous control in process or robotic applications, however, require accurate and consistent control and neural networks are only approximators of various functions so their degree of approximation becomes important.

In this paper, the factors affecting the ability of a feed-forward back-propagation neural network to accurately approximate a non-linear function are explored. Compared to pattern recognition using a neural network for function approximation provides an easy and accurate method for determining the network's accuracy.

In contrast to other techniques, we show that errors arising in function approximation or curve fitting are caused by the neural network itself rather than scatter in the data. A method is proposed that provides improvements in the accuracy achieved during training and resulting ability of the network to generalize after training. Binary input vectors provided a more accurate model than with scalar inputs and retraining using a small number of the outlier x,y pairs improved generalization.

1. Introduction

Hornik *et al.* [1] establish that standard multilayer feedforward networks using arbitrary squashing functions (e.g., sigmoid, hyperbolic tangent) can approximate virtually any function of interest to any desired degree of accuracy, provided sufficiently many hidden units are available. Their results establish multilayer feedforward neural networks as a class of universal approximators and create high expectations for their application. When one considers the expanding use of neural networks in process control [2] it indicates that they may be effective function approximators [3].

It can also be difficult for neural networks to meet the expectation of an exact curve fit [4] and there are surprising failures. Hornik's paper attributes failures in applications to inadequate learning, inadequate numbers of hidden units, or the presence of a stochastic rather than deterministic relationship between the input and target. Inadequate learning can be defined as the inability of the network to converge to the desired accuracy using all of the *x,y* pairs presented during training. With accuracy a key concern in many important applications the ability of neural networks to meet this requirement becomes a factor critical to their use.

The proof of the ability to map from one finite dimensional map to another offered by Hornik does not address the accuracy of the mapping with input vectors that have not been trained i.e., the ability of the network to generalize. Hornik proved that the neural networks achieve convergence with a large enough number of neurons and hidden layers, but he doesn't specify any error bounds or rates of convergence. In pattern recognition, neural networks are known for their fault tolerance i.e., their ability to provide the desired classification with incomplete and inaccurate inputs, and generalization, i.e., their ability to provide the desired classification from subtle patterns with stochastic noise. The binary vector input used in this curve fitting may be analogous to pattern recognition input but the function approximation provides a target value that avoids the ambiguity that may be associated with categorizing patterns.

Computers are deterministic and, despite the complexity of the information flow through the network, the factors that control the accuracy of the neural network can be identified. These factors are explored for the popular feedforward back-propagation network architecture as described in Hornik's paper.
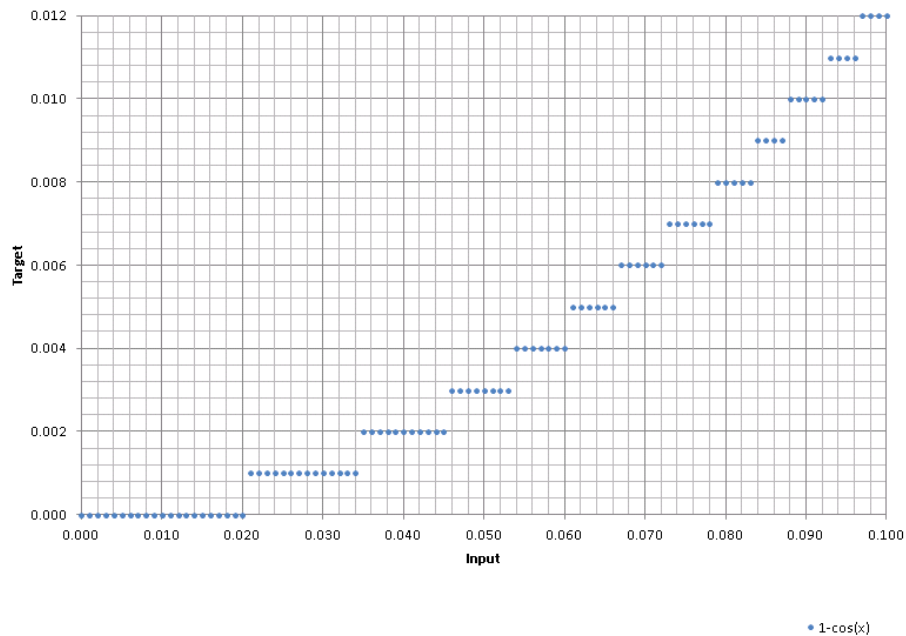
FIGURE 1: Numerical Precision.

2. Neural Network Accuracy

Modeling a known function ensures that a deterministic relationship exists between the input and output. In an area of interest in process control the flow area of a butterfly valve may be modelled by the non-linear function

$$y = 1 - \cos\theta \qquad (1)$$

where,

y = the normalized flow area that is directly proportional to the flow rate when the flow pressure is constant
θ = angle of rotation of the disc in the valve

Equation (1) also provides an exact function to be approximated by the neural network to assess its capability to meet the desired accuracy. The desired accuracy would be defined as having the exact value as the '1-cos' function rounded rather than truncated at the selected degree of numerical precision. Using rounded numerical precision offers the additional benefit of defining a complete set of discrete x,y pairs for the training of and comparison with the neural network.

With a numerical precision of 10^{-3} the normalized input x values fall into the range between 0.000 and 1.000 in steps of 0.001 and the corresponding y value can be calculated and rounded at each step to the same numerical precision. The

detail in the graph of this curve shown in Figure 1 illustrates that numerical rounding produces a series of small steps in the x,y pairs near zero (i.e., within the first 100 x values) and these steps introduce a modeling challenge for the neural network.

The neural network function approximation is given by:

$$g(\ ) = x/y \qquad (2)$$

where,

g( ) = an unknown function to be estimated from the training set,
x = is an input vector,
y = is the scalar output, and
y,x = is a training pair from the training set

As per the basis for Hornik's analysis, a neural network consisting of a hidden layer with the hyperbolic tangent squashing function and an output layer with a linear transfer function was used to develop the approximation. Training was based upon the delta rule and convergence was based upon an exact match between the target y value (10^{-3} precision) and the rounded calculated y value. Training was done with the entire set of 1001 x,y pairs and took about 76 minutes to converge using a single CPU.

TABLE 1: Neural Network Training Results

	Scalar X	Scalar X with Additional Hidden Units	Scalar X Converted to Binary Input Vector
x,y pairs	1001	1001	1001
Number of hidden units	8	100	20
Desired accuracy with rounding	10^{-3}	10^{-3}	10^{-3}
RMS error	1.5×10^{-2}	1.6×10^{-2}	0.000
Number of trained pairs within desired accuracy	27 (2.7%)	29 (2.9%)	1001 (100%)

The epoch error (average Root Mean Square (RMS) error of one iteration through the entire set of *x,y* pairs) and number rounded *y* values that matched the training *y* value exactly were used as the indicator of the adequacy of learning. Additional hidden units were also added to the network to determine their impact upon accuracy.

Similar neural network training was performed with the scalar *x* input values converted to their binary equivalent. Hornik's theorem 2.4 that suggests a single dimension input space would be adequate but the rationale for the binary form of the input may be illustrated using the data space used to developed by Minsky and Papert [10] to show the limitations of the simple two-layer perceptron. The data space available for classification with a vector input with two binary or floating point elements may be represented as per Figure 2.

In contrast the data space available to a single input i.e., a scalar *x* value, is limited to a position on a single line because both (i.e., all) hidden units see the same input value. The common input limits this simple network's ability to classify the input to a single point on this line. The number of degrees of freedom of *x* has been reduced.

The numerical results are presented in Table 1 – Neural Network Training Results. To illustrate the difference between the vector and scalar results the expanded curves are provided in Figures 4 and 5.

As noted in Table 1 converting the scalar value to a binary vector resulted in a network that met the numerical precision completely for the entire set of *x,y* pairs - including all of the small steps in Figure 1 and as illustrated in Figure 5. In comparison we can see that the neural network training with scalar *x* input met the desired accuracy for only small fraction of the total number of *x,y* pairs. Increasing the number of hidden units by an order of magnitude failed to improve the accuracy significantly. Changing the network to include a 'cos' transfer function would improve the results but that should not be required according to Hornik and would also require some knowledge of the curve *a priori*.

By defining the desired accuracy, in this case within a selected numerical precision, the entire input data set is also defined and neural network training provided accurate and completely deterministic results. The small size of a trained network requires very little computational time, the fact that it can be readily trained, the possible use of multiple inputs and outputs, and the ability to model a family of functions may make neural networks an attractive alternative to lookup tables in critical non-linear applications.
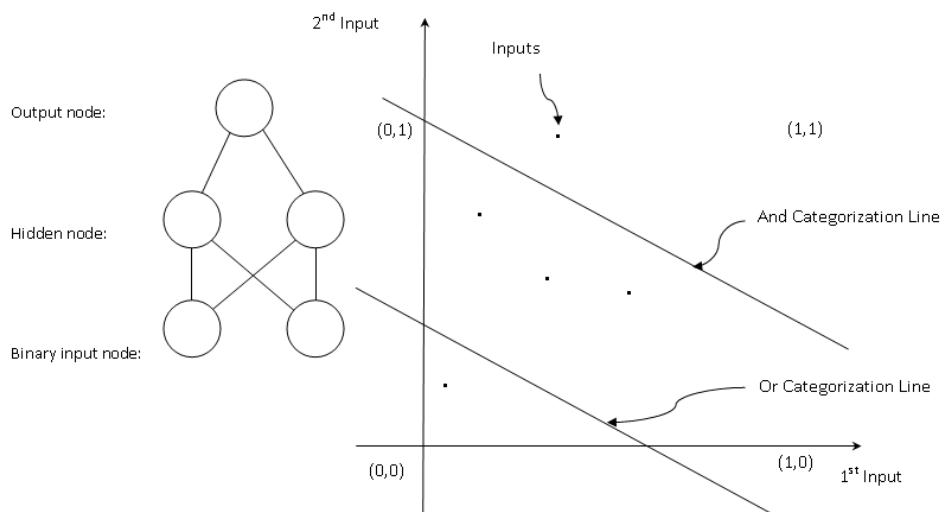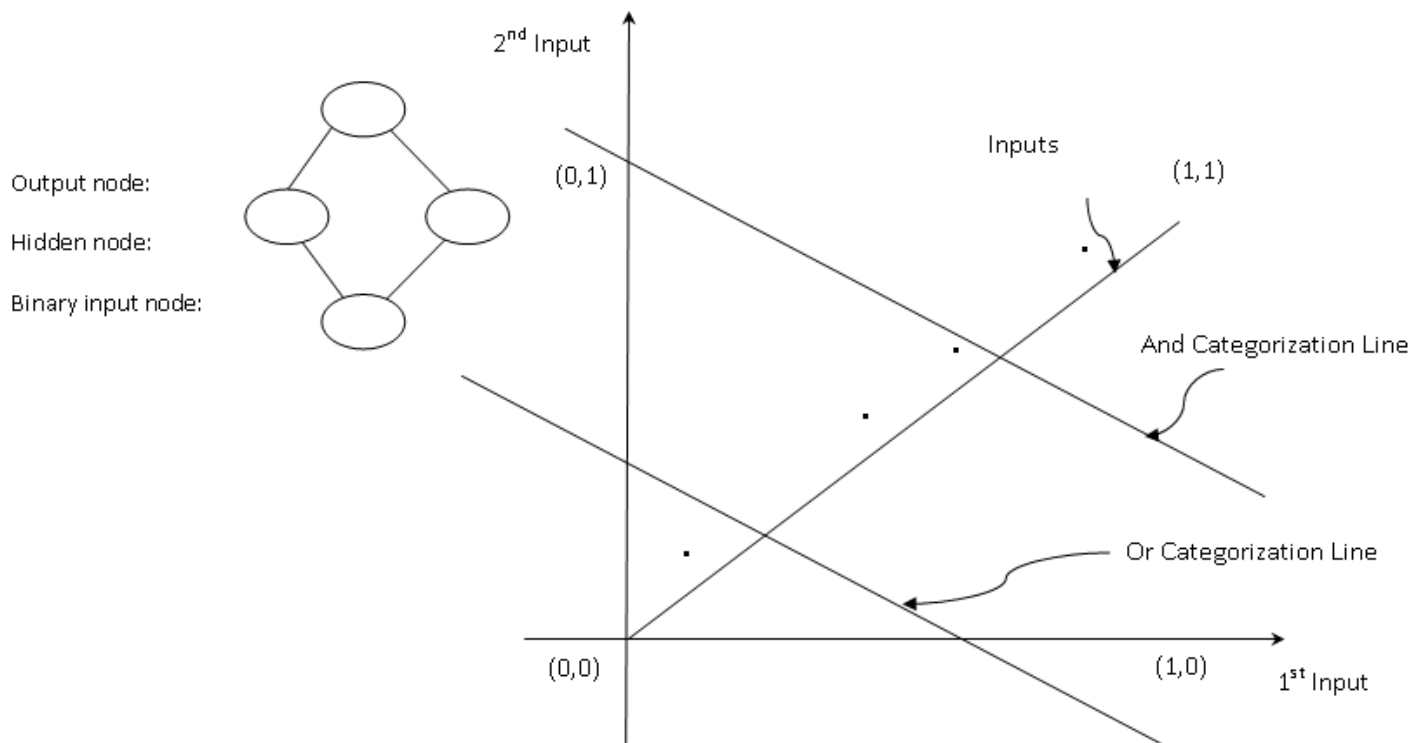

FIGURE 2: Simple 2-Layer Network–Vector input.
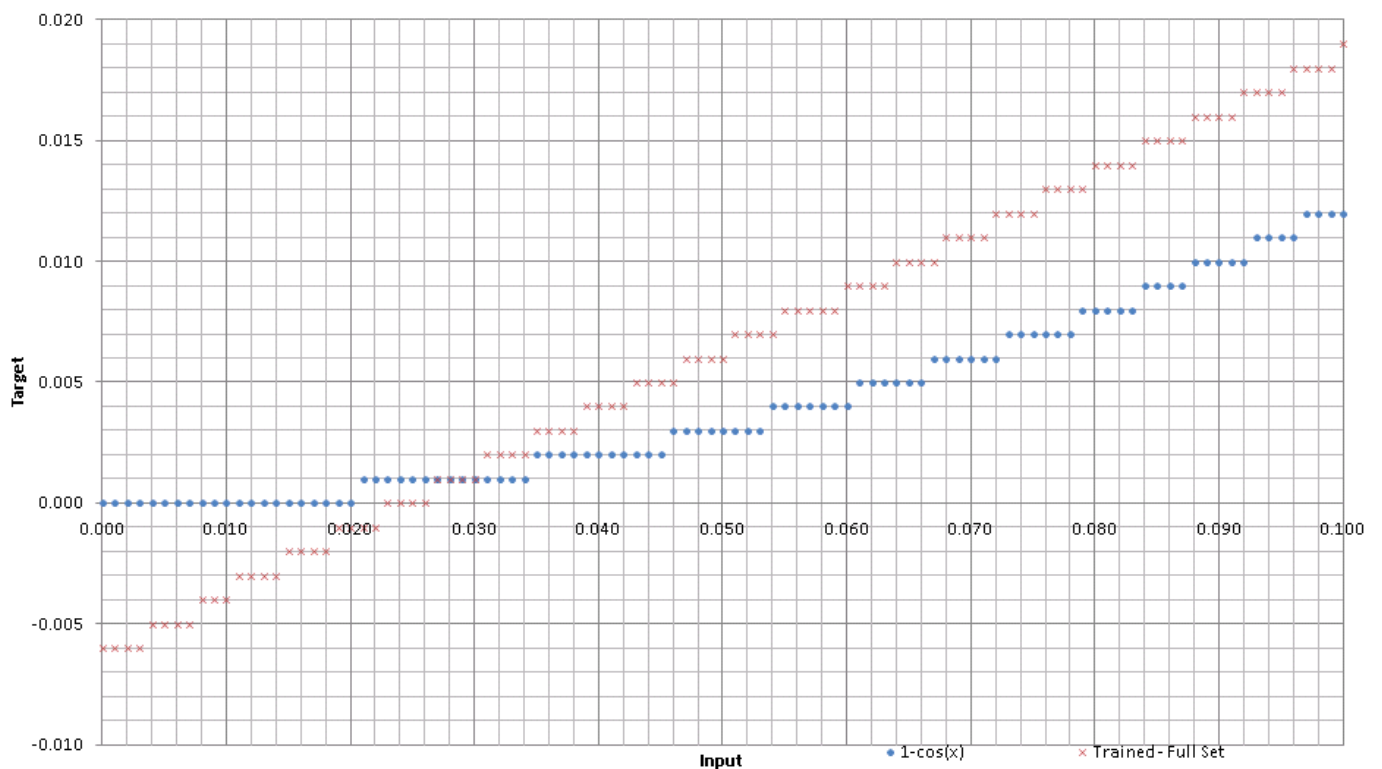
FIGURE 3: One input (scalar).

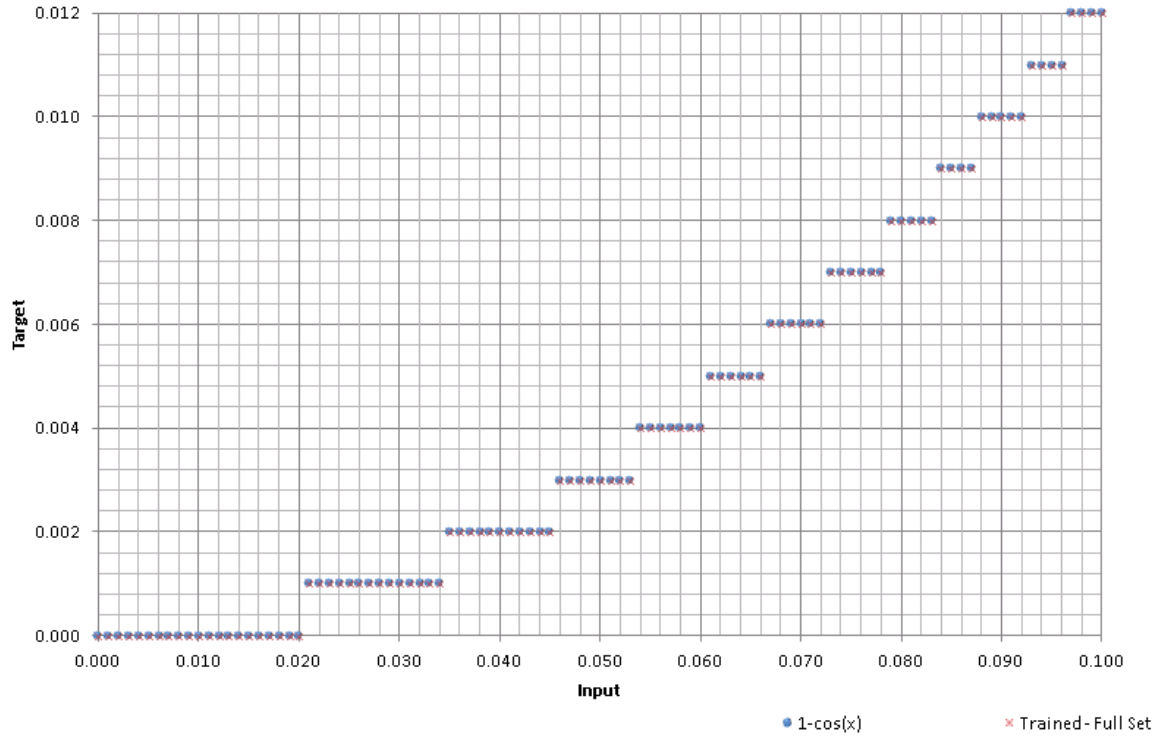FIGURE 4: Detail - training results with scalar input.

FIGURE 5: Detail - Training results with vector input.

3. Neural Network Generalization

If the full set of x,y pairs is available, the desired accuracy may be achieved by training the network on the entire set. In real-time applications the full set of x,y pairs may not be available, the set may change over time, or the time required to train a very large set becomes impractical. In these cases it may be necessary to develop a neural network approximation from a portion of the full set and generalization becomes important.

Poor generalization may result if the data used to train the network is not comprehensive enough despite using vector input and achieving the desired accuracy during training. It is difficult to estimate rigorously the error bounds and the experimental evidence of a required training set size of approximately 30% of the full data set size is often cited.

In the following, albeit an extreme example because the training set is much smaller than recommended sizes, the network was trained with only eleven x,y pairs based upon increments in x in 0.1 steps from 0.0 to 1.0 which represents about 1% of the full set. After training the network had zero RMS error to 10^{-3} precision with the small training set. As illustrated in Figure 6, however, the generalization was very poor even when the full test set was applied, and the resulting output appears random. This phenomenon has been noted elsewhere [4].

The neural network feed forward process was examined in order to determine the source of the error. The following analysis of the change in y (i.e., $y+\Delta y$) with a change in x (i.e., $x+\Delta x$) indicates that the desired accuracy cannot be always expected to be achieved with a sampling of the full set. The origin and impact of small changes in Δx may be determined as follows using the terms describing a node in a neural network. Figure 7 illustrates the elements of the node based upon the Perceptron developed by Frank Rosenblatt in 1957 [5].

$$O_{pi} = TF(A_{pi}) \tag{3}$$

$$A_{pi} = \sum w_{ij}x_{pj} \tag{4}$$

where,

O_{pi} = the ith node output for pattern p (pattern p = training Input/Target pair)
A_{pi} = the ith node activation value i.e., sum for all weights and inputs from previous level
w_{ij} = the weight from j^{th} node (previous level) to i^{th} node
x_{pj} = the input to the ith node from the jth node
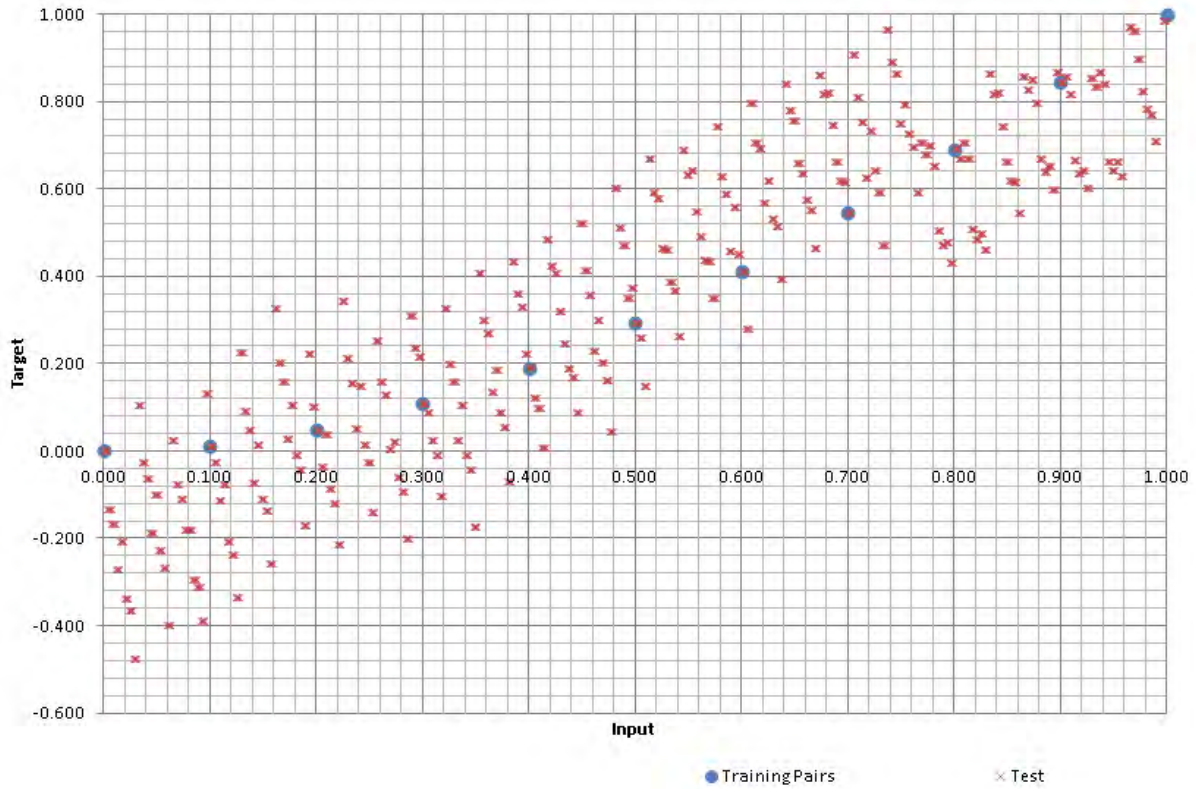TF = the continuous and differentiable transfer function (e.g., sigmoid, hyperbolic tangent, etc.)

FIGURE 6: Poor neural network generalization.

Consider the system $\bar{U}$ modeled by the state equation [6]:
$\bar{U} = f(\upsilon, X)$
where,
$\upsilon = (\upsilon_1.....\upsilon_n)^{\Gamma} \in \Re$ is the state vector at state Γ (i.e., weights are trained)
$X = (x_1....x_n)^{\Gamma} \in \{0,1\}^m$ is the input vector composed of binary representation.

A binary input vector was selected for the analysis because it provides the maximum difference available from normalized data sets i.e., a value of 0 produces no change in the network while a value of 1 produces maximal change. The input vector x can take any configuration among 2^m different column vectors $C_R(x)$ such as:

$$C_R(x) = \left\{ \begin{pmatrix} 0 \\ 0 \\ 0 \\ \vdots \\ \vdots \\ 0 \\ 1 \end{pmatrix} \begin{pmatrix} 1 \\ 0 \\ 0 \\ \vdots \\ \vdots \\ 0 \\ 2 \end{pmatrix} \begin{pmatrix} 1 \\ 1 \\ 0 \\ \vdots \\ \vdots \\ 0 \\ 3 \end{pmatrix} .. \begin{pmatrix} 1 \\ 0 \\ 0 \\ \vdots \\ \vdots \\ 1 \\ R \end{pmatrix} ... \begin{pmatrix} 1 \\ 1 \\ 1 \\ \vdots \\ \vdots \\ 1 \\ 2^m \end{pmatrix} \right\}, R = 1..2^m$$

$$\overset{\leftrightarrow}{\Delta x}$$

where R is an input vector.

Rounding creates a finite set of inputs and a numerical precision of 10^{-3} requires that m=10.

The state vector υ provides the weights for each node and relationship between the input, hidden and output nodes. With feedforward only (i.e., network is trained and the state vector υ is constant) the input is cascaded through the network as follows:

As one input in $C_R(x)$ $_R$=n impacts all hidden nodes the sums for all hidden nodes are determined according to Equation (4).

Although Δx may be defined as the difference between the elements in column vectors C_R at R=n and R=n+1 the impact on the network may not be calculated by algebraic subtraction of the two vectors. As the vectors are presented in sequence to the network and any change in the input vector changes all of the hidden node summations the change in hidden nodes is calculated for each input vector and Δx is specified in terms of the summation change ΔA_{pi}.
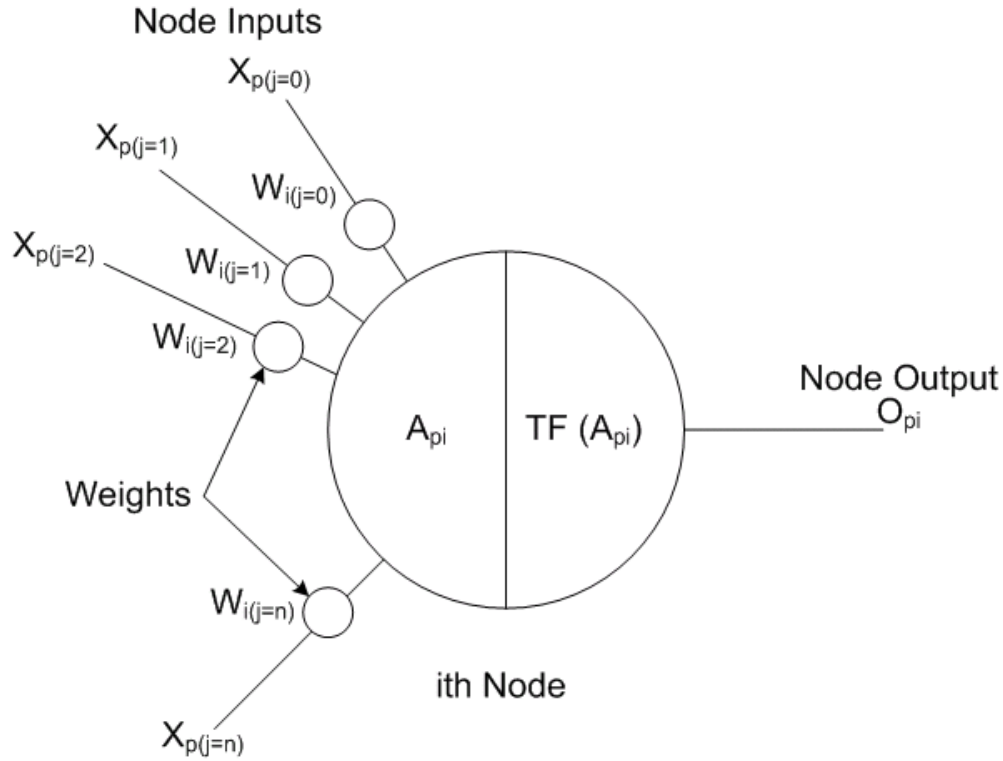
FIGURE 7: Poor artificial neural network node.

For each hidden node 1 to h at $C_R(x)_R = n$

$$[\ (\textstyle\sum_j w_{ij}x_{pj})_1 \ (\textstyle\sum_j w_{ij}x_{pj})_2 \ .... \ (\textstyle\sum_j w_{ij}x_{pj})_h \ ] \ C_R(x)_{R=n}$$
$$= [\ A_{pi=1} \ A_{pi=2} \ .... \ A_{pi=h} \ ] \ C_R(x)_{R=n}$$

Similarly for all hidden nodes at $C_R(x)_R = n+1$;

$$[\ (\textstyle\sum_j w_{ij}x_{pj})_1 \ (\textstyle\sum_j w_{ij}x_{pj})_2 \ .... \ (\textstyle\sum_j w_{ij}x_{pj})_h \ ] \ C_R(x)_{R=n+1}$$
$$= [\ A_{pi=1} \ A_{pi=2} \ .... \ A_{pi=h} \ ] \ C_R(x)_{R=n+1}$$

Then the Δ between $C_R(x)_R = n+1$ and $C_R(x)_R = n$ at each hidden node may be found by;

$$[A_{pi=1} \ A_{pi=2} .... \ A_{pi=h} \ ] C_R(x)_{R=n+1} - [A_{pi=1} \ A_{pi=2} .... \ A_{pi=h}] \ C_R(x)_{R=n}$$
$$= [\Delta A_{p1} \ \Delta A_{p2} ... \Delta A_{ph}]$$

(5)

It should be noted that a row of 0 elements in $C_R(x)$ would not add a value to any of the summations in Equation (5). Conversely, if the network is trained with a 0 element row and then tested with an element equalling 1, all of the summations will be affected.

The output of each hidden node at $C_R(x)_R = n+1$ is given by:
$$O_{pi} = TF(A_{pi}) + TF'(A_{pi}) \ \Delta A_{pi}$$

Where:
O_{pi} = the output at $C_R(x)_R = n+1$
$TF(A_{pi})$ = the output of the transfer function calculated at $C_R(x)_R = n$
$TF'(A_{pi})$ = the first derivative of the transfer function calculated at $C_R(x)_R = n$

The network output y is calculated at the single output node and therefore $y + \Delta y$ is given by:

$$(A_{pi})_{y+\Delta y} = w_{ij}[TF(A_{pi})_1 \ TF(A_{pi})_2 .... \ TF(A_{pi})h] \ C_R(x)_{R=n} +$$
$$w_{ij}[\ TF'(A_{pi}) \Delta A_{pi} \ TF'(A_{pi}) \Delta A_{pi} ... \ TF'(A_{pi}) \Delta A_{pi}] \ C_R(x)_{R=n}$$

where w_{ij} is weight vector from hidden notes to output node.

As the change in output Δy with a change ΔA_{pi} becomes according to Equation (3).
$$O_{y+\Delta y} = TF(A_{pi})_{y+\Delta y}$$

We have achieved the value at $(y + \Delta I)$ in terms of $(x + \Delta A_{pi})$ and ΔA_{pi} is the difference in hidden nodes sums arising from the change in input vector x.

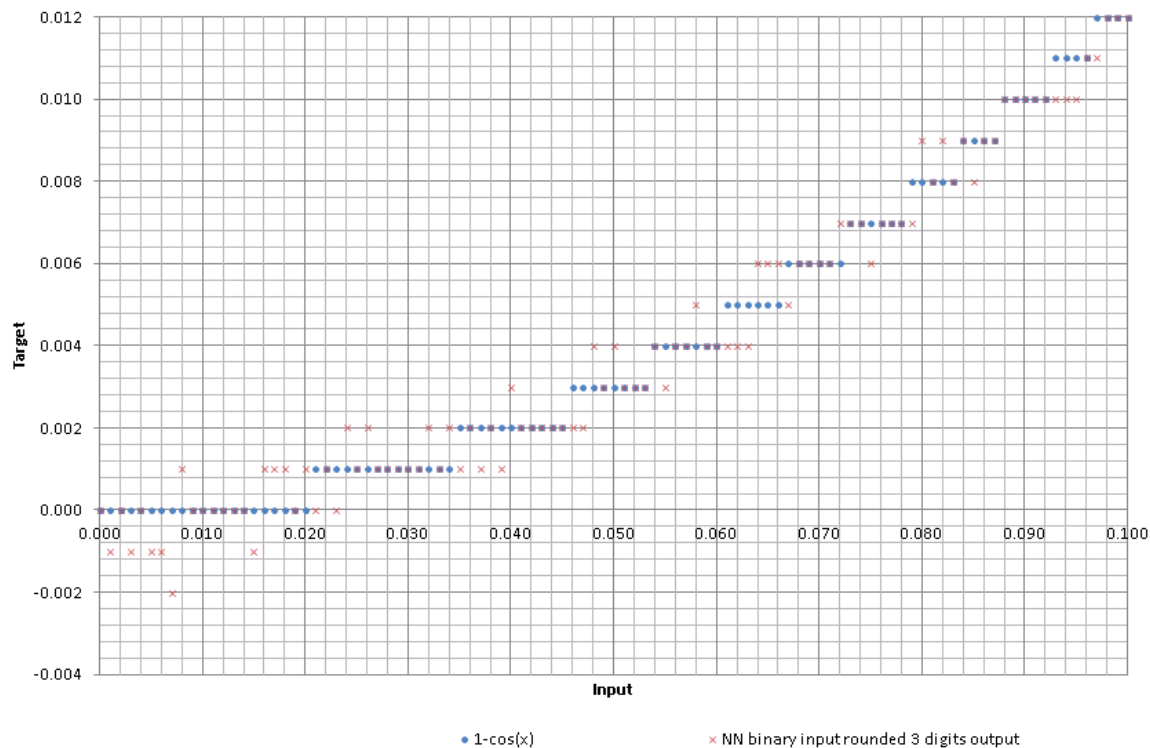FIGURE 8: Generalization with vector input.

FIGURE 9: Detail generalization with vector input.

The key point is that the modeling error arises from the mathematical structure itself, i.e., the state vector in the neural network rather than scatter in the data. Equation (5) indicates that a single change in the value of an input at any position in the input x vector will produce a ΔA_{pi} at all of the hidden nodes and cascade to the output. The state vector υ is constant for a trained network and the weights do not change between inputs. The change in y appears random because weights are assigned randomly during initialization of the network and a new non-zero value in the input vector x will add previously unused weights to all of the sums used in the hidden layer and may produce very inconsistent results.

As the adjacent training points at $C_R(x)_{i=n+1}$ and $C_R(x)_{i=n}$ often have the same higher significant digit values, or as in this case, are the x,y pairs used to train the network, the lower significant digits from the scalar value used to develop the binary vector and tested in the network must cause the ΔA_{pi}.

It should be noted that the cross-linking between all input and hidden nodes means that there is no longer any order of magnitude significance associated with position in the input vector and a change in the x scalar low order digit will convert to a binary digit of equal significance to the neural network as a high order digit with the same impact on the hidden node sum. Reintroducing an order of magnitude significance to input vector elements is a subject of further exploration.

Function generalization may be significantly improved by selecting a number of x,y pairs that condition the weights more fully. As this number may not be known in advance adding additional pairs that are selected from the greatest outliers in the test set can improve the accuracy of the entire set as described in the example that follows.

A training subset of one degree increments from 0 to 90 degrees was arbitrarily selected as providing comprehensive coverage of the entire curve with only 9% of the full set of x,y pairs. Using the input in binary vector form the neural network was trained and achieved the same 100% 10^{-3} accuracy with rounding as before but convergence was achieved in about 1 minute. The ability to generalize was then tested by presenting the full 1001 pairs to the network.

With rounding before their use, the errors between the model value (i.e., Equation (1)) and the neural network output are also in steps of 0.001. The frequency of each error in the 1001 x,y pairs is given in Table 1 and it is clear that the 10^{-3} precision is not maintained when training with a subset. With the exception of the five records that generated the 0.005 RMS errors all of the other errors would maintain the accuracy at the 10^{-2} precision so the

five offending x,y pairs were added to the training set and the network was retrained and so forth with the results noted in the table - repeated training with only the largest error x,y pairs added to the training set each time improved the precision to 10^{-2} which could be adequate for process control.

As expected in a curve fitting exercise, the addition of more x,y pairs yields a much better result and fits the curve more accurately than with scalar input – even with a training set size of less than 10% of the full data set. The difference can be seen in the details between Figure 4 and Figure 9. The additional data ensures that more of the weights in the network are trained. For many systems training at 10^{-3} precision to provide 10^{-2} precision would be more than adequate.

4. Further Work
Back propagation training with only a fraction of the possible inputs does not ensure that all weights will be adjusted to produce output with the desired or even acceptable accuracy. For predictable and accurate results all of the weights in the network must be adjusted to provide the correct summation for the entire range of inputs. The bias values used in the network represent constant inputs and they may also impact upon both generalization and learning.

The factors affecting the accuracy of the function approximation are important to the application of neural networks in process control. The issues of extrapolation, over training, fault tolerance, and noisy or stochastic data can now be addressed in the context of this fundamental behavior.

5. Summary
The approximation of non-linear functions by neural networks can provide the desired accuracy with vector input and with training on the full set of x,y pairs. Under these conditions neural network outputs are consistent, accurate, and reliable which permits their use in more critical applications. The training time required with a large data set may constrain their use in some real-time systems.

Generalization of non-linear functions may be achieved by training the network with a representative but smaller data set. Curve fitting errors will be created by the weights within the network itself. Both the network and data set are smaller and the training performance can be significantly faster. If only the largest outliers identified from the test data are added to the training data the overall accuracy of all of the x,y pairs improves with additional training. The faster training and network performance makes a generalized network attractive for less accurate systems requiring adaptive computing.

Non-linear model predictive control and autonomous control are applications where the accuracy of function approximation of neural networks is important. The remarkable ability of neural networks to model real world system dynamics in real-time provides a tremendous opportunity for their use in these systems [2, 7]. Understanding the factors that control their accuracy and controlling them during system design opens up more opportunities for their use.

REFERENCES

[1] K. Hornik, M. Stinchcombe and H. White, (1989), "Multilayer Feedforward Networks are Universal Approximators", Neural Networks, 2 (5) pp. 359-366.

[2] M. K. O. Ayomoh and M. T. Ajala, (2012), "Neural Network Modeling of a Tuned PID Controller", European Journal of Scientific Research, 71(2), pp. 283-297.

[3] S. Ferrari, R. F. Stengel, (2005), "Smooth Function Approximation UsingNeural Networks", IEEE Trans. Neural Networks, 16(1), pp. 24-38

[4] J. M. Nazzal, Ibrahim M. El-Emary and Salam A. Najim (2008), "Multilayer Perceptron Neural Network (MLPs) For Analyzing the Properties of Jordan Oil Shale", World Applied Sciences Journal, 5(5), pp. 546-552

[5] F. Rosenblatt, (1958), "The Perceptron: A probabilistic model for information storage and organization in the brain", Psychological Review, 65(6), pp. 386-408.

[6] F. Girosi, M. Jones, T. Poggio, (1995), "Regularization Theory and Neural Networks Architectures", Neural Computation, 7(2), pp. 219-269.

[7] V. Ranković, J. Radulović, N. Grujović, D. Divac, (2012) "Neural Network Model Predictive Control of Nonlinear Systems Using Genetic Algorithms", International Journal of Computer Communications, ISSN 1841-9836 7(3) 540-549.

[8] J. Lawrence, (1993), "Introduction to Neural Networks: Design, Theory, and Applications", 5th Edition. California Scientific Software, Nevada City, California.

[9] A. R. Barron, (1993), "Universal Approximation Bounds for Superpositions of a Sigmoidal Function", IEEE Transactions on Information Theory, 39 (3), pp. 930-945.

[10] M. Minsky, S. Papert. (1969) Perceptrons: An Introduction to Computational Geometry. Cambridge, Mass: M.I.T. Press.

Recently, AMEC NSS initiated projects for CANDU® station performance engineering with potentially high returns for the utilities. This paper discusses three initiatives. Firstly, optimization of instrument calibration interval from 1 to 3 years will reduce time commitments on the maintenance resources on top of financial savings ~$3,500 per instrument. Secondly, reactor thermal power uncertainty assessment shows the level of operation which is believed to have an over-conservative margin that can be used to increase power by up to 0.75%. Finally, as an alternative means for controlling Reactor Inlet Header Temperature (RIHT), physical modifications to the High Pressure (HP) feedwater heaters can be useful for partially recovering RIHT resulting in increased production by 10-12 MWe.

Value Addition Initiatives for CANDU® Reactor Operation Performance

V. Chugh[1*], R. Parmar[1], J. Schut[2], J. Sherin[1], H. Xie[1] and D. Zobin[1]

[1]AMEC NSS, 393 University Avenue, 4th Floor, Toronto, ON, Canada M5G 1E6
[2]Bruce Power, Tiverton, Ontario, Canada

*Corresponding author: (416) 217-2104, vinod.chugh@amec.com

1.Instrument Calibration Frequency Optimization

Most instruments in a nuclear power plant are calibrated at regular intervals to ensure that the assumptions in the plant Technical Specifications and/or Safe Operating Envelope (SOE) compliance limits (e.g., As-Found Tolerance) are satisfied. In the Instrument Uncertainty Calculations (IUC), As-Found Tolerance for instrument drift is estimated based on statistical analysis of As-Found (AF) and As-Left (AL) calibration data such as that carried out for Bruce NGS by the Electric Power Research Institute (EPRI) in 1998.

The use of statistical analysis techniques to evaluate instrument drift based on calibration history and implementation of on-line instrument monitoring has enabled some Pressurized Water Reactor (PWR) nuclear plants to extend calibration intervals and, thus, move from an 18-month fuel cycle to a 24-month fuel cycle, since calibration of most instruments can be done only when the reactor is shut down.

Instrument calibration at CANDU® Nuclear Generating Stations (NGS) is not tied to unit outages, and, therefore, annual savings are likely to be significantly lower. However, in addition to the actual savings, reduction in calibration frequency will reduce time commitments on the part of authorized nuclear operators (ANOs) and safety system qualified control maintenance (CM) staff, and will allow more schedule flexibility.

1.1 SOE Assessment for Emergency Coolant Injection (ECI) Instrument Loops

As mentioned previously, EPRI conducted a study in 1998 to quantify instrument drift behaviour [1, 2]. The purpose of the EPRI study was to evaluate the expected performance of the instruments as installed and maintained in the station. More specifically, the study focused on determining a statistically derived tolerance interval for instrumentation drift with a 95% probability and 95% confidence by using historical instrument AF and AL calibration data collected from Bruce B.

The EPRI study included a large amount of AF/AL calibration data, i.e., 7636 calibrations for 1924 instruments. The extensive data quantity and coverage ensured that the quantified drift behaviour had a sound statistical basis.

AECL NUCLEAR REVIEW
VOL 2, NUMBER 1, JUNE 2013

VALUE ADDITION INITIATIVES FOR CANDU® REACTOR OPERATION PERFORMANCE
V. CHUGH, R. PARMAR, J. SCHUT, J. SHERIN, H. XIE AND D. ZOBIN

In the EPRI study, instrument drift was quantified as the difference between the AF output from the current calibration and the AL output from the last calibration, i.e.:

Drift = AF Output current calibration – AL Output last calibration

The statistics for the drift data (mean and 95/95 tolerance interval) were calculated and tabulated for different instrument type, application, make, model, and calibration points. The EPRI drift study is currently used as the basis for specifying drift uncertainties in the SOE IUC.

Instrument Uncertainty Calculations

IUCs are performed on two types of SOE parameters: actuation and indication parameters. Actuation parameters are those that will trigger an automatic actuation when monitored signal (e.g., reactor power) exceeds the set point of Special Safety Systems following a design basis accident. Indication parameters are those that require routine monitoring (e.g., reactor inlet header temperature) during normal operation.

In IUC, Total Uncertainty (TU) is calculated for both actuation and indication parameters. The TU includes random and bias uncertainty components from various sources, including instrument drift. Consistent with the industry practice, the TU is evaluated at 95% probability with 95% confidence (95/95). An important assumption for the 95/95 uncertainty evaluation is that random instrument uncertainty, including drift, is normally distributed. In the EPRI instrument drift study, the normality assumption is checked for the drift data. It is concluded that drift data distribution is more peaked than an ideal normal distribution, and is therefore bounded by the normality

assumption. Random instrument drift beyond 3σ is highly unlikely to occur. If it does occur, a non-random failure mechanism may be the cause for the drift and a repair or replacement would be recommended.

Actuation Loops

In order to ensure compliance with the SOE, the setpoint design criterion for an actuation loop is that the Total Allowance (TA) must be greater than or equal to the TU, where TA is the difference between the Safety Limit (SL) and the nominal setpoint, and TU is the combination of all loop uncertainties (random and bias):

Margin = TA - TU ≥ 0

A zero margin is the minimum that the loop is still in compliance with the SOE (see Figure 1a). Therefore, a sufficient margin (to accommodate for potential instrument drift due to extended calibration period) for any given loop is used as a selection criterion to identify loops that are qualified for calibration interval extension.

Indication Loops

For an indication parameter, the SOE compliance is defined by the Surveillance Limit, which is equal to the Safety Limit minus (or plus) the Total Uncertainty, depending on how the Safety Limit is defined (high or low) relative to the normal operating point range, i.e.:

Surveillance Limit = Safety Limit ± Total Uncertainty

To ensure compliance within the SOE, an indication loop should have sufficient allowance to accommodate instrument uncertainty. This has to be such that the surveillance limit does not intercept with the normal operating range (see Figure 1b). Similar to the criterion

FIGURE 1A AND 1B: SOE Compliance for an actuation (L) and indication (R) parameter.

AECL NUCLEAR REVIEW
VOL 2, NUMBER 1, JUNE 2013

VALUE ADDITION INITIATIVES FOR CANDU® REACTOR OPERATION PERFORMANCE
V. CHUGH, R. PARMAR, J. SCHUT, J. SHERIN, H. XIE AND D. ZOBIN

established for actuation loops, if the margin for an indication loop is sufficient to accommodate potentially increased instrument drift (3σ) due to extended calibration interval, then the instrument would be qualified for a calibration interval extension of up to three years.

1.2 Impact on ECI Unavailability from Reduced Instrumentation Calibration Frequency

The methodology employed for the sensitivity analysis of the effect of the reduced calibration intervals on ECI system unavailability consists of the following steps:

(a)   Solving the latest ECI unavailability model (UM) using baseline failure rates and a 3-year test interval (TI)
(b)   Identification of prior drift failures and additional instrumentation failure events, and associated pre-defined maintenance (PMIDs) in the ECI UM
(c)   Drift failure probability re-estimation for the two sensitivity cases
(d)   Simple human interaction event probability re-calculations
(e)   Solving the ECI UM
(f)   Impact on severe core damage frequency

Only the loops deemed eligible for calibration interval extension by the SOE assessment were considered for the sensitivity analysis.

The impact of reducing the calibration frequency on ECI system unavailability for SOE-related instruments was assessed by revising the calibration interval to three years and re-calculating the ECI system Predicted Future Unavailability (PFU).

2. Reactor Thermal Power Optimization

At Bruce Power, and for reactors operated by other utilities in Canada, the licensed reactor power limit is approved by the Canadian Nuclear Safety Commission (CNSC). The licence limit is established based on a design value and the safety limit is a value used in the safety analysis. The difference between the two is based on our understanding of the uncertainties associated with any selected level of reactor power. The licensed limit for each reactor is about 3% FP lower than the safety limit established for that reactor based on safety analysis work. It has resulted in a level of operation which is believed to be overly conservative in that it forces the reactors to operate at power levels that are lower than they could be, while still ensuring safe operation. The target "Limit" desired by Bruce Power is the safety limit.

This requires establishing the resolution of two issues:
•   Deriving mathematical models to fully describe the behavior of the true reactor power. The models need to be consistent with operating data and assessments of reactor thermal power uncertainties. Included in this work would be a determination on whether the current value of the safety limit is adequately supported, since a firm value for this limit will be needed for any compliance work.

•   Using the developed models to support justification of any proposed change in reactor power level. Justification will need to demonstrate meeting all the requirements associated with the proposed change, including any changes to existing methods and procedures, such as changes to the way reactor thermal power is calibrated and measured.

This initiative considers the first issue and presents the development of a mathematical model for reactor power and compliance. This is based on the recent modeling experience in channel power compliance and Neutron Overpower Protection (NOP) work. The model is then used to analyze historical operating data for reactor thermal power for Bruce Power Units 5 and 8 over a five-year period from 2006 to 2010. Model equations have been solved using maximum likelihood estimation, and preliminary results indicate that for the reactor power set point at 93% FP, the true reactor power is below 94.5%, with 95% confidence, or 1.5% less than the safety limit over the entire period of time. The model is currently being applied to analyze the behavior of the reactor thermal power in Bruce Power Units 6 and 7, and can be used for other CANDU® plants.

2.1 Reactor Thermal Power Measurements and Compliance

2.1.1 Methods of Reactor Power Calculation

It is well known that fissioning of uranium and plutonium nuclides within the core releases quantities of energy which have been well characterized over the past 60 years. The fission energy appears in various forms: kinetic energy of fission fragments, kinetic energy of neutrons, energy in the form of gammas and other radiation in the electromagnetic spectrum, energy carried by neutrinos, and energy carried by beta and other particles.

It is also well understood that not all these energy carriers result in enthalpy increases in the primary heat transport system coolant. Some are lost completely (e.g. the neutrinos). Some are deposited in the moderator (e.g. gammas and neutrons), in structural materials, in end shields, in biological shield (gammas and neutrons), and in structures outside the core altogether, such as containment equipment and containment walls (primarily gammas). Any decision on which of these processes to include in and

AECL NUCLEAR REVIEW
VOL 2, NUMBER 1, JUNE 2013

VALUE ADDITION INITIATIVES FOR CANDU® REACTOR OPERATION PERFORMANCE
V. CHUGH, R. PARMAR, J. SCHUT, J. SHERIN, H. XIE AND D. ZOBIN

to exclude from the definition of reactor power will affect how we interpret a model statement of "reactor power" and how well we can reproduce, through calculations, a physical measure of reactor power.

There are only two practical means of measuring reactor power that are used in the industry. They are measurement of primary side reactor power based on the Reactor Regulating System (RRS) algorithm, also referred to as reactor "indicated thermal" power, and measurement of reactor power as obtained by the secondary side heat balance. These two measurements reflect the third indicator, which is the postulated "true" reactor power, and it is an established practice in most nuclear plants around the world to calibrate the indicated reactor power to the value obtained from the secondary side heat balance. Although the secondary side heat balance is considered best and most accurate measurement of the reactor thermal power, it excludes some energy loss from the core that does not pass to the secondary side. Other reactor side measurements must therefore be used to take into account all significant energy leaving the core, and added to the secondary side heat balance.

2.1.2 Reactor Power Compliance
The word "compliance" normally implies comparison of a measured or calculated value to a standard to determine whether or not a specific criterion has been met.

The Power Reactor Operating Licence (PROL) for a CANDU® reactor states that
• the total power generated in any fuel bundle shall not exceed P_b (max bundle power)
• the total power generated in any fuel channel shall not exceed P_{ch} (max channel power)
• the total thermal power from reactor fuel shall not exceed P_{th} (max thermal power)

However, there is an inconsistency between the current compliance approach for P_{th} compared to P_b and P_{ch}. The values for P_b and P_{ch} specified in the PROL are the same as in the Safety Analysis. However, the value for P_{th} is equal to design reactor thermal power, which is about 3% lower than the safety analysis value. Implementation of a modified compliance approach will not only result in more consistent compliance practices but will also allow increase in reactor power operating levels.

2.1.3 Equations for Estimating True Reactor Power
Definitions and Measurement Errors
For the work being discussed here, the entity of interest (reactor power) has to do with processes occurring within the core. As discussed in the previous section, there are various measures for quantifying this entity, but no two of

them look at exactly the same set of processes, and all of them have associated errors. A good model can, in principle, encompass all these processes and measurements and can be used to make estimates of the associated errors. Let us introduce the following definitions:

True Reactor Power ('un-observable'): RP

Indicated Reactor Power (based on Primary Heat Transport System):

$$RP^{ind} = RP\,(1 + e^{rp}) \quad \text{where, e = estimated error} \qquad (1)$$

Heat Balance Reactor Power (based on Secondary Heat Transport System):

$$RP^{hb} = RP\,(1 + e^{hb}) \qquad (2)$$

RP^{ind} is controlled to set point (SP):

$$RP^{ind} = RP\,(1 + e^{rp}) \approx SP \text{ or } RP = SP\,(1 - e^{rp}) \qquad (3)$$

and is based on Fully INstrumented CHannel (FINCH) measurements.

The "$\approx$" sign reflects the fact that RP^{ind} fluctuates around the SP; however, these fluctuations are small and can be neglected in the derivation of the error equations.

$$RP^{ind} = (1/f) \sum CP_i^m / N_i \qquad (4)$$

where CP_i^m are the measured FINCH powers, N_i are the called FINCH nominals and f is the number of FINCH's.

FINCH measurement error is then given by:

$$CP_i^m = CP_i\,(1 + e^m) \qquad (5)$$

Here we introduce "d", which is referred to as the so-called Channel Power Drift and can be also expressed as:

$$ave(CP) / ave\,(CP_0) = (RP / RP_0)\,(1 + d) \qquad (6)$$

CP_0 and RP_0 are taken at time zero, when changes in nominals take place and therefore the drift is measured, and CP and RP are taken at a later time. If all reactor channels were FINCH's, then d would be equal to zero (nominals would not be required).

In this case, i.e., if all reactor channels were FINCH's, the expression for the true reactor power can be written as:

$$RP = SP\,(1 - e^{rp}) = SP\,(1 + b_0 - d - e^m) \qquad (7)$$

AECL NUCLEAR REVIEW
VOL 2, NUMBER 1, JUNE 2013

VALUE ADDITION INITIATIVES FOR CANDU® REACTOR OPERATION PERFORMANCE
V. CHUGH, R. PARMAR, J. SCHUT, J. SHERIN, H. XIE AND D. ZOBIN

b_0 is the average error in FINCH nominals. This expression is valid only on a time interval with constant FINCH nominals. A description of RP across the time of nominal change is obtained by modeling station procedures when changing nominals, which results in a constraint on b_0.

Regression Model
Heat Balance data:

$$RP^{hb} = RP(1 + e^{hb}) = SP(1 + b_0 - d - e^m)(1 + e^{hb}) \quad (8)$$

or

$$(RP^{hb}/SP - 1) = (b_0 - d) + (e^{hb} - e_m) \quad (9)$$

SORO (Simulation Of Reactor Operation) data:

$$S = CP(1 + e^{rp} + e^{rfs}), \quad RP^{ind} = RP(1 + e^{rp}) \quad (10)$$

Additional equations can be obtained for b_0 and d by replacing CP with S and RP with RP^{ind}.

Solution of Regression Model
Solve Equations (8) – (10) using Maximum Likelihood Estimation [3]:

$b^{est}, d^{est}, \sigma^2 = (\sigma_m)^2 + (\sigma_{hb})^2$, where, σ = standard deviation

$$RP^{est} = SP(1 + b^{est} - d^{est} - e^m) \quad (11)$$

Confidence Limit (RP) =
$$SP(1 + b^{est} - d^{est} \pm t_{n,a}[(\sigma_{est})^2 + (\sigma_m)^2]^{1/2}) \quad (12)$$

RP_{ind} and HB (Heat Balance) data for Units 5 and 8 over a 5 year period (2006-2010) were used.

Unit 5: SP = 90% (2006 – 2007), SP = 93% (2008 – 2010)
Unit 8: SP = 90% (2006 – 2009), SP = 93% (2010 – 2010)

The estimate of the mean true RP and 95% bounds on the true RP were performed for this period.

2.2 Reactor Power Uncertainty Analysis Results
Reactor power obtained from Heat Balance and the estimated true reactor power are shown in Figures 2a and 2b. Comparison between the sets of results confirms that the true reactor power is not sensitive to the random error in the value of the Reactor Power obtained from the Heat Balance. A possible systematic error is normally addressed by regular verification and calibration of station instruments such as feedwater flow and temperature against more accurate methods of measuring the same parameters. Finally, it is important to emphasize that, at 95% confidence level, the true reactor power was within about 1% of the license limit and never exceeded the safety limit.

3. Minor Design Changes for Controlling Reactor Inlet Header Temperatures in CANDU® Reactors
In general, the Reactor Inlet Header Temperature (RIHT) has risen more rapidly in CANDU® units compared to the original aging predictions. A typical example of the RIHT behaviour in recent years is shown in Figure 3. In this example, the RIHT increases by approximately 0.3 °C/year. Thus, RIHT is monitored and high temperature alarms are required to prevent operation outside the safe operating envelope as supported by the safety analysis.

To prevent RIHT alarms, increasing RIHT is being mitigated through changes in unit operating conditions. Boiler secondary side pressures have been lowered and high pressure (HP) feedwater (FW) heater steam supply has been isolated, often leading to electrical output loss.

The main contributor to the RIHT increase is the ongoing accumulation of magnetite deposits on the Inner Diameter (ID) surfaces of both the boiler and preheater tubes. The increasing RIHT trends are reviewed annually, and corrective actions such as ID cleaning of the boiler and preheater tubes can be performed to recover lost heat transfer efficiency. However, the execution of ID boiler tube cleaning has not always been successful in providing long-term relief from high RIH temperature alarms. In some cases RIHT values have returned to pre-cleaning levels within as little as three years of operation. Repeat ID boiler tube cleaning is a very expensive means for controlling RIHT. Some plants have reduced RIHT by installing boiler divider plate skins and increased allowed RIHT by installing smart card delta temperature transmitters for FINCH channels.

Minor design changes may provide a cost-effective means of controlling RIHT as an alternative to ID boiler tube cleaning, and it may also be a cost effective approach to maximize production prior to refurbishment outages. The objective of the work presented in this section was to evaluate two potential minor design changes in the HP FW system for the purpose of achieving lower RIHT by reducing preheater/steam generator feedwater inlet temperatures.

3.1 Feed Water Flow Bypass of High Pressure FW Heater Tube Bundle
In a typical CANDU® turbine cycle, the HP FW heaters increase the FW temperature from around 150 °C after leaving the boiler feed pumps to about 175 °C before entering the shell side of the preheaters / steam generators. A 10 °C drop in FW temperature will result in a RIHT drop ranging from 0.5 to 1 °C depending on the preheater/steam generator design. The heating supply to the HP FW heaters is a normally a combination of extraction steam from the HP turbine outlet and drain flow from the moisture separator/reheaters (MSR). A path for the MSR drains must
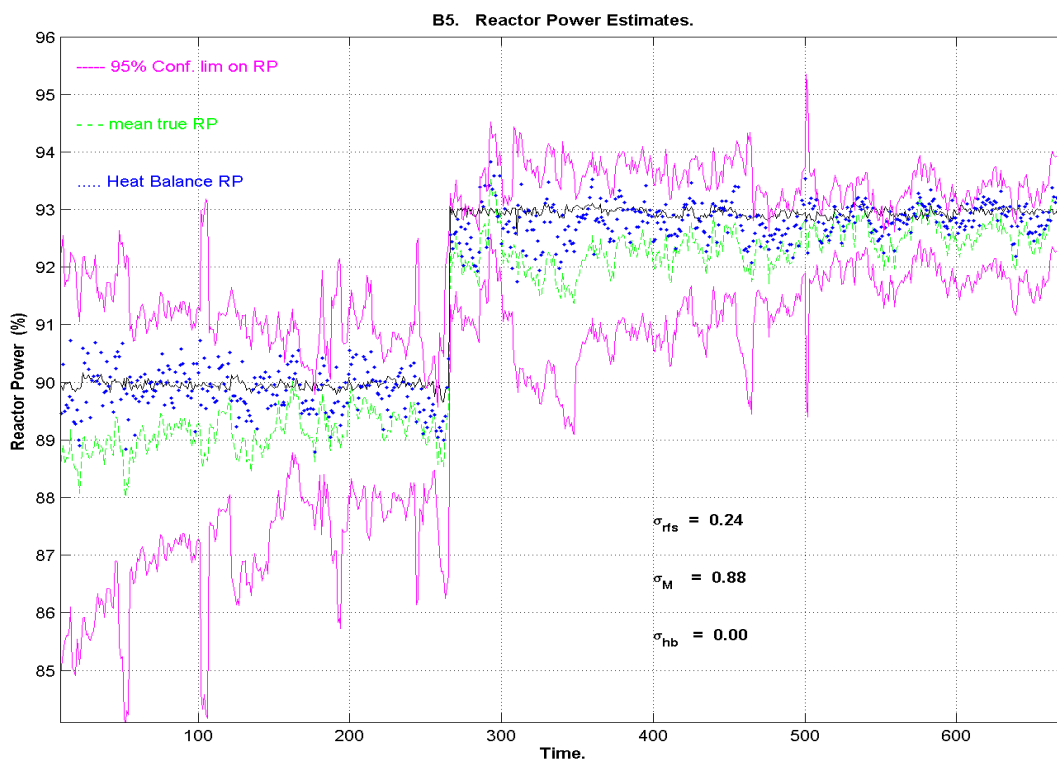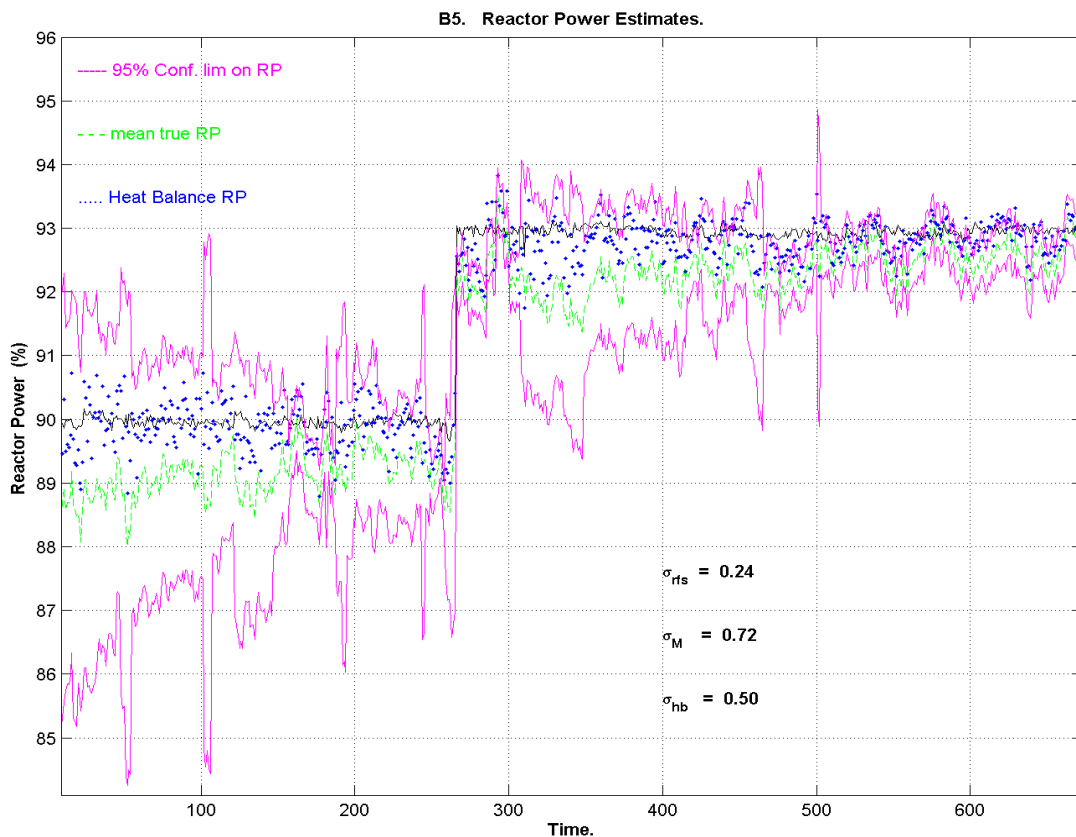
AECL NUCLEAR REVIEW
VOL 2, NUMBER 1, JUNE 2013

VALUE ADDITION INITIATIVES FOR CANDU® REACTOR OPERATION PERFORMANCE
V. CHUGH, R. PARMAR, J. SCHUT, J. SHERIN, H. XIE AND D. ZOBIN

FIGURE 2A AND 2B: Reactor power for 2006-2010 for σHB=0 and σHB=0.5.

AECL NUCLEAR REVIEW
VOL 2, NUMBER 1, JUNE 2013

VALUE ADDITION INITIATIVES FOR CANDU® REACTOR OPERATION PERFORMANCE
V. CHUGH, R. PARMAR, J. SCHUT, J. SHERIN, H. XIE AND D. ZOBIN
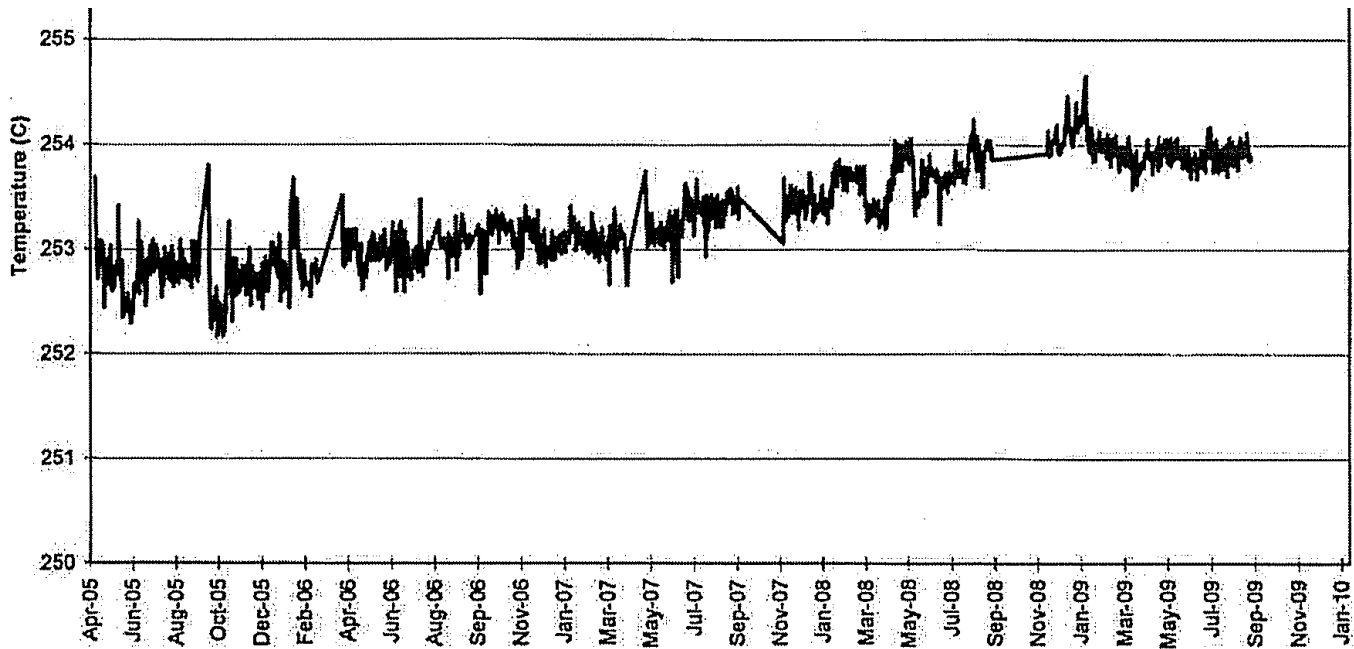
FIGURE 3: Typical RIHT trend with time.
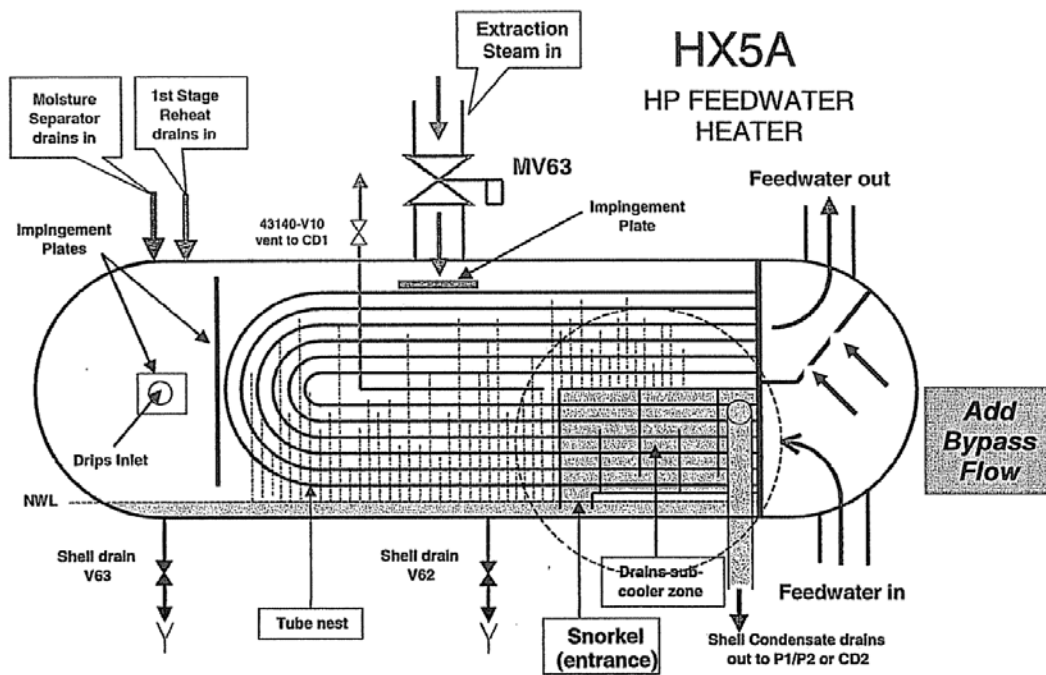
FIGURE 4: FW bypass flow of HP W heater tube bundle.

AECL NUCLEAR REVIEW
VOL 2, NUMBER 1, JUNE 2013

VALUE ADDITION INITIATIVES FOR CANDU® REACTOR OPERATION PERFORMANCE
V. CHUGH, R. PARMAR, J. SCHUT, J. SHERIN, H. XIE AND D. ZOBIN
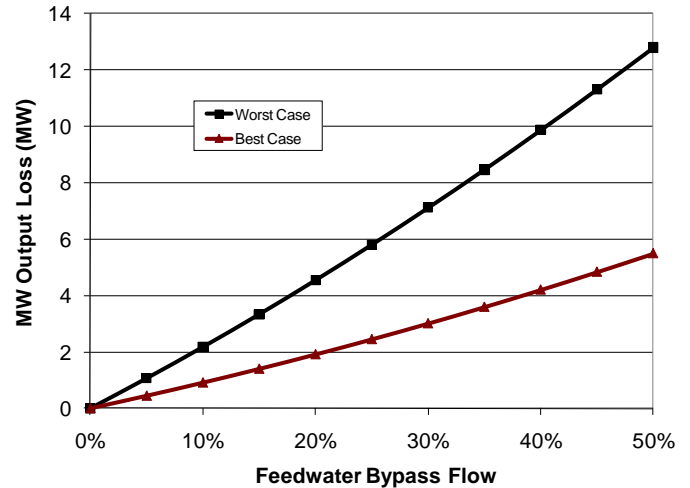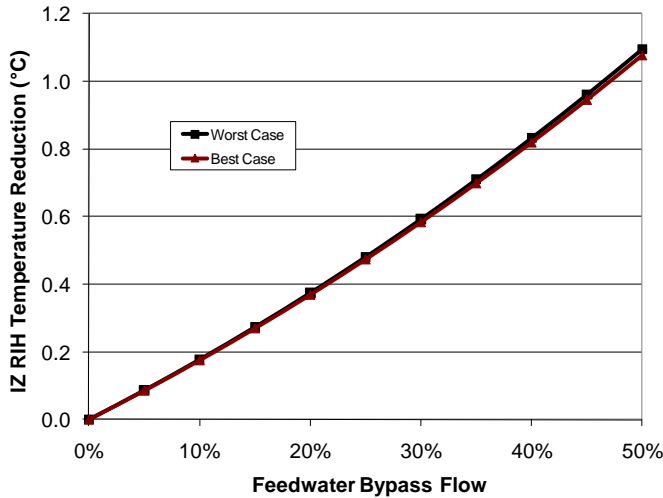
FIGURE 5A AND 5B: RIHT drop and gross electrical output loss due to FW bypass flow.

be maintained at high power operation and therefore if the HP heaters are not available to accept the drains, the flow must be diverted to the condenser resulting in high thermal losses. The extraction steam flow to the HP heater, however, can be reduced or isolated in such a way that the steam remains in the steam path minimizing thermal losses. Therefore, in order to reduce HP FW heating with the least impact on overall cycle efficiency, normal MSR drain paths must be maintained while reducing the extraction flow to the heaters. In some plants isolating extraction steam to the HP heaters while maintaining normal drain paths is possible. In the latter case, minor design changes could be a better approach for controlling RIHT.

The first minor design change considered was to provide a means of bypassing a portion of the FW flow around the tube side of the HP FW heater, as shown in Figure 4. The objective is to manage high RIH temperatures by reducing FW temperatures while minimizing trade-off in lower cycle efficiency.

The feasibility of the design change was studied using the Performance Evaluation of Power System Efficiencies (PEPSE) turbine cycle modelling software [4] to simulate this minor design change. Due to the complexity of modeling moisture separator drain piping, two bounding cases were simulated with respect to drain flow response to changing conditions in the HP FW heater and impact on cycle efficiency as Best Case and Worst Case. The Best Case assumes that drain flows remain unchanged either by control action or compensating changes in the drain line water column. The Worst Case assumes no control action or change in the drain line water column. In this case, reheating steam load is expected to increase and superheat to the LP turbines is expected to drop resulting

in increased cycle efficiency losses. Two sensitivity studies were therefore carried out with varying degrees of FW bypass flow from 0% to 50% of the total FW flow under Worst Case and Best Case conditions.

For one case studied, the trends of the RIH temperature drop and MW output loss due to increased FW bypass flow are shown in Figures 5.a and 5.b. If there is 50% FW flow bypassing the HP heater tube bundle, the RIH temperature will drop by about 1.1 °C. However, the gross electrical output will also be reduced by between 5.5 MW and 12.8 MW depending on the overall impact on cycle efficiency.

It was noted that the worst case production losses are similar in magnitude to the production losses incurred using boiler pressure reduction when turbine governor valves are at maximum opening, which is typical of units combating high RIH temperatures. However it was also observed that by reducing feedwater temperatures, less steam is generated in the boilers allowing additional boiler
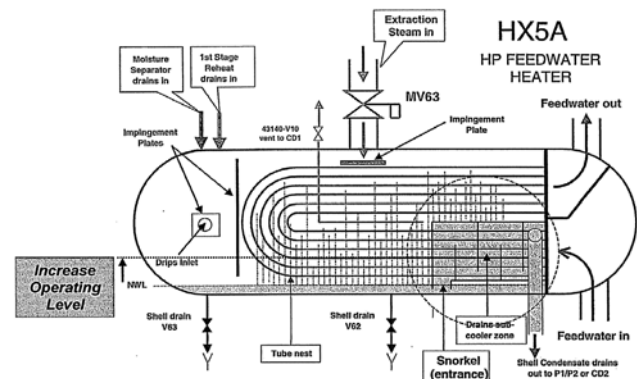

FIGURE 6: Partial flooding of HP FW heater shell side.

AECL NUCLEAR REVIEW
VOL 2, NUMBER 1, JUNE 2013

VALUE ADDITION INITIATIVES FOR CANDU® REACTOR OPERATION PERFORMANCE
V. CHUGH, R. PARMAR, J. SCHUT, J. SHERIN, H. XIE AND D. ZOBIN

pressure reduction without additional production losses and essentially doubling the achievable RIH temperature reduction. In the one example studied, by combining a 25% flow bypass with additional boiler pressure reduction, a 1.0 °C reduction was achieved with a 4 to 6 MW output loss compared to a 16 MW output loss using boiler pressure reduction alone.

The design envelope for the HP heaters must be considered as part of any design change in the plant. The HP heater shell pressure will be increased due to FW bypass flow, but is expected to be well within the shell design pressure. The FW temperature at the exit of the HP heater tube bundle will also increase and in one case studied the tube design temperature was exceeded if there was more than 30% bypass flow. In one worst case study, with more than 40% bypass flow, the reheater drains flow increased beyond the reheater drains pump performance capacity.

3.2 Partial flooding of HP FW Heater Shell Side

Shell side flooding of the HP FW heaters is an undesirable condition from the thermal performance point of view, but it can provide another means of reducing final FW temperatures for controlling RIH temperatures. As more and more tubes are covered in the horizontal heaters, as shown in Figure 6, the condensing area of the tube bundle is reduced, resulting in less heat transfer and increasing shell side pressure. This option may be effective alone or in combination with a fixed FW bypass flow providing a means of fine tuning final FW temperatures through changes in the heater operating levels.

The PEPSE turbine cycle model was used again to simulate this design changes and the aforementioned Worst Case and Best Case conditions were also applicable. Two sensitivity studies were carried out with varying amounts of tubing length assigned to the condensing section from 90% (normal operating state) to 70% of the total tubing length of the HP heaters under Worst Case and Best Case conditions, respectively. Structural considerations within the heater shell limited the reduction in condensing tube area to 70%.
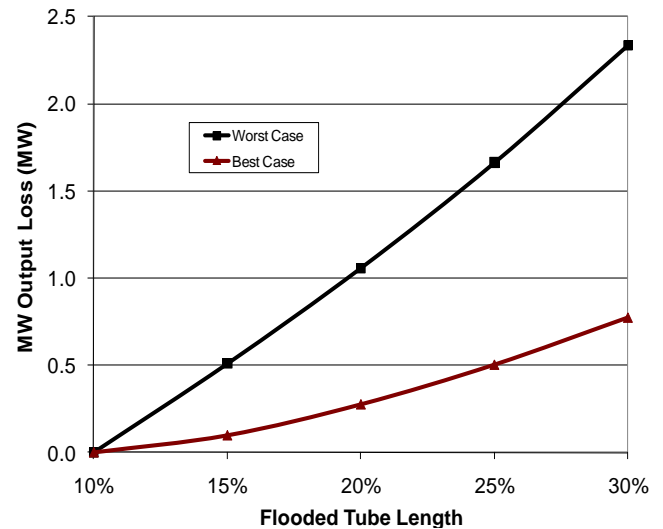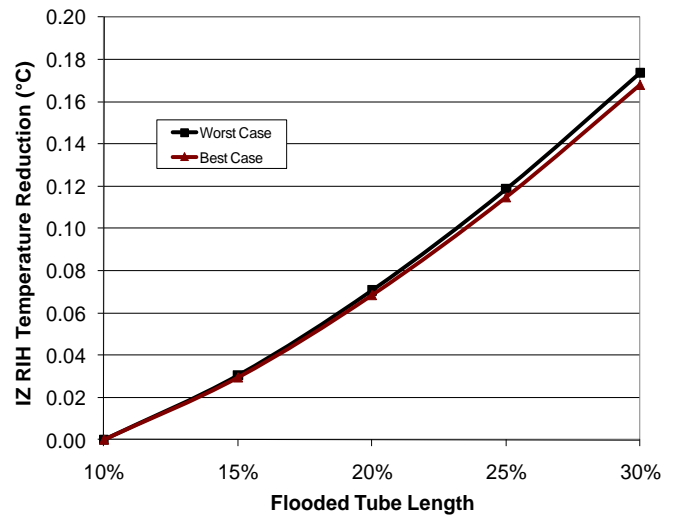

FIGURE 7A AND 7B: RIHT drop and electrical output loss due to partial flooding.

TABLE 1: Bruce B ECI PFUs

Baseline ECI PFU and Sensitivity Cases (Limit 1.00E-03) (For Instruments Eligible for Calibration Interval Extension by SOE Assessment)			
Accident Scenario	PFU at TI=1 Year (2010 Failure Rates)	PFU at TI=3 Years	
		2010 Failure Rates	2011 Failure Rates
Large LOCA	7.8E-04	8.8E-04	7.71E-04
Very Small LOCA	4.2E-04	5.3E-04	4.55E-04
In-core LOCA	7.9E-04	9.2E-04	7.51E-04

AECL NUCLEAR REVIEW
VOL 2, NUMBER 1, JUNE 2013

VALUE ADDITION INITIATIVES FOR CANDU® REACTOR OPERATION PERFORMANCE
V. CHUGH, R. PARMAR, J. SCHUT, J. SHERIN, H. XIE AND D. ZOBIN

The trends of the RIH temperature drop and MW output loss due to increased flooding are shown in Figures 7.a and 7.b. If the tubing length assigned to the condensing section is reduced from 90% (normal operating state) to 70%, i.e., the flooded tube length is increased from 10% to 30%, the RIH temperature will drop by about 0.17 °C. However, the gross electrical output will also be reduced by between 0.8 MW and 2.3 MW. Since the turbine inlet steam flow will also drop as the condensing tube length is reduced, as discussed previously, additional RIH temperature drop can be achieved for the same amount of flooding and MW loss. The HP heater shell pressure and reheater drains flow will be increased due to flooding, but are still expected to be below the shell design pressure and the reheater drains pump performance capacity.

4. Conclusions

4.1 Instrument Calibration Interval Optimization
To establish the proof of concept, As-Left/As-Found tolerances and available margins have been evaluated for the Bruce B ECI system instrument loops. This determines whether an extension of the current calibration period of one or two years to a three year period is justifiable. The incremental risk of non-compliance with the SOE is small and is acceptable. Out of a total of 277 instruments that were analyzed, 166 instruments (60%) are qualified for calibration interval extension up to three years. Sensitivity assessment of the effect of proposed changes in calibration intervals for 60% of the instruments on the ECI system unavailability has also been performed using the current Bruce Power ECI unavailability model. The results are shown in Table 1. Making these changes in the ECI system alone can result in ~$150k/year savings and maintenance scheduling flexibility at a fraction of the cost.

4.2 Reactor Thermal Power Optimization
A statistical model for reactor power compliance has been developed and applied to Bruce Power Units 5 and 8. The results are promising, showing feasibility of the model since it fits data well

• Preliminary results indicate that, with 95% confidence, we can state that the true reactor power is below 94.5% over the entire period of time when Set Power=93%.

• The robustness of the methodology is demonstrated by the fact that the average "sigma" estimates for Units 5 and 8 are the same.

• 0.5-0.75% of additional power production is predicted to be available once this study is completed.

4.3 Minor Design Changes for Controlling Reactor Inlet Header Temperatures in CANDU® Reactors
Based on the study findings, the design change feasibility is ranked high for HP FW heater bypass flow modification but marginal for HP FW heater level increase due to the significantly lower impact on RIH temperatures. The physical modification to the HP heater can be as simple as drilling holes in the channel partition plate to provide a bypass path for the flow or new bypass piping and valving could be installed around the HP heater to provide a means of adjusting the bypass flow for optimum RIH temperature control. Implementation of the minor design modification can provide significant increases in production over using boiler pressure reduction alone and can also be used to extend operating periods between steam generator cleanings for optimizing outage planning. In the one example studied, by combining a 25% flow bypass with additional boiler pressure reduction, a 1.0 °C reduction in RIHT was achieved with a 4 to 6 MWe output loss compared to a 16 MWe output loss using boiler pressure reduction alone.

REFERENCES
[1] D.L. Funk, E.L. Davis and John Lewis, 1998, "Instrument Drift Study: Ontario Hydro Bruce Nuclear Generating Station", EPRI Report TR-111348.
[2] E.L. Davis and D.L. Funk, 1998, "Guidelines for Instrument Calibration Extension/Reduction -- Revision 1: Statistical Analysis of Instrument Calibration Data", EPRI Report TR-103335-R1.
[3] A. Stuart and J.K. Ord, 1991, "Kendall's Advanced Theory of Statistics", Vol. 2, Oxford University Press, Oxford, United Kingdom.
[4] G.L. Minner et el, 2008, "PEPSE Use Input Description, Volume 1, Version 73", SCIENTECH a Curtiss Wright Flow Control Company, Cromwell, CT, USA.

Direct harvesting of Helium-3 (³He) from heavy water nuclear reactors

G. Bentoumi*, R. Didsbury, G. Jonkmans, L. Rodrigo and B. Sur

Atomic Energy of Canada Limited, Chalk River Laboratories, Chalk River, Ontario, Canada, K0J 1J0

*Corresponding author: (613) 584-3311, bentoumig@aecl.ca

The thermal neutron activation of deuterium inside a heavy-water-moderated or -cooled nuclear reactor produces a build-up of tritium in the heavy water. The in situ decay of tritium can, for certain reactor types and operating conditions, produce potentially useable amounts of ³He, which can be directly extracted via the heavy-water cover gas without first separating, collecting and storing tritium outside the reactor. It is estimated that the amount of ³He available for recovery from the moderator cover gas of a 700 MWe class Pressurized Heavy Water Reactor (PHWR) ranges from 0.1 to 0.7 m³ (STP) per annum, varying with the tritium activity buildup in the moderator. The harvesting of ³He would generate approximately 12.7 m³ (STP) of ³He, worth more than $30M at current market rates, over a typical 25-year operating cycle of the PHWR. This paper discusses the production of ³He in the moderator of a PHWR and its extraction from the ⁴He moderator cover gas system using conventional methods.

1. Introduction

³He is a rare isotope of helium that was previously produced mainly by the decay of tritium contained in thermonuclear warheads [1]. It has applications in science, industry and mainly in nuclear security and safeguards and medicine. ³He-gas-filled proportional counters are used, as neutron detectors, for the detection of illicit nuclear-materials at border security and control points. In medicine, ³He is used for real-time visualization of a patient's lung capacity and function.

Prior to 2001, the ³He production exceeded the demand and the ³He stockpile grew to about 235 m³. After that date, the demand for ³He for national-security-related applications greatly surpassed the production [1-3]. According to available data, the ³He produced in the USA at the current rate, alone, cannot meet the anticipated worldwide demand. The actual shortage raises ³He price to more than $2500 per litre. This new economic situation pushes research for new alternative sources of ³He.

Commercial PHWRs use heavy water (D_2O) in the moderator and the heat transport systems. Tritium (³H) is produced mostly in the moderator through thermal neutron activation of deuterium (²H) via the $^2H(n,\gamma)^3H$ capture reaction. ³He is then formed in the moderator as a result of tritium β-decay. The ³He formed can also be converted back to tritium via the reaction $^3He(n,p)^3H$. The thermal neutron absorption cross-section of $^3He(n,p)^3H$ reaction is about seven orders of magnitude greater than the cross-section for the reaction $^2H(n,\gamma)^3H$ [4]. However, due to its very low solubility in the heavy water, ³He escapes irreversibly in to the moderator cover gas. The residence time of ³He in the moderator water is therefore too short to convert a significant amount back to tritium. Consequently there is the potential to recover ³He from operating PHWRs.

2. Production of ³He in PHWRs

The moderator cover gas system circulates relatively pure helium gas (⁴He), and controls the amount of D_2 and DT present in the cover gas from radiolysis of the heavy water by catalytic recombination with oxygen. The total ⁴He inventory in the cover gas system of a typical 700 MWe class PHWR is about 7.65 m³. The solubility of ³He in the heavy water is very low. Consequently almost all of the ³He produced in the moderator is expected to reach the moderator cover gas.

AECL NUCLEAR REVIEW
VOL 2, NUMBER 1, JUNE 2013

DIRECT HARVESTING OF HELIUM-3 (3He) FROM HEAVY WATER NUCLEAR REACTORS
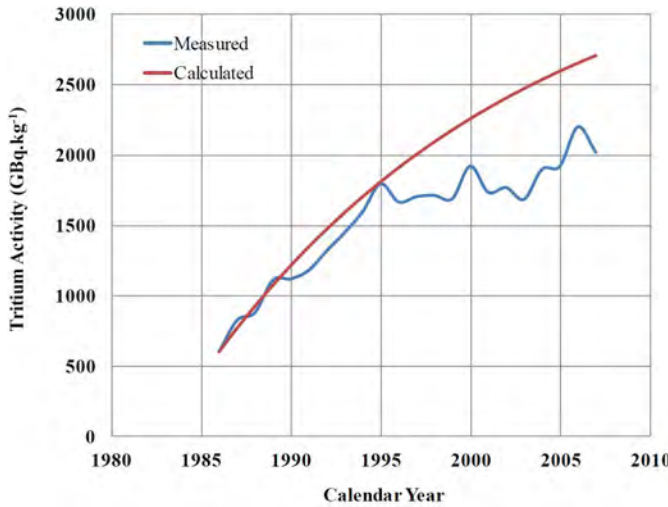G. BENTOUMI*, R. DIDSBURY, G. JONKMANS, L. RODRIGO AND B. SUR

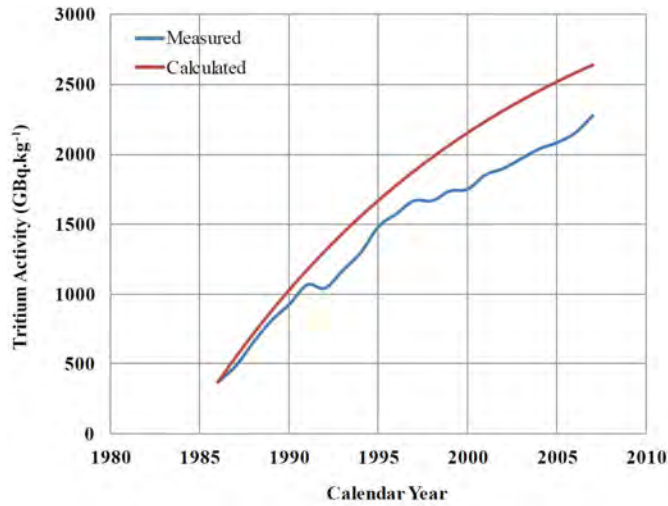FIGURE 1: Tritium activity in the moderator as a function of time at Canadian PHWR #1.

FIGURE 2: Tritium activity in the moderator as a function of time at Canadian PHWR #2.
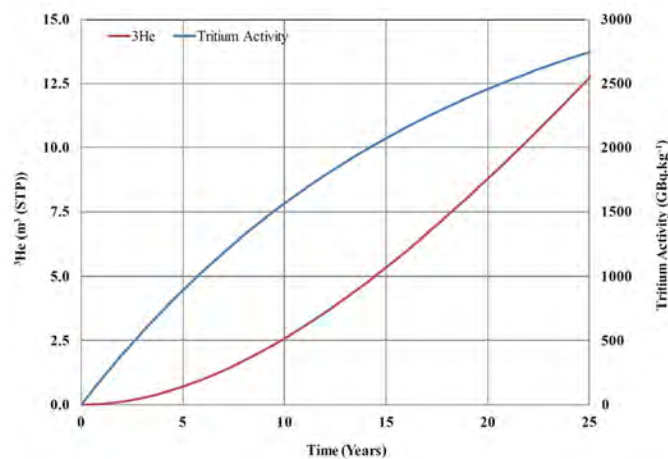

FIGURE 3: 3He volume and tritium activity as a function of time for a typical PHWR.

The rate of 3He production in the moderator is given by the rate of tritium β⁻ decay. Assuming that the rate of the 3He(n,p)3H reaction is negligible, the 3He production rate (atoms·s⁻¹) can be written as:

$$\frac{dN_{3He}}{dt} = M\lambda N_T = MA \tag{1}$$

where M is total heavy water inventory in the moderator (kg), N_{3He} is total number of 3He atoms in the moderator at time t (atoms), N_T is concentration of tritium atoms in the moderator (atoms·kg⁻¹), t is time (s), A is tritium activity (Bq·kg⁻¹), and λ is tritium decay constant (s⁻¹).

To solve equation (1), an estimate of the tritium concentration in the moderator as a function of time t is required. This can be done by using a mass balance for tritium in the moderator as given in reference [5]. The tritium activity in the moderator of a PHWR is then given by:

$$A = \lambda N_T = S(1 - e^{-\lambda t}) \tag{2}$$

with $\quad S = \varphi \sigma N_D \frac{m}{M} a$

where N_D is number density of deuterium atoms in the moderator (atoms·kg⁻¹), a is the reactor capacity factor, m is heavy water inventory under the neutron flux (kg), φ is thermal neutron flux (neutrons·cm⁻²·s⁻¹), and σ is thermal neutron absorption cross-section (cm²).

Equation (2) is derived based on the key simplifying assumption that the conversion of 3He back to tritium is negligible and make-up heavy water flow and heavy water loss rate are null. These assumptions lead to an overestimation of the tritium activity in the moderator. To calculate the tritium activity in the moderator of a 700 MWe class PHWR as a function of time, we have used the reference parameter values as shown in Table 1 [5]. The use of equation (2) to estimate the evolution of the moderator tritium activity with time was validated by comparing the obtained data, using equation (2), and real moderator activity measured at two Canadian PHWRs. These comparisons are shown in Figures 1 and 2. Considering the simplifying assumptions used in the derivation of equation (2), the calculated moderator activity values follow the measured values reasonably well. As expected, the calculated values are higher than the measured values as no loss of tritium from the moderator, other than from decay, was assumed in the derivation of equation (2). Also these results suggest that the contribution of reaction 3He(n,p)3H to the production of 3H in the moderator is not important. The results confirm the validity of Equation 2 for use in estimating the tritium activity in the moderator of PHWR reactors.

AECL NUCLEAR REVIEW
VOL 2, NUMBER 1, JUNE 2013

DIRECT HARVESTING OF HELIUM-3 (³HE) FROM HEAVY WATER NUCLEAR REACTORS
G. BENTOUMI*, R. DIDSBURY, G. JONKMANS, L. RODRIGO AND B. SUR

The ³He production rate in the moderator can now be written as:

$$\frac{dN_{3_{He}}}{dt} = MS(1 - e^{-\lambda t}) \qquad (3)$$

Table 2 shows the calculated ³He production rate as a function of the tritium activity in the moderator. Integration of Equation (3) gives an upper-bound estimate of the total number of ³He atoms in the moderator as a function of time. Even with a high activity, the maximum amount of ³He available for recovery from the helium cover gas is 0.67 m³ per annum (STP). Figure 3 shows that over the nominal operating life of the pressure tubes (25 years), a typical PHWR generates at most about 12.7 m³ (STP) of ³He in the moderator.

3. Recovery of ³He from the Moderator Cover Gas

There are several processing options available for consideration to recuperate ³He from the moderator cover gas of PHWRs. The schematic representation in Figure 4 illustrates some aspects of a heavy-water reactor. It includes a calandria containing a heavy-water moderator, calandria tubes with fuel channels, a system to circulate and control the chemical purity and temperature of the moderator and a moderator-cover-gas system to circulate and process the moderator-cover gas.

When the reactor is operated, a quantity of ³He gas is produced within the moderator liquid. Due to the extremely low solubility of ³He gas in heavy water, and as illustrated using arrows, the ³He gas preferentially migrates into the cover gas volume. As a result, the composition of the cover gas changes from pure ⁴He to a mixture of gases that could be extracted from the head space via the existing vapour recovery output. The cover gas outlet can be connected to any suitable downstream apparatus to separate ³He from the other gases (D_2, O_2, ⁴He, N_2...). Several processing options are available for consideration for the processing of moderator cover gas to extract high purity ³He. These include:

- Pre-enrichment with "heat-flush" method and final enrichment with distillation [7-10],
- Pre-enrichment with "super-leak" method and final enrichment with distillation [7-12], and
- Pre-enrichment with "super-leak" method and final enrichment with thermal diffusion [6, 7, 11, 12].

Most of the information available on these processes is based on small-scale laboratory systems. Consequently some R&D effort will be required for concept testing and for obtaining design information. Assuming an average processing time of 100 days per year, a system capable of
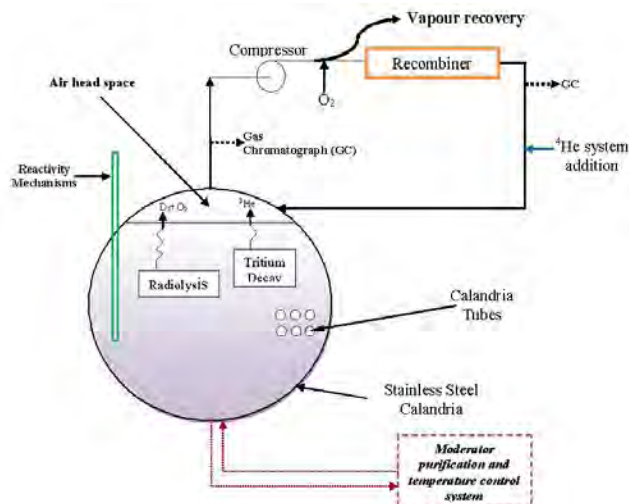

FIGURE 4: A schematic representation of a heavy water nuclear reactor.

producing the final product at a maximum rate of 5 L.d⁻¹ is more than adequate for processing the recovered cover gas.

The ³He extraction stream can be drawn from the moderator cover gas system while the reactor is in use. In this configuration, the gas outlet stream may be extracted at a generally uniform flow rate. Alternatively, the flow rate of the gas-outlet stream may vary over time and/or in response to operating conditions of the reactor. Operating continuously in an online configuration may allow the ³He gas to be constantly extracted from the moderator cover gas. While this on-line configuration has the advantage of minimizing ³He loss, it is also likely to consume more power. The alternative is to run the ³He extraction process occasionally, say during the periodic maintenance outage of

TABLE 1: Typical Parameter Values for 700 MWe Class PHWR

Parameter	Value
M	2.57×10^5 kg
N_T	Variable (atoms.kg⁻¹)
N_D	6.01×10^{25} (atoms.kg⁻¹)
a	85%
m	1.90×10^5 (kg)
φ	2.30×10^{14} (neutrons.cm⁻².s⁻¹)
σ	4.19×10^{-28} (m²)
λ	1.78×10^{-9} (s⁻¹)

AECL NUCLEAR REVIEW
VOL 2, NUMBER 1, JUNE 2013

DIRECT HARVESTING OF HELIUM-3 (^{3}HE) FROM HEAVY WATER NUCLEAR REACTORS
G. BENTOUMI*, R. DIDSBURY, G. JONKMANS, L. RODRIGO AND B. SUR

TABLE 2: Estimated ^{3}He Production Rate
per Year in a 700 MWe class PHWR

Moderator Activity (GBq·kg^{-1})	^{3}He Production Rate (m^3(STP)·a^{-1})
370	0.11
740	0.22
1110	0.34
1480	0.45
1850	0.56
2220	0.67

TABLE 3: Estimated Percent of ^{3}He
in the Recovered Helium Gas

Moderator Activity (GBq·kg^{-1})	^{3}He in Recovered Helium (PPMv)
370	130
740	260
1110	410
1480	540
1850	670
2220	800

the plant. However, in such a batch mode, the consequence of helium loss becomes much more serious. The daily helium-loss rate associated with the purges and cover gas leaks could typically be as high as 30% of the moderator cover gas inventory. Consequently, to efficiently recover ^{3}He from the moderator cover gas system, it is necessary to collect all the helium lost due to cover-gas purges and from leaks during operations and treat the collected gas in batch mode. This means a need to collect ~838 m^3 per year of helium to recover most of the ^{3}He produced in a PHWR reactor. Table 3 shows the amount of ^{3}He in the recovered helium gas, as a function of the average moderator activity. Even in this inflated cover gas volume (because of the need to recover all the purge and leaked gas), the amount of ^{3}He in the recovered helium moderator cover gas is significantly higher by a factor of ~100 to ~600 than the amount of naturally abundant ^{3}He (1.37 ppmv) found in the atmosphere.

4. Conclusion

The production and extraction of ^{3}He directly from the moderator cover gas system in PHWRs is discussed. The amount of ^{3}He that can be potentially recovered from the moderator-cover gas depends on the moderator tritium activity and is in the range from ~0.1 to 0.7 m^3 (STP) per year for a typical single-unit 700 MWe class PHWR reactor. A crucial factor in determining the optimum method and cost of ^{3}He recovery is the loss and make-up rate of the moderator cover gas which can be as high as 30% of the total cover gas inventory per day. Consequently, the feasibility of efficiently harvesting ^{3}He from the cover gas depends on the ability to either process the cover gas continuously at a rate comparable to or greater than the loss rate or to recover most of the helium that escapes the cover-gas system in order to run a batch-mode-extraction process.

References
[1] D.A. Shea and D. Morgan. The Helium-3 Shortage: Supply, Demand, and Options for Congress, Congressional Research Service, 2010 December. Available at URL: http://www.fas.org/sgp/crs/misc/R41419.pdf
[2] J. Bentz et al., US Government Approach to Addressing the He-3 Shortage. 2011 July. www.cstsp.aaas.org/Helium3/USGApproach.pdf
[3] M. McElroy, AAAS News Release - AAAS Workshop Explores How to Meet Demand for Helium-3 in Medicine, Industry, and Security, 2010 April. Available from URL: http://www.aaas.org/news/releases/2010/0423helium3.shtml.
[4] G.F. Thomas, Evolution of the Isotopic in CANDU™ Moderator Systems and in the Thermal Neutron Activation of Helium-3, Ann. Nucl. Energy, 19(7) pp. 409-412 (1992).
[5] M.J. Song, S.H. Son, C.H. Jang, Tritium inventory prediction in a CANDU plant, Waste Management Journal, 15(8), pp. 593-598(1995)
[6] B.B. Mcinteer, L.T. Aldrich, A.O. Nier, Concentration of He^3 by Thermal Diffusion, Phys. Rev. 74(8), pp. 946-949 (1948).
[7] W.R. Wilkes, A continuous-distillation apparatus for the separation of He^3 from He4, Advances in Cryogenic Engineering, 16, pp. 298-301 (1970).
[8] C.T. Lane, H.A. Fairbank, L.T. Aldrich, A.O. Nier, He^3 Separation by a Heat Flux in Liquid Helium II, Phys. Rev. 73(3), pp. 256-257 (1948).
[9] T. Soller, W.M. Fairbank, A.D. Crowell, The Rapid Separation of He^3 from He^4 by the "Heat Flush" Method, Phys. Rev. 91(5), pp. 1058-1060 (1953).
[10] C.A. Reynolds, H.A. Fairbank, C.T. Lane, B.B. Mcinteer, A.O. Nier, "Heat Flush" Method of He^3 Separation, Phys. Rev. 76(1), pp. 64-66 (1949).
[11] J.G. Daunt, R.E. Probst, H.L. Johnston, The Separation of the Isotopes He^3 and He^4 in the Liquid Phase, J. Chem. Phys., 15(10), pp. 1759-760 (1947).
[12] K.R. Atkins, D.R. Lovejoy, A Method of Concentrating He^3-He^4 Mixtures, Can. J. Phys., 32(11), pp. 702-707 (1954).
[13] V.V. Dmitriev, L.V. Levitin, V.V. Zavjalov, D. Ye Zmeev, Separation of ^{3}He from ^{3}He-^{4}He Mixture by means of Adsorption, J. Low. Temp. Phys., 138 (3/4), pp. 877-880 (2005).

A New Safety Principle for the SLOWPOKE-2 Reactor

S. Yue[1], S. Polugari[1,2], V. Anghel[1], J. Hilborn[3] and B. Sur[1]

[1] Atomic Energy of Canada Limited, Chalk River Laboratories, Chalk River, Ontario, Canada, K0J 1J0
[2] Ryerson University, Toronto, Ontario, Canada
[3] Deep River, Ontario, Canada

Nomenclature

SLOWPOKE	Safe LOW-POwer Critical Experiment
LEU	Low Enriched Uranium
SLOWKIN	a software name for SLOWPOKE reactor simulation
PI controller	Proportional-Integral controller

SLOWPOKE-2 (LEU core) is a pool-type nuclear reactor with a maximum nominal thermal power of 20 kW. It uses a pelletized uranium oxide fuel (19.9% enrichment) and provides a useful high neutron flux in the order of 10^{12} n.cm^{2}s^{-1}. The key safety features built into the reactor design are the strictly limited amount of excess reactivity and the negative reactivity feedback characteristics, which provide a demonstrably safe self-limiting power excursion response to large reactivity insertions. However, the limited amount of excess reactivity also limits continuous prolonged reactor operation at full power. With a 4 mk excess reactivity, the reactor can operate for about one day at full power, 20 kW, before criticality is lost due to temperature effects and xenon poisoning. A new safety concept is proposed in this paper that enables the continuous operation to a few months by increasing the excess reactivity from 4 mk to 8 mk. A Matlab/simulink model of SLOWPOKE-2 has demonstrated that core operation life can be extended to several months without adding a beryllium shim.

1. Introduction

The SLOWPOKE-2 reactor is a small pool-type nuclear reactor with a light water moderator. The reactor container consists of a lower and an upper section, with the critical assembly being contained in the lower section. The upper section is essentially an extension tube providing the depth of water necessary for effective radiation shielding and cooling of the core.

The outside diameters of both reactor container sections are 61 cm. The lower section is 0.83 m deep, and the upper section is 4.44 m long [1]. The critical assembly is located in the lower section and consists of fuel core, beryllium reflector, and water reflector. Detailed information of the reactor and pool can be found in reference [1] for a SLOWPOKE core.

With an excess reactivity of 4 mk, the LEU reactor core can operate continuously at nominal full power of 20 kW for about one day depending on the cooling water temperature of the pool water. Eventually, xenon buildup and the increasing pool temperature restrict the operation at full power. To return the reactor back to full power, it has to be shut down for an appropriate time to allow the xenon to decay and pool water to cool. The main source of long-term reactivity loss is due to the slow growth of the stable poison isotope samarium-149 and the burn-up of uranium-235, which is currently compensated by beryllium plate addition on top of the core, but at extra cost.

Higher excess reactivity is needed in order to continuously operate the reactor for longer periods. However, the current license of all SLOWPOKE-2 installations states that the maximum excess reactivity shall not exceed 4 mk. Hence, a detailed analysis is required to demonstrate that the SLOWPOKE-2 reactor could be operated safely at higher excess reactivity.

2. Safety Principle of Current SLOWPOKE and New Proposal

From the beginning, inherent safety has been a cornerstone of the SLOWPOKE-2 concept. Here are the original safety principles:

- Maximum excess reactivity less than prompt critical by design.
- Core lattice under-moderated.
- Negative temperature and void coefficients of reactivity.
- Core sub-critical in water without the reflectors.

With these safety principles applied in the design, the SLOWPOKE-2 reactors have the specific safety feature of an inherent self-limiting feedback, which allows fully remotely attended operation and justifies the absence of an engineered, fast-response shutdown system.

Transient tests at Chalk River Laboratories in 1970 demonstrated that loss-of-control accidents approaching prompt critical can be safely limited by the negative reactivity coefficients. A rapid removal of the control rod injecting 6.8 mk of reactivity, resulted in a power peak of 180 kW and a coolant temperature peak of 95 °C [2].

Operation at full power (20 kW) is limited to about one day, before the reactivity loss from rising temperature and increasing Xe-135 exceed the maximum allowable excess reactivity. To overcome this limitation, John Hilborn, one of the original designers of SLOWPOKE-2, proposed the following new safety principles, which permits higher power with much greater reactivity loss from xenon and temperature, without complex engineered shutdown systems, stringent safety requirements and electrical sequencing of control rods.

Instead of limiting maximum excess reactivity to less than prompt critical by design, the rate of reactivity addition is limited by design.

- Reactivity worth of multiple motor-driven control absorbers each less than prompt critical by design.
- Removal times of motor-driven absorbers are designed to match the inherent negative reactivity rates of SLOWPOKE as follows:
  - Start-up and automatic control (4 mk) – 20 seconds;
  - Xenon (2 mk) – 24 hours;
  - Samarium and fuel burn-up (2 mk) – 180 days.

Assuming the total range of reactivity control is –1 mk to +8 mk, full withdrawal of the start-up and automatic control rod in 20 seconds adds 4 mk, as in the current SLOWPOKE reactor. That absorber will control the fast-power transient

at startup caused by delayed neutrons, and then compensate for rising temperature over a period of minutes and hours. The maximum xenon reactivity worth at nominal full power of 20 kW is about 2.6 mk [1]. Hence a 2 mk absorber rod is used to compensate for xenon-135 poisoning. Since xenon reduces the reactor reactivity by ~ 2 mk after 1 day, the full travel time of this rod is set to 24 hours. Then for a period of years, the main source of long-term reactivity loss is due to the slow growth of the stable poison isotope samarium-149 and the burn-up of uranium-235.

At 40 kW·a, the reactivity loss of the core is about 10 mk [1], which means that the reactor loses 5 mk for one year of continuous operation at full power (20 kW). In this study, a 2 mk burn-up compensation rod is used only for the purpose of demonstration. Since the burn-up takes place slowly, the withdrawal time of this fuel burn-up compensation rod is set at 180 days.

With the above configuration, the reactor needs to be shimmed up to 8 mk excess reactivity, which is slightly less than prompt critical at 8.19 mk [3]. The reactor would be prompt critical if all these excess reactivities were applied to a fresh core at once. The withdrawal speed of the control rods then plays an important role in the transient behavior of the reactor.

Validating and licensing the new safety principles would be a first step towards up-rating the SLOWPOKE-2 reactor to a higher maximum excess reactivity limit. These new safety principles are demonstrated with two slow-speed absorbers and one higher speed absorber using a SLOWPOKE-2 simulator. The loss-of-control accident, starting from shutdown, is demonstrated by turning off the pool-water cooling system and withdrawing all three absorbers at their maximum speeds.

3. Computer Dynamic Model

A computer dynamic model for SLOWPOKE-2, which is called SLOWKIN, was developed at École Polytechnique de Montreal in the 90's. The SLOWKIN model was intended to simulate reactor transients caused by the single control rod displacements during commissioning of the new LEU core [3]. However, to implement the current proposal, a more flexible model is required. Therefore, the equations used in SLOWKIN were taken as reference and implemented in Simulink/MatLab for the present work.

Because the core is tightly coupled neutronically, only about 0.227 m high and 0.221 m in diameter, a point kinetics model is used to predict the change of reactor power with time. The core region is then subdivided into 10 axial planes in the vertical direction, and only radial (horizontal) heat transfer is considered. The power from each axial plane is

calculated based on the flux shape in the vertical direction. The coolant in the reactor vessel is in natural circulation, and the flow rate is calculated based on the measured inlet and outlet temperatures. The heat transfers between the fuel, the coolant, the beryllium reflector, the container of the reactor, the pool water and the pool-cooling system are all taken into account.

The Zr-4 fuel sheath temperature exceeds the water saturation temperature during a transient or high-power operation. In this case, the onset of nucleate boiling will occur. Therefore, the void fraction is calculated in this model. The void is highly dependent on local conditions, mainly the sheath temperature. So the fuel pins are grouped into 10 sub-groups for each of the axial planes based on the radial neutron flux shape. The sheath temperatures of each sub-group are calculated from their power and then the void fraction is computed. At high power, the void fraction could dominate the negative reactivity feedback.

This work introduces three rods, two slow rods and one fast rod, into the control system. It is assumed that all three rods are withdrawn simultaneously, but at different rates, which are limited by a fail-safe mechanism. A PI controller is used for the fast control rod to stabilize the reactor to target power. The two slow rods simply follow the xenon buildup and the burn-up of the reactor core. For fast transient analysis, the controller is disabled and all three rods are withdrawn in parallel at their maximum withdrawal rate. The model has been tested and fine-tuned to be consistent with SLOWKIN.

4. Simulation of Reactor Fast Transients
A fast transient happens in a few minutes; hence the burn-up of the core does not play a role. However, the analysis in this section considers that all of the three rods are withdrawn in parallel at their maximum withdrawal speed.

As the first step of proving the safety principle in the proposal, we assume the fast-control-rod reactivity worth is the same as the current SLOWPOKE-2 control rod, which brings the reactor reactivity to about 4 mk with full withdrawal [1]. A 2 mk worth xenon reactivity compensation rod with a full travel time of 1 day is used in the simulation. The burn-up compensation rod also has 2 mk reactivity worth, but with much longer travelling time, 180 days. With all of the three rods full inserted in the fresh core, the reactor reactivity is negative 1.2 mk.

Various scenarios have to be considered in the safety analysis. Here, as the author is limited by the length of the paper, only one scenario is presented. In this scenario, all three control rods are simultaneously withdrawn at full speed, starting from cold shutdown, the peak power should still be self-limited and not significantly exceed 69 kW, which is consistent with the self-limiting peak power during École Polytechnique LEU commissioning with 4 mk excess reactivity.

Figure 1 (a) shows the simulations with all three rods being withdrawn. As a comparison, Figure 1 (b) shows the results with only the fast rod withdrawn at the fastest speed. If all rods are withdrawn simultaneously, the fast rod is fully withdrawn in 20 seconds at 0.26 mk/s, while the slow xenon compensation rod only moves at 2mk/3600/24 = 0.000023 mk/s. This is 10,000 times slower than the fast control rod. The burn-up compensation rod has an even slower speed. The peak occurs at about 270 seconds, when the reactivity worth from the two slow rods is minimal, about 0.0063 mk. Compared to the 4 mk reactivity worth from the fast rod, this slow rod does not make any difference, which can be seen from the transient curves in Figure 1 a) and b). Since no self-limiting power transient for SLOWPOKE-2 (LEU core) has been published in the public domain, a measured transient of a HEU core with 3.97 mk reactivity insertion is shown in Figure 2 [2]. The peak power is similar to the simulation, but with a slower rise rate.

5. Simulation of Reactor Long-term Operation
In this section, the long-term operation at full power (20 kW) is simulated with various configurations. Since the reactor power has to be stable at 20 kW, a rod controller is introduced in the model to manipulate the three rods to stabilize the reactor power. The fast control rod is controlled by a PI controller to take immediate action for adjusting the power. The xenon compensation rod follows the Xenon accumulation, but with a limited withdrawal speed (2 mk/day). The burn-up compensation rod is withdrawn at very slow speed (2 mk/180 days) to compensate for the burn-up negative reactivity. In this simulation, this burn-up compensation rod is automatically controlled. However, in reality, this rod can be manually withdrawn once a week or once a month with a slightly higher speed.

Four sets of simulation results are presented with the configurations of: 1) only the fast control rod functioning, 2) xenon compensation rod and fast control rod functioning, 3) all three control rods functioning, 4) all three control rods functioning and with very high-efficiency pool-cooling system functioning.

a. Only fast control rod functioning

The reactor can operate at full power (20 kW) for about one day with only the fast rod. Figure 3 shows the reactor power and the coolant temperature changes in this case. Because the coolant temperature and fuel temperature
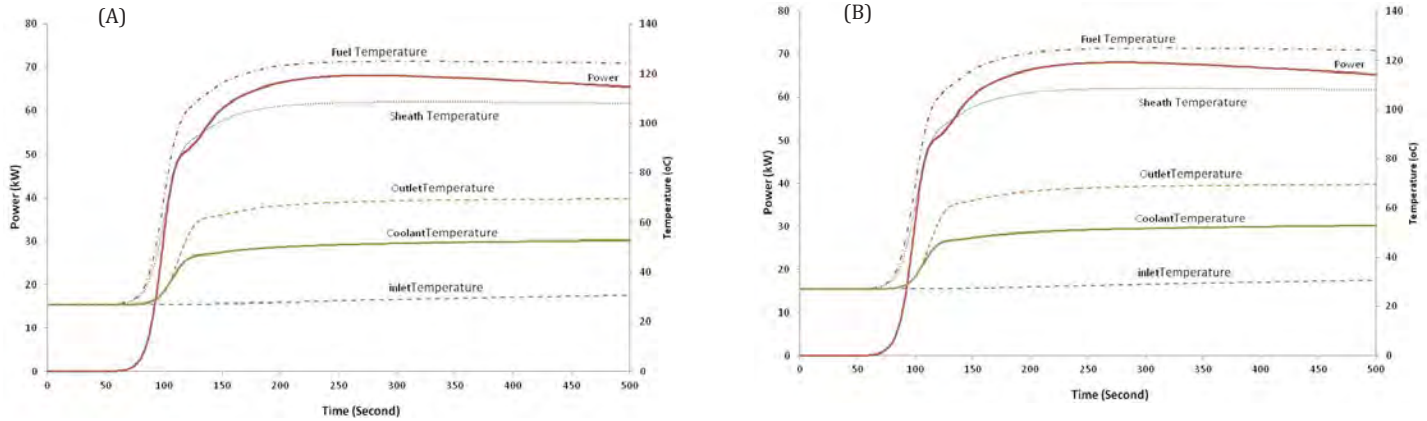
FIGURE 1: Transient simulation with a) one control rod b) three control rods.

are increasing with time, the negative reactivity from temperature feedback is also increasing in the first 24 hours. The reactivity variations from coolant temperature and the xenon accumulation are shown in Figure 4.

The fast rod is controlled by the PI controller to maintain the reactor power at 20 kW. To compensate for the reactivity loss, the controller withdraws the fast rod slowly and reaches the maximum, 4 mk, in about 24 hours. Without enough reactivity compensation, the reactor power starts to decrease after 24 hours. Hence, the coolant temperature decreases and the xenon reactivity starts to stabilize at about -1.8 mk.

b. Fast control rod and xenon compensation rod functioning

The purpose of the slow xenon compensation rod is to compensate for the temporary reactivity loss due to xenon poisoning. A 2 mk reactivity worth is assigned to this rod

in the simulation. With both rods functioning, the reactor can operate continuously for about 60 hours, as shown in Figure 5. The xenon reactivity reaches equilibrium at about 2.4 mk after 2 days. However, the pool-water temperature increases continuously. Consequently, it causes the coolant temperature to increase accordingly. Eventually, the strong negative feedback from higher coolant temperature brings the reactor power down to a lower level as shown in Figures 5 and 6.

c. All three rods functioning

The purpose of the burn-up compensation rod is to compensate for the permanent reactivity loss from the stable-poison isotopes, such as samarium-149, and the burn-up of uranium-235. For demonstration purposes, a 2 mk reactivity is assigned to the burn-up compensation rod, which has a full travel time of 180 days. In this simulation, the pool-water temperature, coolant temperature, fuel temperature all start from 20 ^{o}C.
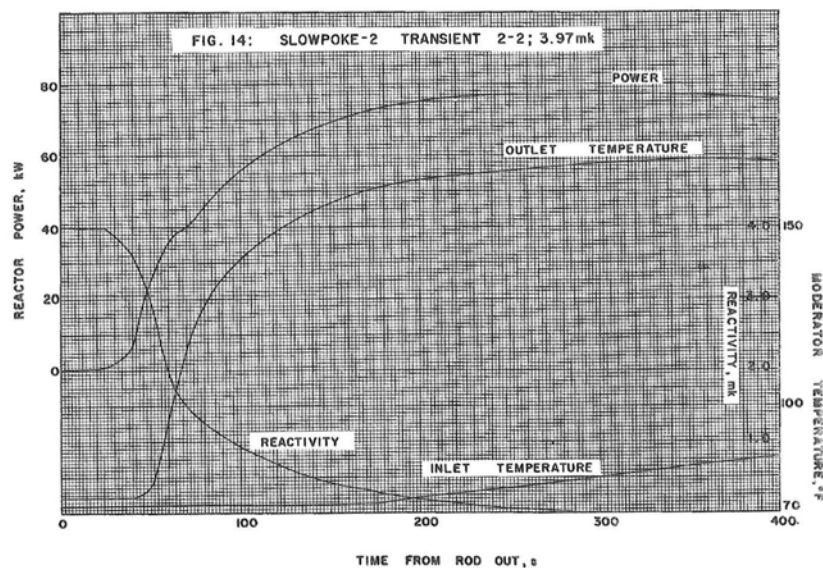

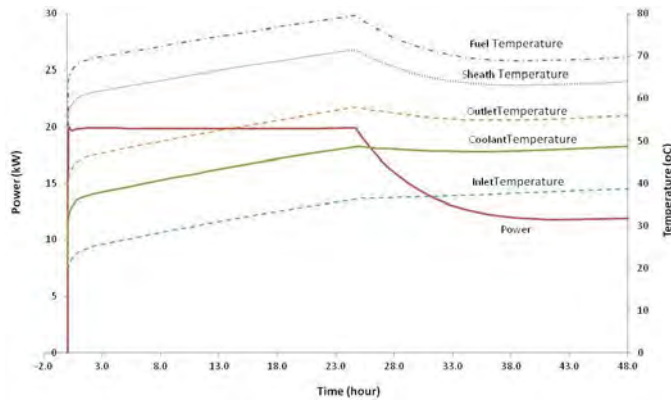FIGURE 2: Transient of SLOWPOKE-2 (HEU,3.97 mk) [2].

FIGURE 3: Power & temperature,
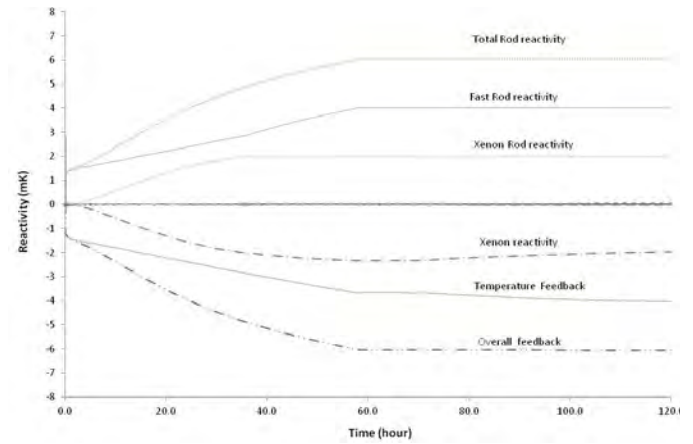operation at 20 kW with 1 fast rod.

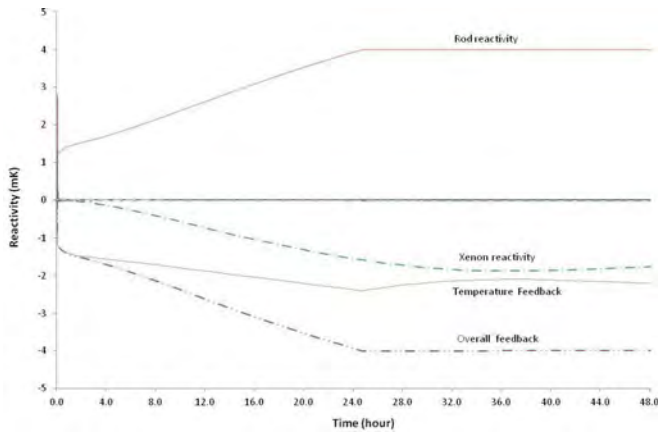FIGURE 6: Reactivity feedback, operation
at 20 kW with two rods.

FIGURE 4: Reactivity feedback, operation
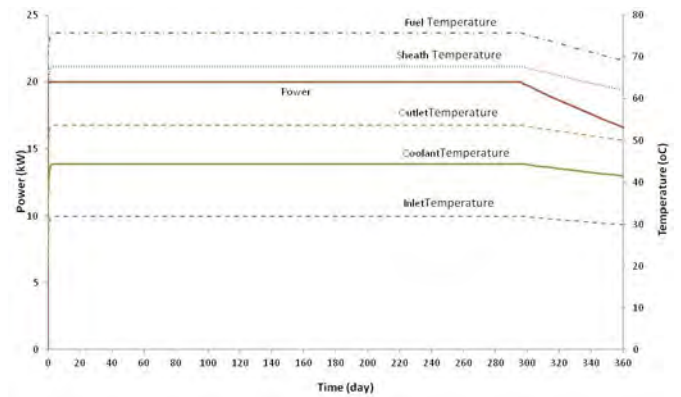at 20 kW with 1 fast rod.

FIGURE 7: Power & temperatures, operation
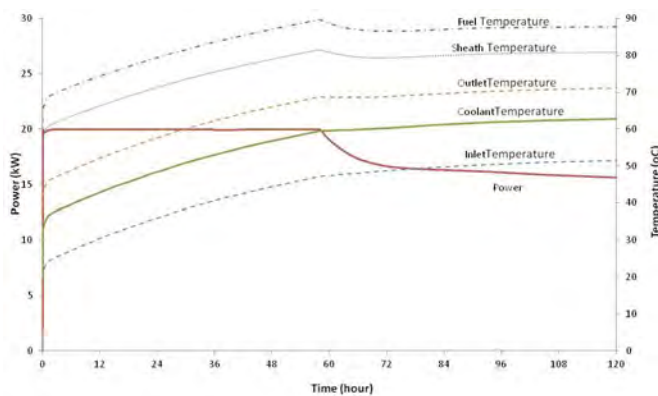at 20 kW with three rods, high cooling.

FIGURE 5: Power & temperatures,
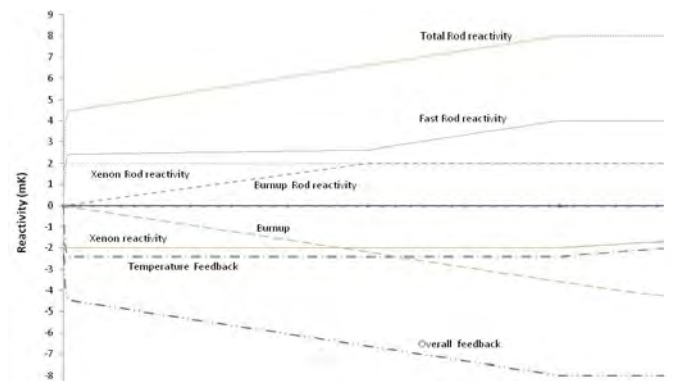operation at 20 kW with two rods.

FIGURE 8: Reactivity feedback, operation
at 20 kW with three rods, high cooling.

It was expected that the reactor should run for weeks or months with this burn-up compensation rod. However, the results show exactly the same curves as Figures 5 and 6. The reactor power decreases after about 60 hours.

The fact is that the slow rod for burn-up compensation has not taken effect at 60 hours because of its slow withdrawal rate (2 mk/180 days). Only the xenon compensation rod provides an extra 2 mk reactivity to reduce the xenon poisoning. With the power at 20 kW, the pool-water temperature increases continuously, eventually the strong negative feedback from higher coolant temperature causes the reactor power to drop.

The pool water has a very large volume, but limited cooling capability. A cooling coil, with about 1.29 m^2 heat transfer area, is immersed in the pool to remove the heat. City water is normally passed through the coil and then discharged to the building drain. At the maximum cooling water flow, 4 kW/hour of the heat could be removed with a temperature difference of 9 ^{o}C between the pool water and the cooling water. The temperature rise for eight hours operation at 20 kW would be about 5.2 ^{o}C [1]. This is not significant for short-period operation of the SLOWPOKE reactor. However, for continuously operation, this cooling coil limits the total operation time.

d. All three rods functioning with a high efficiency pool cooling system

To improve the heat removal capability of the pool, we assume that the cooling coil has five times the current heat exchange area. The simulation results are shown in Figures 7 and 8.

The coolant temperature increases only about 12 ^{o}C at 20 kW power for long-term operation with the high-efficiency cooling system. In this case, the negative reactivity feedback from the water temperature is about 2 mk compared with 4 mk using the current cooling system. With the pool temperature limited, both the xenon compensation rod and the burn-up compensation rod function as expected. The reactor could operate continuously for about 300 days when started with a fresh core.

6. Conclusion
The current reactivity management system for SLOWPOKE reactors ensures that the overall reactivity of the reactor will never exceed prompt critical. Hence, the self-limiting power-excursion feature of the reactor keeps the reactor inherently safe. However, continuous operation time is constrained by this limited excess reactivity.

The new safety principle, proposed by John Hilborn, deploys a fast control rod and two slow compensation rods for xenon poisoning and long-term burn-up respectively with limited withdrawal speed matching the xenon poison accumulation and the burn-up rate. The overall reactivity worth of the rods could exceed prompt critical. However, any single rod reactivity worth is still lower than the prompt critical.

This study demonstrates that the new safety principle for the SLOWPOKE reactor works well. However, the low capacity of the current pool-cooling system needs to be improved in order to allow the reactor to operate continuously for long time periods.

REFERENCES:
[1] R.E. Kay, P.D. Stevens-Guille, J.W. Hilborn, and R.E. Jervis, 1973, "SLOWPOKE: A New Low Cost Laboratory Reactor," Int. J. Appl. Radiation and Isotopes, 24(9), pp. 509-518.
[2] R.E. Kay, J.W. Hilborn and N.B. Poulsen, The Self-limiting Power Excursion Behaviour of the SLOWPOKE Reactor, Results of Experiments and Qualitative Explanation, Report AECL-4770, January 1976.
[3] D. Rozon and S. Kaveh, SLOWKIN: A Simplified Model for the Simulation of Transients in a SLOWPOKE-2 Reactor, Report IGE-219 Rev 1, Ecole Polytechnique, 1997 August. Available from https://canteach.candu.org/Content%20Library/20043405.pdf.

Erratum, for "The Supersafe© Reactor: A Small Modular Pressure Tube SCWR"

M. Yetisir[1], J. Pencer[1*], M. McDonald[1], M. Gaudet[1], J. Licht[1] and R. Duffey[2]

[1] Atomic Energy of Canada Limited, Chalk River Laboratories, Chalk River, Ontario, Canada, K0J 1J0
[2] DSM Associates Inc., Idaho, USA

*Corresponding Author: (613) 584-8811 x46267, pencerj@aecl.ca

Erratum

In the December 2012 edition of the *AECL Nuclear Review, Volume 1, Number 2,* in Section 5 of the article "The Supersafe© Reactor: A Small Modular Pressure Tube SCWR", when defining the two Figure of Merit (FOM) formulas, the dose rate variable D is the dose rate in rem/hr at a distance of 1 meter. It was omitted that this dose rate should be calculated for a mass of 0.2M, where M is the bare critical mass (in kilograms) of the material.